



**HAL**  
open science

# Significance of Coupling of Distributed Fibre Optic Sensor Systems for Vertical Seismic Profiling

Sven Schilke

► **To cite this version:**

Sven Schilke. Significance of Coupling of Distributed Fibre Optic Sensor Systems for Vertical Seismic Profiling. Earth Sciences. Université Paris sciences et lettres, 2017. English. NNT : 2017PSLEM042 . tel-01789878

**HAL Id: tel-01789878**

**<https://pastel.hal.science/tel-01789878>**

Submitted on 11 May 2018

**HAL** is a multi-disciplinary open access archive for the deposit and dissemination of scientific research documents, whether they are published or not. The documents may come from teaching and research institutions in France or abroad, or from public or private research centers.

L'archive ouverte pluridisciplinaire **HAL**, est destinée au dépôt et à la diffusion de documents scientifiques de niveau recherche, publiés ou non, émanant des établissements d'enseignement et de recherche français ou étrangers, des laboratoires publics ou privés.

# THÈSE DE DOCTORAT

de l'Université de recherche Paris Sciences et Lettres  
PSL Research University

Préparée à MINES ParisTech

Significance of Coupling of Distributed Fibre Optic Sensor Systems for  
Vertical Seismic Profiling

Importance du couplage des capteurs distribués à fibre optique dans le cadre  
des VSP

**École doctorale n°398**

GÉOSCIENCES, RESSOURCES NATURELLES ET ENVIRONNEMENT

**Spécialité** GÉOSCIENCES ET GÉOINGÉNIERIE

## COMPOSITION DU JURY :

M. Frédéric Pellet  
Professeur, MINES ParisTech  
Président du jury

M. Guy G. Drijkoningen  
Professeur associé, TU Delft  
Rapporteur

M. Douglas R. Schmitt  
Professeur, University of Alberta  
Rapporteur

M. Arthur H. Hartog  
Directeur de Recherche, Schlumberger  
Examineur

M. James E. Martin  
Directeur de Recherche, Reece Innovation  
Examineur

Mme Daniela Donno  
Chargée de Recherche, MINES ParisTech  
Examinatrice

M. Hervé Chauris  
Professeur, MINES ParisTech  
Examineur

Soutenue par **Sven SCHILKE**  
le 16 juin 2017

Dirigée par **Hervé CHAURIS**





## Acknowledgements

Over the past three and a half years a lot of people helped and contributed to this work. First of all, I want to thank my two supervisors Daniela Donno and Arthur Hartog. I would like to thank them for their persistence and encouragement throughout the PhD. Their continuous help and advice and thorough knowledge of seismics and fibre optics made it easier, if not possible, for me to complete this PhD work.

I need to thank Ian Bradford who convinced me to continue my academic career with a PhD and who continued the PhD supervision until he sadly passed away.

I wish to thank Alireza Farahani for long discussions about continuum mechanics and letting me benefit from his enormous expertise of the finite-element analysis before he left Schlumberger. I also want to acknowledge Iamid Pico from the SLB research centre in Moscow for his help and advisory related to the FEA.

I would like to thank Hervé Chauris for his help and careful reviews and to take the project under his supervision and Véronique Lachasse for her help with all the administrative matters I encountered in France.

I want to thank Doug Schmidt and Guy Drijkoningen to agree to review the thesis as well as Frédéric Pellet. I thank James Martin for initiating the PhD project and remaining a part of the jury.

I would like to acknowledge Daniele Molteni, Gwenola Michaud, Ali Özbek and John Michael Williams from the Schlumberger Gould Research Center in Cambridge for fruitful discussions during bi-weekly meetings.

Last but not least, I want to thank my parents Michael and Heidi and my brother Björn for their support throughout my life and their encouragement whenever I need it.



## Abstract

In exploration geophysics, Vertical Seismic Profiling (VSP) is a class of borehole seismic measurement. The purpose of VSP surveys is usually the development of velocity profiles, the calibration of pre-existing surface seismic data profiles, or more advanced surveys like permanent reservoir monitoring. Depending on the final goal and on the desired spatial resolution, many surveys require a significant number of conventional seismic sensors to be placed in short spatial increments along the well. As boreholes can span a length of several kilometers, the number of required point sensors is large, while at the same time the high temperature and the high hydrostatic pressure in boreholes can lead to damage or failure of downhole electronics. Consequently, many VSP surveys are carried out such that the sensors are lowered into the borehole temporarily, data is acquired and the sensors are recovered. This temporary installation complicates or even prevents surveys like time-lapse seismic and permanent monitoring. In order to avoid frequent replacement of conventional seismic sensors and allow installation of permanent sensors in the borehole, recent developments aim to use Distributed Acoustic Sensing (DAS) to detect seismic waves. DAS is a new technology of seismic acquisition that relies on traditional fibre-optic cables to provide inline strain measurement. In contrast to point sensors, DAS is a distributed acoustic measurement system and can record particle movement along the entire optical cable length. The basic principle is based on optical time-domain reflectometry, where light pulses are traveling through the fibre and are backscattered at intrinsic inhomogeneities of the silica glass. Seismic wavefields displace the position in space of these individual inhomogeneities, thus allowing the system to be sensitive to seismic waves. The DAS deployment techniques during VSP surveys can be categorised in three methods: the optical cable can be either cemented behind the casing, attached to the tubing or loosely lowered down the borehole, also called wireline deployment. The data quality obtained by the different strategies of fibre optical cable deployment varies significantly, with the lowest signal-to-noise ratio

being recorded using wireline deployment. During a field trial where DAS data was acquired in a 600 m vertical fluid-filled well, a significant increase in signal-to-noise ratio was observed when tension of the wireline cable was released to the maximum possible extent.

In this thesis, we are addressing the problem of coupling of the DAS cable in VSP surveys during wireline deployment.

We compared numerical simulations of a 3D seismic wave propagation model using the finite element method with real data. This model allowed us to analyse seismic waves in fluid filled boreholes induced by elastic wave-fields. Numerical results were similar to conventional seismic data and to DAS data when the DAS cable was considered perfectly coupled. However, poor coupling conditions could not be analysed using this model. Therefore, we employed other numerical methods to identify the precise position and movement of the cable, when more cable was lowered into the borehole. This model allowed us to conclude why DAS recordings vary significantly in signal-to-noise ratio: the cable requires being in immediate contact with the borehole wall and in equilibrium conditions to be well coupled. Those conditions are found when a certain amount of contact force between the borehole wall and the cable is established. Based on those findings, we proposed solutions to further optimise DAS acquisitions: we analysed the change in detected signal by the cable when coupled to the borehole wall. We modified the contact force and the elastic properties of the DAS cable and observed that this improves the recorded signal significantly. Additionally, we proposed an algorithm for detecting good cable coupling, based on the nature of noise that DAS records when it is considered to be poorly coupled.

# Contents

<b>1</b>	<b>Introduction</b>	<b>1</b>
1.1	Distributed acoustic sensing (DAS)	7
1.2	Description of the DAS measurement	10
1.3	Processing of DAS data	12
1.4	DAS and conventional seismics	14
1.4.1	Land seismic acquisition	15
1.4.2	Borehole seismic acquisition	21
1.5	Motivation and thesis outline	26
1.5.1	Motivation - using DAS as a seismic sensor for VSP surveys	26
1.5.2	Thesis outline	27
1.5.3	Realisations and contributions	29
<b>2</b>	<b>Constitutive equations</b>	<b>31</b>
2.1	Introduction	32
2.2	Governing variables	32
2.2.1	Forces $\mathbf{F}$ and moments $\mathbf{M}$	33
2.2.2	Stress $\boldsymbol{\sigma}$	33
2.2.3	Displacement $\mathbf{u}$ , velocity $\mathbf{v}$ , acceleration $\mathbf{a}$	34
2.2.4	Strain $\boldsymbol{\epsilon}$	35
2.3	Seismic wave equations	36
2.4	Seismic wave expressions in a fluid-filled borehole	39
2.5	Coupling	44
2.5.1	Principles of coupling for a geophone	44
2.5.2	Physics of contact forces	45
2.6	Conclusions	52
<b>3</b>	<b>Numerical modelling and simulation</b>	<b>53</b>
3.1	Introduction	54
3.2	Review of FEM	55
3.2.1	Description of the method	56

## Contents

3.2.2	Implicit vs explicit	59
3.2.3	Comparison with other numerical methods	61
3.3	Numerical model set-up using the FEM	63
3.3.1	Geometry, elements and material properties	64
3.3.2	Loads and boundary constraints	66
3.3.3	Analysis of numerical results	66
3.4	FEA of seismic wave expressions in fluid-filled boreholes	73
3.4.1	Numerical model	74
	Geometry	74
	Elements and material properties	74
	Meshing	75
	Boundary conditions	81
3.4.2	Numerical results	82
3.5	FEA of cable coupling	83
3.5.1	Numerical model	85
	Geometry	85
	Element and material properties	85
	Boundary conditions	87
3.6	Conclusions	89
<b>4</b>	<b>Applications to real data</b>	<b>91</b>
4.1	Introduction	92
4.2	Real data application I - Bottesford	92
4.2.1	Analysis of recorded seismic waves using DAS, VSI and numerical data	93
4.2.2	Cable coupling	99
	Numerical results of cable movement	101
4.3	Real data application II - Livingston	102
4.3.1	Cable coupling	102
	Numerical results of cable movement	104
4.4	Conclusions	104
<b>5</b>	<b>Optimising coupling using DAS</b>	<b>109</b>
5.1	Introduction	109
5.2	Contact forces	110
5.2.1	Numerical analysis	110
5.3	Elastic properties	114
5.3.1	Numerical analysis	114
5.4	Exploiting cable noise for DAS coupling	122
5.4.1	Noise recordings	122
5.4.2	Feature detection	126
5.5	Conclusions	129

<b>6</b>	<b>Conclusions and perspectives</b>	<b>133</b>
6.1	Conclusions	134
6.1.1	The coupling of DAS in borehole VSP	134
6.1.2	Analysis to improve the coupling using DAS	135
6.2	Perspectives	136
6.2.1	Numerical modelling improvements	136
	Modelling poor coupling conditions	136
	Efficient modelling using wavefield grid injection	136
6.2.2	Practical improvements	139
	Adding robustness to the coupling detection algorithm	139
	Multi-component DAS to record the entire wavefield	141
	Performance test using different cable designs	141
	A fibre with densely spaced reflectors to increase the SNR	142
	A higher spatial resolution with DAS	142



## Acronyms

<b>APDL</b>	Ansys Parametric Design Language
<b>AWD</b>	Accelerated Weight Drop
<b>BC</b>	Boundary Condition
<b>C-OTDR</b>	Coherent-Optical Time-Domain Reflectometry
<b>CGFEM</b>	Continuous Galerkin Finite Element Method
<b>DAS</b>	Distributed Acoustic Sensing
<b>DFT</b>	Discrete Fourier Transform
<b>DTS</b>	Distributed Temperature Sensing
<b>FEA</b>	Finite Element Analysis
<b>FEM</b>	Finite Element Method
<b>hDVS</b>	heterodyne Distributed Vibration Sensing
<b>HWC</b>	Helically Wound Cable
<b>ODE</b>	Ordinary Differential Equation
<b>OTDR</b>	Optical Time-Domain Reflectometry
<b>PDE</b>	Partial Differential Equation
<b>PML</b>	Perfectly-Matched-Layer
<b>PRM</b>	Permanent Reservoir Monitoring
<b>RMS</b>	Root-Mean-Square

*Contents*

**SNR** Signal-to-Noise Ratio

**STFT** Short-Time Fourier Transform

**VSI** Versatile Seismic Imager

**VSP** Vertical Seismic Profiling

## Résumé du chapitre

L'objectif de ce travail est de comprendre dans quelles circonstances la qualité des données acquises en utilisant la technologie des senseurs à fibre optique distribuée (DAS) peut être améliorée. Hartog et al. (2014) ont présenté les résultats d'un essai sur le terrain où ils ont acquis des données DAS de bonne qualité en utilisant un déploiement le long d'un câble dans un puits vertical de 600 m. Ils ont montré que lorsque la tension du câble est relâchée en abaissant plus de câble dans le puits, le rapport signal sur bruit des données acquises augmente. Quand la quantité maximale de câble est abaissée dans le puits, la première arrivée de l'énergie sismique est détectée avec le DAS tout au long de la longueur du puits. Avant ce travail, il n'était pas clair pourquoi et quand des données avec une telle qualité pouvaient être acquises. Des simulations numériques ont été développées durant le doctorat pour (1) comprendre comment le mouvement des particules à l'intérieur du puits rempli de liquide est enregistré par DAS et comment cela se rapporte aux enregistrements sismiques classiques, (2) déterminer les conditions dans lesquelles un signal haute fidélité peut être obtenu pour un câble DAS et (3) optimiser le couplage du DAS avec les parois du puits. Le chapitre 2 présente les équations constitutives qui seront utilisées dans les chapitres suivants. Le chapitre 3 présente les principes de la méthode des éléments finis (FEM) qui sera utilisée dans nos simulations numériques, ainsi que les deux modèles numériques employés dans nos expériences. Le chapitre 4 présente l'application des modèles numériques aux données réelles. Le simple déplacement du câble DAS à l'intérieur du puits dans notre solution numérique ne permet pas d'expliquer les différences observées dans les données réelles. Par conséquent, le second modèle numérique présenté dans le chapitre 3 a été employé pour suivre le mouvement du câble. Le chapitre 5 utilise les informations du chapitre 2 et les observations faites dans les données réelles présentées au chapitre 4 pour optimiser les acquisitions du DAS, en analysant comment les propriétés des matériaux des câbles utilisés pour les acquisitions

DAS puissent influencer la qualité des données acquises, et en proposant un algorithme de détection de couplage qui permet d'avoir des informations fiables sur le bon couplage du câble, même avant le déclenchement d'une source sismique. Au chapitre 6, les principales conclusions sont résumées et les perspectives des recherches futures discutées.

## Introduction

In hydrocarbon exploration, sensors detecting seismic waves are used to characterise the subsurface, in particular the presence of oil and gas reservoirs (Sheriff and Geldart, 1995; Yilmaz, 2001). The seismic waves are artificially generated and controlled by one or more seismic sources. In offshore acquisitions, the seismic sources are usually airguns that are fairly large pressurised chambers towed behind vessels. When the compressed air is released, a pulse of acoustic energy is produced. In onshore acquisitions, the seismic source can be e.g. a truck-mounted seismic vibrator, an accelerated weight drop (AWD), small amounts of dynamite or portable airgun tanks, all transmitting vibrations into the Earth. The energy in both cases is travelling towards the target rock where reflections are generated. The seismic energy of interest for oil exploration is the one travelling through the reservoir, or reflected within the reservoir, and finally recorded at the surface (Aki and Richards, 1980; Chapman, 2004; Zoback, 2009). The sensors detecting seismic waves can be hydrophones, measuring acoustic waves as changes in pressure over time, or geophones, measuring elastic waves in terms of particle displacement. Hydrophones are therefore used in acoustic media such as in fluid-filled boreholes or in marine acquisitions where hydrophones are mounted on streamer towed behind a seismic vessel. Geophones instead are commonly used onshore, where they are coupled with a spike into the ground or in borehole seismic acquisitions, where they are clamped to the borehole wall. The cost for a conventional single sensor can go up as high as \$200, which does not include additional equipment, e.g. power cables. The cost is even higher for broad-band seismic sensors.

Different types of seismic surveys are carried out depending on the environment, objectives and feasibility. Vertical Seismic Profiling (VSP) is a class of borehole seismic measurement (Galperin, 1974; Hardage, 1983; Balch and Lee, 1984). The purpose and goal of VSP surveys are usually the calibration of pre-existing surface seismic data to ensure a correct depth profile, the development of velocity profiles of the subsurface or more advanced surveys like Permanent Reservoir Monitoring (PRM) (Lumley, 2001). VSP surveys usually benefit from a naturally higher frequency content since Earth filtering effects of the weathered layer only perturb the seismic signals once. High resolution of the final seismic data is commonly desired in order to detect as many rock features as possible. The most reliable way to produce high resolution data is to place a significant number of sensors with short spatial increments

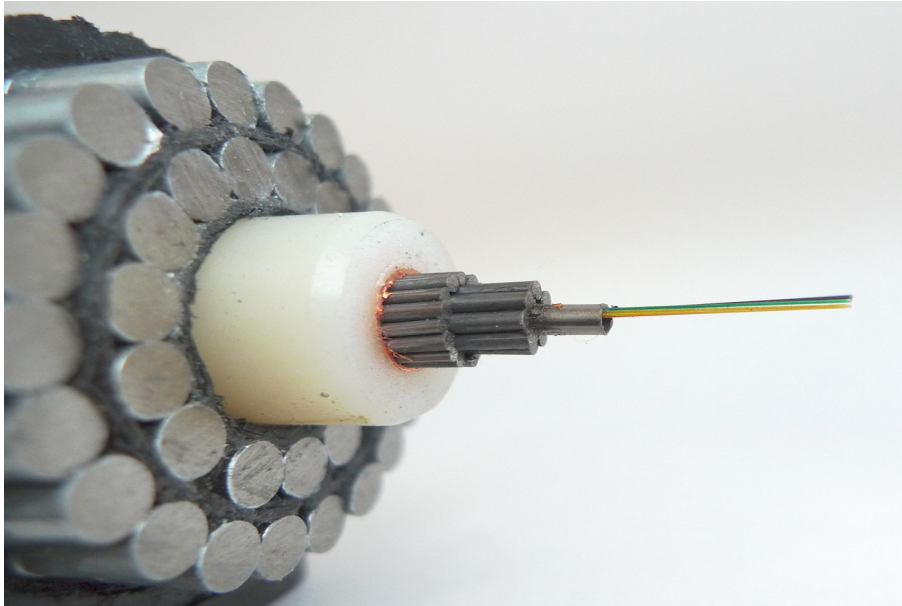


Figure 1.1: Submarine fibre optical cable used for data transition, similar to the wireline cable that is used for VSP with a diameter of 1 cm.

along the well. As boreholes can span a length of several kilometers, the number of required point sensors can add up rapidly, thus driving operation cost. Moreover, temperature and pressure gradients in boreholes create further difficulties. High temperature and high hydrostatic pressure cause the sensitive sensors to be subject to very harsh environments, especially for reservoirs at depth beyond 3000 m, where temperature and pressure can go up as high as 375°C and 3200 psi, respectively (Cressler and Mantooth, 2012). Consequently, those sensors often fail and need to be replaced frequently. When replacing a single sensor in a borehole, the entire geophone array needs to be detached from the casing and taken out of the borehole, leading to additional cost. Consequently, most VSP surveys are carried out on an *intervention* basis, i.e. the sensors are lowered down temporarily, data is acquired and the sensors are recovered. This temporary installation complicates or even prevents concepts like PRM. In order to avoid frequent replacement of conventional seismic sensors and allow installation of permanent sensors in the borehole, recent developments use optical sensors, based upon Michelson interferometers (Blanco et al., 2006). They have a longer operating lifetime but they are similar to conventional seismic sensors in that they can be considered to be point sensors.

In the past few years Distributed Acoustic Sensing (DAS) has emerged. This is a new technology for seismic acquisition, where fibre optic technology is used to detect seismic events (Figure 1.1). In contrast to point sensors, DAS is a distributed acoustic measurement system and therefore records sampling points along the entire optical cable length (Figure 1.2). The

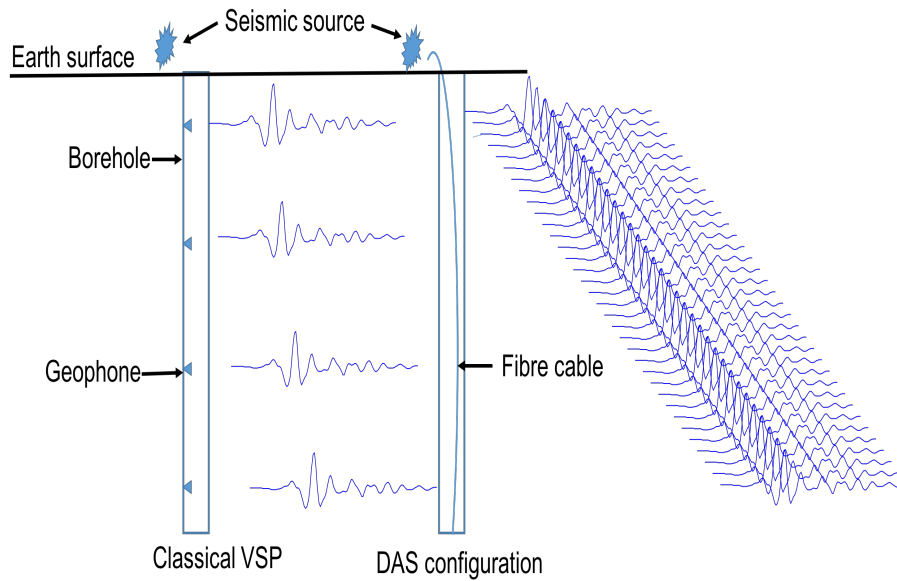


Figure 1.2: Sketch of a VSP survey using an array of conventional point sensors (left) and DAS technology (right).

system is based on Optical Time-Domain Reflectometry (OTDR) exploiting the principle of Rayleigh backscattering (Hartog, 2017). The technology and its application in the context of exploration geophysics will be explained in much more detail in Section 1.1. Being a cost-effective alternative to conventional seismic acquisition, recent research and field trials of DAS surveys have shown promising results in terms of acquired data (Madsen et al., 2012; Mestayer et al., 2012; Hartog et al., 2013; Hornman et al., 2013; Verliac et al., 2015; Papp et al., 2017). Even though R&D is in its early stages, many significant findings to improve DAS systems have been published in terms of acquisition and design of the fibre cable. Some improvements aim to *optimise processing algorithms*: Hartog et al. (2016) propose the multi-frequency system hDVS where three or more light pulses of different frequency are sent through the fibre cable leading to three different outputs. The results can be summed, similar to stacking in classical processing of geophysical data, to improve the signal-to-noise ratio (SNR) and to eliminate ambient noise. Dean et al. (2015) propose to improve the SNR by calibrating the gauge length of the system, since the gauge length acts as a moving-average filter and thus suppresses short-term fluctuations. Others aim to *optimise the acquisition setup*: Kuvshinov (2016) from a mathematical point of view and Hornman (2017) from a more practical point of view developed a solution to increase the sensitivity of DAS to broadside signals by changing the physical layout of the cable. The patent (Den Boer et al., 2013) describes a so-called Helically Wound Cable (HWC) where the fibre cable is wrapped helically around another body resulting in almost omnidirectional sensitivity. A similar idea has also been patented by Crickmore and Hill (2014). Martin et al.

(2013) filed a patent on particular fiber patterns that are spatially distributed in non-parallel planes to separate velocity components of the acoustic wavefield relative to the orthogonal axes. Initially developed for land seismic acquisitions, the idea can also be used for borehole seismic acquisition.

DAS is largely used for VSP surveys since DAS represents a good trade-off between operation cost and data quality. The deployment techniques of DAS during VSP can be categorised in three methods: the optical cable can be either *cemented behind the casing* (Cox et al., 2012; Mateeva et al., 2014; Reinsch et al., 2015; Bettinelli and Frignet, 2015), *attached to the tubing* (Barberan et al., 2012; Mateeva et al., 2013; Daley et al., 2013; Dean et al., 2016) or *loosely lowered down the borehole* (Hartog et al., 2014; Constantinou et al., 2016). The recorded data quality is in general better when the cable is cemented behind the casing or attached to the tubing because the sensing cable is better coupled to the elastic medium. However, the latter deployment technique is the most cost-effective and latest developments appear to be promising to record high signal fidelity. Munn et al. (2017) propose to improve the coupling by using a borehole liner to push the cable against the borehole, thus establishing a solid-solid interface with the casing. But the solution only works for shallow wells up to 400 m. Farhadiroushan et al. (2015) propose to increase the general sensitivity of the measurement to acoustic waves by calibrating the cable properties. Besides these few contributions, very little R&D has been committed to improving the coupling of the optical sensors in VSP surveys on wireline cable which can become a key factor determining data quality (Schilke et al., 2016).

Even though the quality of data acquired by conventional seismic sensors is generally higher than that provided by DAS, the latter technology offers a range of advantages, namely:

- **Higher resolution:** In conventional VSP surveys geophones or hydrophones are placed at spatial increments of a few meters. High resolution data to identify differences in arrivals at close locations along the well is always desired, but because of tight budget restrictions and considering that sensors need to be replaced frequently, placing sensors at very small increments is generally not feasible (Figure 1.2). DAS measurements can interrogate points up to a spatial increment of typically 0.3 m. Boreholes spanning a length of more than 3000 m, leads to obtaining around  $10^4$  interrogation points. While DAS requires a cable withstanding high pressure and high temperatures as well as microbending, the cost are still minor compared to placing tens of thousands seismic sensors along the borehole.
- **Well coverage:** DAS measurement systems easily allow recordings along the entire cable length which can be of a few kilometer (Figure 1.2). For conventional seismic sensors, providing a better well coverage means either that the arrays include more sensors or, that for

a particular array such as the versatile seismic imager (VSI) (Arroyo et al., 2003), after each shot point the array is moved to a different depth in the well and the acquisition is repeated. The first approach is limited by the increased rig-up time and the second requires more acquisition time; in both cases the time taken by the acquisition crew at the well site is increased. VSI are devices that are attached to a slickline cable and can be lowered up and down the borehole, while carrying 3C geophones. However, the risk of the tool to get stuck and thereby losing tool and borehole, when attaching multiple VSIs on a single cable, is high and its application to deviated well even prohibited. Moreover, the time to rig-up the toolstring is immense, therefore acquisition to obtain a wider well coverage is at the cost of a broad spatial sampling.

- **Cheaper deployment:** There exist different strategies to deploy the fibre optical cable in a borehole. The fibre cable can be cemented behind the casing, clamped to the tubing and loosely lowered down the borehole. The latter deployment method is by far the most cost-effective and, additionally, a pre-existing fibre cable is not required. Moreover, fibre cables are sometimes already found in place (cemented behind casing) when used for sensing purposes such as distributed temperature sensing (DTS) or as a downlead to a pressure gauge. In all these cases, installation cost can be avoided. Additionally, the wire-line deployed DAS allows the data to be provided earlier in the life of the well, before it is completed. Conventional sensors, on the other hand, always need to be deployed carefully and attached to the borehole wall, which is time-consuming, expensive and also complicated, in particular because most wells follow deviated paths and an irregular pattern.
- **Robustness:** With increasing depth, temperature and pressure gradients create extreme operation environments. High temperatures in boreholes often result in damage and eventually failure of downhole electronics such as geophones. DAS can operate stably up to temperatures of 350°C. This is the temperature that is generally found at depth around 6000 m, considering a geothermal gradient of 25°C per 1000 m (Sheriff and Geldart, 1995) while neglecting local temperature variations caused by the reservoir (Batzle and Wang, 1992) and increasing temperatures due to steam-assisted oil recovery (Chopra et al., 2012). In contrast, the temperature of the environment for geophones should not exceed 80°C, while downhole tools, such as the VSI, can withstand a temperature of 175°C even though this upper limit requires special measures and quick operations (Arroyo et al., 2003).

A DAS system without any limitations would replace any kind of conventional seismic measurement. However, there are some major disadvantages when acquiring seismic data using DAS:

- **Lower signal-to-noise ratio:** A major obstacle of DAS systems is the signal-to-noise ratio (SNR) of acquired data. The general sensitivity of the system to seismic waves is lower compared to conventional seismic sensors and the noise floor higher. First breaks in VSP acquisitions are usually detectable throughout the entire well when deployed properly. The detection of further reflections is complicated due to the high level of ambient noise, but ways to improve data quality have been presented (Dean et al., 2015; Hartog et al., 2016).
- **Single-component measurement system:** DAS is sensitive to axial strain only (along the cable direction). It is therefore a single component measurement system and not sensitive to compressional waves in cross-line direction. Three-component geophones on the other hand, can capture the entire wavefield with reliable accuracy. Den Boer et al. (2013); Crickmore and Hill (2014); Kuvshinov (2016) and Hornman (2017) show that physically changing the cable layout can increase broadside sensitivity. In addition, DAS systems measure the wavefield in terms of strain, the spatial derivative of particle displacement. Therefore, the direction of arrival cannot be directly identified (Papp et al., 2017). A modified data extraction method to distinguish between the direction of arrival has been presented by Poletto et al. (2016).
- **Poor coupling:** Even though the deployment of DAS cables is in general an advantage due to the cheaper installation cost, coupling can become a limiting factor deteriorating data quality. It has been observed that the system barely records any signal if not well coupled and therefore, even advanced processing algorithms cannot be applied to improve the data. While attention has been given to improve the SNR and to address the directionality problem, only a little effort has so far been dedicated to improve coupling (Farhadiroushan et al., 2015; Munn et al., 2017).

As any new technology, DAS still suffers from some disadvantages preventing the system from replacing reliable and well developed acquisition systems. We believe that these disadvantages can be certainly overcome with further research investigations.

## 1.1 Distributed acoustic sensing (DAS)

In order to further understand the physics of DAS measurements, we review here the main principles. The DAS technology used by Schlumberger is called heterodyne distributed vibration sensing (hDVS) and was developed by Hartog and Kader (2012). As any other DAS system, the hDVS measurement system is also based on optical time-domain reflectometry and exploits the principle of Rayleigh scattering.

**Rayleigh scattering** The silica glass, that is the travel medium of the light in a fibre cable, comprises heterogenities that are intrinsic i.e. caused randomly during the manufacturing process and are therefore also randomly distributed along the optical fibre cable. Figure 1.3 illustrates a zoom section of the silica glass where the heterogenities are sketched as dots. The heterogenities cause local fluctuations of the refractive index. Rayleigh, Brillouin and Raman scattering are the three scattering processes, which occur when a light pulse is propagating through the silica glass. Brillouin and Raman scattering are used to measure static strain and temperature data. Rayleigh scattering enables dynamic strain measurements. The optical loss due to Rayleigh scattering is governed by the attenuation coefficient  $\alpha_r$  (Senior and Jamro, 2009):

$$\alpha_r = \frac{8\pi^3}{3\lambda^4} n_f^8 p^2 \beta_c K T_F, \quad (1.1)$$

where  $\lambda$  is the wavelength of the light pulse,  $n_f$  the refractive index,  $p$  an average photoelastic coefficient,  $\beta_c$  the isothermal compressibility and  $K$  is the Boltzman constant.  $T_F$  is the fictive temperature that approximates the thermodynamic state of the silica glass at the point when it is frozen (Schroeder et al.; Mauro et al., 2009). The transmissivity of the Rayleigh contribution is expected to decay exponentially as the light travels further along the fibre length (Beales et al., 1979; Ainslie et al., 1981; Jeunhomme, 1982; Maughan, 2001):

$$T_r = e^{-\alpha_r L}, \quad (1.2)$$

where  $L$  is the length of the fibre cable.

**OTDR** The process of Rayleigh backscattering is exploited by OTDR. A schematic diagram of OTDR is illustrated in Figure 1.3. Here, the light pulse is launched into the sensing optical fibre. Based on Rayleigh scattering the light is scattered in all directions and a small fraction of the light pulse - in the order of 0.1 - 1% - is re-directed, so that it propagates back to the optical device (Hartog, 2017). The time delay of each individual backscatter is given as

$$\tau_k = 2 \frac{n_f}{c} z_k, \quad (1.3)$$

where 2 accounts for the two-way traveltime,  $n_f$  is the refractive index that is a constant for a given fibre,  $c$  the speed of light in vacuum and  $z_k$  the position of the backscatter. Re-arranging, we obtain the location  $z_k$  of each backscatter using OTDR:

$$z_k = \frac{1}{2} \frac{c}{n_f} \tau_k. \quad (1.4)$$

Note that Equation 1.4 assumes single scattering. Since less than 1% of emitted light is propagating back to the optical device, multiple scattering along

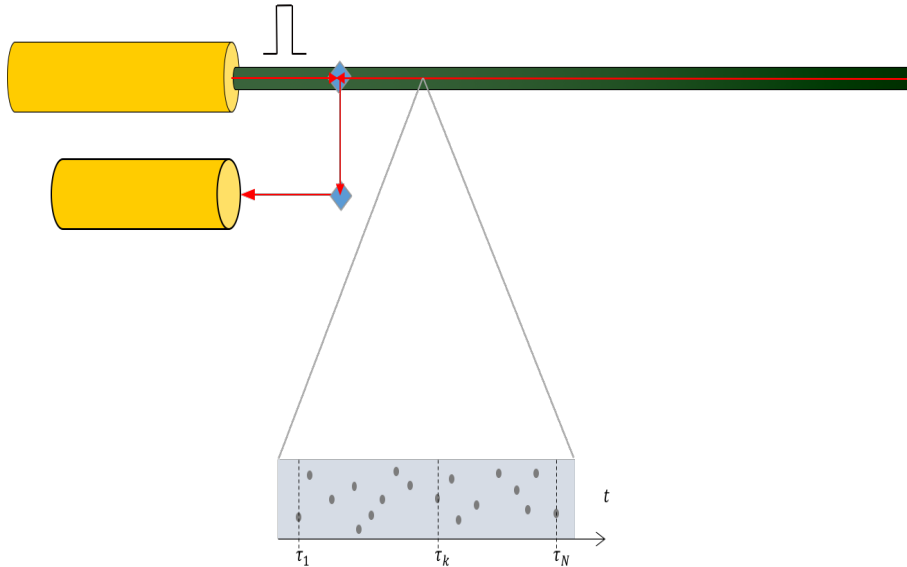


Figure 1.3: Rayleigh backscattering and OTDR.

the fibre cable is unlikely: at 1500 nm the scattering coefficient is about  $4.6 \cdot 10^{-5} \text{ m}^{-1}$  and of that at most 1% is recaptured (Hartog, 2017). The intensity of double-scattered light would therefore be 6-7 orders of magnitude lower compared to the first-order scattered light and consequently too weak to be detectable.

**DAS** There exist several implementations of a DAS system and a summary for different approaches is discussed in Hartog et al. (2013). The DAS system, based on Coherent Optical Time-Domain Reflectometry (C-OTDR) after Hartog and Kader (2012), is shown in Figure 1.4. The backscatter signal is mixed with a sample of the laser output, detected by a photodetector and the recorded voltage is filtered, amplified and digitised, before advanced signal processing algorithms are applied. Moreover, the probe pulse has been frequency shifted by a pre-determined amount before it has been sent through the fibre. Providing that frequency of the laser and state of the fibre are kept constant, the light is scattered by each elemental scatterer with a fixed phase relative to other scatterers within a section of the fibre that is occupied by the probe pulse. As a result, amplitude and phase are constant when the fibre is not perturbed. An axial strain applied to the fibre cable leads to modulation of the backscatter in terms of amplitude and phase in an unpredictable, non-linear manner. However, as the applied strain alters the position of all scatterer within the field of the disturbance and for all points beyond the region where strain is applied, linear phase shifts are induced. As the linear phase shift enables the system to track local disturbances of the fibre, repetitively launched light pulses (in the order of 1-10 kHz) enable the system to be sensitive to seismic waves. These phase shifts result therefore

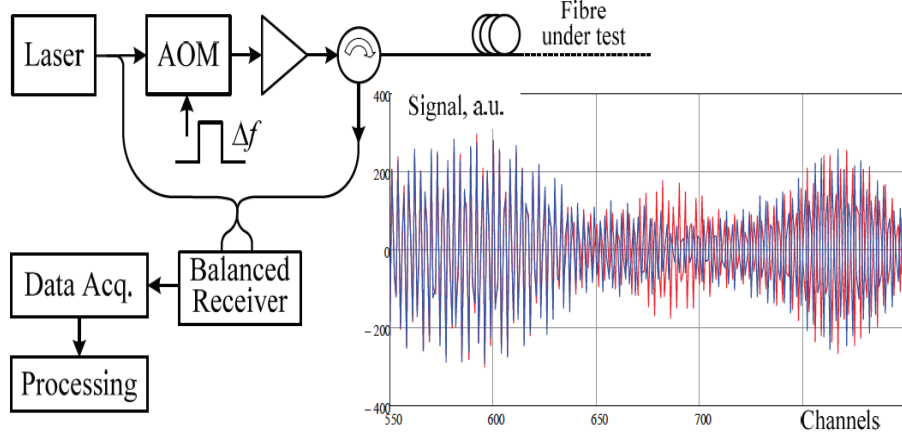


Figure 1.4: Schematic arrangement and specimen signals DAS system with coherent optical detection (adapted from [Hartog et al. \(2013\)](#)).

in an output that can be related to displacement as commonly used in classical geophysical measurements. Differentiation of phase at two locations within a predetermined window gives a measure of strain. For more details about measurement principle of DAS the reader is referred to [Hartog \(2017\)](#).

## 1.2 Description of the DAS measurement

While the physics of the measurement has been discussed in general terms so far, the recorded signal of the fibre cable can also be formulated in a mathematical framework. The acquisition of optical data is based on the backscattering Rayleigh principle which can be described using linear filter theory ([Healey, 1984](#)). Let consider:

$$y(t) = x(t) * h(t), \quad (1.5)$$

where  $t$  denotes time,  $x(t)$  is the short modulated pulse of light injected by the laser and  $h(t)$  is the fibre response. Let  $x(t)$  be defined as

$$x(t) = g(t) \cdot \cos(2\pi ft), \quad (1.6)$$

where  $g(t)$  is the pulse envelope, which is modulated by a sinusoid at the optical frequency  $f$ . Assuming that the recorded signal is due to a number of scatterers behaving as small reflections and being normally distributed along the fibre, the fibre response can be written as

$$h(t) = \sum_{k=1}^N a(\tau_k) \cdot \delta(t - \tau_k), \quad (1.7)$$

## 1.2 Description of the DAS measurement

where  $N$  is the number of scatterers,  $\tau_k$  is the traveltime of the  $k$ -th scatterer,  $a(\tau_k)$  its relative amplitude and  $\delta$  the Dirac delta function. Note that attenuation, mentioned in Equation 1.2, is neglected.  $\tau_k$  is a function of the speed of light  $c$ , the refractive index  $n_f$  and the position of the scatterer at location  $z_k$  as given by Equation 1.3.  $n_f$  is considered to be homogeneous throughout the fibre, but varies over fibre types i.e. single-mode, multi-mode and special purpose fibres have different refractive indices.

Inserting Equation 1.6 and 1.7 into 1.5, consequently the backscattered signal becomes:

$$y(t) = \sum_{k=1}^N a(\tau_k) \cdot g(t - \tau_k) \cdot \cos(2\pi f(t - \tau_k)). \quad (1.8)$$

It should be noted that this response is valid only if the position of the scatterer and the laser frequency are stationary. The stationary case (Equation 1.8), is defined as fast-time  $t$ , which corresponds to the spatial axis in a classical geophone-based seismic measurement.

As DAS is predominantly used as a tool for seismic acquisition, an impinging seismic wavefield may alter the position of scattering points and consequently modify the fibre response. When the position of a scatterer is altered from its stationary position, the new delay becomes:

$$\tau_k(p) = \tau_k + \Delta\tau_k(p), \quad (1.9)$$

where the delay  $\tau_k$  of the  $k$ -th scatterer at the "rest" position is changed by  $\Delta\tau_k(p)$  which is the variation induced by an external event e.g. a seismic wavefield. The concept is shown in Figure 1.5. The new time coordinate  $p$  is also called slow-time and corresponds to the temporal axis in a classical geophone-based seismic measurement.

The delay variation  $\Delta\tau_k(p)$  can be described as

$$\Delta\tau_k(p) = 2\frac{n_f}{c}d(z_k, p) \quad (1.10)$$

where  $d(z_k, p)$  is the difference in position of the scatterer  $\tau_k$  at  $z_k$  due to the external event.

Hence, the backscattered signal in fast-time  $t$  and slow-time  $p$  can be written as

$$y(t, p) = \sum_{k=1}^N a(\tau_k) \cdot g(t - \tau_k) \cdot \cos(2\pi f(t - \tau_k) - 2\pi f\Delta\tau_k(p)), \quad (1.11)$$

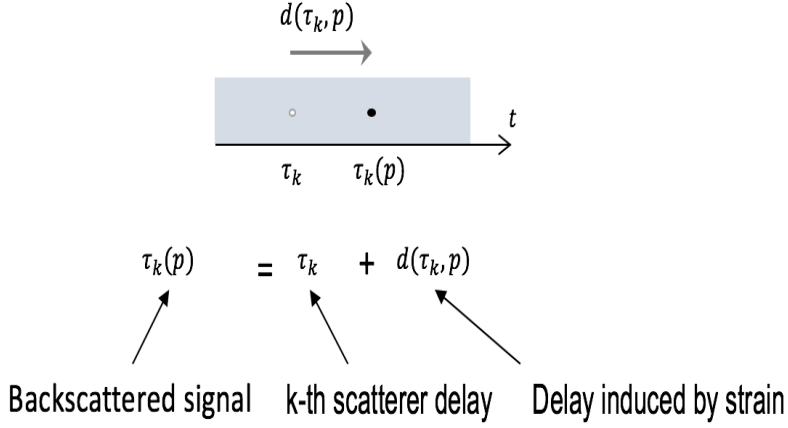


Figure 1.5: Displaced position of an individual backscatter with traveltime  $\tau_k$  shown in Figure 1.3.

or, in exponential notation, as:

$$y(t, p) = \sum_{k=1}^N a(\tau_k) \cdot g(t - \tau_k) \cdot e^{i\omega[t - \tau_k - \Delta\tau_k(p)]}, \quad (1.12)$$

where  $\omega = 2\pi f$ . We also assumed the medium to vary smoothly, compared to the wavelength based on the high frequency approximation (Bleistein et al., 2001), and therefore approximated  $a(\tau_k + \Delta\tau_k) = a(\tau_k)$  and  $g(t - \tau_k - \Delta\tau_k) = g(t - \tau_k)$ . Equation 1.11 and 1.12 provide the general and simplified explanation that DAS systems are sensitive to seismic waves, while any non-linearity in the system has been neglected. The term  $d(z_k, p)$  in Equation 1.10 represents the equivalent to particle displacement of the spike using geophones. However, it will be shown in the next section, that due to the processing chain of DAS systems the final output  $y(t, p)$  is not given in particle displacement but in strain. Strain is estimated from the phase term, hence the imaginary part of the complex signal as discussed in Section 1.1. Even though the reader should be familiar with the basic terminology of seismic acquisition using DAS after this section, DAS results are interpreted in terms of depth/length and time, instead of fast-time and slow-time in order to avoid confusion.

### 1.3 Processing of DAS data

After acquiring DAS data  $y(t, p)$ , the recorded time-domain signal can be decomposed as any complex signal into its real and imaginary part to analyse amplitude and phase information. Since the phase term of the fibre response  $y(t, p)$  derived in Equation 1.11 is sensitive to displacement (see Equation 1.10), the difference of two backscatter along the fibre cable in fast-time,

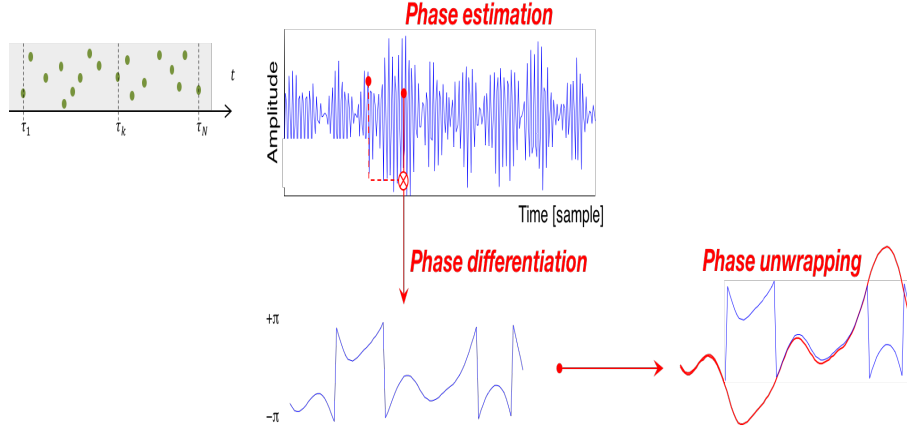


Figure 1.6: Processing of optical data.

i.e. space, gives an output similar to strain. In order to derive phase information of the signal and furthermore obtain the final output, a few signal processing steps are required. Raw data processing consists of three elementary steps (Figure 1.6):

- phase estimation
- phase differentiation
- phase unwrapping

In order to estimate the phase of a continuous signal, real and imaginary parts of the complex signal need to be derived. The most common methods are the Fourier and Hilbert transform. In the case of hDVS, the phase is estimated using the discrete Fourier transform (DFT). The DFT is applied within a sliding window along  $t$  by keeping  $p$  fixed. The phase  $\phi(t, p)$ , contained in the argument of the exponent of Equation 1.12, is then estimated by taking the arctangent of imaginary and real part of the signal:

$$\phi(t, p) = \tan^{-1} \left( \frac{\text{Re}\{y\}}{\text{Im}\{y\}} \right). \quad (1.13)$$

In DAS, the length of the injected light pulse is usually a few meters depending on the pulse duration, which depends on the number of photons used. The pulse repetition frequency of a typical DAS system is in the range of 5 – 10 kHz. Therefore, the sample separation in slow-time is usually less than the length of the light pulse. In order to ensure a monotonic response, the estimated phase is differentiated along the fast-time over  $\Delta t$  (Hartog, 2017):

$$\Phi(t, p) = \phi(t, p) - \phi(t - \Delta t, p), \quad (1.14)$$

where  $\Delta t$  is also called the gauge-length and acts like a moving-average filter. Note that Equation 1.14 may seem similar to  $\Phi = \frac{\partial \phi}{\partial t}$ , but  $\Phi$  is the difference

between two backscatter along the fibre, similar to taking the difference of recorded displacement values between adjacent geophones.  $\Delta t$  is commonly chosen such that the spatial resolution of DAS is 10 m.

At fixed peak power, more photons would theoretically lead to more backscatter, hence to a better SNR at the expense of a longer pulse duration, and therefore a lower spatial resolution. However, the peak power can not be increased to arbitrary levels owing to the appearance of optical non-linear effects (Hartog, 2017). Conversely, a shorter pulse duration is required if a smaller gauge length is used; in this case, a finer spatial resolution is achieved at the expense of fewer photons used, i.e. a lower pulse energy, and consequently a lower SNR.

The last step of basic pre-processing is unwrapping. This step is employed as the phase result  $\phi(t, p) \in (\pi, -\pi)$  is subject to wrapping effects (Blackledge, 2006). The unwrap operator is applied along the fast-time to reconstruct the final signal. Radian phase angles are corrected by adding or subtracting  $2\pi$  to all of the following samples if  $|\Phi(t, p) - \Phi(t - \Delta t, p)| \geq \pi$ .

Overall, phase estimation results in the computation of cumulative strain, or displacement, because the DAS system is measuring the linear phase shifts that are induced by the displaced position of the scatterer similar to the displacement recorded by the spike of the geophone. Then, phase differentiation leads to a measure of strain, because the phase difference between individual backscatter is computed similar to the spatial derivative of displacement values recorded by adjacent geophones. The unwrapping is a required operator as the phase is subject to wrapping effects (Blackledge, 2006). These steps are critical in order to produce an output that can eventually be compared to conventional seismic data and be interpreted by geophysicists. Note that these steps are essential for hDVS, the proprietary technology used by Schlumberger. In other systems the phase is differentiated naturally in the optical domain, hence prior to processing, which can become a limiting factor, while hDVS acquires the raw data and an optimal trade-off between spatial resolution and SNR can be evaluated during data processing (Hartog, 2017).

### 1.4 DAS and conventional seismics

In this section we compare DAS and conventionally acquired seismic data. The aim of this section is to illustrate the limitations of DAS, as described in the previous sections, when compared to geophone data and to show that more research is needed. First, DAS and seismic data acquired on land will be presented with emphasis on the directionality of the measurement, the general sensitivity of DAS to seismic waves and finally the influence of coupling.

Then, DAS and seismic data acquired during VSP surveys will be shown with emphasis on different deployment strategies, that have an impact on coupling and the quality of the acquired data.

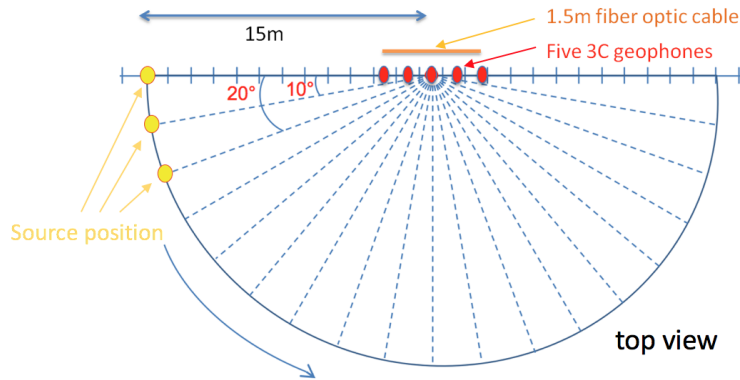


Figure 1.7: Survey design for Chambon dataset, with a walkaround geometry measurements to test the response of the fiber at different angles of incidence.

### 1.4.1 Land seismic acquisition

In this section, we show data from two land acquisitions: the first dataset was acquired in Chambon, France at the observatory belonging to the Institute de Physique du Globe de Paris (IPGP), while the second dataset has been acquired in Cambridge, UK on a site adjoining the Schlumberger research centre. For both surveys, we compare the data from trenched fibre cable buried 10 cm below the surface and three-component geophones. The first part focuses on the directionality and dynamic range of DAS, while the second part introduces the topic of coupling.

One disadvantage is the limitation of DAS of being sensitive to axial strain only. Therefore DAS is considered a single-component measurement system, preventing reliable recordings of the entire elastic wavefield, composed of compressional as well as tangential motion.

The first field test was done in Chambon. The purpose of this dataset was to analyse directionality and, as will be shown later, coupling of DAS systems. This was a small scale field test that allowed to better control the parameters of the measurement. Instead of hDVS, a fiber optic Michelson's interferometer has been used. Even though it is a different interrogation system, data processing for extracting the signal of interest is similar (see [Papp et al. \(2017\)](#) for more details). The fibre data was bandpass-filtered to have the same frequency band of the 3C geophones (natural frequency of 5 Hz). The survey design is shown in Figure 1.7. 1.5 m of fibre cable is buried next to five 3C geophones where the in-line component of the geophones was oriented parallel to the fibre optic cable. The output of the optical fibre cable used here corresponds to a single-gauge length, that is a single spatial measurement like a geophone. However, the system is still distributed because it senses the dynamic strain over the gauge length as in conventional DAS

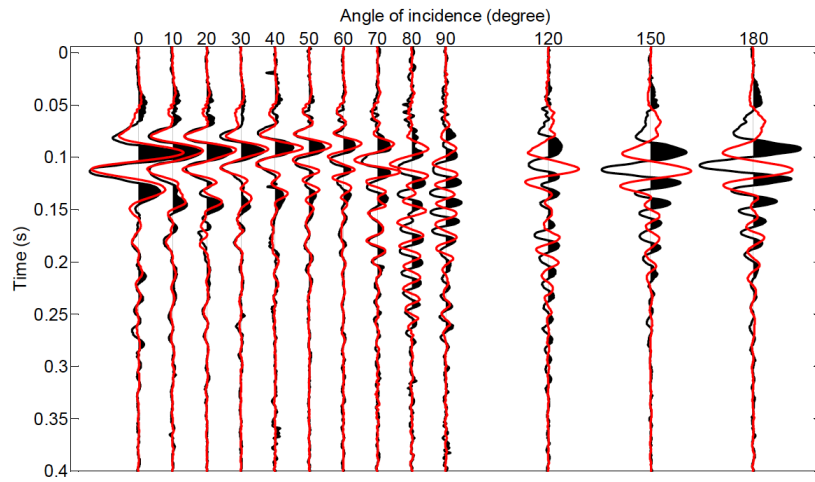


Figure 1.8: Comparison of in-line component of geophones (black) and the bare fiber measurement (red) (adapted from (Papp, 2013)).

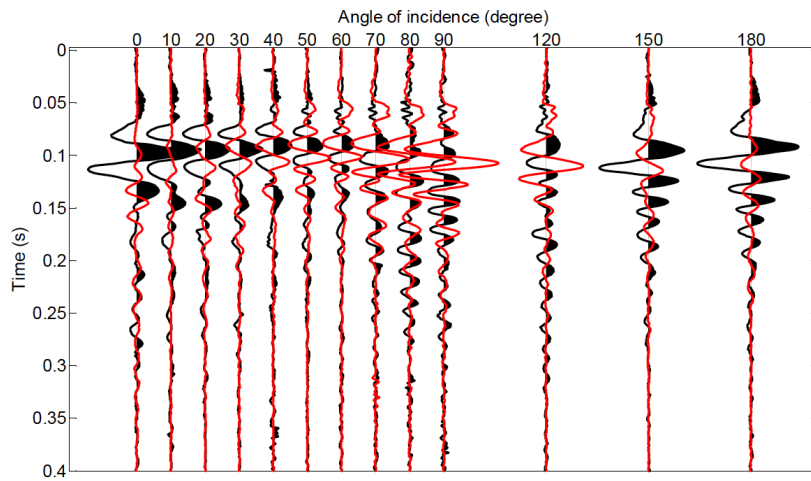


Figure 1.9: Comparison of cross-line component of geophones (black) and the bare fiber measurement (red) (adapted from (Papp, 2013)).

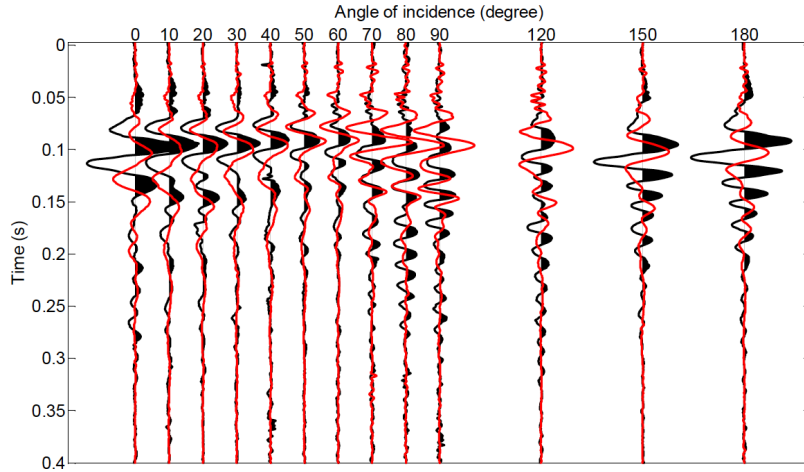


Figure 1.10: Comparison of vertical component of geophones (black) and the bare fiber measurement (red) (adapted from (Papp, 2013)).

data. The seismic source is a sledge hammer and has an offset of 15 m from the receiver and it is moved along a walk-around using an interval of  $10^\circ$  or  $30^\circ$  depending on the acquisition.

Figure 1.8 – 1.10 show the results to analyse the directionality of the DAS system where the geophone response is indicated in black and the fibre response in red. The vertical axis represents the time samples and the horizontal axis represents the angle of incidence (or source position) equivalent to the arrangement shown in Figure 1.7. The in-line component of particle velocity is shown in Figure 1.8, the cross-line component in Figure 1.9 and the vertical component is shown in Figure 1.10. The fibre that has been used to record the seismic waves was a bare fibre. Since DAS is sensitive to axial strain, while the in-line component of the geophones was oriented parallel to the fibre optic cable, the best match of recorded signal is seen in Figure 1.8 as expected. The differences of recorded signal between cross-line and vertical components of particle velocity and DAS are higher. Kuvshinov (2016) and Papp et al. (2017) described the problematic of directionality in DAS measurements. Moreover, a sign difference between the fibre and geophone data in the section from  $90^\circ$  to  $180^\circ$  can be observed in Figure 1.8 because the processed output of DAS data is given in strain. As strain is defined as

$$\epsilon = \frac{\partial u(t, z)}{\partial z}, \quad (1.15)$$

where  $u$  is displacement and  $z$  is the spatial coordinate, DAS systems do not recover the sign of the incident wave. However, Poletto et al. (2016) have presented a method that enables DAS systems to be sensitive to the direction of arrival and demonstrated the capability to separate up- and downgoing wavefields using DAS. Here, they used the strain rate  $s(t, z) = \partial\epsilon/\partial t$  to

## 1 Introduction

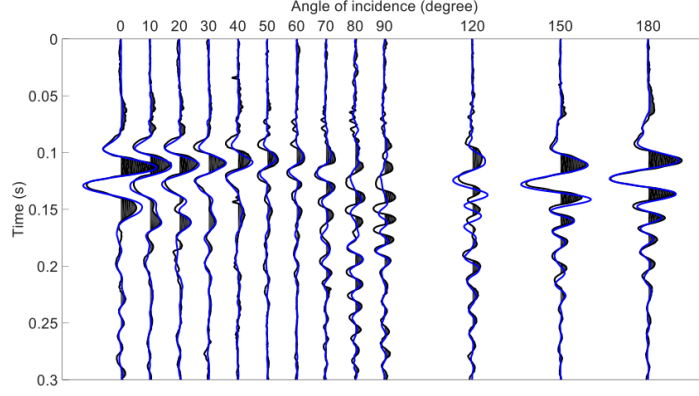


Figure 1.11: Comparison of in-line component of geophones transformed into strain (blue) and the bare fiber measurement (black).

integrate to particle acceleration  $a$  over the receiver space domain:

$$a(t, z) = \frac{d}{dt} \int_z \epsilon(t, n) dn, \quad (1.16)$$

thus recovering the sign, or polarity, of the signal. Up- and downgoing strain-rate signals are then computed as

$$s_{DW}(t, z) = \frac{s(t, z) - Ca(t, z)}{2} \quad (1.17)$$

and

$$s_{UP}(t, z) = \frac{s(t, z) + Ca(t, z)}{2}, \quad (1.18)$$

where subscripts DW and UP denote downgoing and upgoing, respectively, and  $C$  is a scaling coefficient. Moreover, [Papp et al. \(2017\)](#) proposed a transfer function where geophone data is transformed into strain to allow valid comparisons to DAS data. This function first obtains displacement  $u$  from the particle velocity from the geophone by time integration. Then, strain  $\epsilon$  is computed by considering the discrete spatial derivative of displacement traces, i.e. taking the spatial difference between receiver pairs  $u_i - u_{i+1}$ . Finally, the displacement differences are summed  $\sum_{N=1}^{i=1} (u_i - u_{i+1})$  taking the distributed nature of the measurement into account. The application of that transfer function to the data presented in [Figure 1.8](#) is shown in [Figure 1.11](#). Here, the residuals between geophone and DAS data are negligible.

The second field test in Cambridge was set up to analyse the sensitivity of DAS compared to conventional seismics in terms of SNR and dynamic range. 48 3C geophones were installed close to the buried fibre optic cable. Geophones were spaced 2 m apart and the inline-components were oriented parallel to the fibre optic cable. An accelerated weight drop has been used to generate vibrations. The survey setup is shown in [Figure 1.12](#). The seismic source was positioned at different distances (ranging from 2 m to 40 m)

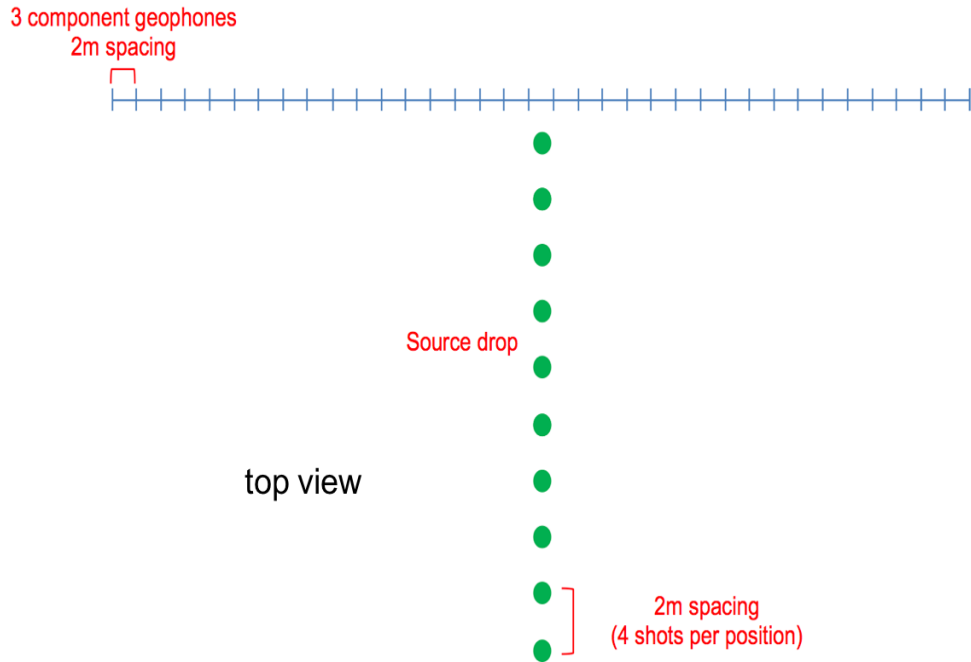


Figure 1.12: Survey design of the dataset acquired in Cambridge.

relative to the line of sensors, such that the source power detected by the sensors changed. It has been observed that as geophone data had a larger dynamic range than DAS data, a better SNR could be acquired. In particular for very near source offsets the DAS system was not capable of acquiring high data quality. In the presented example, an offset of 30 m is shown providing reasonable data quality for both systems. The DAS response is shown on the left, while the in-line component of particle velocity of the geophones is plotted in the center in Figure 1.13. The vertical axis represents the time samples and the horizontal axis represents the receiver station equivalent to the arrangement in Figure 1.12. These two measurements are relatively comparable because DAS data is compared solely with the in-line component of the 3C geophones. However, DAS is still sensing strain, while geophones record the particle velocity. Moreover, the gauge-length of the DAS system has been chosen such that the spatial resolution is 10 m, while geophone data was sampled with 2 m spacing. The transfer function discussed earlier (Papp et al., 2017) has been applied and the results are shown on the right of Figure 1.13. While geophone data is assumed to be more sensitive to seismic waves than DAS and register in general a broader band of frequencies (Molteni et al., 2016), the difference after the application of the transfer function to obtain comparable results is not significant, since the main difference between the two datasets was the high level of noise in the DAS data. The noise level of the geophone data has increased after the application of transfer function (probably because of the spatial derivative computation) allowing us to obtain a similar results to the DAS data.

## 1 Introduction

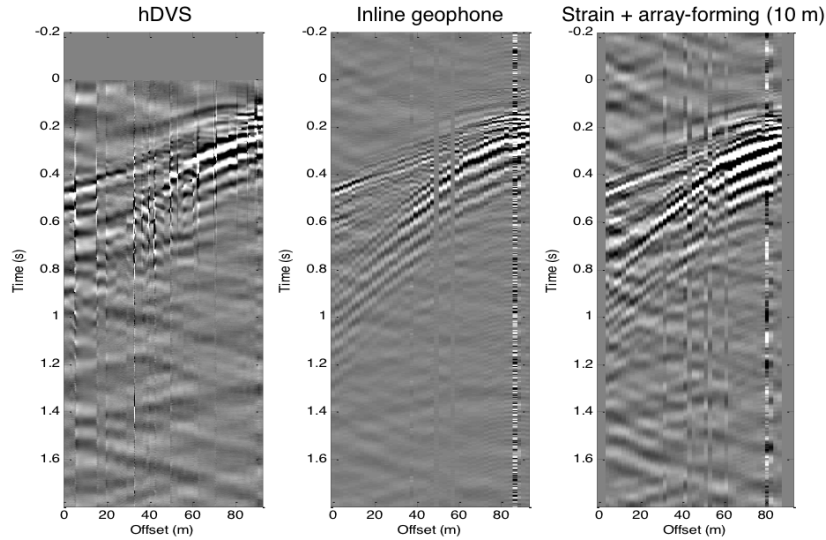


Figure 1.13: Comparison of hDVS data (left), inline-component of geophone (center) and inline-geophone data after transform to reproduce hDVS data (right).

The results of the two field tests presented so far raised the problematic of directionality of DAS measurements. Another topic that has not been discussed yet is coupling. In conventional seismic acquisitions the spike of geophones is controlling coupling conditions. Instead, for land acquisitions, the fibre cable is simply buried. However, different coatings can simulate diverse coupling conditions since the contrast between the fibre cable and its coupled medium change.

Papp (2013) not only analysed the directionality of the measurement but also the coupling by recording data of fibre with different coatings. The data was acquired in Chambon with the same acquisition setup as shown in Figure 1.7. Those fibre cables are presented in Figure 1.14:

- (1) 9/125  $\mu\text{m}$  Low Smoke, Zero Halogen (LSZH) kevlar jacketed cable
- (2) SMF-28e bare fibre inside a 1 mm diameter metal tube
- (3) 900  $\mu\text{m}$  buffered fibre
- (4) SMF-28e bare fibre

The results of the bare fibre (4) have already been presented (Figure 1.8). Results of the bare fibre inside the metal tube (2) are shown in Figure 1.15, while results of the 900  $\mu\text{m}$  buffered fibre (3) are presented in Figure 1.16. Recordings of the 9/125  $\mu\text{m}$  LSZH kevlar jacketed cable (1) are not shown because heavy rain corrupted the results and would not allow a fair comparison. The measurements using the bare fiber clearly show the best match (Figure 1.8). Even though not all data is presented here, alignment with

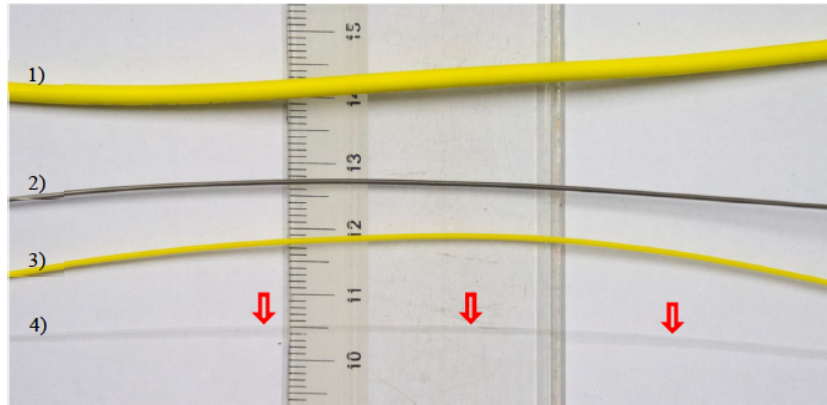


Figure 1.14: Different fibre samples side by side: (1) 9/125  $\mu\text{m}$  Low Smoke, Zero Halogen (LSZH) kevlar jacketed cable; (2) SMF-28e bare fibre inside a 1 mm diameter metal tube; (3) 900  $\mu\text{m}$  buffered fibre; (4) SMF-28e bare fibre (adapted from Papp (2013)).

geophone data differed from coating to coating, whereas data acquired with thick coatings did not align well as the data obtained with thinner coatings. The fiber cable with metal tubing shows a really good match with geophones (Figure 1.15), while the alignment decreases using 900  $\mu\text{m}$  buffered fibre (Figure 1.16). It appears that the interface, or coupling, between the fibre and formation can have a significant influence on DAS recordings. Only the coating has changed between different measurements for these figures, and therefore the cable elastic properties, i.e. Young's modulus, density and Poisson's ratio. In its essence, the elastic properties of the sensing cable alter the recorded signal and could potentially determine the level of coupling.

Since the first seismometer was invented nearly 150 years ago, research and development of conventional seismic sensor has already a long history. In contrast, DAS is a new technology and its application for seismic surveys started only a few years ago. The field trials have shown that the technology is promising but not fully developed.

### 1.4.2 Borehole seismic acquisition

The application that seems destined for the earliest adoption in the field of seismic acquisition of DAS lies in borehole seismic measurements as the long-term interest of leading oil companies is the implementation of DAS as a stand-alone tool for PRM and VSP surveys. For VSP surveys, capturing the entire wavefield and guaranteeing good coupling to record high SNRs is essential.

Deployment of DAS in VSP surveys can be grouped into three general methods sketched in Figure 1.17. Configuration 1 shows the setup where the cable is attached with rigid clamps to the tubing and then cemented behind

## 1 Introduction

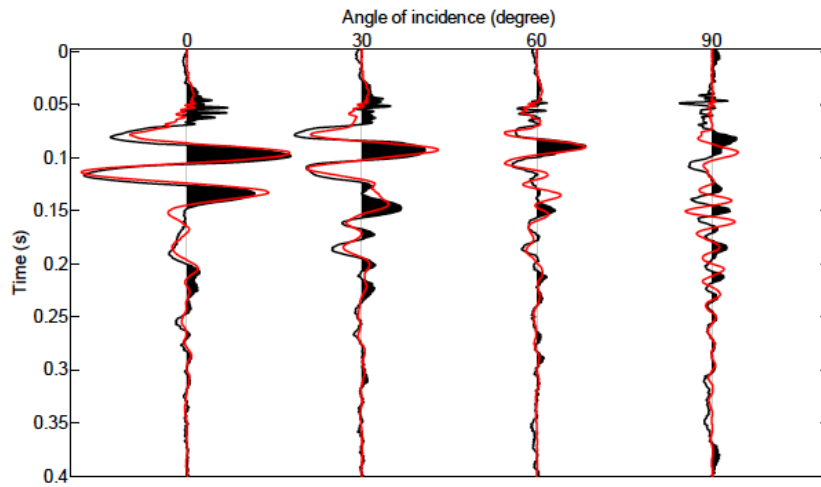


Figure 1.15: Comparison of in-line component of geophones (black) and the fiber with metal tubing measurement (red) (adapted from (Papp, 2013)).

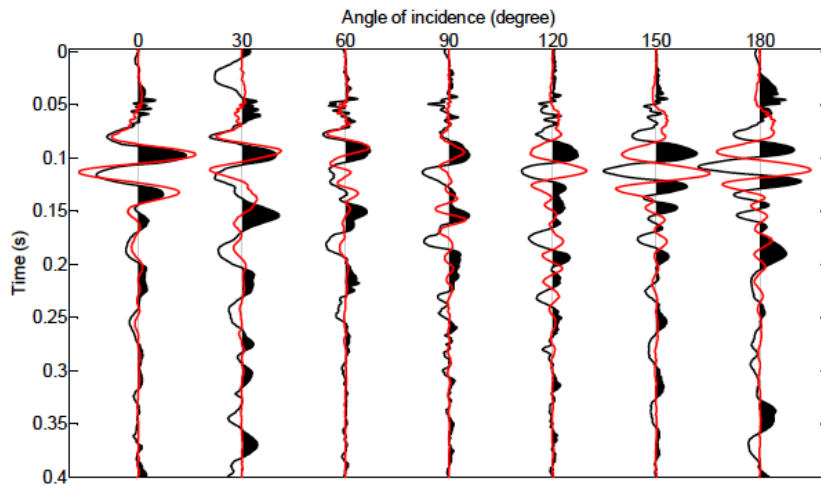


Figure 1.16: Comparison of in-line component of geophones (black) and the 900  $\mu\text{m}$  buffered fiber measurement (red) (adapted from (Papp, 2013)).

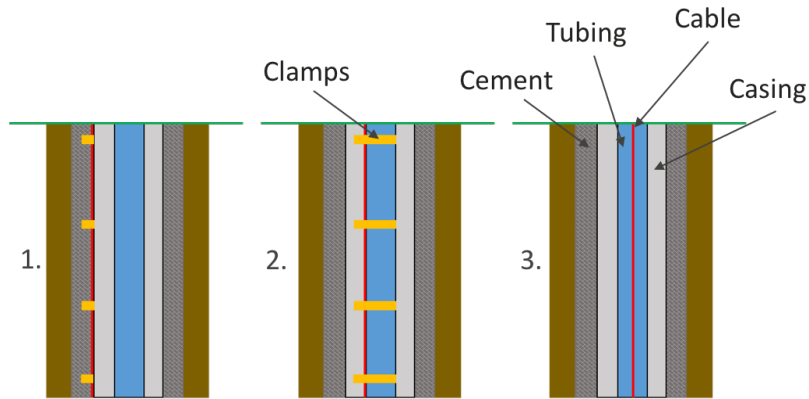


Figure 1.17: Deployment techniques using DAS for VSP surveys. 1. on the left the cable is cemented behind the casing, 2. in the center the cable is attached with rigid clamps to the tubing, and 3. on the right the cable is loosely lowered down the borehole, also called wireline deployment.

the casing. In the second setup the cable is clamped to the tubing and in the third setup the cable is loosely lowered down the borehole.

Over the past few years companies acquiring seismic data using DAS have run trials for all three configurations. Therefore it is possible to derive preliminary conclusions.

It appears that the first deployment method records the highest signal fidelity. Figure 1.18 shows a linear stack of 10 shots of a field trial acquired in Belgium where the cable has been cemented behind the casing in a 1000 m long vertical well. The source was located at zero-offset position. The first arrival is detectable throughout the entire well and also other events can be identified. Due to the fact that the cable is cemented behind the casing, the noise level is kept to a minimum and tube waves have only minor impact due to their exponential decay of axial displacement in radial direction (Hardage, 1983; Cheng and Toksöz, 1984). Furthermore the solid-solid interface guarantees that the DAS cable is measuring the seismic signal more accurately while the seismic signal can be altered and attenuated if a fluid interface would be present (Schoenberg, 1986).

In the second deployment method the cable is clamped to the tubing. Figure 1.19 shows results of a field trial in the south of France (Barberan et al., 2012). The well is nearly vertical and 4300 m long. The source, a vibrating truck, was located at zero-offset position and the result in Figure 1.19 shows a linear stack of 20 sweeps. During this deployment method the fibre optical cable is only clamped to the tubing at regular intervals (e.g. every 15 m). Hence, the cable establishes a direct contact with the borehole in these points, but between those the fibre can move. This can lead to coherent noise events, called 'ringing', visible in the real data. As those noise events are co-

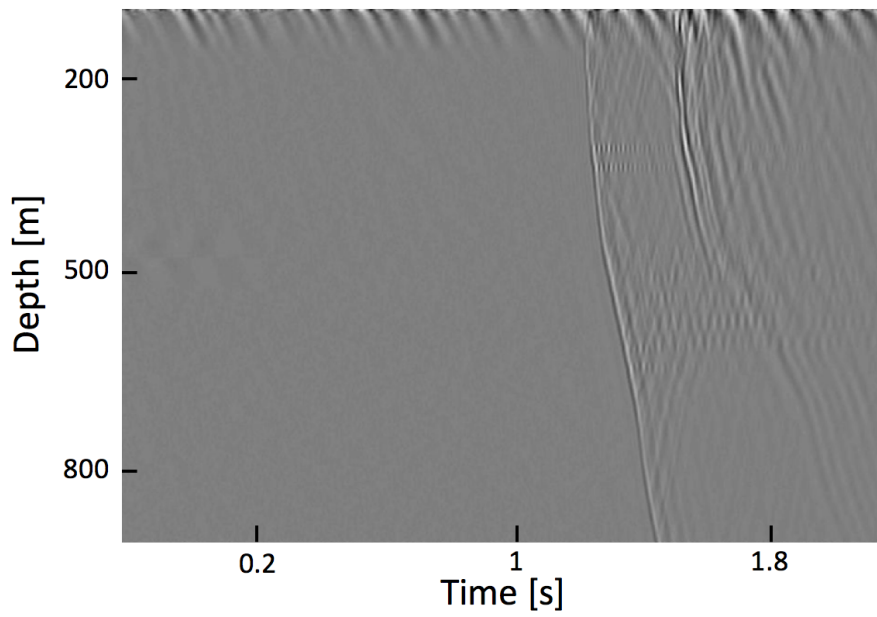


Figure 1.18: Fibre recordings when cemented behind the casing. Linear stack of 10 shots in 1000 m long vertical well.

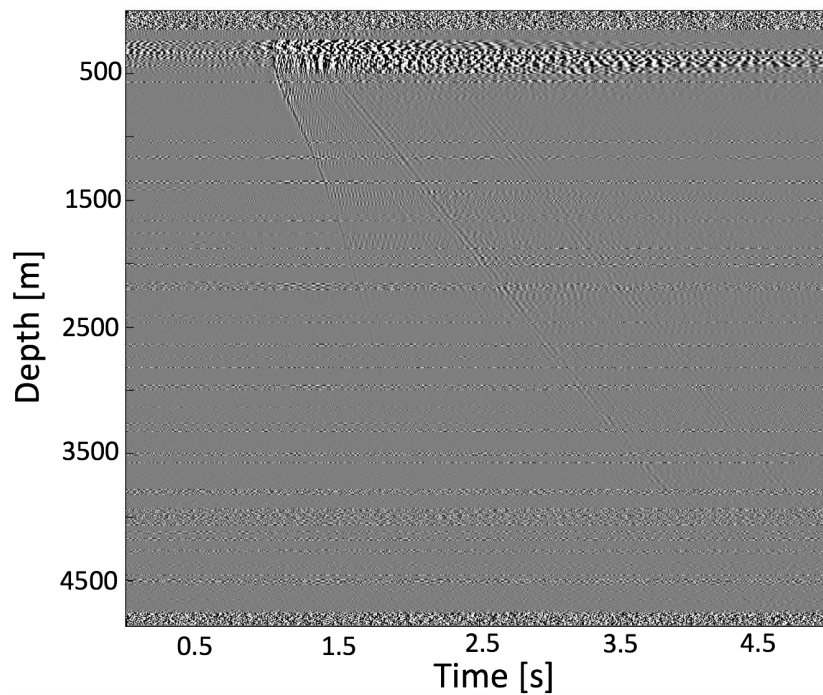


Figure 1.19: Fibre recordings when clamped to the tubing. Linear stack of 20 sweeps in 4300 m long vertical well (adapted from [Barberan et al. \(2012\)](#)).

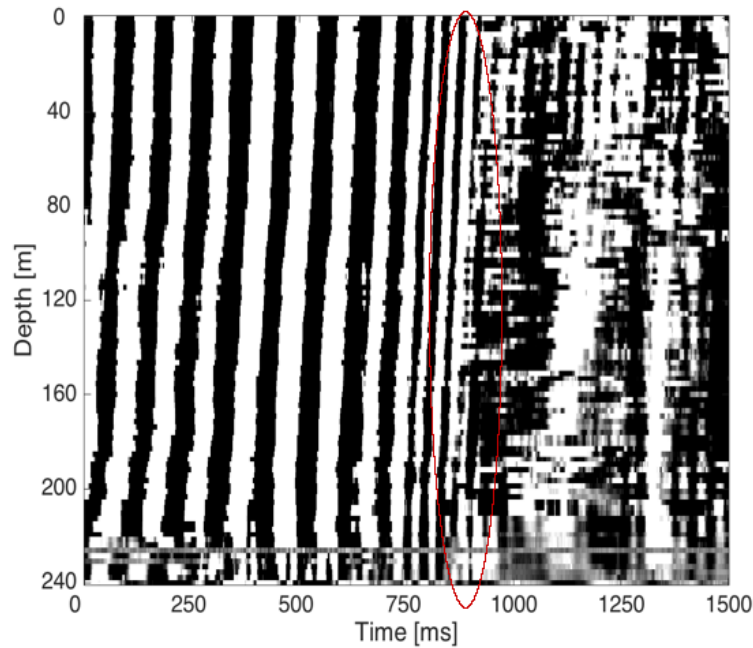


Figure 1.20: Fibre recordings when deployed on wireline cable, where the signal is expected to be around 850 ms and indicated with a red circle. Linear stack of 8 shots in a 240 m long vertical well.

herent, they can be eliminated using signal processing techniques e.g. dip filtering. Moreover, as the cable is not necessarily in contact with the borehole wall or casing between the mentioned clamping points, the fluid-structure interface causes amplitude attenuation and phase variations (Schoenberg, 1987). Also tube waves can interfere with signal of interests, especially if the time between shotpoints is limited since they can travel up and down the borehole multiple times (Hardage, 1981; Galperin, 1985).

The third deployment method generally allows recording the lowest quality of signal. Figure 1.20 shows recordings of a fibre optical cable deployed on wireline cable. Data was acquired in a 225 m long vertical well. The seismic source was a seismic airgun located in portable airgun tank (Clark and Mackie, 2013) 30 m away from the well. The result that is shown is a stack of 8 seismic shots. During this deployment technique the cable is simply lowered down the borehole and it attempts to detect seismic waves. Because the precise position of the cable in the borehole is not known, it is speculative to predict a direct contact of the cable with the borehole-wall, which can, however, occur. It has been observed that keeping the cable under full tension or providing only minor tension release leads to high amplitude ambient noise as well as harmonic noise superimposing any signal of interest, i.e. first arrivals.

## 1.5 Motivation and thesis outline

### 1.5.1 Motivation - using DAS as a seismic sensor for VSP surveys

The data quality of the results obtained by different strategies of fibre optical cable deployment presented in the Section 1.4.2 varied significantly. While the cable cemented behind the casing recorded a high signal fidelity (Figure 1.18), clamping it at regular intervals to the tubing generated coherent noise but also increased the ambient noise level (Figure 1.19). The lowest SNR has been recorded using wireline deployment, where the cable was simply lowered down the borehole (Figure 1.20). However, when there is not a permanently installed DAS cable in place, this deployment technique is by far more cost-effective compared to conventional seismic acquisitions tools, such as the VSI. The main limitation of DAS is the lower data quality that is usually obtained compared to the VSI, but DAS offers advantages namely:

- VSI requires a few minutes for each level of depth to acquire data while DAS allows acquiring data of the whole borehole depth in one shot;
- the total rig time for VSI acquisitions is several hours to days while it is typically a few minutes for DAS;
- solely VSI recordings are able to be measured during the survey, while other measurements can run simultaneously when acquiring DAS data;
- the VSI (and possibly more than one unit) needs to be clamped to the wireline cable thus increasing the overall cost of the survey, while the fibre optical cable is already integrate within the wireline cable.

As already mentioned the biggest advantage of DAS compared to conventional seismic acquisition is the lower cost of acquisition. The motivation of this PhD work is to understand under which circumstances improved data quality can be acquired using the wireline deployment method. For this reason, [Hartog et al. \(2014\)](#) presented results of a field trial where they acquired DAS data using wireline deployment in a 600 m vertical fluid-filled well shown in Figure 1.21. Figure 1.21 (a) shows recordings when the wireline cable was fully under tension. In (b) a minimum amount of tension has been released from the cable. (c) shows an intermediate tension release while in (d) recordings were made when it was not feasible to lower more cable down the borehole. While any signal of interest was superimposed by high amplitude and sinusoidal noise in (a) the first break was detectable, when tension of the cable was released by lowering more cable into the borehole. When lowering the maximum amount of cable down the borehole (Figure 1.21 (d)), the first break was detectable throughout the entire well length.

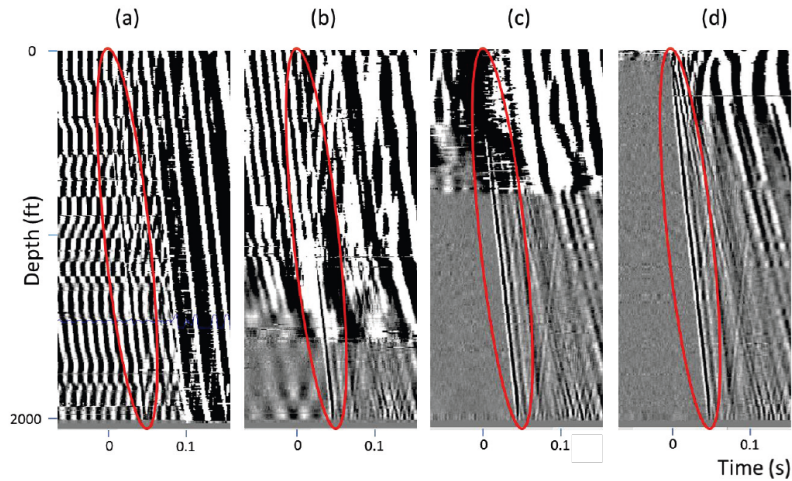


Figure 1.21: hDVS data using different cable length; a) cable under tension b) small tension release c) intermediate tension release d) maximum tension release (adapted from [Hartog et al. \(2014\)](#)).

At the beginning of the PhD it was unclear why and when data quality as seen in Figure 1.21 can be acquired. The objective of this study was to use numerical simulations with the aim (1) to understand particle motion inside the fluid-filled well recorded by DAS and how this relates to conventional seismic recordings, (2) to determine the conditions under which a high fidelity signal can be obtained for a wireline DAS cable and (3) to optimise the coupling of a DAS cable in wireline mode .

## 1.5.2 Thesis outline

The thesis is structured as follows:

- Chapter 2 is called constitutive equations because it forms the mathematical basis for the following chapters.

In the first part a short overview of the fundamental concepts of physics is given: the physical quantities of force, displacement, stress and strain are discussed.

Based on those physical quantities, seismic wave equations are described in terms of velocity-stress formulations. Both acoustic as well as elastic wave equations are derived.

Then, seismic wave expressions in fluid-filled boreholes are discussed highlighting the differences between seismic wave motion in the fluid-filled borehole and the surrounding elastic formation.

The last part of Chapter 2 introduces another essential part of the thesis: coupling. First, coupling of conventional geophones is reviewed.

Then, a first attempt to address the coupling of DAS is made by reviewing the mechanics of contact and the variables of corresponding equations - force, geometry and elastic properties. It will be shown in Chapter 5 that those variables are controlling the differences between the seismic signal recorded at the borehole-wall and at the fibre cable.

- Chapter 3 introduces the Finite-Element-Method (FEM) and its application. A comparison to other numerical methods will be given and the motivation to use explicit FEM stated.

Following, the FEM scheme to solve a real world problem is introduced, starting from defining the geometry, elements and material properties, to discretising the area of interest and solving the system of equations. Then, numerical results of seismic wave propagation, solved using commercial software packages LS-dyna and AnSYS, will be shown. Starting from 1D plane wave propagation, we validate the modelling results using analytical observations, while the model becomes increasingly complex.

Then a model with a fluid-filled borehole is modeled, thus simulating a zero-offset VSP survey. In addition, the wireline cable is modeled in the center of the borehole while the grid size (1.5 mm for the cable while the formation is discretized every 3 m) only allowed to assume a constant cross-section without modeling finer parts, e.g. cladding or the silica glass. Results are interpreted with analytical solutions derived in Chapter 2.

Moreover, another numerical model is created to track the movement of the cable during wireline deployment. The numerical simulation is used to derive conclusions about when the fibre cable is considered to be well coupled and when more cable needs to be lowered down the borehole.

- Chapter 4 presents the application of the numerical model to real data. P-, S- as well as tube waves are detectable in DAS, VSI and numerical data. However, all three wave types are only visible on DAS data after lowering more cable down the borehole when using wireline deployment (Section 1.4.2). Simply moving the cable in our numerical solution inside the borehole did not explain differences observed in real data. Therefore, a different numerical model has been generated to track the movement of the cable. The resulting conclusion that a direct contact of the cable with the borehole-wall is necessary to record high data quality could be confirmed by a second field trial in a different well.
- Chapter 5 uses information from Chapter 2 and observations made in real data presented in Chapter 4 to optimise DAS acquisitions. The

difference in recorded signal at the borehole-wall and at the fibre cable can be minimised by increasing the contact force and calibrating the cable elastic properties. Furthermore, a coupling detection algorithm is presented to provide reliable information on whether the cable is well coupled or not even prior to triggering any seismic source.

- In Chapter 6, the main conclusions are summarised and future perspectives discussed.

### 1.5.3 Realisations and contributions

Signal processing algorithms to process optical data in Matlab and C++ have been built by the signal processing team at the Schlumberger Fibre Optic Technology Centre (SFTC) in Southampton and a research group from Peter the Great St. Petersburg Polytechnic University. A few minor adjustments have been implemented so that all codes could be used for the purposes of the PhD. Codes in Ansys Parametric Design Language (APDL) to find boundary value problems for partial differential equations using AnSYS and LS-dyna have been built from scratch.

The main contributions of this PhD thesis are:

- obtaining a numerical model that explains the behavior of a DAS cable in fluid-filled boreholes;
- constructing a numerical model that stimulates the cable movement in boreholes;
- obtaining a match between acquired field data and numerical data, allowing to explain observed data;
- developing a numerical model to optimise DAS acquisitions;
- developing a coupling detection algorithm to ensure DAS recordings with high SNRs prior to acquisition.

Results and conclusions of these developments not only allow a better understanding of DAS recordings but also provide explicit answers to why and when recordings with high SNRs are acquired. Even though this work has been carried out in a R&D environment, the strong collaboration with the engineering team in Schlumberger often required immediate results and applications. Part of those results have been presented in

- Schilke, S., Donno, D., Hartog, A., Chauris, H. (2017): DAS and its coupling during VSP on wireline cable. EAGE/DGG Workshop on Fibre Optics Technology in Geophysics, 31 March, Potsdam, 2017;
- Schilke, S., Donno, D., Hartog, A., Chauris, H. (2017): DAS for borehole VSP. 3rd WAVES Workshop, 26-29 March, Cambridge, 2017;

## 1 Introduction

- Schilke, S., Donno, D., Hartog, A., Farahani, A., Pico Y., Chauris, H. (2016): Numerical evaluation of sensor coupling of distributed acoustic sensing systems in vertical seismic profiling. SEG International Exposition and 86th Annual Meeting, 16-21 October, Dallas, 2016;
- Schilke, S., Donno, D., Hartog, A., Farahani, A., Chauris, H. (2016): A numerical study of coupling of fibre optical cables. 78th EAGE Conference and Exhibiton, 16-19 June, Vienna, 2016.

## Constitutive equations

### Résumé du chapitre

Ce chapitre fournit un aperçu des équations constitutives qui seront utilisées dans les modèles numériques décrits aux chapitres 3 et 4, et une introduction à la mécanique des contacts. L'objectif est de formuler une base mathématique pour interpréter les résultats et identifier les limites des approximations numériques. Dans la section 2.2, les concepts fondamentaux de la physique et les variables de gouvernance de nos problèmes sont présentés: la force et les moments, le déplacement, la vitesse et l'accélération ainsi que la déformation et la contrainte sont définis. Ces concepts clés permettent la dérivation des équations d'ondes élastodynamiques linéaires en termes de vitesse et de contrainte présentées dans la section 2.3. On définit l'équation d'onde élastique et acoustique en termes de vitesse de la particule et de contraintes pour en suite analyser la vitesse de la particule dans le milieu élastique ainsi que dans les forages remplis de fluide décrits dans la section 2.4. Même si les longueurs d'ondes sismiques ont tendance à être plus grandes que les diamètres des forages, de telle sorte que la présence du puits ne modifie pas les vitesses particulières trouvées à l'extérieur du puits et dans le fluide de forage, il existe des différences entre la vitesse des particules dans le milieu élastique et le fluide du puits. Notez que nous négligeons la diffraction sismique dans ce cas (Klem-Musatov et al., 2016). Enfin, la section 2.5 traite le problème du couplage, comme aucune recherche n'a été effectuée pour analyser le couplage du capteur à fibre est utilisée pour présenter la physique et les principales variables de la mécanique des contacts. Ceci est essentiel pour mettre en évidence les mécanismes de contrôle du contact entre deux supports élastiques qui peuvent induire le couplage du câble du capteur à fibre optique distribuée (DAS) avec le milieu de l'acquisition et donc la sensibilité de la mesure.

## 2.1 Introduction

This chapter provides an overview of the constitutive equations and their relationship that are used in the numerical models described in Chapter 3 and 4, and an introduction to the topic of contact mechanics. The purpose is to formulate a mathematical basis in order to be able to interpret results and identify limitations of the numerical approximations. In this thesis we denote lowercase letters for scalars, lowercase bold letters for vectors and uppercase bold letters for second-order tensors or higher. The sign convention is such that tension force is positive and compression force is negative.

In Section 2.2 the fundamental concepts of physics and the governing variables for our problems are presented: force and moments, displacement, velocity and acceleration as well as stress and strain are defined. These key concepts enable the derivation of linear elastodynamic wave equations in terms of velocity and stress presented in Section 2.3. Defining elastic and acoustic wave equation in terms of particle velocity and stress aids to understand the comparison of particle velocity in the elastic formation and fluid filled boreholes described in Section 2.4. Even though seismic wavelengths tend to be much larger than borehole diameters, such that the borehole presence should not alter particle velocities found outside the borehole and in the borehole fluid, differences between particle velocity in the elastic formation and the borehole fluid exist. Note that we are neglecting seismic diffraction in this case (Klem-Musatov et al., 2016). Finally, Section 2.5 addresses the coupling problem. As there has not been any research carried out to analyse the coupling of DAS in VSP surveys, we review here the basics of contact mechanics after having presented the principles of coupling of conventional seismic sensors.

In contrast to the first part of this chapter, which is used to derive the equations being solved in the numerical simulation in Chapters 3 and 4, the last part is used to present the physics and key variables of contact mechanics. This is critical in order to highlight the governing mechanisms of contact between two elastic media that might induce the coupling of the DAS cable and therefore the sensitivity of the measurement.

## 2.2 Governing variables

Before presenting partial differential equations or PDEs of seismic wave motion, the governing variables will be briefly reviewed. Based on the definitions of time and space, mass and forces are the physical quantities initiating propagation of acoustic and elastic wavefields. Elastic and acoustic wave propagation is commonly described in terms of particle displacement as well as stress and strain relationships (Aki and Richards, 1980; Chapman, 2004). Note that entire books are written about structural mechanics (Johnson, 1985; Holzapfel, 2001), whereas this section should only serve as a brief

introduction to the topic so that the reader can recall the physical quantities and their meaning.

### 2.2.1 Forces $\mathbf{F}$ and moments $\mathbf{M}$

The four fundamental concepts in physics are space, time, mass and force. It is easiest to present those concepts using rigid bodies and hence ignore deformations. Space and time can describe the situation when a body is being displaced, is moving with a constant velocity or is accelerating. The mass is used to characterise the relationship between the acceleration of an object and the acting force that causes the change in velocity. This relationship is defined by Newton's laws of motion, where Newton's second law is defined as

$$\mathbf{F} = m\mathbf{a}, \quad (2.1)$$

where  $\mathbf{F}$  is the resultant force measured in Newton [N],  $m$  is the mass measured in kilogram [kg] and  $\mathbf{a}$  is acceleration in units [ $\text{m}/\text{s}^2$ ].  $\mathbf{F}$  is the resultant force as it is the sum of all force contributions along the three coordinate axes  $x$ ,  $y$ ,  $z$ :

$$\mathbf{F} = \begin{pmatrix} F_x \\ F_y \\ F_z \end{pmatrix}. \quad (2.2)$$

Equation 2.1 states that if the resultant force  $\mathbf{F}$  is non-zero, the particle accelerates in proportion to, and in the same direction as, the resultant force

The moment  $\mathbf{M}$  of a force  $\mathbf{F}$  about an axis through a point  $o$  is defined as:

$$\mathbf{M}_o = \mathbf{F}d, \quad (2.3)$$

where  $d$  is the distance perpendicular to the line of action of  $\mathbf{F}$  and  $o$  (Figure 2.1). The moment describes the tendency of the body to rotate.

### 2.2.2 Stress $\sigma$

Certain physical phenomena consider the body to be continuously distributed, thus occupying the entire space. This body can be divided into infinitesimal elements and, therefore, the force acting over an area is a more convenient variable of measurement. This introduces the concept of stress  $\sigma$  defined as:

$$\sigma = \frac{\mathbf{F}}{A}, \quad (2.4)$$

where  $A$  is the area measured in [ $\text{m}^2$ ], and therefore  $\sigma$  is measured in [ $\text{kg} / \text{m s}^2$ ] or [Pascal]. Surface or contact stress occurs if an object gets in contact with a second object. According to Newton's third law of motion, a stress

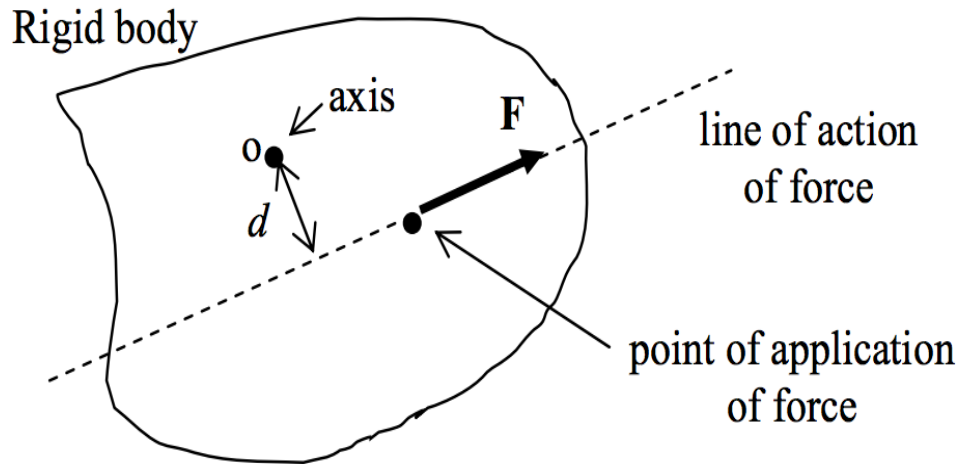


Figure 2.1: The moment of a force  $\mathbf{F}$  about an axis  $o$  (adapted from Kelly (2013)).

equal in magnitude but opposite in direction is created by the second object. The total force can be calculated by integrating the stresses over the area  $A$ :

$$\mathbf{F} = \int_A \boldsymbol{\sigma} dA. \quad (2.5)$$

The stresses in rigid body motion are normal stresses ( $\sigma_{xx}, \sigma_{yy}, \sigma_{zz}$ ), being perpendicular to the surface. Forces that act tangentially to surfaces are called shear forces inducing shear stresses ( $\sigma_{xy}, \sigma_{xz}, \sigma_{yx}, \sigma_{yz}, \sigma_{zx}, \sigma_{zy}$ ). While shear stresses occur in elastic media, they do not exist in non-viscous fluids.

In contrast to surface forces, body forces are forces that act at a distance on small volume elements of the object, the easiest example being gravity  $\mathbf{g}$ . Similar to Equation 2.5, the weight force  $\mathbf{F}_w$  is defined as

$$\mathbf{F}_w = \int_V \rho \mathbf{g} dV, \quad (2.6)$$

where  $V$  is the volume on which the force is acting and  $\rho$  the density.

### 2.2.3 Displacement $\mathbf{u}$ , velocity $\mathbf{v}$ , acceleration $\mathbf{a}$

In kinematics, displacement  $\mathbf{u}$  is also called the position vector and a function of time and space. Velocity  $\mathbf{v}$  and acceleration  $\mathbf{a}$  are obtained from displacement time derivatives. They are all vector quantities and can describe e.g. the propagation of seismic wavefields. Acceleration is generated by acting forces  $\mathbf{F}$  onto an object with mass  $m$  as seen in Equation 2.1. Acceleration

is defined as the rate of change of velocity of an object w.r.t. time, hence the integral form reads:

$$\mathbf{v}(t) = \int \mathbf{a}(t)dt, \quad (2.7)$$

while  $\mathbf{v}$  is the rate of change of position of an object w.r.t. time, and therefore

$$\mathbf{u}(t) = \int \mathbf{v}(t)dt. \quad (2.8)$$

In differential formula this can be written as:

$$\mathbf{a}(t) = \frac{\partial \mathbf{v}(t)}{\partial t} = \frac{\partial^2 \mathbf{u}(t)}{\partial t^2}. \quad (2.9)$$

### 2.2.4 Strain $\epsilon$

Strain tensor  $\epsilon$  is a measure of deformation of an object and therefore excludes rigid body dynamics. It can be computed as the partial derivative of displacement w.r.t. space,  $\epsilon = \frac{1}{2}(\nabla \mathbf{u} + (\nabla \mathbf{u})^T)$ , as it represents a measure of how rapidly the relative displacement changes in the body of interest. The computation of strain is relevant since DAS outputs are measured in terms of strain rather than displacement or velocity because of the nature of the DAS data and of its processing described in Chapter 1.

In the generalised Hooke's law for elastic media, stress and strain are related by a 4<sup>th</sup> rank elastic stiffness tensor  $C_{ijkl}$  using Einstein notation on repetitive indexes:

$$\sigma_{ij} = C_{ijkl}\epsilon_{kl}. \quad (2.10)$$

The stiffness tensor  $C_{ijkl}$  is symmetric and describes the resistance of a body of being deformed elastically. For an isotropic material, one that behaves the same in any orientation, it depends only on the Lamé parameters  $\lambda$  and  $\mu$ . Then, stress  $\sigma$  can be related to strain  $\epsilon$  via the Young's modulus  $E$ :

$$\sigma = E\epsilon. \quad (2.11)$$

Normal strain components are obtained as

$$\begin{aligned} \epsilon_{xx} &= \frac{1}{E} \left( \sigma_{xx} - \nu(\sigma_{yy} + \sigma_{zz}) \right), \\ \epsilon_{yy} &= \frac{1}{E} \left( \sigma_{yy} - \nu(\sigma_{zz} + \sigma_{xx}) \right), \\ \epsilon_{zz} &= \frac{1}{E} \left( \sigma_{zz} - \nu(\sigma_{xx} + \sigma_{yy}) \right), \end{aligned} \quad (2.12)$$

## 2 Constitutive equations

where  $\nu$  is Poisson's ratio for an isotropic material. Recall that  $\lambda = \frac{E\nu}{(1+\nu)(1-2\nu)}$  and  $\mu = \frac{E}{2(1+\nu)}$ . Strain will increase with decreasing Young's modulus and increasing Poisson's ratio, meaning that the stiffer the material, the less strain is induced.

The concepts of forces, moments, stress, strain and displacement have been reviewed. Those physical quantities form the basis of the elastodynamic equations, that are presented in the next section, which are governed by three constitutive equations (Malvern, 1977; Holzapfel, 2001): (1) the kinetic equation

$$\boldsymbol{\epsilon} = \frac{1}{2}(\nabla\mathbf{u} + (\nabla\mathbf{u})^T), \quad (2.13)$$

where  $\nabla\mathbf{u}$  is the gradient of displacement; (2) the dynamic equation

$$\mathbf{F} = m\mathbf{a}, \quad (2.14)$$

where  $\mathbf{F}$  comprises body forces on volumes and stress on surfaces; and (3) the concept of linear elasticity

$$\boldsymbol{\sigma} = \mathbf{C}\boldsymbol{\epsilon}. \quad (2.15)$$

## 2.3 Seismic wave equations

Waves of interest in the field of geophysics and seismology are acoustic and elastic waves. Since shear stresses do not exist in non-viscous fluids such as air, the acoustic wave equation models only compressional body waves propagating within the considered domain, while the elastic wave equation models both compressional and shear waves. Despite other intrinsic properties of the medium of interest, the governing variables for both acoustic and elastic wave equations are force, stress and strain, pressure and particle displacement which have all been introduced in Section 2.2.

In a time-domain approach and a Cartesian coordinate system, elastic wave equations can be described in terms of the particle velocity-stress formulation (Virieux, 1984, 1986):

$$\frac{\partial v_x}{\partial t} = \frac{1}{\rho} \left( \frac{\partial \sigma_{xx}}{\partial x} + \frac{\partial \sigma_{xy}}{\partial y} + \frac{\partial \sigma_{xz}}{\partial z} + f_x \right), \quad (2.16)$$

$$\frac{\partial v_y}{\partial t} = \frac{1}{\rho} \left( \frac{\partial \sigma_{xy}}{\partial x} + \frac{\partial \sigma_{yy}}{\partial y} + \frac{\partial \sigma_{yz}}{\partial z} + f_y \right), \quad (2.17)$$

$$\frac{\partial v_z}{\partial t} = \frac{1}{\rho} \left( \frac{\partial \sigma_{xz}}{\partial x} + \frac{\partial \sigma_{zy}}{\partial y} + \frac{\partial \sigma_{zz}}{\partial z} + f_z \right), \quad (2.18)$$

$$\frac{\partial \sigma_{xx}}{\partial t} = (\lambda + 2\mu) \frac{\partial v_x}{\partial x} + \lambda \left( \frac{\partial v_y}{\partial y} + \frac{\partial v_z}{\partial z} \right), \quad (2.19)$$

$$\frac{\partial \sigma_{yy}}{\partial t} = (\lambda + 2\mu) \frac{\partial v_y}{\partial y} + \lambda \left( \frac{\partial v_x}{\partial x} + \frac{\partial v_z}{\partial z} \right), \quad (2.20)$$

$$\frac{\partial \sigma_{zz}}{\partial t} = (\lambda + 2\mu) \frac{\partial v_z}{\partial z} + \lambda \left( \frac{\partial v_y}{\partial y} + \frac{\partial v_x}{\partial x} \right), \quad (2.21)$$

$$\frac{\partial \sigma_{xy}}{\partial t} = \mu \left( \frac{\partial v_x}{\partial y} + \frac{\partial v_y}{\partial x} \right), \quad (2.22)$$

$$\frac{\partial \sigma_{xz}}{\partial t} = \mu \left( \frac{\partial v_x}{\partial z} + \frac{\partial v_z}{\partial x} \right), \quad (2.23)$$

$$\frac{\partial \sigma_{yz}}{\partial t} = \mu \left( \frac{\partial v_y}{\partial z} + \frac{\partial v_z}{\partial y} \right), \quad (2.24)$$

where  $v_x, v_y, v_z$  are the velocity components,  $\rho$  the density,  $\sigma_{xx}, \sigma_{xy}, \sigma_{xz}$ , *etc.* the components of the stress tensors,  $f_x, f_y, f_z$  body forces acting as source term and  $\lambda$  and  $\mu$  the Lamé parameters. Note that they depend on  $(x, y, z, t)$ , where  $x, y, z$  is space and  $t$  is time. In non-viscous fluids, shear stress components do not exist ( $\sigma_{xy} = \sigma_{xz} = \sigma_{yz} = 0$ ) and

$$\mu = 0, \quad (2.25)$$

which let us obtain an expression for the fluid stress tensor  $\mathbf{P}$ :

$$\mathbf{P} = p\mathbf{I}, \quad (2.26)$$

where  $p$  is the hydrostatic pressure and  $\mathbf{I}$  is the unit tensor. The hydrostatic pressure  $p$  is defined as the negative average of the normal stresses:

$$p = -\frac{1}{3}(\sigma_{xx} + \sigma_{yy} + \sigma_{zz}), \quad (2.27)$$

Consequently, Equations 2.16 - 2.24 reduce to:

$$\frac{\partial v_x}{\partial t} = -\frac{1}{\rho} \frac{\partial p}{\partial x} + f_x,$$

$$\frac{\partial v_y}{\partial t} = -\frac{1}{\rho} \frac{\partial p}{\partial y} + f_y, \quad (2.28)$$

$$\frac{\partial v_z}{\partial t} = -\frac{1}{\rho} \frac{\partial p}{\partial z} + f_z,$$

$$p = -\kappa \left( \frac{\partial u_x}{\partial x} + \frac{\partial u_y}{\partial y} + \frac{\partial u_z}{\partial z} \right), \quad (2.29)$$

where  $\kappa$  is the bulk modulus with  $\kappa = \lambda + \frac{2}{3}\mu$  and  $u$  is displacement.

Equation 2.29 states that an infinitesimal small change in volume ( $\nabla \cdot u$ )

## 2 Constitutive equations

will induce pressure on one face of the small volume equivalent to Hooke's law for acoustics. Furthermore, according to Newton's law of motion there must be an internal force (acceleration) balancing external forces, so we obtain for any arbitrary force distribution:

$$\nabla p = -\rho \begin{pmatrix} \partial v_x / \partial t \\ \partial v_y / \partial t \\ \partial v_z / \partial t \end{pmatrix}. \quad (2.30)$$

The first-order acoustic wave equations are obtained by differentiating Equation 2.29 twice w.r.t. time and multiplying Equation 2.30 with  $\frac{1}{\rho}$  before applying the divergence ( $\nabla \cdot$ ):

$$\frac{\partial^2 p}{\partial t^2} = -\kappa \nabla \cdot \begin{pmatrix} \partial v_x / \partial t \\ \partial v_y / \partial t \\ \partial v_z / \partial t \end{pmatrix} + \frac{\partial^2 f}{\partial t^2}, \quad (2.31)$$

and

$$\nabla \cdot \left( \frac{1}{\rho} \nabla p \right) = -\nabla \cdot \begin{pmatrix} \partial v_x / \partial t \\ \partial v_y / \partial t \\ \partial v_z / \partial t \end{pmatrix}. \quad (2.32)$$

First-order wave equations in terms of pressure, velocity and stress have been presented so far, because in the seismic wave expressions in fluid-filled boreholes, as discussed in the next section, particle velocity in the elastic formation is compared to particle velocity in the acoustic borehole-fluid.

For the sake of completeness, we present here the second-order wave equations. The second-order elastic wave equation written in terms of vector field particle velocity  $v$  is defined as:

$$\rho \frac{\partial^2 v}{\partial t^2} = (\lambda + 2\mu) \nabla (\nabla \cdot v) - \mu \nabla \times (\nabla \times v) + f, \quad (2.33)$$

while the acoustic wave equation with  $\mu = 0$  reduces automatically to:

$$\frac{1}{c^2} \frac{\partial^2 v}{\partial t^2} = \nabla^2 v + f, \quad (2.34)$$

where  $c = \sqrt{\frac{\kappa}{\rho}}$  denotes velocity.

## 2.4 Seismic wave expressions in a fluid-filled borehole

After having presented the equations of seismic wave propagation, we review motion inside fluid-filled wells. The purpose of reviewing the seismic wave expression in a fluid-filled borehole, generated by an impinging elastic wavefront, is to be able to interpret borehole seismic data, and in particular particle velocities in the fluid. The analytical solutions analysed here will be then used to validate the solution of the numerical model presented in Chapter 3. Furthermore, quantifying particle motion in the borehole fluid will allow to understand DAS measurements which is the objective of this PhD work.

Seismic wavelengths ( $\lambda = v/f$ , where  $f$  is the central frequency) in exploration geophysics are in the range of 20 – 500 m, while the borehole diameter is typically only 30 cm or less. When analysing motion in fluid filled boreholes, the borehole is commonly considered to be transparent to the seismic waves, i.e. normal stress components inside the borehole are identical to normal stress outside the borehole. However, many borehole seismic surveys have shown that particle velocity can vary significantly because of the presence of the borehole, and even additional wave types can be generated such as tube waves (Hardage, 1983).

Schoenberg (1986) developed an analytical solution of an elastic wave impinging on a fluid-filled borehole, based on plane wave approximations. As seismic wavelengths are larger than borehole diameters, solutions have been expanded in powers of a dimensionless frequency:

$$\Omega = \frac{\omega r_b}{\beta}, \quad (2.35)$$

where  $\omega$  is the radial frequency,  $r_b$  the borehole radius and  $\beta$  the shear-wave speed in the formation. Schoenberg's analysis is suitable for very small numbers for  $\Omega$  (in the range 0.1 – 0.25), which is a reasonable approximation for the practical borehole scenario in geophysics (e.g. for a frequency of 150 Hz,  $\beta$  is about 1.4 km/s and for  $r_b$  around 15 cm,  $\Omega$  is about 0.1).

Let us consider a homogeneous elastic medium of density  $\rho$ , compressional - wave speed  $\alpha$  and shear-wave speed  $\beta$ . The borehole can be considered as an infinite cylinder, with radius  $r_b$  and fluid-filled. The fluid density and velocity are  $\rho_f$  and  $\alpha_f$ , respectively. The axis of the borehole is considered to be the  $z$  axis (Figure 2.2). A plane wave of frequency  $\omega$  impinges on the borehole with angle  $\delta$  with respect to the  $z$  axis. The solutions are expressed in cylindrical coordinates. Radial (or horizontal) and axial (or vertical) motions are defined at the borehole wall and in the fluid column. The contributions of P-, SV- and SH-waves to the particle motions are found

## 2 Constitutive equations

analytically. The boundary conditions that allow continuity at the interface between the elastic formation and the acoustic fluid-filled borehole can be found in Appendix C in Schoenberg (1986). In order to avoid reciting Schoenberg's whole paper, we present here only the results of the motions expressed in the fluid-filled borehole, even though Schoenberg's research article is a comprehensive study of the motion in the elastic formation and in the borehole fluid.

For an **incident P-wave**, the vertical component of particle velocity in the fluid-filled borehole is found as

$$v_z = \frac{c_T^2 \cos \delta (1 - 2\gamma \cos^2 \delta)}{\beta^2 1 - (c_T/\alpha)^2 \cos^2 \delta} + \frac{i\Omega_L r \cos \theta}{r_b} \cos \delta \sin \delta, \quad (2.36)$$

and the two radial motions follow:

$$v_r = \frac{i\Omega_L r c_T^2 (1 - 2\gamma \cos^2 \delta)(1 - (\alpha_f/\alpha)^2 \cos^2 \delta)}{2r_b \gamma a_f^2 1 - (c_T/\alpha)^2 \cos^2 \delta} + \cos \theta \sin \delta + \frac{i\Omega_L r \cos 2\theta}{(1 - \gamma)r_b} \sin^2 \delta, \quad (2.37)$$

$$v_\theta = -\sin \theta \sin \delta - \frac{i\Omega_L r \sin 2\theta}{(1 - \gamma)r_b} \sin^2 \delta, \quad (2.38)$$

where  $r_b$  is the radius of the borehole and  $r$  is used to define the surrounding elastic formation ( $r > r_b$ ).  $\gamma = \beta^2/\alpha^2$  is a dimensionless quantity describing the dynamic behavior of an elastic medium.  $\Omega_L$  is simply defined as  $\omega r_b/\alpha$  and  $\Omega_f = \omega r_b/\alpha_f$ .  $c_T$  is the velocity of the tube wave as it will be given in Equation 2.47.

The expression for an **incident SV-wave** yields:

$$v_z = \frac{c_T^2}{\beta^2} \frac{2 \sin \delta \cos^2 \delta}{1 - (c_T/\beta)^2 \cos^2 \delta} + \frac{i\Omega r \cos \theta}{r_b} \cos^2 \delta, \quad (2.39)$$

and the radial motions read:

$$v_r = \frac{i\Omega r c_T^2 \sin \delta \cos \delta (1 - (\alpha_f/\alpha)^2 \cos^2 \delta)}{r_b a_f^2 1 - (c_T/\beta)^2 \cos^2 \delta} + \cos \theta \cos \delta + \frac{i\Omega r \cos 2\theta}{(1 - \gamma)r_b} \sin \delta \cos \delta, \quad (2.40)$$

$$v_\theta = -\sin \theta \cos \delta - \frac{i\Omega r \sin 2\theta}{(1 - \gamma)r_b} \sin \delta \cos \delta. \quad (2.41)$$

The vertical component of particle velocity for an **incident SH-wave** is obtained as

$$v_z = \frac{i\Omega_L r \sin \theta}{r_b} \cos \delta, \quad (2.42)$$

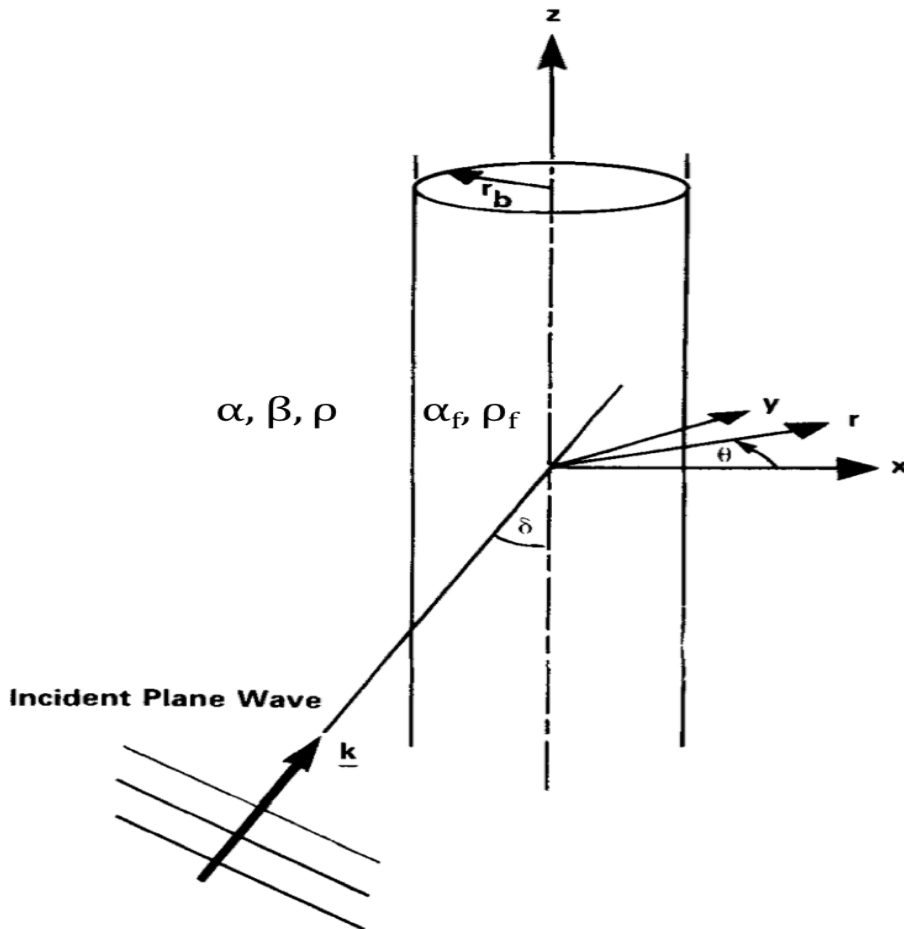


Figure 2.2: An elastic plane wave with wavenumber vector  $\mathbf{k}$  incident on a circularly cylindrical fluid-filled borehole at an angle  $\delta$ . The borehole axis and  $\mathbf{k}$  define the  $x, z$ -plane and the azimuthal angle  $\theta$  is measured from the  $x$ -axis as shown.  $\alpha_f$  and  $\rho_f$  are the sound speed and density, respectively, of the fluid.  $\alpha$ ,  $\beta$ , and  $\rho$  are the compressional wave velocity, shear-wave velocity, and density, respectively, of the elastic medium (Schoenberg, 1986).

## 2 Constitutive equations

and the two radial motions yield:

$$v_r = \sin \theta + \frac{i\Omega r \sin 2\theta}{(1 - \gamma)r_b} \sin \delta, \quad (2.43)$$

$$v_\theta = \cos \theta + \frac{i\Omega r \cos 2\theta}{(1 - \gamma)r_b} \sin \delta. \quad (2.44)$$

Given that the fibre optic cable is assumed to be in a straight position in a vertical well, and knowing that DAS is sensitive to axial strain only, the vertical component of particle velocity is the quantity of main interest for us. Two situations are worth to investigate analytically, that are plane waves arriving parallel ( $\delta = 0$ ) and perpendicular ( $\delta = \pi/2$ ) to the borehole axis. These results will be used to validate the numerical solution introduced in Chapter 3.

A plane wave arriving parallel at the borehole axis is of particular interest for a zero-offset VSP survey. Inserting the angle of propagation  $\delta = 0$  in Equations 2.36, 2.39 and 2.42, we can note that vertical motion is induced inside the borehole since we get  $v_z \neq 0$ . Moreover, comparing these results with the results for the elastic formation (Equations 19, 21, 23 in Schoenberg (1986)), the vertical component of particle velocity between formation and fluid differs:  $v_z(\text{formation}) \neq v_z(\text{fluid})$ . An example is the P-wave expression for  $v_z$  in the elastic formation and in the fluid-filled borehole.  $v_z$  induced by the P-wave in the elastic formation (Equation 19 in Schoenberg (1986)) is defined as

$$v_z = \cos \delta + i\Omega_L \cos \theta \left( r/r_b + 2r_b/r \right) \cos \delta \sin \delta, \quad (2.45)$$

for  $r > r_b$  and reduces to  $v_z = 1$  when  $\delta = 0$ . In contrast the term in the fluid-filled borehole ( $r < r_b$ ) becomes

$$v_z = \frac{c_T^2}{\beta^2} \frac{(1 - 2\gamma)}{1 - (c_T/\alpha)^2}. \quad (2.46)$$

The main points to emphasize here are that a wave traveling parallel to the borehole axis *induces vertical motion in the fluid and its expression is different from the one of the vertical motion in the elastic formation.*

The other extreme scenario would be a wave that is arriving perpendicular to the borehole wall i.e.  $\delta = \pi/2$  which corresponds to a source at far offsets, or in the case of deviated wells. Inserting  $\delta = \pi/2$  in the equations of vertical motion  $v_z$  inside the borehole fluid generated by P-, SV- and SH-waves (Equations 2.36, 2.39 and 2.42)  $v_z$  reduces to 0. Therefore particle movement in the vertical direction is not produced in the fluid column. DAS data confirmed those analytical solutions. In Barberan et al. (2012), the authors showed that when the direction of arrival of the source is almost per-

pendicular to the borehole wall, the sensitivity of DAS recordings is low. We believe this is also due to the fact that DAS is mainly sensitive to the axial movements, which corresponds to the vertical direction in vertical borehole experiments. However, it has to be kept in mind that Schoenberg's solution is an approximation using plane wave expressions, which is not fully reliable to quantify differences in  $v_z$  in the elastic formation and the borehole fluid in real cases with complex wavefronts.

Other conclusions of the Schoenberg's paper that might be of interest when validating the numerical model in Chapter 3 are that motion in the elastic formation and in the borehole fluid induced by P- and SV-waves are similar but differ significantly from the motion induced by SH-waves.

Moreover, Schoenberg (1986) also found that the horizontal components of particle fluid velocity generated by P- and SV-waves in the borehole follow the horizontal components of particle solid velocity in the elastic formation. In other words, equations for horizontal motion in the elastic formation and in the fluid-filled borehole are identical.

The vertical component of particle motion induced by P- and SV-waves differ. Governed by the ratio of the particle fluid velocity and the particle solid velocity (Equation 26 in Schoenberg (1986)), Schoenberg found that the part of  $v_z$  in the borehole fluid generated by P-waves are in-phase, whereas the part of  $v_z$  caused by impinging SV-waves appears to be out-of-phase compared to  $v_z$  in the elastic formation. Furthermore, amplitudes in the borehole fluid are altered compared to amplitudes in the elastic formation as a function of velocity contrast between the formation and the borehole fluid (Figure 2 in Schoenberg (1986)).

Moreover, in the limit of  $\Omega \rightarrow 0$  the borehole is completely transparent to SH-waves, therefore vertical and horizontal motion generated by SH-waves are identical in the borehole fluid and in the elastic formation (Equations 22 and 23 in Schoenberg (1986)).

We now give a quick review on tube waves which can be beneficial in order to interpret numerical solutions in the following chapters. Tube waves are considered low frequency Stoneley waves propagating in a borehole and are generated when surface waves are crossing the well head or when body waves impinge on the borehole (Cheng and Toksöz, 1981). Schoenberg (1987) defined their wave speed as:

$$c_T^{-2} = a_f^{-2} + \frac{\rho_f}{\mu_s}, \quad (2.47)$$

where  $a_f$  is the compressional wave velocity and  $\rho_f$  the density in the fluid and  $\mu_s$  the shear modulus of the formation. In the center of the borehole the radial displacement vanishes and the axial displacement is largest. The particle motion is then rectilinear along the borehole axis. The ratio of radial to axial displacement increases closer to the borehole wall (Biot, 1952; Cheng

and Toksöz, 1984). At the fluid-structure interface, the axial displacement drops by a factor of 100 or more when the tube wave frequency is 80 Hz or lower (Hardage, 1983). Therefore, tube waves serve as a good indicator for sensor coupling.

## 2.5 Coupling

The analysis of the particle movement (with contributions from P-, SV- and SH-waves) in the borehole fluid (Section 2.4), generated by an impinging seismic wave, is of concern when the sensing unit, i.e. the DAS cable, is placed in a straight position inside the well without actual contact to the borehole wall. However, when the DAS cable is perfectly coupled to the formation, i.e. when the cable is cemented behind the casing, the analysis of the particle displacement in the borehole fluid is of negligible concern, since the particle displacement of the cable will follow the particle displacement of the elastic medium to which it is coupled.

In this PhD project, we analyse the deployment method when the cable is lowered down the borehole on wireline cable (Figure 1.17), therefore, after analysing the particle movement in the borehole fluid, it is important to consider the mechanism of contact between the fibre cable and the borehole wall. In this case, the problem of contact mechanics is more complex since the contact is assumed to be rather loose if established. This section provides a general introduction to the topic of coupling and contact mechanics in order to be able to better understand the behavior and recordings of sensors when coupled to another medium.

In the first part of this section the physics of geophone coupling is briefly discussed. For conventional seismic sensors, coupling is already well understood and considered a key factor influencing data quality (Krohn, 1984; Tan, 1987; Vos et al., 1995; Drijkoningen, 2000). In the second part, first attempts to address the coupling issue of the optical fibre cable are provided by discussing the basics of contact mechanics.

### 2.5.1 Principles of coupling for a geophone

A geophone is a particle velocity sensor used in seismic surveying and consists of a moving coil placed within the magnetic field of a permanent magnet; the sensor is usually mounted on a spike is inserted into the ground. In conventional seismics, seismic waves perturb the geophone spike causing a relative movement of the magnet with respect to the coil. According to Faraday's law of electromagnetic induction, a voltage  $V$  is generated, proportional to

$$V \propto \frac{dx}{dt}, \quad (2.48)$$

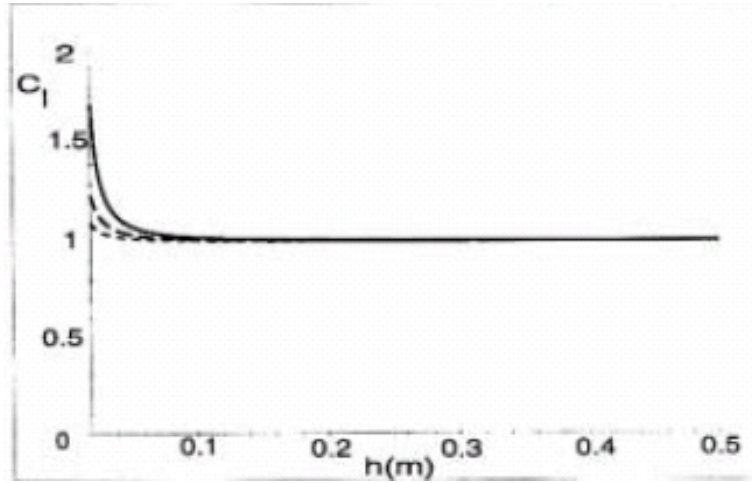


Figure 2.3: Contrast response  $C$  varying with the length (in m) of the spike  $h$ . The density of the geophone is  $\rho_{geophone} = 7800 \text{ kg/m}^3$ , and the densities of the ground are  $\rho_{soil} 2000 \text{ kg/m}^3$  (solid line),  $3000 \text{ kg/m}^3$  (long dashed line) and  $4000 \text{ kg/m}^3$  (short dashed line) (adapted from Vos et al. (1995)).

with  $dx$  being the displacement of the magnet relative to the coil over time  $dt$ . Thus the triggered voltage corresponds to the rate of ground motion with time and hence the sensor measures particle velocity (m/s).

For geophones, it has been observed that the physical coupling of the spike in the ground and the contrast of the medium's properties (sensor and ground) play a significant role when acquiring seismic data. Vos et al. (1995) defined the ratio of the velocity recorded by the geophone (assuming perfectly coupled)  $v_{geo}$  and the velocity of the ground in absence of the geophone  $v_{gr}$  as an indicator for coupling quality:

$$C = \frac{v_{geo}}{v_{gr}}. \quad (2.49)$$

Figure 2.3 illustrates the contrast response  $C$  of a geophone with density  $\rho_{geophone} = 7800 \text{ kg/m}^3$  when varying the densities of the ground  $\rho_{soil}$  with values  $2000 \text{ kg/m}^3$ ,  $3000 \text{ kg/m}^3$  and  $4000 \text{ kg/m}^3$ . It has been observed that the closer the properties (e.g. densities) of geophone and ground, the better the coupling because the contrast response  $C$  is smaller.

### 2.5.2 Physics of contact forces

While in conventional seismic acquisition the spike of the geophone determines the coupling quality, the DAS cable is the medium that establishes contact with the borehole wall in VSP surveys. Since no literature exists on the subject of coupling of DAS systems, a first approach is to discuss which parameters play an important role in the mechanics of contact of such scenario.

## 2 Constitutive equations

The general objective is to derive which key factors influence the area of surface contact. Assuming that a bigger contact area between the DAS cable and the borehole wall lead to a better signal detection, the physics of contact forces could potentially provide further insight into the coupling of DAS.

Normal contact has first been investigated by [Hertz \(1881\)](#) who analysed two (cylindrical) bodies, each considered as an elastic half-space loaded over an elliptical contact area of its plane surface. With this assumption, contact stress and the general distribution of stresses inside the bodies can be treated separately. Those conditions are obtained when the dimension of the contact area is (1) smaller than the dimension of the individual bodies, to guarantee that the two bodies can be relatively considered as elastic half-spaces, and (2) smaller than the relative radii of curvature of the surfaces, to ensure that the contact region can be approximated by the plane surface of a half-space and that (3) strains are small enough to satisfy the assumption of elasticity of the considered bodies. Furthermore, (4) the bodies are assumed to be frictionless, hence only normal stress is transmitted between them and tangential forces are neglected. Following the formalism of [Johnson \(1985\)](#), the previous conditions can be summarised in the following four assumptions, where  $A$  denotes the radius of contact area,  $R_1$  and  $R_2$  the radii of each body,  $R$  is the relative radius of curvature ( $1/R = 1/R_1 + 1/R_2$ ) and their dimensions laterally and in depth when in contact are denoted by  $l$ .

### Assumptions

1. Surfaces are continuous and non-conforming (implying that the area of contact  $A$  is smaller than the dimension of the bodies):  $A \ll R$
2. Each body is an elastic half-space:  $A \ll R_{1,2}$ ,  $A \ll l$
3. Strains are small and within the elastic limit:  $A \ll R$
4. Surfaces are frictionless.

Considering a cylindrical body pressed onto a flat elastic halfspace in 2D (Figure 2.4), [Popov and Hess \(2015\)](#) found the vertical displacement  $u_z$  of a spring at a distance  $x$  from the middle point of the contact as:

$$u_z(x) = d - \frac{x^2}{2R_1}, \quad (2.50)$$

where  $d$  is the depth of indentation and  $R_1$  the radius of the cylindrical body. The normal force can be found from Hooke's law as  $F_N = k \cdot u_z$ , where  $k$  being the stiffness. Thus it reads:

$$F_N(x) = E^* u_z(x) \Delta x = \left( d - \frac{x^2}{2R_1} \right) E^* \Delta x, \quad (2.51)$$

where  $\Delta x$  is the horizontal distance between each spring shown in Figure 2.4 and the effective elastic (Young's) modulus  $E^*$  is defined as

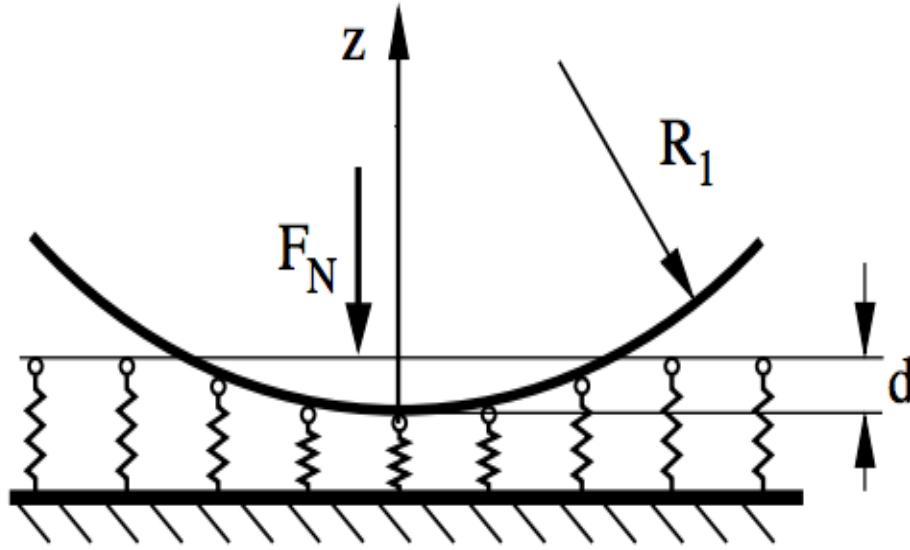


Figure 2.4: One-dimensional mapping of contact loaded normally (adapted from Popov and Hess (2015)).

$$\frac{1}{E^*} = \frac{1 - \nu_1^2}{E_1} + \frac{1 - \nu_2^2}{E_2}, \quad (2.52)$$

where  $E_1$  and  $E_2$  are the elastic modulus and  $\nu_1$  and  $\nu_2$  the Poisson's ratio of each body. Rearranging Equation 2.50 and under the condition  $u_z(A) = 0$ , we obtain the radius of contact area:

$$A = \sqrt{2R_1d}. \quad (2.53)$$

For numerical implementation and to simulate a more realistic scenario we extended the model to a 3D model where a cylinder is pressed onto a cubical half-space. The area of contact changes to an elliptical shape and after Johnson (1985) and Hertz (1881) the total load reads after integrating:

$$P = \frac{1}{4}\pi A^2 E^* R_1. \quad (2.54)$$

Following, the analytical solution for  $A$  can be derived as a function of force and elastic properties contributions:

$$A = \sqrt{f_N \frac{4}{\pi} \frac{1}{R_1} \left( \frac{(1 - \nu_1^2)}{E_1} + \frac{(1 - \nu_2^2)}{E_2} \right)}. \quad (2.55)$$

Figure 2.5 shows the cross-section of the setting of the model that we want to implement. Here, a cylindrical body with elastic properties  $E_1, \nu_1, \rho_1$  is

## 2 Constitutive equations

pressed on a block ( $E_2, \nu_2, \rho_2$ ) with a constant force  $F_N$ , similar to the theory we reviewed. We used the finite element method (FEM) for implementing our simulations. FEM will be described in more details in Chapter 3. The numerical implementation is shown Figure 2.6. This is a snapshot taken when contact between the cylinder and the block occurred. The length of the cylinder and the flat surface are 0.5 m while the cylinder has radius  $R_1$  of 0.01 m. The grid size of the mesh was 0.025 m for the flat surface, and around 0.015 m for the the cylinder. For comparison we apply loads of several magnitude on the cylinder and we compute the area of surface contact, trying to match analytical and numerical data. Figures 2.7 and 2.8 show results of the analytical (line) and numerical (dots) solutions. The y-axis represents the radius of area of surface contact  $A$ , while the x-axis denotes the increase of the contact force. The flat surface has a Young's modulus  $E_2$  of  $270 \cdot 10^9$  Pa, Poisson's ratio  $\nu_2 = 0.25$  and a density  $\rho_2$  of  $7000 \text{ kg/m}^3$ , while the cylinder has a Young's modulus  $E_1$  of  $270 \cdot 10^9$  Pa in Figure 2.7 and  $450 \cdot 10^9$  Pa in the results of Figure 2.8, with Poisson's ratio  $\nu_1 = 0.33$  and density  $\rho_1 = 5000 \text{ kg/m}^3$  remaining constant. The numerical results of both configurations tie in with analytical data.

Figure 2.9 gives more insights when changing the elastic properties of the bodies to simulate commonly used materials. In this simulation, we considered a half-space made of steel (like, for example, the material of the borehole casing), and we considered cylinders with different materials: steel, aluminum and Low Smoke, Zero Halogen (LSZH). The considered materials could represent the effective material properties of the DAS cable coatings. It is obvious that more flexible and lighter cables (low  $E$  and low  $\rho$ ) are more deformed and therefore forming a larger area of surface contact with the flat surface. It is reasonable to argue that those materials are more desirable than stiffer materials like steel (high  $E$ , high  $\rho$ ) for creating a better contact (and therefore a better coupling) between the half-space and the cable. However, damping plays a major role in composite materials like fibre optical cables and acoustic damping is usually high if the fibre is coated with materials similar to LSZH or polymers both being light and deformable (low  $E$  and low  $\rho$ ). Furthermore, a certain degree of stiffness is required during wireline deployment (Figure 1.17) since the cable would accumulate at the very bottom of the borehole if it is too deformable.

While it is highly speculative to draw final conclusions about the coupling of fibre optical cables using this simple example, Equation 2.55 reveals, however, important information about the key parameters in contact mechanics that are the contact force  $F_N$ , the elastic properties  $E_1, E_2, \nu_1$  and  $\nu_2$  of the bodies and their geometry  $R$ . It will be shown (Chapter 5) that contact force and cable elastic properties are indeed the controlling mechanisms when acquiring seismic data using DAS on wireline cable.

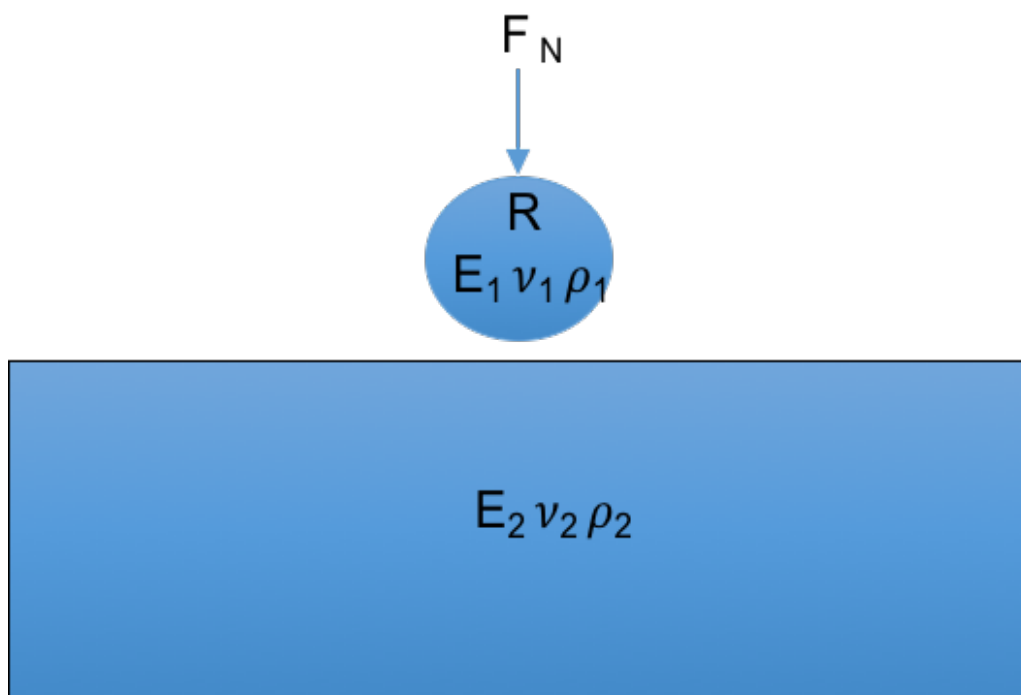


Figure 2.5: Setting of a simple model with a pressure load ( $F_N$ ) pressing the cylinder onto a flat surface.  $R = 2R_1$  denotes the diameter of the cylinder, while  $E_1$ ,  $E_2$  are the Young's modulus of the cylinder and the half-space,  $\nu_1$ ,  $\nu_2$  their Poisson's ratios and  $\rho_1$ ,  $\rho_2$  their densities, respectively.

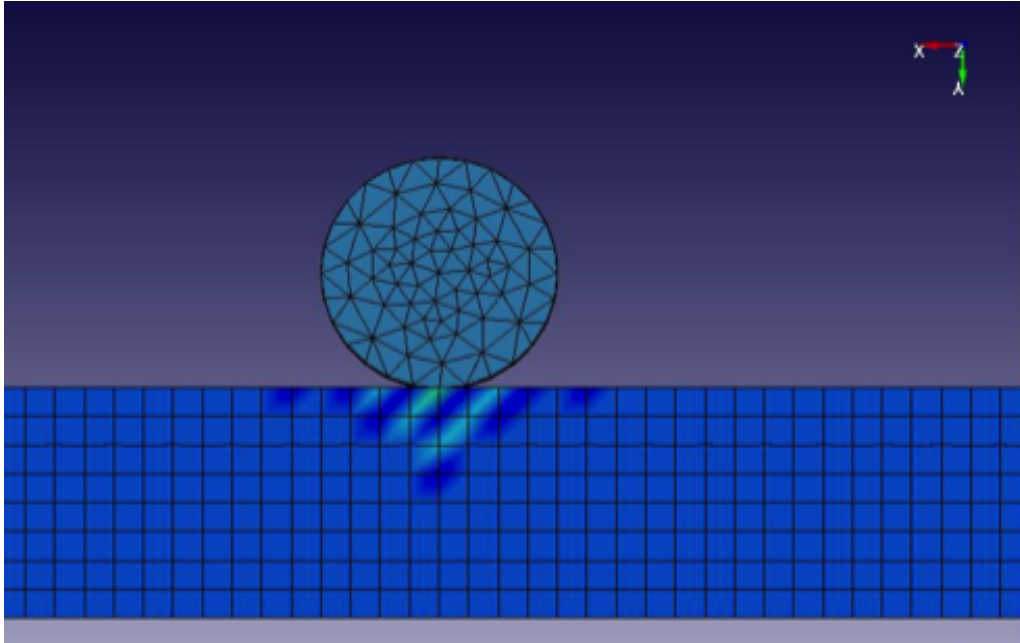


Figure 2.6: Snapshot of the simulation when the contact between the two bodies occurred. On the bottom part of the flat elastic half-space, nodes have been constrained to prevent any vertical displacement. The load (vertical force  $F_N$  in Equation 2.55) pressing the cylinder onto the flat surface has been applied on all nodes of the cylinder.

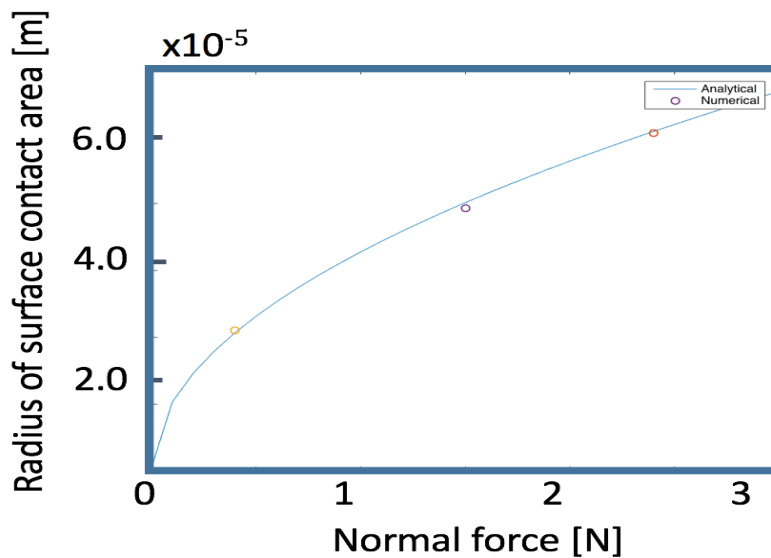


Figure 2.7: Radius of contact area with increasing contact force. The solid line denotes the analytical solution (Equation 2.55), while the dots are results of the numerical approximation. The cylinder has a Young's modulus of  $2.7 \cdot 10^{11}$  Pa.

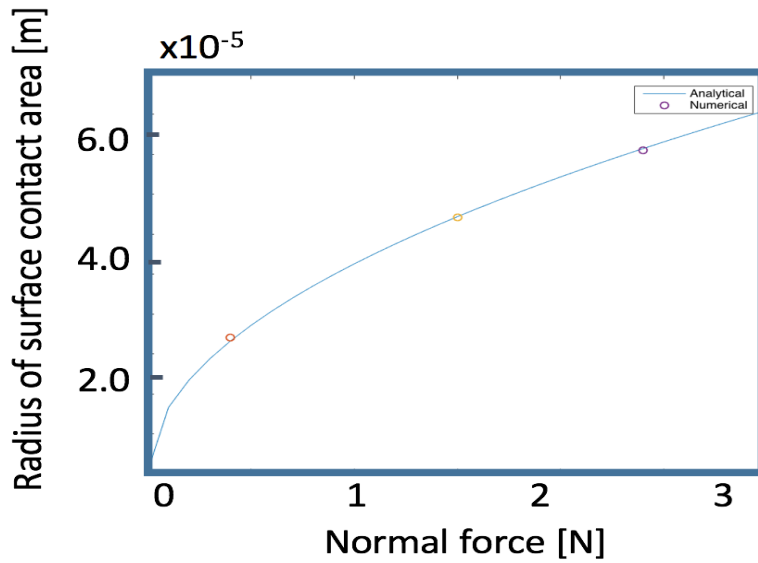


Figure 2.8: Radius of contact area with increasing contact force as seen in Figure 2.7. The Young's modulus of the cylinder has been modified to  $4.5 \cdot 10^{11}$  Pa.

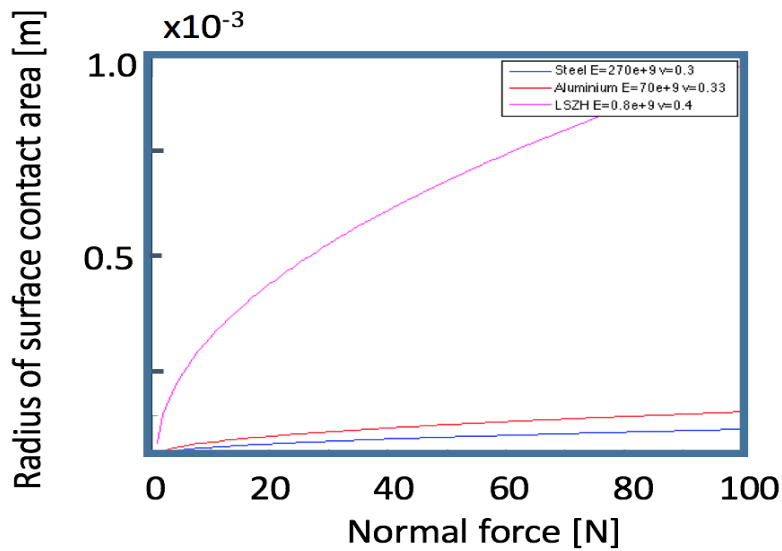


Figure 2.9: Radius of contact area with increasing contact force and varying elastic properties. While stiff and heavy materials (high  $E$ , high  $\rho$ ) only form a small contact area, more flexible and lighter materials (low  $E$ , low  $\rho$ ) form a bigger contact area.

## 2.6 Conclusions

We provided an overview of the constitutive equations and their relationships that are used in the numerical models in the following chapters. Furthermore, an introduction to the topic of contact mechanics has been discussed.

First, the fundamental concepts in physics, which are the basis of all partial differential equations, have been reviewed: force & moments and stress & strain. Moreover, in the context of linear elastodynamic wave equation, the relationship between displacement, velocity and acceleration has been provided. The elastic and acoustic wave equations were then derived in terms of velocity-stress formulations in order to highlight the direct relationship between stress and particle velocity.

These particle velocity-stress formulations are also useful, because particle velocities in the elastic formation and particle velocities in the fluid-filled borehole has been discussed in Section 2.4. Analytical solutions have been reviewed to identify the differences in particle motion in the elastic formation and in the fluid-filled borehole when an elastic plane wave impinges on the well. It has been observed that, despite the small diameter of the borehole, seismic waves are perturbed at the interface and particle velocities in the borehole fluid differ from the particle velocities in the formation depending on the angle of incidence of the plane wave and the wave type. Additionally, more modes of propagation such as tube waves are generated.

Finally, the topic of coupling was addressed. While the density contrast of the geophone's spike and the medium, to which the spike is coupled, determine the coupling quality, also the elastic properties of the fibre cable could potentially determine acquired data quality. In order to evaluate the coupling, a simple numerical model has been developed where a cylindrical body (e.g. a fibre cable) has been pressed onto an elastic half-space (e.g. the ground). It has been observed that the area of surface contact changes when the elastic modulus of the cylindrical body is modified. Assuming that a larger surface contact area leads to a better seismic signal detection, materials with lower density and lower elastic modulus, seem to be ideal for seismic data acquisition since the radius of surface contact area increases. For real surveys, however, such cables are unrealistic since the tensile strength would be too low. At this point we cannot draw conclusions about the coupling but in Chapter 5, we will show the effect of force and elastic properties of cables on the quality of the recorded signals.

## Numerical modelling and simulation

### Résumé du chapitre

Les solutions analytiques fournissent une solution exacte à un problème considéré, mais leur application est limitée à des problèmes très spécifiques, généralement simples, et nécessite donc des simplifications et des idéalizations. Les problèmes géophysiques sont généralement décrits par des équations différentielles partielles régissant la physique du modèle géologique (par exemple, les fonctions multivariées définissant la propagation des ondes en milieu élastique dans les équations 2.16 à 2.24). La résolution de ces équations analytiquement est très compliquée voire impossible, donc on préfère des méthodes numériques. De plus, dans notre problème, nous devons considérer la propagation des ondes sismiques dans le voisinage d'un puits rempli de liquide. Un tel scénario nécessite une approche de modélisation flexible, qui puisse prendre en compte en même temps des composants avec des dimensions très différentes, passant du milieu géologique, au puits jusqu'au câble à fibre optique. Pour cette raison, nous avons décidé d'utiliser la méthode des éléments finis (FEM) car elle permet la modélisation des géométries complexes (Section 3.2). Nous avons d'abord utilisé des modèles simples de propagation des ondes sismiques pour valider les solutions données par le logiciel utilisé (section 3.3). Nous présentons dans ce chapitre deux modèles numériques avec l'objectif d'expliquer les observations faites par Hartog et al. (2014) dans la figure 1.21. Le premier modèle numérique sert à décrire et analyser la façon dont le câble DAS détecte un champ d'ondes sismiques dans les acquisitions VSP (section 3.4). Une solution analytique pour ce problème, basée sur les approximations d'une onde plane est discutée dans la section 2.4. Cependant, l'approche analytique n'est pas suffisante pour expliquer les observations des données réelles (Figure 1.21) et, par conséquent, nous utilisons des méthodes numériques, et nous utilisons les résultats analytiques de la section 2.4 pour valider la solution numérique. Dans un premier temps, nous modélisons numériquement seulement le cas d'un câble en position verticale dans le trou du puits et détectant le mouvement de la particule suite à une onde

sismique. Un deuxième modèle numérique est ensuite utilisé pour étudier le couplage entre le câble et la paroi du puits lorsque plus de câble est baissé dans le puits (section 3.5). Au lieu de résoudre les équations d'ondes sismiques, ce modèle décrit les moments de déplacement et de flexion du câble lors du ralentissement, détermine quand le câble est en contact avec la paroi du trou et lorsque des conditions d'équilibre sont trouvées, de sorte que le câble soit considéré comme bien couplé.

## 3.1 Introduction

Analytical solutions provide an exact solution of a considered problem but their application is constrained to very specific, usually simple problems and therefore require simplifications and idealisations (e.g. for the calculation of the surface contact area of two bodies, where the four assumptions in Equation 2.55 needed to be satisfied). They are useful for calibrating numerical solutions and for understanding the main contributions of numerical solutions. Geophysical problems are usually described by partial differential equations (PDEs) governing the physics of the underlying geological model (e.g. the multivariable functions defining wave propagation in elastic media in Equations 2.16 – 2.24). Solving PDEs analytically usually is based on finding a proper change of variable, thus transforming the equations into a solvable form or based on finding an integral form of the solution. This task can be sometimes very complicated to impossible. Another way to solve a PDE is to approximate its solution using numerical methods. There are a number of numerical methods attempting to approximate the solution each in a different way. Depending on the discretisation and the employed numerical method, numerical results can provide very accurate estimates. Knowing which numerical method provides optimal performance in terms of accuracy and rate of convergence in order to keep a limited computation cost while satisfying the required degree of accuracy of the solution is critical. While in global seismology the modelling scale can be up to hundreds of kilometers with a desired resolution of hundreds of meters, in exploration geophysics interest lies within the first few kilometers and requires resolutions to a few tens of meter or less. Moreover, for different media, different PDEs need to be solved: while in acoustic media often only pressure is computed (Equation 2.34), elastic media require to solve for a vector field, hence transverse and longitudinal motion, because both the source function and the displacement are vector quantities (Equation 2.33). Additionally, a combination of two or more media, the free surface, sharp variations in velocity, anisotropy, complex topography, the requirement to simulate arbitrary shapes of objects, etc. might complicate the modelling approach.

Another special case is seismic wave propagation in the neighborhood of a fluid-filled borehole. Such a scenario requires a flexible modelling approach to implement features like the casing and the borehole fluid. Therefore we

decided to utilise the finite-element method (FEM) because **FEM allows the modelling of complex geometries** (Section 3.2). We initially used some simple models of seismic wave propagation to validate the solution provided by the available software and to analyse the required gridding size and the implementation of absorbing boundary conditions (Section 3.3). The first main numerical solution that we present is used to describe and analyse how the DAS cable senses an impinging seismic wavefield in VSP surveys (Section 3.4) since the objective is to explain observations made by Hartog et al. (2014) in Figure 1.21. An analytical solution based on plane-wave approximations has been discussed in Section 2.4 to describe the particle motion induced inside a fluid-filled borehole by an impinging seismic wavefront. We use the results of Section 2.4 to validate the numerical solution. However, the analytical approach is not sufficient to explain the real data observations (Figure 1.21), and therefore we employ numerical methods. In these numerical models, we only consider the case of a straight wireline cable in the borehole sensing the particle motion. A second numerical model is used to investigate the coupling between the cable and the borehole wall when more cable is lowered down the borehole (Section 3.5). Instead of solving for seismic wave equations, this model describes the displacement and bending moments of the cable during slacking, determines when the cable is in contact with the borehole wall and when equilibrium conditions are found, such that the cable is considered to be well coupled.

## 3.2 Review of FEM

Differential equations are equations that contain functions with independent variables and their derivatives. If there exist only one function of one independent variable and its derivative (e.g.  $t$  for time) the differential equation is called ordinary differential equation (ODE). In situations where an initial conditions is provided, i.e.  $t_0$ , an analytical solution to ODEs can often be found. However, most of the time the laws of physics cannot be explained by ODEs since there are usually variations of a physical property over time and space and sometimes more than one physical property in the same equation. Hence, the considered differential equations usually contain multivariable functions, more than one independent variable and its derivatives (i.e.  $x, y, z, t$ ). Those equations are called partial differential equations (PDEs). PDEs can often not be solved analytically in contrast to ODEs. Hence, an alternative option is to approximate the solution with numerical methods.

In this section, we present a review of the finite element method (FEM) that will be used in this thesis to approximate the solutions for our problems (Zienkiewicz, 1971; Bathe, 1996). After giving a brief introduction to the basic concepts of FEM in Section 3.2.1, we discuss the main differences between the commercial FEM solvers available for this thesis in Section 3.2.2.

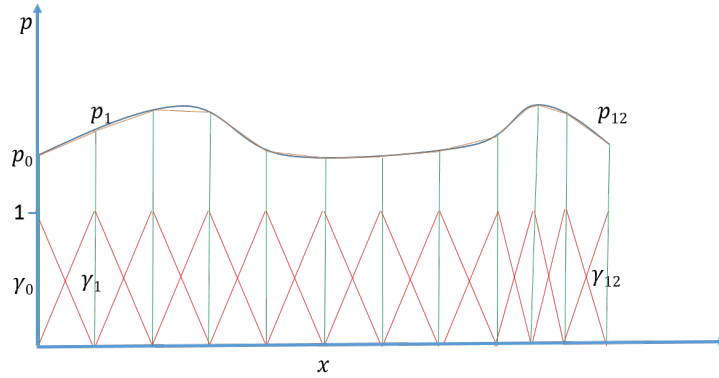


Figure 3.1: A set of basis functions  $\gamma_i$  used to approximate  $p$ .

Finally, we present the advantages and disadvantages of FEM with respect to other numerical approaches in Section 3.2.3.

### 3.2.1 Description of the method

The finite element method is used to calculate approximations of PDEs. Throughout this thesis, we refer to its practical application as finite element analysis (FEA). The main idea of the finite element method is to subdivide a large problem into smaller, simpler parts that are called finite elements. The simple equations that model these finite elements are then assembled into a larger system of equations that model the entire problem (Reddy, 2005; Larson and Bengzon, 2013). For a given PDE, e.g. for the seismic wave equation, the finite element method yields approximate values of the unknowns, e.g. displacement  $\mathbf{u}$  in the elastic or pressure  $p$  in the acoustic case, at discrete points over the considered domain. Then, solutions at the discrete points are interpolated using basis functions, also referred to as test or more often as shape functions.

Let us consider a generic variable in a PDE called  $p$ , where  $p$  could be, for instance, a certain pressure in a tube. The function  $p$  can be approximated by a linear combination of basis functions  $\gamma_i$  such that

$$p(x) = \sum_i p_i \gamma_i(x). \quad (3.1)$$

Figure 3.1 illustrates the concept of basis functions for the approximation of a function  $p$ , where the  $x$ -axis denotes the length of the discretized tube and the  $y$ -axis the pressure  $p$ . The advantage of FEM, in this case, is that this method offers opportunities and freedom in the selection of the basis functions. They can be more closely spaced to achieve more accuracy, or do not necessarily need to be linear functions but they could be polynomials of higher degree.

The general PDE problem solved using FEM can be written in a matrix form as

$$\mathbf{M} \frac{\partial \mathbf{u}}{\partial t} + \mathbf{C} \mathbf{u} + \mathbf{K} \mathbf{u} = \mathbf{f}, \quad (3.2)$$

and for a second-order system as

$$\mathbf{M} \frac{\partial^2 \mathbf{u}}{\partial t^2} + \mathbf{C} \frac{\partial \mathbf{u}}{\partial t} + \mathbf{K} \mathbf{u} = \mathbf{f}, \quad (3.3)$$

where  $\mathbf{f}$  is the source function,  $\mathbf{u}$  is the vector of unknowns,  $\mathbf{M}$  is the so-called mass matrix,  $\mathbf{C}$  is the damping matrix and  $\mathbf{K}$  is the stiffness matrix. Equation 3.3 is generally used to formulate the equation of motion for dynamic systems. In this case,  $\mathbf{M}$  usually stores initial terms and properties of the system,  $\mathbf{C}$  describes viscous terms and  $\mathbf{K}$  contains the wave equation's material properties and spatial derivatives, thus dictating the stiffness of each discretized region. The damping matrix  $\mathbf{C}$  is in elastodynamic systems often neglected, hence only matrices  $\mathbf{M}$  and  $\mathbf{K}$  are present when computing seismic wave propagation.

The finite element method does not actually approximate the original PDE but rather the weak form of the original PDE. The purpose of the weak form is to satisfy the equation in the "average sense", so that we can approximate solutions that are discontinuous or otherwise poorly behaved. In its essence, the weak formulation means that we rewrite the PDE in a new form, such that we relax the requirements of the original PDE on the solutions (called weak solutions). Weak solutions are important because many differential equations encountered in modelling real world phenomena do not admit sufficiently smooth solutions and then, the only way of solving such equations is using the weak formulation. In this way, complex geometries and media can be easily considered when discretising the numerical model.

The two main methods to derive the weak formulation are

- Variational methods
- Weighted residual methods.

Variational methods are based on minimising a functional (i.e. total potential energy of a system), while weighted residual methods are based on minimising the weighted average error after an initial estimate of the solution has been made (Zienkiewicz, 1971; Bathe, 1996). Furthermore, different methods have been developed within each methodology, while the most common variational method is the Rayleigh-Ritz method and the most popular weighted residual methods is the Galerkin approach (Zienkiewicz, 1971; Bathe, 1996). The mathematical concept of formulating the weak form using the Galerkin approach follows a general procedure for any PDE and is shown in Figure 3.2. Here, the PDE is multiplied by test functions, integrated over a

total domain and then integrated by parts. Since the weak formulation is in integral form, the problem can be decomposed into small subdomains to approximate the PDE locally. Subdomains represent elements in the numerical model and can have arbitrary shapes, thus making FEM particularly attractive for complex geometries. The integral over the entire domain is the sum of all contributions. The contribution of each element can then be assembled in the global stiffness matrix.

The formulation of the weak form of the second-order elastic wave equation using the Galerkin approach is presented for convenience. Equation 2.16 – 2.24 can be formulated using the Einstein convention on repetitive indexes as

$$\rho \partial_{tt} u_i = \partial_{x_j} \sigma_{ij} + f_i, \quad (3.4)$$

where  $u$  is displacement and  $\sigma$  the stress tensor. Virieux et al. (2011) have applied the continuous Galerkin finite element method (CGFEM), equivalent to the workflow in Figure 3.2, to Equation 3.4 in order to obtain the weak form. Multiplication with a test function  $\gamma_i$  and integration over the domain  $\Omega$  yields

$$\int_{\Omega} d\mathbf{x} \rho \partial_{tt} u_i \gamma_i = \int_{\Omega} d\mathbf{x} \partial_{x_j} \sigma_{ij} \gamma_i + \int_{\Omega} d\mathbf{x} f_i \gamma_i, \quad (3.5)$$

while after integration by parts it follows

$$\int_{\Omega} d\mathbf{x} \rho \partial_{tt} u_i \gamma_i = - \int_{\Omega} d\mathbf{x} \sigma_{ij} \partial_{x_j} \gamma_i + \int_{\partial\Omega} d\mathbf{x} \sigma_{ij} \gamma_i n_j + \int_{\Omega} d\mathbf{x} f_i \gamma_i, \quad (3.6)$$

where  $n_j$  are vector components normal to the boundary  $\partial\Omega$ . Note that at the free surface (i.e.  $\sigma_{ij} n_i = 0$ ) or when the test functions are chosen as null on the boundary (i.e. Dirichlet conditions), the surface integral, obtained with Green's theorem (Green, 1828), is also zero. Hence, we omit the surface contribution which is the advantage of the CGFEM since the free-surface boundary condition is intrinsically satisfied.

Furthermore,  $\gamma_i$  and  $u_i$  are part of the same function space and Virieux et al. (2011) defined  $u_i$  and  $\sigma_{ij}$  as

$$u_i(\mathbf{x}, t) = \hat{u}_i^p(t) \gamma_i^p(\mathbf{x}), \quad (3.7)$$

and

$$\sigma_{ij} = \sum_k c_{ijkl} \hat{u}_k^p(t) \partial_{x_l} \gamma_k^p(\mathbf{x}), \quad (3.8)$$

where  $\hat{u}_k^p(t)$  and  $\gamma_k^p(\mathbf{x})$  denote that field and test function are part of the same function space with  $p$  basis functions. With this condition, Equation 3.6

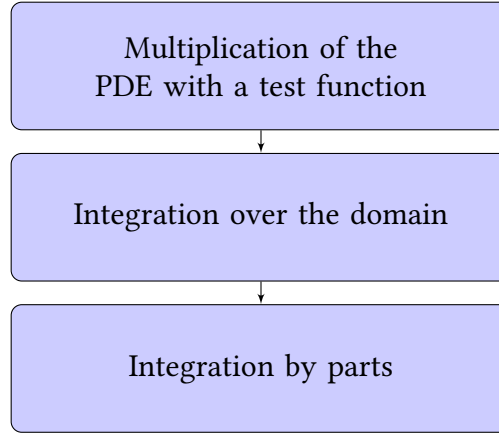


Figure 3.2: Scheme of the general procedure followed by weighted residual methods, such as the Galerkin approach.

yields (Virieux et al., 2011):

$$\int_{\Omega} \sum_i d\mathbf{x} \rho \gamma_i^p \gamma_i^q \partial_{tt} \hat{u}_i^p = - \int_{\Omega} \sum_i \sum_k d\mathbf{x} c_{ijkl} \hat{u}_i^p \partial_{x_l} \gamma_k^p \partial_{x_j} \gamma_i^q + \int_{\Omega} \sum_i d\mathbf{x} f_i \gamma_i^q. \quad (3.9)$$

The first term of the equation holds information about the inertia of the system, while stiffness and source functions are defined in the second terms. Since the equation is in integral form, the domain  $\Omega$  can be decomposed in several subdomains  $\Omega_e$ . For each individual  $\Omega_e$  Equation 3.9 can be formulated in a matrix form as

$$\mathbf{M}_e \partial_{tt} \hat{\mathbf{u}}_e = \mathbf{K}_e \hat{\mathbf{u}}_e + \mathbf{f}_e. \quad (3.10)$$

Note that this matrix form is the same to the one that has already been presented in Equation 3.3. The subscript  $e$  denotes that the subdomain  $\Omega_e$  represents an element in the numerical model. Therefore,  $\mathbf{M}_e$  and  $\mathbf{K}_e$  are the mass and stiffness matrices of the element  $e$ , respectively, while  $\hat{\mathbf{u}}_e$  and  $\mathbf{f}_e$  are the unknown and source vectors, respectively. Each contribution of the matrix form for each subdomain is then assembled in an overall matrix formulation for the entire domain. Finally, the system is inverted for the total unknown vector  $\hat{\mathbf{u}}$ .

### 3.2.2 Implicit vs explicit

In Equation 3.3 the general matrix formulation of a FEA problem has been presented. A solution for this system of equations can be obtained using either an implicit or an explicit solving approach. The solution for  $\mathbf{u}_{t+\Delta t}$  using the **explicit** methods only depends upon quantities at time  $t - \Delta t$  and  $t$ . The solution for  $\mathbf{u}_{t+\Delta t}$  using the **implicit** methods depends upon quantities at time  $t - \Delta t$ ,  $t$  as well as on unknown quantities at  $t + \Delta t$ . In the

following we discuss both methods. First, we present the explicit time integration scheme based on the central difference method (Bathe, 1996). Then, we derive the solution for the implicit time integration scheme based on the Houbolt method (Houbolt, 1950). Finally, we discuss both methods and highlight their differences.

One explicit approach is the central difference method (Bathe, 1996). Here  $\mathbf{v}$  and  $\mathbf{a}$  are approximated via  $\mathbf{u}$  as

$$\mathbf{v}_t = \frac{1}{2\Delta t}(-\mathbf{u}_{t-\Delta t} + \mathbf{u}_{t+\Delta t}) \quad (3.11)$$

and

$$\mathbf{a}_t = \frac{1}{\Delta t^2}(\mathbf{u}_{t-\Delta t} - 2\mathbf{u}_t + \mathbf{u}_{t+\Delta t}). \quad (3.12)$$

The solution for  $\mathbf{u}$  at time  $t + \Delta t$  is obtained via Equation 3.3:

$$\mathbf{M}\mathbf{a}_t + \mathbf{C}\mathbf{v}_t + \mathbf{K}\mathbf{u}_t = \mathbf{f}_t. \quad (3.13)$$

Inserting Equation 3.11 and 3.12 into Equation 3.13 allows us to solve for  $\mathbf{u}_{t+\Delta t}$ :

$$\left(\frac{1}{\Delta t^2}\mathbf{M} + \frac{1}{\Delta t^2}\mathbf{C}\right)\mathbf{u}_{t+\Delta t} = \mathbf{f}_t - \left(\mathbf{K}\frac{2}{\Delta t^2}\mathbf{M}\right)\mathbf{u}_t - \left(\frac{1}{\Delta t^2}\mathbf{M} - \frac{1}{\Delta t^2}\mathbf{C}\right)\mathbf{u}_{t-\Delta t}. \quad (3.14)$$

In elastodynamic problems, such as seismic wave propagation, velocity - dependent damping is often negligible, and therefore  $\mathbf{C}$  is not considered. Furthermore, by paying attention using lower-order elements, e.g. using a 3-node triangle instead of a 8-node quadrilateral 2D elements,  $\mathbf{M}$  becomes a lumped matrix which allows a fast inversion since matrix decomposition is not required. A variation of the central difference method has been proposed by Wood (1990) who uses the approximations of displacement  $\mathbf{u}_{t+\Delta t}$  and velocity  $\mathbf{v}_{t+\Delta t}$ , instead of  $\mathbf{v}_{t+\Delta t}$  and  $\mathbf{a}_{t+\Delta t}$  in Equations 3.11 and 3.12, to solve the algebraic system of equations in Equation 3.13 for acceleration  $\mathbf{a}_{t+\Delta t}$ .

An alternative approach is the implicit time integration scheme, i.e. the Newmark (Newmark, 1959) or the Wilson (Wilson et al., 1973) method. A similar method to the central difference method was proposed by Houbolt (1950), also called Houbolt method, in that he proposed to approximate acceleration  $\mathbf{a}$  and velocity  $\mathbf{v}$  in terms of  $\mathbf{u}$  as

$$\mathbf{v}_{t+\Delta t} = \frac{1}{6\Delta t}(11\mathbf{u}_{t+\Delta t} - 18\mathbf{u}_t + 9\mathbf{u}_{t-\Delta t} - 2\mathbf{u}_{t-2\Delta t}) \quad (3.15)$$

and

$$\mathbf{a}_{t+\Delta t} = \frac{1}{\Delta t}(2\mathbf{u}_{t+\Delta t} - 5\mathbf{u}_t + 4\mathbf{u}_{t-\Delta t} - \mathbf{u}_{t-2\Delta t}). \quad (3.16)$$

The solution for  $\mathbf{u}$  at time  $t + \Delta t$  is obtained via Equation 3.3:

$$\mathbf{M}\mathbf{a}_{t+\Delta t} + \mathbf{C}\mathbf{v}_{t+\Delta t} + \mathbf{K}\mathbf{u}_{t+\Delta t} = \mathbf{f}_{t+\Delta t}. \quad (3.17)$$

Similar to Equation 3.13, inserting Equations 3.15 and 3.16 into Equation 3.17 yields:

$$\begin{aligned} \left( \frac{1}{\Delta t^2} \mathbf{M} + \frac{11}{6\Delta t^2} \mathbf{C} + \mathbf{K} \right) \mathbf{u}_{t+\Delta t} &= \mathbf{f}_{t+\Delta t} - \left( \frac{5}{\Delta t^2} \mathbf{M} + \frac{3}{\Delta t^2} \mathbf{C} \right) \mathbf{u}_t \\ &- \left( \frac{4}{\Delta t^2} \mathbf{M} + \frac{3}{2\Delta t^2} \mathbf{C} \right) \mathbf{u}_{t-\Delta t} + \left( \frac{1}{\Delta t^2} \mathbf{M} + \frac{1}{3\Delta t^2} \mathbf{C} \right) \mathbf{u}_{t-2\Delta t}. \end{aligned} \quad (3.18)$$

Note that the knowledge of  $\mathbf{u}_t$ ,  $\mathbf{u}_{t-\Delta t}$  and  $\mathbf{u}_{t-2\Delta t}$  is required to solve for  $\mathbf{u}_{t+\Delta t}$ . However, the main difference is that the stiffness matrix  $\mathbf{K}$  is a coefficient matrix to the unknown displacement vector  $\mathbf{u}_{t+\Delta t}$ .  $\mathbf{K}$  stores most of the information that is required for the entire computation including the unsparse  $4^{th}$  order compliant stiffness tensor  $C_{ijkl}$  (Wriggers, 2008). Consequently  $\mathbf{K}$  is highly unsparse and requires factorization such as Cholesky (Gentle, 1998) or LU decomposition (Bunch and Hopcroft, 1974) before inversion.

This leads to the main difference between the two methods. Equilibrium in implicit methods is considered at  $t + \Delta t$ , while in explicit method it is considered at  $t$ . Therefore, a critical timestep in implicit methods is not required, while it does exist in explicit methods. Hence, explicit methods are considered conditionally stable while implicit methods are unconditionally stable. The time step in implicit methods can be chosen several magnitudes higher than in explicit methods. The critical time step in an explicit analysis must satisfy the so-called Courant - Friedrichs - Lewy (CFL) condition defined as:

$$CFL = \frac{v_{max} \cdot \Delta t}{l}, \quad (3.19)$$

where  $v_{max}$  is the maximum wave velocity,  $\Delta t$  the time step and  $l$  is the length of the smallest line element.  $CFL$  is required to be lower than 1 for 1D and lower than  $1/\sqrt{3}$  for 3D. In 3D, it means that the time step should satisfy:

$$\Delta t \leq \frac{l}{v_{max} \sqrt{3}}. \quad (3.20)$$

From a practical point of view, the decision to use either implicit or explicit problems depends on the physics of the problem. If the response of the problem mainly depends upon lower frequencies, implicit methods are ideal. If the solution depends upon higher frequencies such as seismic wave propagation where the solution is required to have a small timestep in any case, explicit methods are more suitable.

### 3.2.3 Comparison with other numerical methods

FEM is, however, not the only available method for solving PDEs. The most common methods can be divided into two classes:

- finite-difference and/or finite-volume methods
- finite-element methods

Each method has its advantages and drawbacks, highly depending on the purpose and objective of the analysis. Here we detail the main differences between these methods. For more information the reader is referred to [Morton and Mayers \(2005\)](#) for a general overview of the different methods and to [Virieux et al. \(2011\)](#) who described the differences of the methods w.r.t. geophysical problems.

**Finite-difference and finite-volume methods** While in FEM a weak form of the PDE is solved, finite-difference methods or finite-volume methods solve the strong form of PDEs. Here, the PDE needs to be solved locally at discrete nodes or elements. In finite-difference methods each derivative is replaced by the difference formula derived usually via Taylor series expansion. The solution can thus be discretised and explicitly calculated at each node. While in finite-difference methods the differential form of the PDE is solved, finite-volume methods exploits the integral form. Therefore, the discretized domain are no longer individual nodes but finite volumes. While finite-difference methods require a regular gridding, since the differential form is calculated, finite-volume methods offer more freedom when discretising the model.

**Finite-element methods** PDEs are solved globally in FEM using their weak formulation. The domain is decomposed into subdomains, i.e. elements. Thanks to this decomposition the topography and interfaces can be better represented and local mesh refinement is allowed. The weak formulation of the PDE of each subdomain is then assembled in the global stiffness matrix. Either the stiffness matrix (implicit) or the mass matrix (explicit) will be inverted to compute the variable of interest. A simplified flow is shown in Figure 3.3. A special case of the FEM is the spectral element method ([Šolín et al., 2003](#)). This method employs higher degree piecewise polynomials as basis functions and benefit from naturally diagonal mass matrices. Similarly, the h-p FEM employs elements of variable size ( $h$ ) and polynomial degree ( $p$ ) ([Babuska and Guo, 1992](#)). In h-FEM, the mesh is refined locally creating discontinuities at the irregular nodes, i.e. where the edges of a refined element meet at the midsides of a coarser one ([Arney and Flaherty, 1990](#)). This local element refinement, while keeping  $p$  fixed, reduced the total number of elements, since a regular gridding can be ignored. Furthermore, [Babuška et al. \(1981\)](#) have presented the p-FEM, where the degree of the polynomial approximation is increased until a desired precision is reached, while  $h$  is fixed, similar to the spectral element methods. They have shown that the rate of convergence of the p-FEM is twice that of the conventional FEM using a uniform mesh.

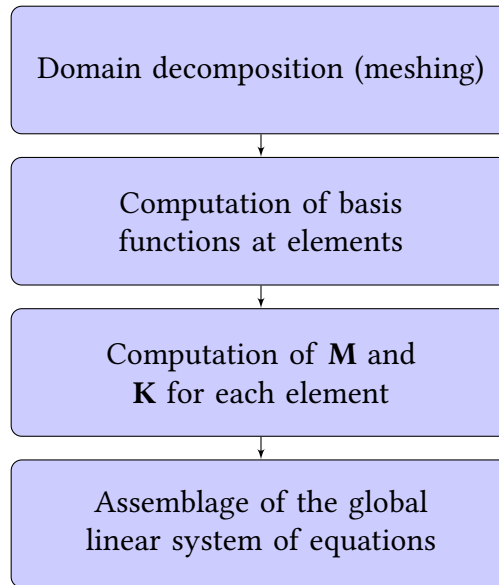


Figure 3.3: FEM summarised in 4 steps.

### 3.3 Numerical model set-up using the FEM

Two FEM software packages were available for this thesis: AnSYS, developed by John Swanson in 1970, that uses an implicit solver, and LS-dyna, developed by John Hallquist at the Lawrence Livermore National Laboratory in 1976, which uses an explicit one. Numerically simulating wave propagation in a medium requires in general large scale models, thus increasing the dimension of the stiffness matrix  $\mathbf{K}$ . Moreover, we are interested in frequencies up to 150 Hz, thus in a small timestep. If  $\mathbf{K}$  is sparse and small, and interest is in low frequencies, implicit methods are ideal, while explicit methods are more suitable when we need to handle large stiffness matrices and are interested in higher frequencies (see Section 3.2.2). Considering the available computer resources (a cluster with 24 CPU cores, 128 GB of RAM memory and 500 GB of hard drive storage), a wave propagation simulation might run for several weeks using an implicit solver. Moreover, in our problem there is a big difference in scale between the propagating medium (tens of hundreds of meters between the source and the borehole) and the borehole size as well as casing and streamer (approx. 0.01 meter). The number of grid elements being used might increase computation cost immensely since the dimension of the matrices in the algebraic system of equation, that needs to be solved, become larger. In addition, AnSYS does not provide absorbing boundary condition to the elastic wave equation. Only linear elastic dampers can be implemented which have proven to be not very effective in attenuating waves reaching medium boundaries. Therefore, we decided to make use of the explicit finite element program LS-dyna.

The numerical solution of a PDE using FEM is composed of several ele-

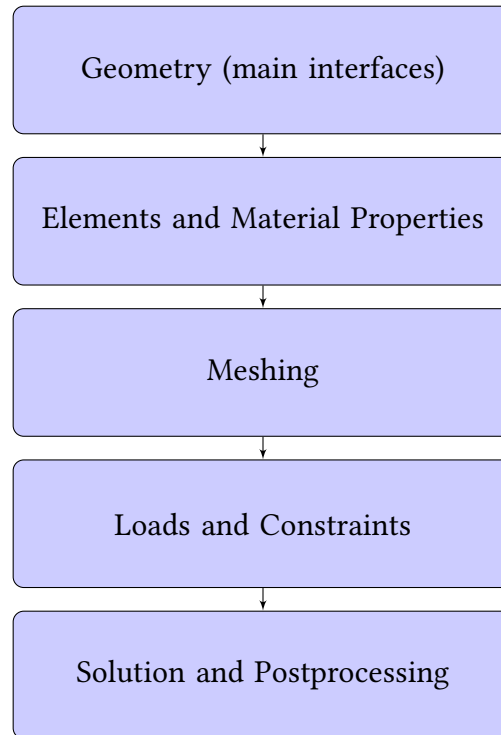


Figure 3.4: Workflow of a typical FEA job.

ments as illustrated in Figure 3.4. First, we need to build the geometry of the problem and to define the elements and material properties. The region of interest is then discretized and boundary conditions are applied. The medium is divided into a number of discrete elements connected at discrete nodes (Figure 3.5), equivalent to the decomposition of  $\Omega$  into  $\Omega_e$  as derived from Equation 3.9. The variables of interest (e.g. acceleration, velocity or displacements) are evaluated at these elements.

In Section 3.3.1, we present the finite elements and their geometries and discuss the material properties. The geometry (or shape) of the finite element determines the dimension of the problem (1D, 2D or 3D) and the way the system of equations are solved. The material properties are the intrinsic properties of the medium, required to solve the PDE of interest. Then, we review boundary conditions in Section 3.3.2. Finally, first numerical results are discussed in Section 3.3.3. These are simple numerical models solving elastic and acoustic wave equations and that are validated by analytical solutions. Numerical models of 1D, 2D and 3D seismic wave propagation are evaluated as well as the implementation of absorbing boundary conditions.

### 3.3.1 Geometry, elements and material properties

The geometry (or shape) of a finite element determines the dimension of the problem and the number of degrees of freedom, which, in turn, determ-

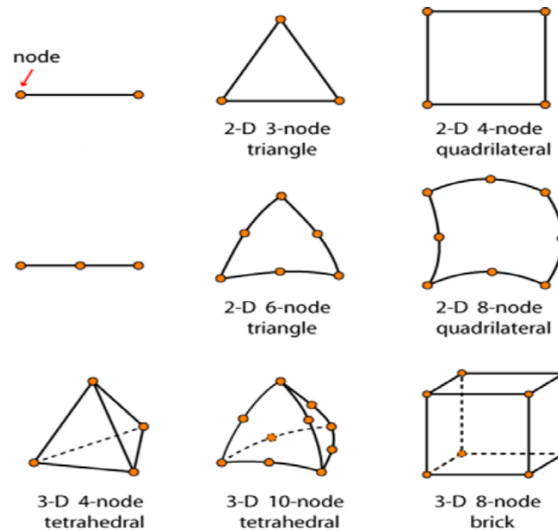


Figure 3.5: Example of different finite elements (adapted from [Dean \(2016\)](#)).

ines the total number of computed equations for each element. An overview of different finite elements is shown in Figure 3.5. Here, a 1D element is always a line element. For 2D problems, linear triangular elements are commonly used. For most 3D simulations, we make use of brick elements that are hexahedral-shaped elements with six faces, thus we have 8 nodes per element, with each node having six degrees of freedom (three for translations and three for rotations in  $x$ ,  $y$  and  $z$ ). Using hexahedral- instead of tetrahedral-shaped elements has the advantage that numerical implementation using Ansys Parametric Design Language (APDL) is more straightforward and a coarser gridding can be kept without highly skewed elements. Changes in the grid size would either increase the computational cost (when decreasing the grid size) or decrease the numerical accuracy (when increasing the grid size). A sudden change in element size, which often occur in highly skewed elements, causes artificial reflections ([Kittur and Huston, 1989](#)). Moreover, the presence of individual small line elements further increase the computation time because of the decreasing of the time marching scheme (Equation 3.19).

The material properties that are assigned in an elastic, isotropic medium are density  $\rho$ , Poisson's ratio  $\nu$  and Young's modulus  $E$ , as those are the required properties to solve the PDE in order to assemble the mass matrix  $\mathbf{M}$  and the stiffness matrix  $\mathbf{K}$ . In cases where only acoustic media are concerned and we deal with non-viscous, incompressible fluids,  $\nu$  and  $E$  are ignored. Hence, the required material properties depend on the PDEs that are solved for.

### 3.3.2 Loads and boundary constraints

A load represents the source function to which a node, element or a group of elements are exposed to. In a thermal analysis loads can be temperature or heat flux, in a fluid analysis they can be pressure or fluid particle velocity and in a stress analysis the load might be displacement or its temporal derivatives. Usually the application of boundary constraints are required as they are necessary to limit the motion, heat flux, etc. In thermal analysis typical constraints can be a particular temperature. Fluid constraints are specific pressures and in structural analysis constraints are usually zero displacements specified in all  $(x, y, z)$  or in specific directions but also absorbing boundary conditions as often used in seismic modelling. Note that both loads or constraints are always considered as boundary conditions that are imposed on individual nodes.

### 3.3.3 Analysis of numerical results

First numerical results obtained using LS-dyna will be shown in this section. It is necessary to ensure that the numerical solutions to seismic wave equations work correctly by comparing the numerical approximation to an analytical, exact solution. This step is critical since variations of this numerical model will be used in the following part of this chapter, and further application is found in Chapter 4. Therefore, some effort has been spent on this section because this step is essential for the rest of the thesis, since we would lose credibility by not validating our numerical results with exact solutions.

While we want to make sure that the numerical solution is correct, we also want to optimise the numerical model to keep the computation time to a minimum. In addition to the total number of elements used, the size of individual elements control the time-step, and thus also contribute to the total computation time. According to Equation 3.19, the coarser the grid size, the larger the timestep and therefore the faster the computation. However, arbitrary long element lengths are problematic, since the grid size determines the dispersion error and thus the accuracy of the numerical solution (Aki, 1989; Zhu and Cancellaris, 2006). It has been shown that in FEMs the phase-error of the calculated wave correlates with the grid size and the wavelength  $[(h/\lambda)^2]$ , where  $h$  is the grid size and  $\lambda$  the wavelength (Lee and Cancellaris, 1992). Hence, smaller grid sizes minimise the error between the exact and approximated solution.

The first numerical model is a square with lengths of 400 m (Figure 3.6). Since it is 2D, the 3D velocity-stress formulations derived in Equations 2.16 – 2.24 reduce to Equations 2.16, 2.17, 2.19, 2.20 and 2.22. The medium is isotropic, homogeneous with wave velocities  $V_p = 2449$  m/s and  $V_s = 1412$  m/s. The seismic source is located at the free surface and is a directional (vertical) source governed by Lamb's problem (Lamb, 1904). A Ricker wavelet of 45 Hz

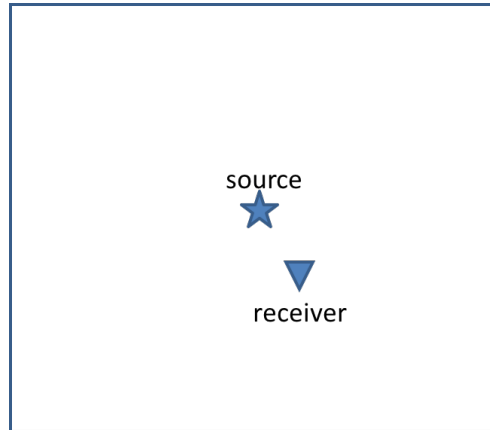


Figure 3.6: 2D Numerical model with dimensions 400 m x 400 m. The seismic source is located in the center, and a receiver is placed at distance offset  $x=50$  m and  $y=25$  m.

central frequency is applied to the vertical component of velocity. A receiver is placed at an offset  $x=50$  m,  $y=25$  m. The numerical solutions in this section are validated with a semi-analytical solution (Diaz and Ezziani, 2010) that was obtained through the Cagniard-de Hoop method (de Hoop, 1960).

In order to reduce the dispersion error and therefore minimise the error between the exact and approximated solution, Figure 3.7 presents the comparison of analytical and numerical data with increasing mesh refinement. The numerical solution is in blue, while the analytical solution is in red. In the left panel, the vertical component of particle velocity  $v_y$  is shown, while in the right panel the horizontal component  $v_x$  is plotted. The grid size of the numerical solution in 1a and 1b is 5 m, equivalent to 10 elements per wavelength of the P-wave. While the first break coincides in both solutions, the two waveforms gradually become out-of-phase over time which is a clear indication of the dispersion error mentioned in the beginning of this section. Therefore, the grid size has been progressively decreased in order to increase the element per wavelength ratio and therefore to minimise the phase error of the numerical solution. 2a and 2b are the results with a grid size of 3 m equivalent to 18 elements per wavelength of the P-wave. It can be observed that the first part of the wave, the part of the compressional wave, matches nearly perfectly with the analytical solution, while only 8 elements per wavelength of the S-wave naturally cause bigger phase errors of the later part of the waveform. The grid size has therefore been further decreased. 3a and 3b show the results with a grid size of 2 m, while results in 4a and 4b have been solved using a grid size of 1 m. With a 1 m grid size, there are 20 elements per wavelength of the S-wave and the residuals between the analytical and numerical solution are negligible.

In summary, we can conclude that the numerical simulation works correctly for the applied case. It has been shown that approximately 20 elements

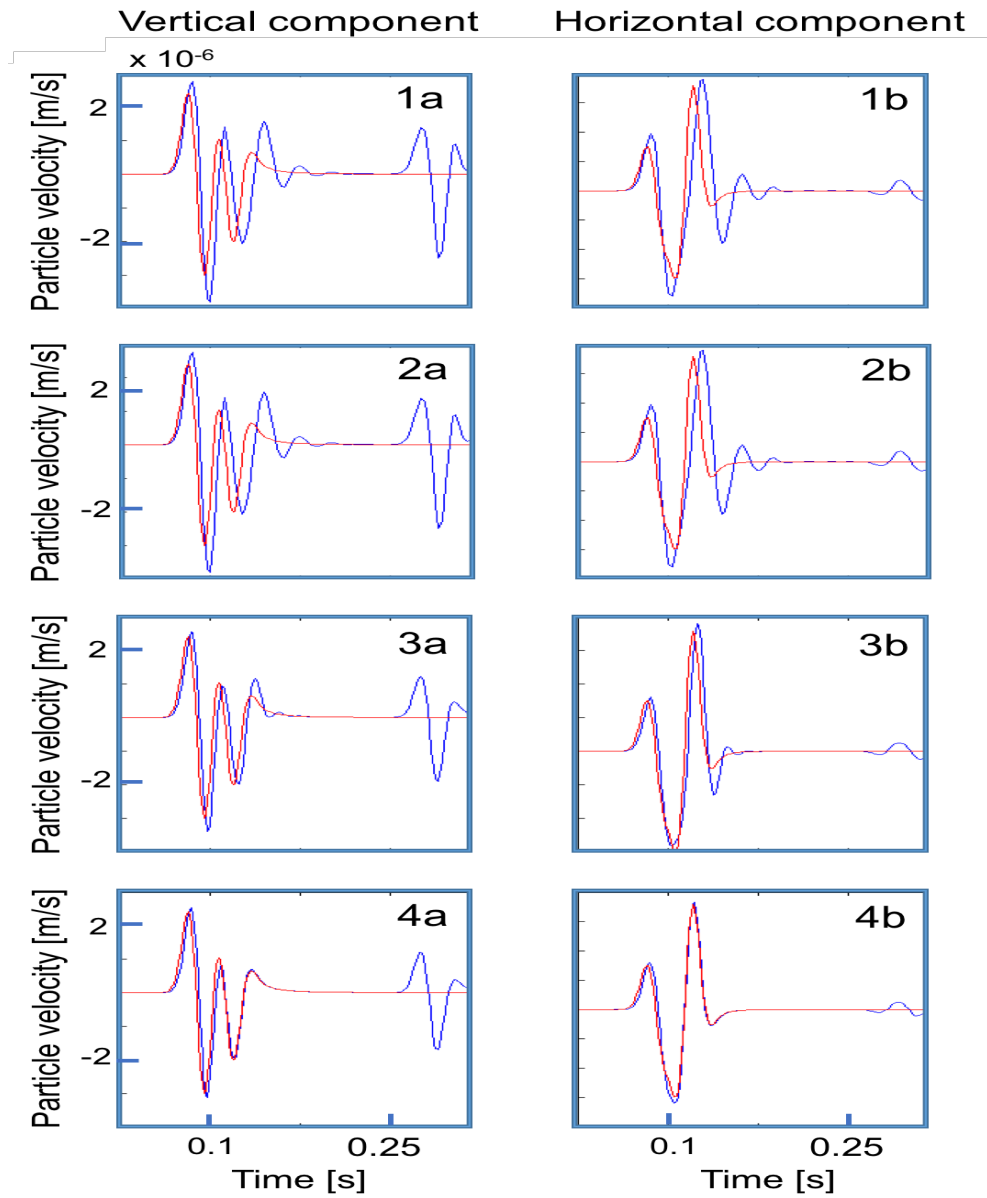


Figure 3.7: Numerical (blue) and analytical (red) solution of the vertical (left panel) and horizontal (right panel) components of particle velocity for different grid sizes. 5 m of grid size is presented in 1a and 1b, 3 m in 2a,b, 2 m in 3a,b and in 4a,b a grid size of 1 m is shown.

per wavelength are required to obtain a numerical approximation which is very close to the exact solution. However, since the computational domain is finite, seismic wave energy is reflected at the boundaries of the domain. Those artificial reflections are visible after the first arrival (Figure 3.7). In order to simulate an infinite medium, boundary conditions need to absorb the wave energy. The best practice is the implementation of perfectly-matched-layer (PML) (Berenger, 1994; Komatitsch and Tromp, 2003). The theory of PML will be reviewed in more detail in Section 3.4.1. Since the application of PML using LS-dyna requires 3D elements, they are implemented at the end on the face of a beam structure (Figure 3.8). In addition, the horizontal components of particle displacement have been constrained, so that the velocity-stress formulations reduce to the 1D case defined in Equations 2.16, 2.19 and 2.22. The propagation of the P-plane wave is shown in Figure 3.8. A source function has been applied to all nodes at one end of the beam, while a group of elements at the other end of the beam behave as PML and absorb the seismic wave energy. The dimensions of the beam are 20 m x 20 m x 400 m. Figure 3.9 shows the particle velocity of a receiver at  $x=10$  m,  $z=10$  m and  $y=350$  m. The upper panel illustrates the particle velocity without PML, while the lower panel shows recordings with PML included. The results reveal that the PML are absorbing nearly all energy of artificial reflections.

Since the required grid size using 2D seismic wave propagation in terms of the elements per wavelength ratio has been investigated and absorbing boundary conditions have been successfully implemented, while we validated our results with a semi-analytical solution (Diaz and Ezziani, 2010), the model has been extended to a 3D case. Hence, the elastodynamic equations derived in Equations 2.16 – 2.24 hold. The numerical medium is a cube with dimensions 230 m x 230 m x 230 m (Figure 3.10).

We analysed purely elastic cases (Figure 3.10) and a layered medium with an elastic and acoustic interface (Figure 3.11). In the first case, the source  $s(t)$  is again a directional source  $v_y = s(t)$  located at the center on the free surface (Lamb, 1904). In the second case, the source is a directional source, but buried in the elastic formation at  $y=75$  m. In both cases, the source signature is a Ricker wavelet of 45 Hz central frequency. Figure 3.11 presents a cross-section of the results at time  $t_1=0.126$  s and  $t_2=0.154$  s. This image should emphasize the successful energy transmission between the elastic and acoustic medium and the effectiveness of the absorbing boundary conditions for both the elastic and acoustic waves.

This section has been used to optimise, but more importantly, to validate the numerical solution. Therefore, we have verified the numerical results with a semi-analytical solution (Diaz and Ezziani, 2010). However, in addition to the results presented here, we have also analysed different boundary constraints. We imposed particle displacement  $u$ , velocity  $v$  and acceleration  $a$  as source terms to analyse amplitudes of the different outputs, that are functions of the frequency  $f$ . Let consider the harmonic equation of a

### 3 Numerical modelling and simulation

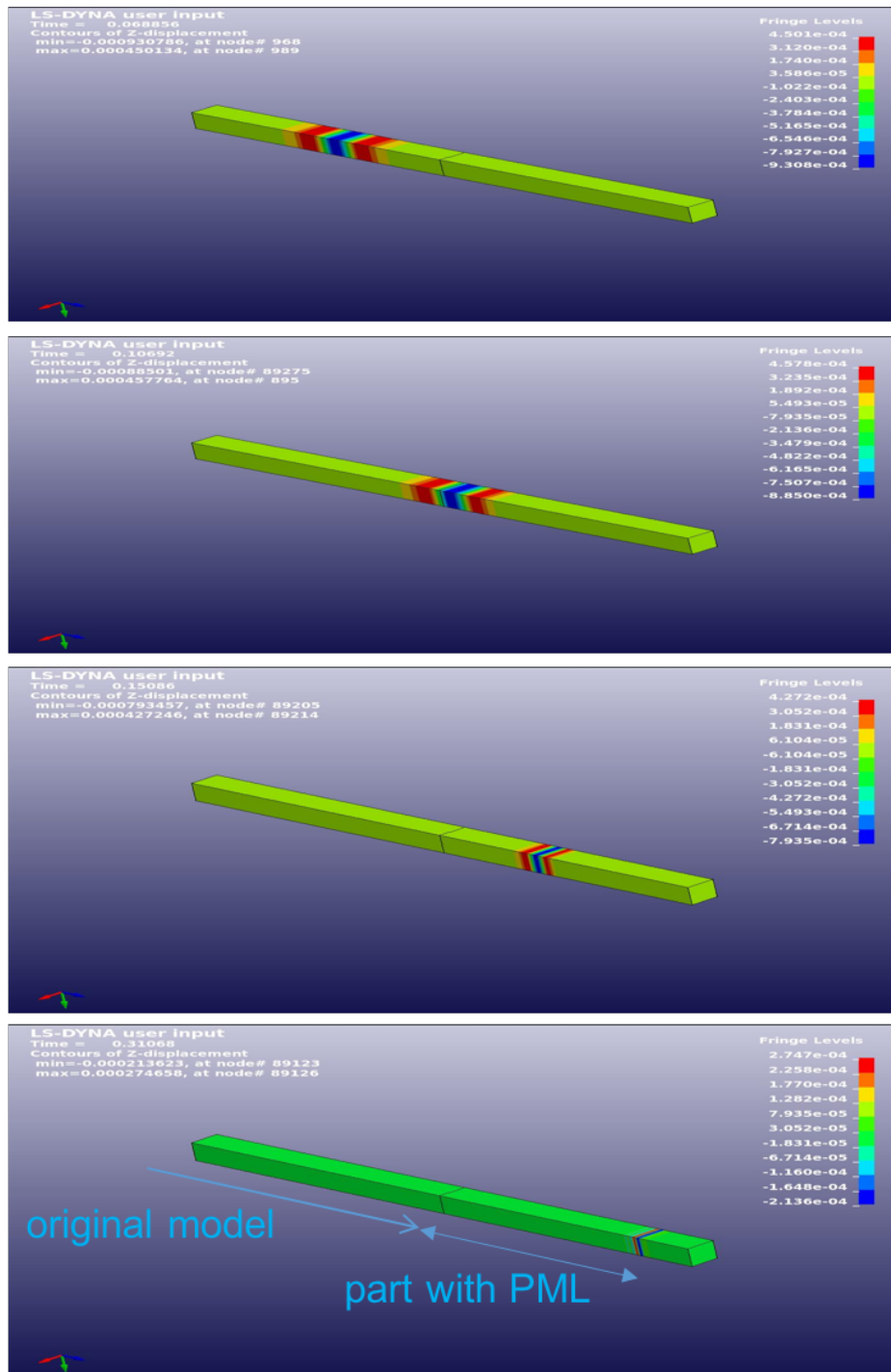


Figure 3.8: Plane P-wave propagation in a beam structure with PML applied at one end.

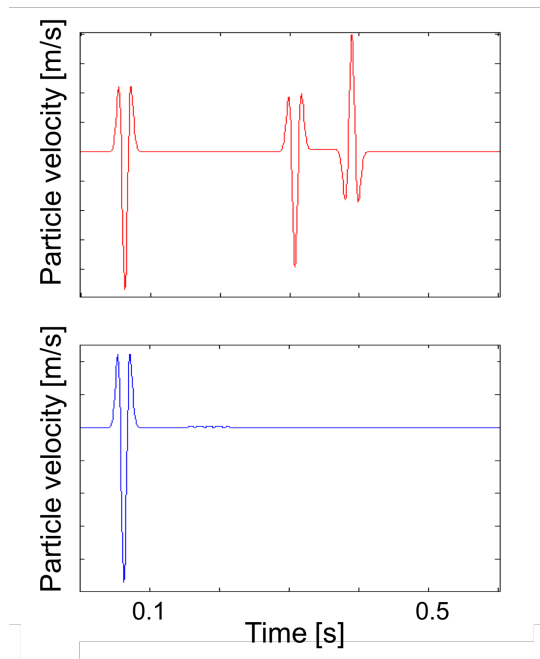


Figure 3.9: Particle velocity at a receiver at  $y=350$  m in Figure 3.8. Upper panel:  $v_y$  without PML; lower panel:  $v_y$  with PML included

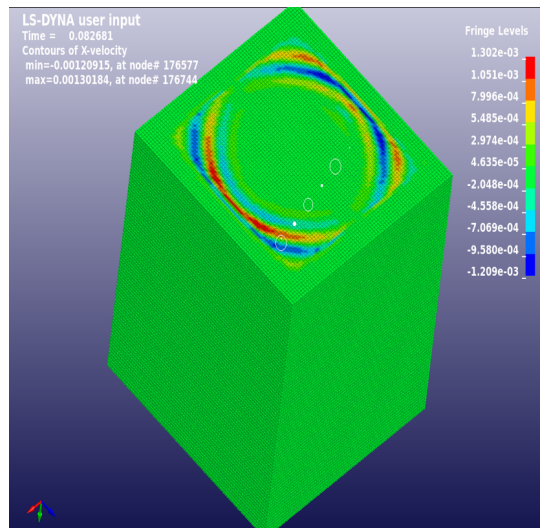


Figure 3.10: Numerical model for 3D elastic wave propagation. The directional point source is located in the center of the free surface. PML have been implemented on the edges.

### 3 Numerical modelling and simulation

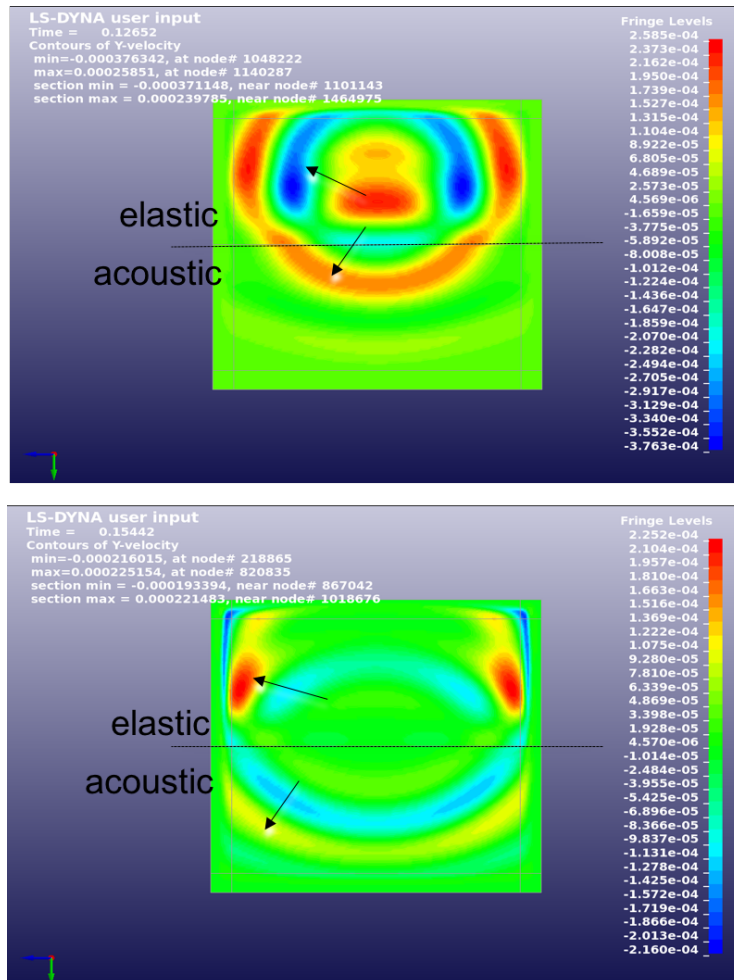


Figure 3.11: Cross-section of the numerical model, where upper part of the numerical model is elastic medium, and the lower part is acoustic medium. The upper panel shows wave propagation at  $t = 0.1256$  s and the lower panel at  $t = 0.1544$  s. The directional point source is buried in the elastic medium.

sine wave:

$$u(t) = A \sin(2\pi ft), \quad (3.21)$$

where  $u(t)$  is the displacement at time  $t$  and  $A$  is the amplitude and let

$$\omega = 2\pi f, \quad (3.22)$$

so that we obtain the expression for displacement as

$$u(t) = A \sin(\omega t). \quad (3.23)$$

Then, we obtain for velocity  $v$  and acceleration  $a$ , respectively:

$$v(t) = \frac{\partial u}{\partial t} = A\omega \cos(\omega t) \quad (3.24)$$

and

$$a(t) = \frac{\partial^2 u}{\partial t^2} = -A\omega^2 \sin(\omega t). \quad (3.25)$$

Note that the absolute value of velocity increases linearly, while acceleration increases exponentially. Therefore amplitudes and type of load has to be chosen with caution to ensure that the numerical solutions stay within elastic limits, thus avoiding the yield point where nonlinear (elastic and plastic) deformation begins (Holzapfel, 2001). Furthermore, we also validated the numerical model when imposing kinematic boundary conditions (BC) (or free surface conditions) and dynamic BC in plane wave scenarios. While waves are reflected with the same polarity at the free surface, because the stress  $\sigma$  normal to the surface  $n$  vanishes (Equation 3.27 or  $\sigma n = \mathbf{0}$ ), while displacement is continuous (Aki and Richards, 1980; Chapman, 2004), dynamic BC reflect the wave with opposite polarity ( $\sigma n = -\sigma n$ ).

### 3.4 FEA of seismic wave expressions in fluid-filled boreholes

In this section we present the FEM numerical model that we create to reproduce the analytical solution discussed in Section 2.4 on the expression of seismic waves in fluid-filled boreholes. Once this model is validated by comparing it with the analytical solution, variations of the model can be compared to DAS and conventional seismic datasets to draw further conclusions and to better understand DAS acquisitions. To build the numerical model, a workflow equivalent to the one presented in Figure 3.2 is followed. The geometry of the physical model is determined, element and material properties are defined, the meshing algorithm is presented and geophysical sources and applied constraints are explained. Then, we briefly summarise the main findings in Schoenberg (1986) and compare those findings with the numerical solution.

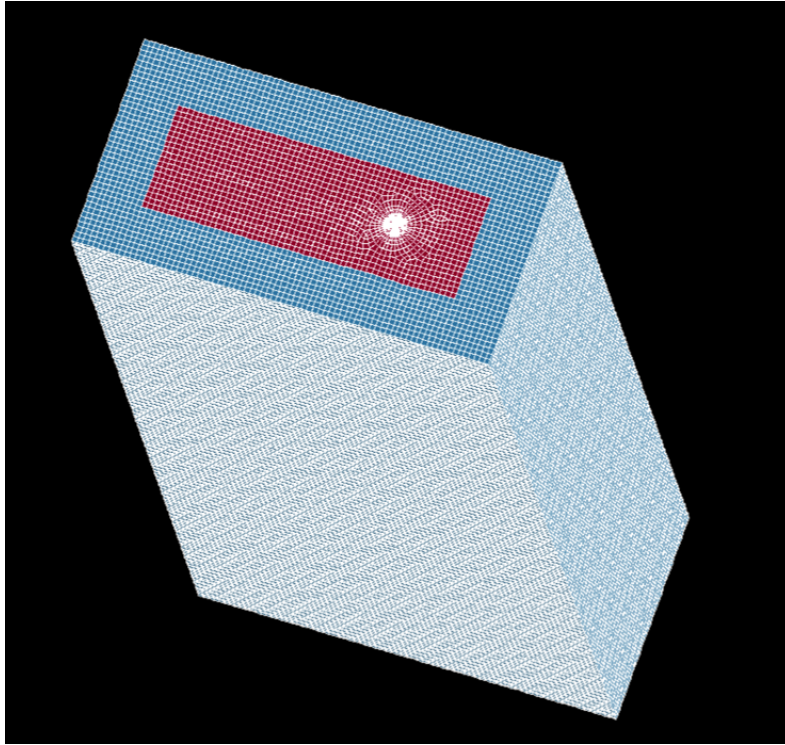


Figure 3.12: Numerical model with dimensions 240 m x 120 m x 600 m. The red part illustrates the region of linear isotropic element i.e. where seismic wave propagation is computed, while the blue elements are perfectly matched layer to simulate an infinite domain.

### 3.4.1 Numerical model

#### Geometry

The geometry of the model is a cube of dimensions 240 m x 120 m x 600 m (Figure 3.12). This size of the model allows us to simulate 3D seismic wave propagation, while having a reasonable wavefield separation in order to ease interpretation. Furthermore, different surveys can be simulated with the same model from zero-offset to mid-offset and far-offset VSP type of acquisition. The central part of the model mainly represents the formation solving for the elastic and acoustic wave equations, while in the outer part are perfectly-matched-layers (PML) which are used to simulate an infinite domain (more in Section 3.4.1). The borehole diameter is 0.25 m, while the streamer has a diameter of 0.01 m and the thickness of the casing is 0.02 m (Figure 3.13).

#### Elements and material properties

All elements used for modelling are 3D brick elements (Figure 3.5). They comprise 8 nodes, each having 6 degrees of freedom (three translations and

### 3.4 FEA of seismic wave expressions in fluid-filled boreholes

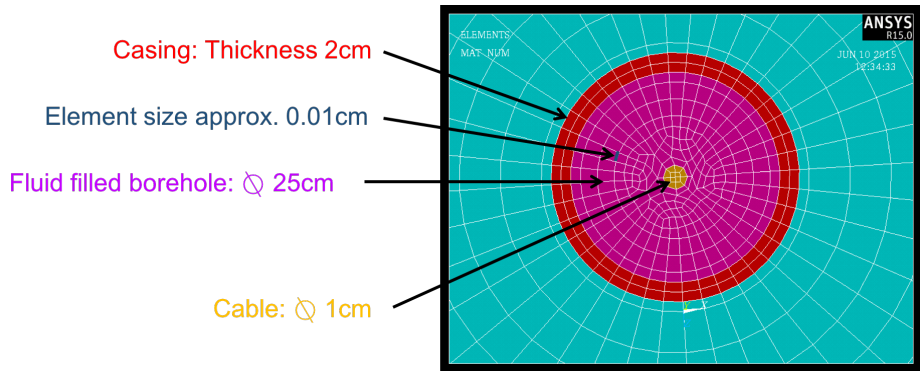


Figure 3.13: Zoom region of the borehole. The part of the formation is visible in turquoise, in red is the casing, in pink the fluid column and in yellow the streamer. The grid size is approximately 0.001 m.

three rotations in x, y and z). Material properties are linear isotropic and listed in Table 3.1 and corresponding velocities can be found in Table 3.2. All of these properties well describe the parameters of a typical VSP seismic survey.

Object	Material Property	Value	Unit
Formation	$\rho$ Density	3000	kg/m <sup>3</sup>
	$\nu$ Poisson's ratio	0.25	<i>dimensionless</i>
	$E$ Young's Modulus	25*10 <sup>9</sup>	kg/(m · s <sup>2</sup> )
Casing	$\rho$ Density	8000	kg/m <sup>3</sup>
	$\nu$ Poisson's ratio	0.2	<i>dimensionless</i>
	$E$ Young's Modulus	28*10 <sup>10</sup>	kg/(m · s <sup>2</sup> )
Fluid	$\rho$ Density	1100	kg/m <sup>3</sup>
Cable	$\rho$ Density	4451	kg/m <sup>3</sup>
	$E$ Young's Modulus	1.83*10 <sup>11</sup>	kg/(m · s <sup>2</sup> )
	$\nu$ Poisson's ratio	0.33	<i>dimensionless</i>

Table 3.1: Material properties

#### Meshing

The most straightforward strategy to discretise the model is to use the implemented automatic meshing option available in AnSYS (Moaveni, 2007). However, due to irregular geometries (e.g. cylindrical borehole or streamer) an automatized mapped meshing using robust hexahedral-shaped elements cannot be utilized, thus tetrahedral elements are created (Figure 3.14). The problem with the presence of tetrahedral elements in the model is that the size of line elements of tetrahedral-shaped elements cannot be controlled and as the time step is chosen according to the CFL condition (Equation 3.19), a

Object	Type	Value	Unit
Formation	P-wave	3430	m/s
	S-wave	1790	m/s
Casing	P-wave	6230	m/s
	S-wave	3810	m/s
Fluid	P-wave	1410	m/s
Cable	P-wave	7880	m/s
	S-wave	3930	m/s

Table 3.2: Seismic velocities

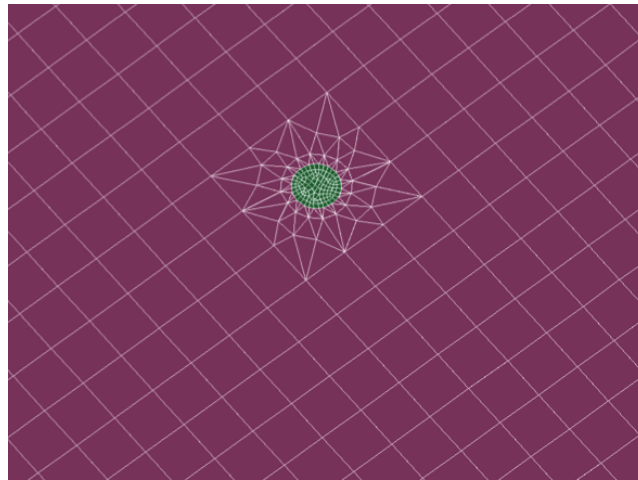


Figure 3.14: Automatised meshing creating tetrahedral-shaped brick elements. The sudden decrease in grid size from 3 m to 0.01 m causes strong artificial reflections due to the apparent stiffness of the elements.

single small line element in the simulated model will explode the computation time. For this reason, although initially more time consuming, we decided to discretise the model manually using Ansys Parametric Design Language (APDL) (Moaveni, 2007). Nodes, lines (1D), areas (2D) and volumes (3D) are therefore explicitly defined to build 3D elements. The advantage of the manually discretized model is that once the APDL code for it is obtained, the code can be automatized and modified easily, parameter testing is straightforward and geometries can be adjusted quickly while the whole modelling process remains automatised and repetitive. Another reason to use a controlled mesh is the smooth transition from coarse to fine sized elements. A sudden increase in mesh size (Figure 3.14) can cause numerical artifacts due to apparent stiffness of the elements (Kittur and Huston, 1989). Considering that the central focus of the simulation is the borehole, we propose an azimuthally and horizontally optimised mesh grid that allows avoiding numerical artifacts and guarantees a valid seismic wave propagation

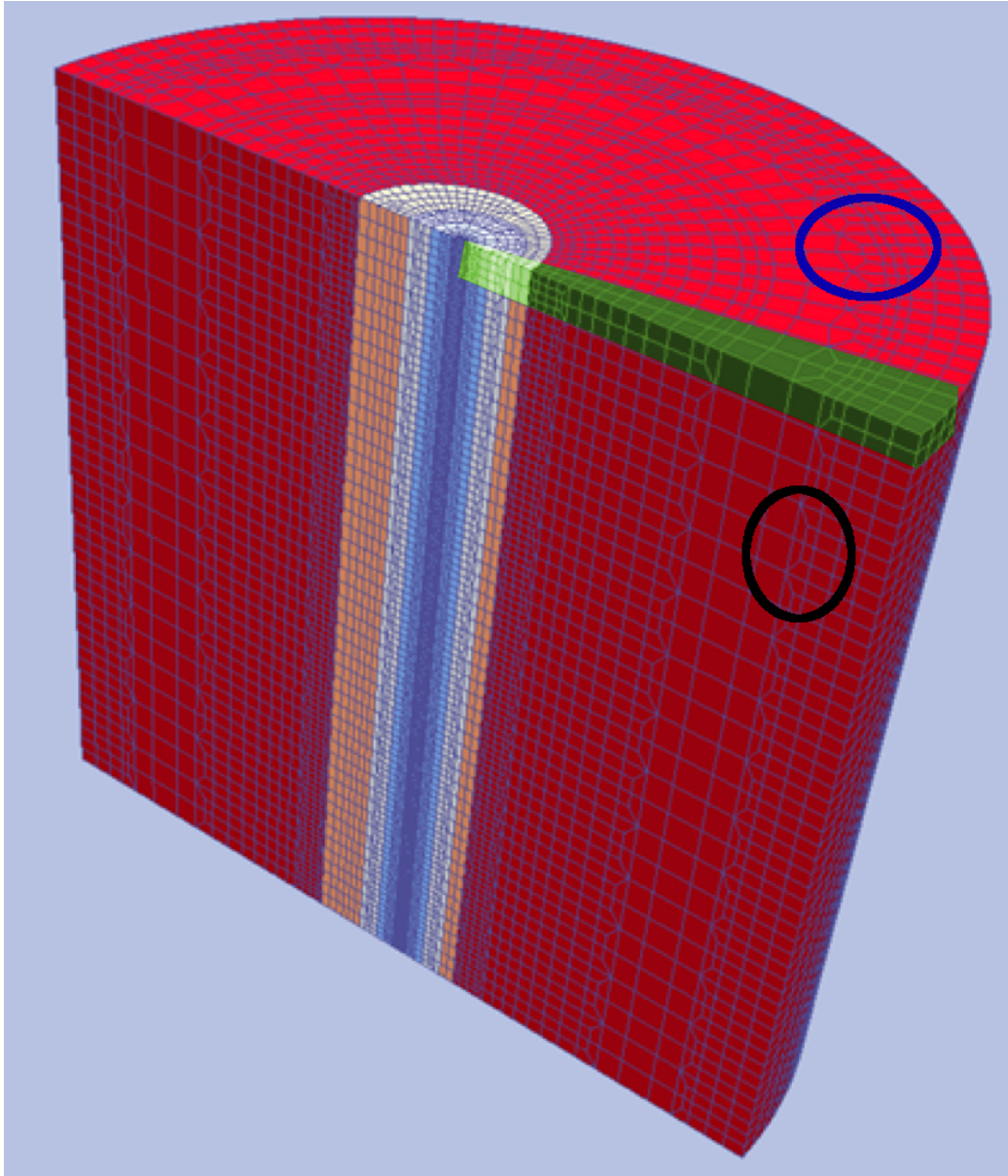


Figure 3.15: A numerical model to test mapped meshing with the objective to develop a horizontally (black circle) and azimuthally (blue circle) optimised meshing algorithm to avoid artificial reflections commonly found when a sudden change in element size occurs.

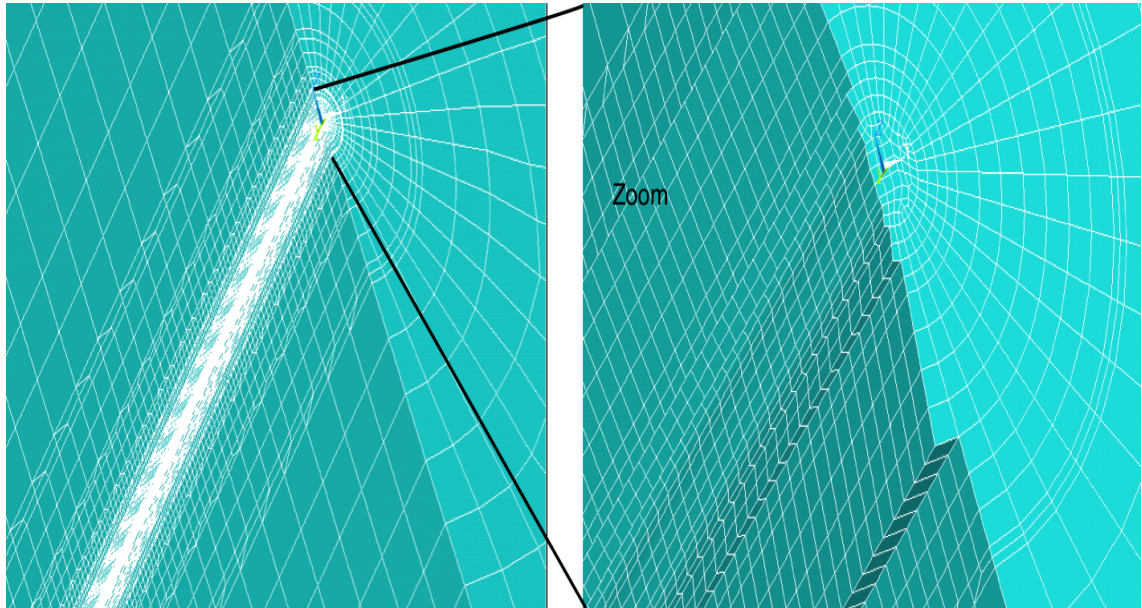


Figure 3.16: Mapped meshing with continuous refinement of elements. An azimuthally and horizontally optimised mesh grid prevents strong artificial reflections, but is more difficult to implement as a repetitive meshing needs to be coded beforehand.

from coarse to very fine sized elements. One of the first examples utilising this technique of mesh refinement to simulate a fluid-filled borehole is shown in Figure 3.15. Note that the model has been refined towards its center and the mesh has been horizontally (black circle) and azimuthally (blue circle) refined (1) without any mesh distortion, (2) while avoiding tetrahedral-shaped elements. Furthermore, only a single 2D face is initially required where the location of nodes and line elements needed to be defined. Azimuthal extrusion of the 2D face produced a 3D volume highlighted in green. Based on this volume, the entire model can be easily modelled. Extrusion of the volume in angular direction around 180 degrees results in a first semicircle. Extrusion of the semicircle in the vertical direction leads to an 3D model of arbitrary depth. This whole process, if done correctly, is automatised and repetitive. A similar approach has been applied to create the numerical model to investigate the seismic wave expressions in a fluid-filled borehole. For the formation a grid size of 3 m has been used, equivalent to 25 elements per wavelength of P-wave and 14 elements per wavelength of S-wave. The streamer and fluid domain consists of elements with sizes of about 0.01 m, while the exterior part with a radius of 11 m has been used to consecutively doubling/halving the element size while fitting sufficient elements within each step of refinement (Figure 3.16). Note that we require one additional node, and three line elements (black circle in Figure 3.15) to reduce the element size by a factor of 2. Therefore, 11 iterations ( $0.5^{11} \cdot 3 \text{ m} = 1.4 \cdot 10^{-3} \text{ m}$ ) of mesh refinement are necessary to obtain the desired grid size around the borehole area.

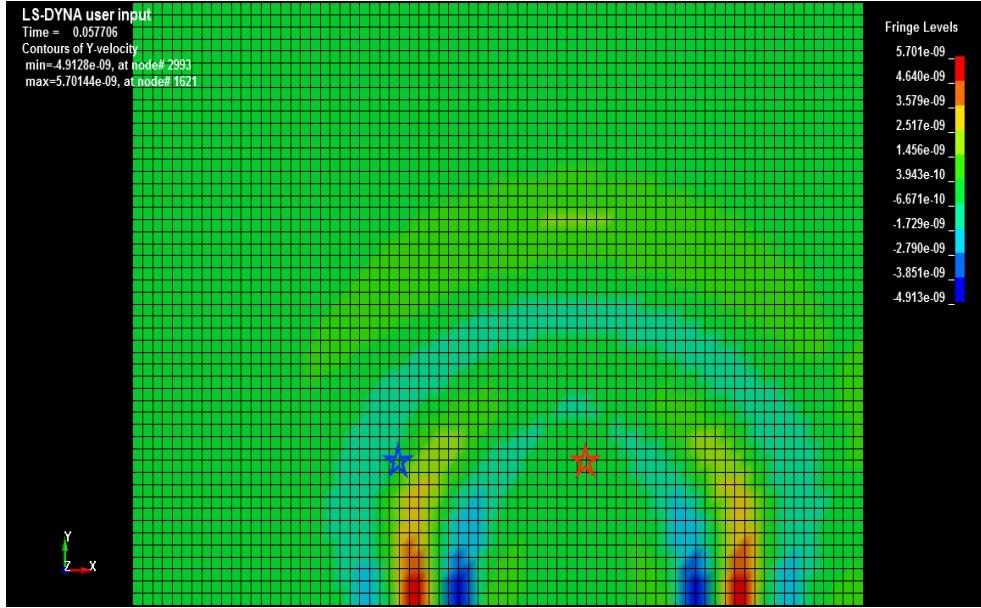


Figure 3.17: 2D seismic wave propagation in the numerical model with uniform meshing. The seismic source is located at  $x=24$  m.

This novel meshing technique was tested in a 2D model. In one model the grid size was 3 m, while in the mesh refined model the center of the model at  $x=0$  m was refined with element sizes up to  $1.4 \cdot 10^{-4}$  m. The 2D model was  $x=110$  m in length and  $y=220$  m in depth. The source was a directional point source with the waveform of a Ricker wavelet of 40 Hz central frequency. The source was located at the free surface ( $y=0$  m) and  $x=24$  m in both cases. The P-wave velocity was 3340 m/s and the S-wave velocity was 1670 m/s. Figures 3.17 and 3.18 show a snapshot at approximately 0.057 s. The particle velocity for a receiver at  $x=24$  m,  $y=46$  m (denoted with a red star in Figure 3.17 and 3.18) is shown in the upper panel in Figure 3.19 and the particle velocity for a receiver at  $x=-24$  m,  $y=46$  m (denoted with a blue star in Figure 3.17 and 3.18) is shown in the lower panel in Figure 3.19. The snapshot of the wavefield, and the single trace plot demonstrate that we implemented the meshing approach without causing artificial reflections due to apparent stiffness of the elements. Hence, we will use this technique to discretise the 3D model.

The reduction in computational cost using a manual meshing technique is immense. The automatic meshing method implemented elements as small as  $1.5 \cdot 10^{-5}$  m, while the smallest line element in our approach is  $1.4 \cdot 10^{-3}$  m.

According to the CFL condition, the timestep in our approach yields  $\frac{1.4 \cdot 10^{-3} \text{ m}}{3400 \text{ m/s} \cdot \sqrt{3}} = 2.5 \cdot 10^{-7} \text{ s}$ , where 3400 m/s is the value of  $V_p$ , while the implemented meshing technique implemented in AnSYS/LS-dyna produces a timestep of  $\frac{1.5 \cdot 10^{-5} \text{ m}}{3400 \text{ m/s} \cdot \sqrt{3}} = 2.5 \cdot 10^{-9} \text{ s}$ .

### 3 Numerical modelling and simulation

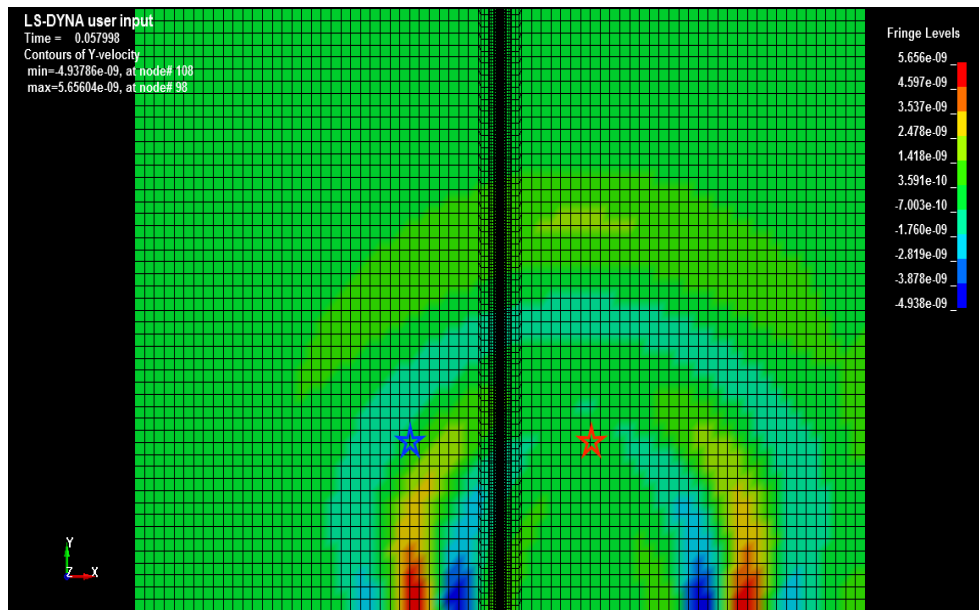


Figure 3.18: 2D seismic wave propagation in the mesh refined numerical model. The seismic source is located at  $x=24$  m and the mesh refined area is around  $x=0$  m.

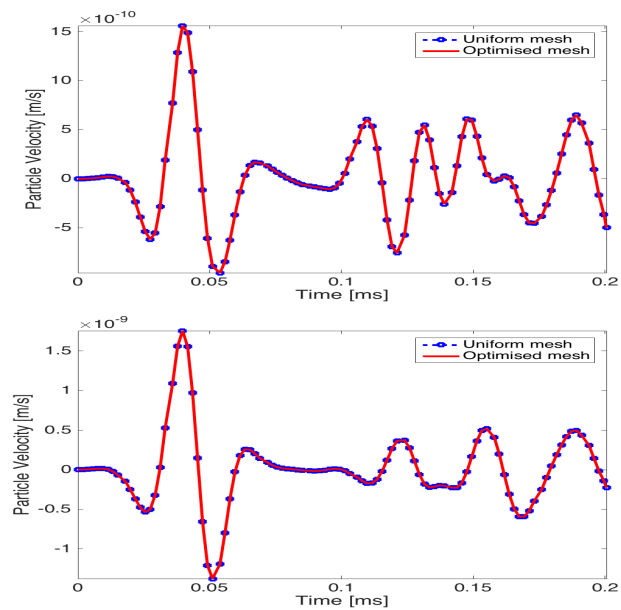


Figure 3.19: Comparison of the vertical component of particle velocity between the model with uniform mesh and the model with the mesh refined area. The upper panel shows the particle velocity at  $y=46$  m and  $x=23$  m and the lower panel shows the particle velocity at  $y=46$  m and  $x=-23$  m.

Considering that the numerical simulation time is 0.5 s, the number of required iterations to solve the transient model is  $1.9 \cdot 10^6$  and  $1.9 \cdot 10^8$ , respectively. In practice, while our approach leads to a computation time of around 62 hours to solve the numerical model, the computation time using the automatic meshing approach stopped at 100 hours since we reached the limit of the computational resources.

### Boundary conditions

**Loads** The external source function used here is a directional point source in vertical direction:  $v_z = s(t)$  (Lamb, 1904). For convenience a Ricker wavelet was injected:

$$s(t) = (4\alpha^2 t^2 - 2\alpha)e^{-\alpha t^2}, \quad (3.26)$$

where  $\alpha$  contains information of the dominant frequency  $2\pi f$  of the wavelet and  $t$  is the time vector. Although it is not a very realistic source signature, the Ricker wavelet is commonly used in geophysical applications. We used a dominant frequency  $f$  of 40 Hz, time shifted according  $1/f$  to obtain a causal wavelet.

**Constraints** The top of the model (at depth  $z = 0$ ) resembles a free surface. The free surface conditions, that are intrinsically satisfied in the numerical solution (Equation 3.6), are Neumann boundary conditions, which are obtained by satisfying zero stress conditions of the vector normal to the surface (Levander, 1988):

$$\begin{aligned} \sigma_{zz}|_{z=0} &= 0 \\ \sigma_{zx}|_{z=0} &= 0 \\ \sigma_{zy}|_{z=0} &= 0 \end{aligned} \quad (3.27)$$

At the bottom of the finite model (at depth  $z = 600 \text{ m}$ ) and at all its edges perfectly-matched-layer (PML) are implemented to simulate an infinite domain which is necessary to avoid numerical reflections in the computational domain. The original idea of PML dates back to Berenger (1994) using Maxwell's equation to apply absorbing boundary conditions in electromagnetic wave propagation. PML allow to achieve a zero reflection coefficient for all angles of incidence and all frequencies. Komatitsch and Tromp (2003) and Basu and Chopra (2003, 2004) formulated an implementation of PML for seismic modelling where first the PMLs are computed in the frequency domain and then transformed back into the time domain by special coordinate-stretching functions. In our experiment, we found that at least 20 elements per wavelength are necessary to accurately absorb seismic waves and to prevent numerical reflections. In particular, the absorption of energy of surface waves is rather difficult due to their dispersive character since PML equations are derived in the frequency domain. It has been found that a possibility to keep the amount of surface wave reflectivity to a minimum is to chose a PML length equal to the wavelength of the surface wave. It adds more elements

	Radial motion $v_r$	Vertical motion $v_y$
P-wave contribution	$v_{elastic} = v_{fluid}$	$v_{elastic} \neq v_{fluid}$
S-wave contribution	$v_{elastic} = v_{fluid}$	$v_{elastic} \neq v_{fluid}$
Tube-wave contribution	-	only $v_{fluid}$

Table 3.3: Analytical solution for a VSP zero-offset survey after [Schoenberg \(1986\)](#).

to the whole computational model but guarantees lower artificial amplitude reflections and therefore smaller errors in the interpretation of the numerical results.

### 3.4.2 Numerical results

The numerical solution used to validate the numerical model presented in this section has been discussed in detail in Section 2.4. The main outcomes can be described in terms of horizontal and vertical motion as well as wave types. Even though the model is 3D, we only display two components: the vertical component of particle velocity  $v_y$  and the radial component of particle velocity  $v_r$ . Results are validated for a VSP zero-offset survey ( $\delta = 0$ ) and particle velocity in the elastic formation is compared with particle velocity in the borehole fluid.

First, the analytical solution for radial motion is validated. In Figure 3.20 numerical results of 1200 receiver points are plotted. The y-axis shows depth or receiver position, while the x-axis shows time samples. According to results of [Schoenberg \(1986\)](#), partly summarised in Table 3.3, radial motion generated by P- and S-waves in the borehole fluid follows exactly the motion in the elastic formation. Moreover, the contribution of tube waves should be missing in both media. The analytical solutions are confirmed by the numerical approximation in Figure 3.20. The recordings of a receiver at 300 m depth reveal that both waveforms have nearly identical amplitude and phase information. Furthermore, the gray scale plot shows that in both media tube waves are absent.

Secondly, the numerical solution for vertical motion is validated. Receiver points and length of time recordings in Figure 3.21 are identical to the parameters used in Figure 3.20. The analytical solution predicts differences in amplitude and phase of particle velocities induced by impinging P- and S-waves in the borehole fluid when compared to the expressions in the elastic formation. Those predictions are confirmed by the numerical model in Figure 3.21. Here, significant differences in particle motion are recorded in the borehole fluid compared to the borehole wall. Furthermore, the tube wave, colored in green in the gray scale plot (Figure 3.21), is not propagating in the elastic formation.

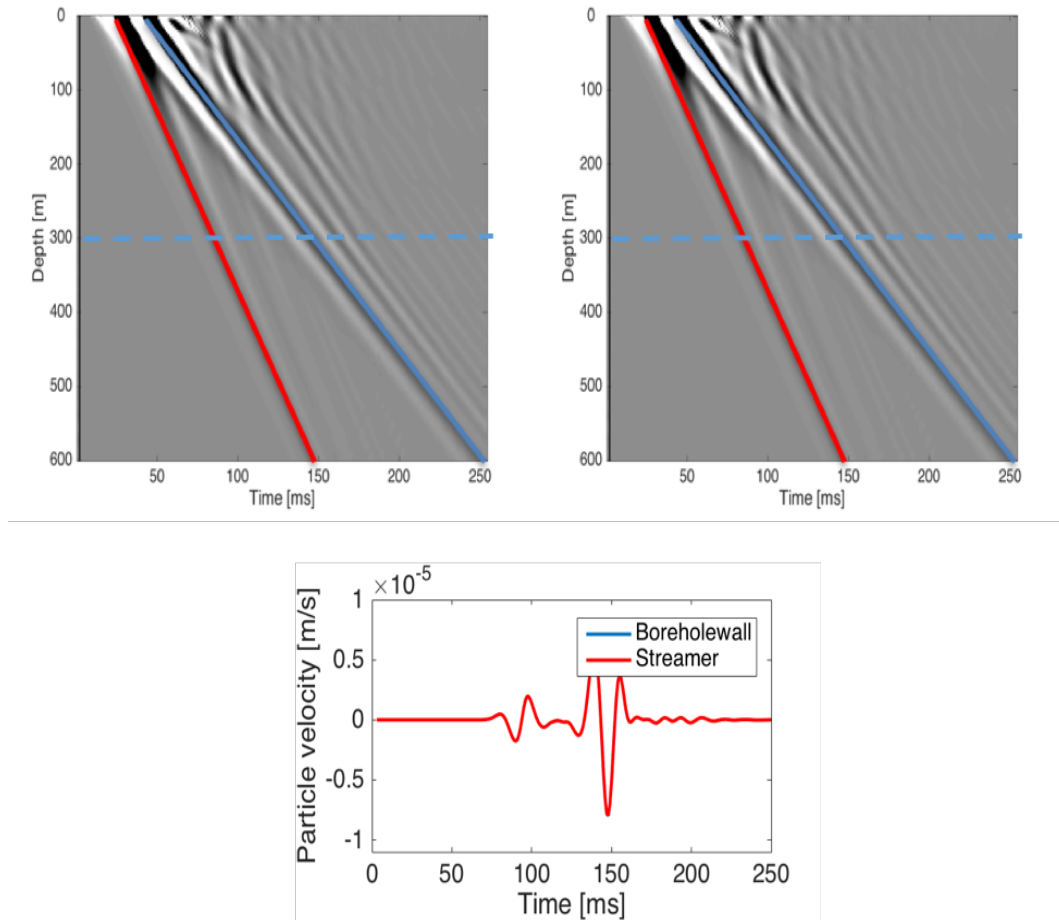


Figure 3.20: Horizontal motion. The gray scale plot in the upper left corner shows the radial particle velocity of the streamer in the borehole fluid. The radial particle velocity at the borehole wall is presented in the upper right corner. A single trace plot of both results at 300 m depth is shown in the bottom plot highlighting the similarity of the two measurements.

Since the numerical solution ties in with analytical observations, the numerical model can be reliably used to analyse different scenarios. In particular, we are interested in comparing the numerical results with real data. In Chapter 4, we will apply variations of this model, e.g. different locations and varying elastic properties of the cable, different material properties of the casing, a changing viscosity of the borehole fluid... to further analyse real data recordings.

### 3.5 FEA of cable coupling

Besides the particle velocity induced by an impinging elastic wavefield, it is just as important to be aware of the actual position and movement of

### 3 Numerical modelling and simulation

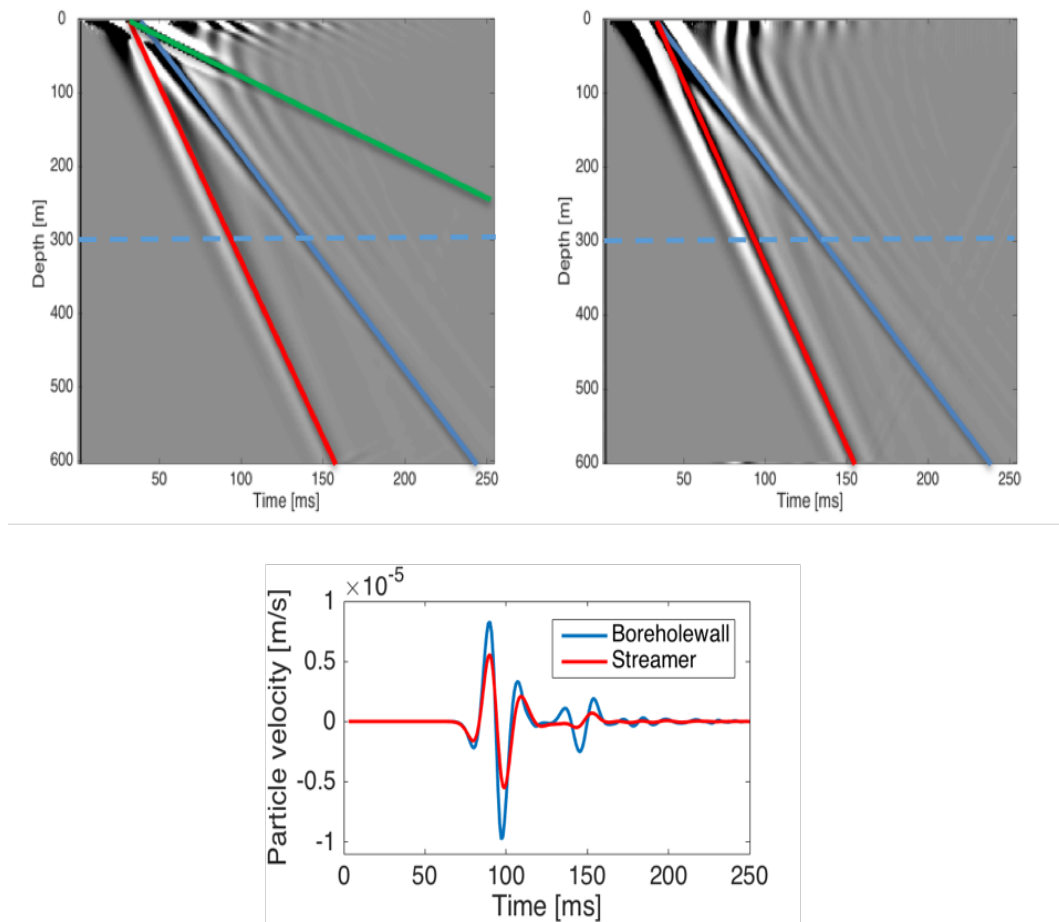


Figure 3.21: Vertical motion. The gray scale image in the upper left corner presents the vertical particle velocity of the streamer in the borehole fluid. The vertical particle velocity at the borehole wall is shown in the upper right corner. A single trace plot of both results at 300 m depth is shown in the bottom plot.

the cable inside the borehole when using wireline deployment. During this deployment technique gravitational forces are acting on the cable, causing momentum of the cable and thus displacement and bending when tension of the cable is released. Furthermore, over time more cable length will be added into the borehole to study the effect of cable slack as observed in real data (Hartog et al., 2014). When taking inertia of the cable into account, a high mesh distortion would evolve due to large displacements of the cable leading to a dramatic increase in the computation time. Since LS-dyna does not provide mesh free methods (Liu, 2005) or moving boundary methods (Wall and Ramm, 1998; Tezduyar, 2004), it is more effective to track the movement of the cable using another numerical model that we present in this section. Since only the displacement of bending moments of the cable are of interest, a model solving for wave equations is no longer required, when we ignore the effect of the wave on the cable motion, and therefore the extensive seismic model used in the previous section is not used.

### 3.5.1 Numerical model

#### Geometry

In the model presented in this section, only the borehole and the cable are modelled. The model of the borehole is shown in Figure 3.22, where inside the borehole a beam element is placed simulating the DAS cable. The thickness of the borehole wall is only 2 cm since the borehole should simply act as a physical boundary for the moving cable. The depth and inner diameter of the borehole and dimensions of the cable will be adjusted depending on the dimensions used in real data.

#### Element and material properties

The borehole is modelled using rigid elements. In rigid bodies, the distance between two given points remains constant, hence deformation is neglected. This reduces the computation time significantly since translation and rotations of rigid body with respect to the reference frame are derived using basic ODEs. A numerical model of the cable is shown in Figure 3.23. The three fibre cables are indicated in red, while other materials serve for electricity transmission and for cable reinforcement purposes. The mass of the cable, being torque-balanced to resist twisting when under load, is known. In order to account for the borehole fluid in the numerical solution,  $\rho_{water}$  has been subtracted from the defined mass of the cable  $m_{cable}$ :

$$m_{cable} = (\rho_{cable} - \rho_{water}) \cdot V_{cable}, \quad (3.28)$$

where  $m$  denotes the mass,  $\rho$  is the density and  $V$  is the volume. However, in the numerical simulation we will not use this exact cable model because

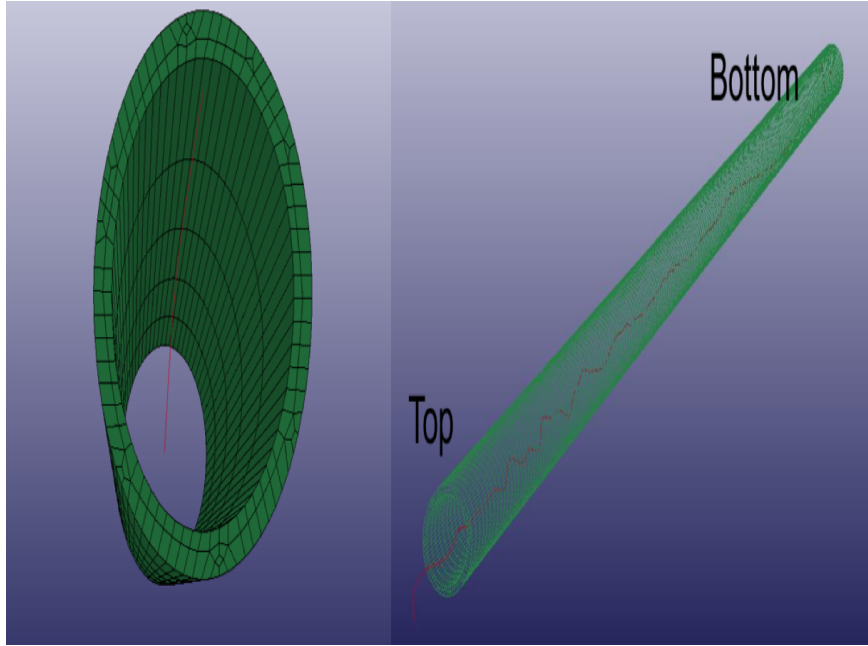


Figure 3.22: The numerical model that is used to analyse the movement and position of the cable during the DAS VSP survey on wireline cable. The borehole wall is in green, while the DAS cable is in red. A topview is shown on the left, and a side-view is given on the right.

discretising every single layer will be computationally too expensive. We derived the cable elastic properties such as Young's modulus and Poisson's ratio in a separate static analysis. Then, we used those properties to model the cable using a beam formulation (Bauchau and Craig, 2009). Geometrically a beam is a straight bar and can be of arbitrary cross-section. Beams are extensions of trusses as they carry in addition to information about displacement, also information about bending moments. Based on the Bernoulli-Euler theory, a beam consists of a centroidal axis along the  $z$ -axis, a particular cross sectional area, second moment of area about the  $x$ -axis,  $I$ , and a Young's modulus,  $E$ . The resulting displacements  $u_z$  and  $u_x$  in the  $z$ - and  $x$ -directions are generated when the beam is under the load of a bending moment,  $M$  as well as shear force and axial force (Astley, 1992). A beam element of length  $L$  is shown in Figure 3.24 with transverse displacements,  $u_{x1}$  and  $u_{x2}$  (axial displacements  $u_{z1}$  and  $u_{z2}$  are not considered), rotation of the end planes  $\theta_1$  and  $\theta_2$  and rotation of the neutral axis  $\xi_1$  and  $\xi_2$ . Assumptions are that plane sections initially perpendicular to the centroidal axis, remain plane and perpendicular to the axis after deformation and therefore cross-sections remain perpendicular to the neutral axis (Pickhaver, 2006):

$$\theta_1 = \xi_1 \quad (3.29)$$

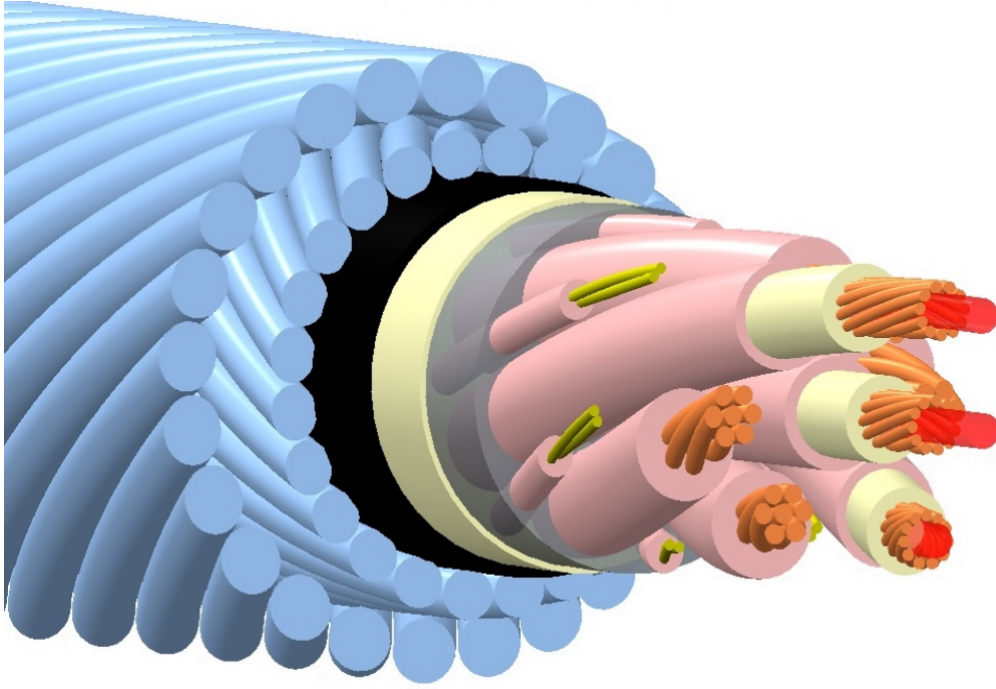


Figure 3.23: Model of the heptacable. The three fibre cables are indicated in red, while other materials are for electrical or cable reinforcement purposes.

and

$$\theta_2 = \xi_2. \quad (3.30)$$

Based on this assumption and with  $\xi = du_x/dz$ , [Timoshenko \(1957\)](#) derived the deflection for a beam:

$$\frac{d^2 u_x}{dz^2} = \frac{-M}{EI}. \quad (3.31)$$

As only the position of the cable and its bending is of interest, Hughes-Liu beams have been used ([Hughes and Liu, 1981](#)), where rigid body rotations do not generate strains in contrast to formulations presented in [Timoshenko \(1921\)](#) and [Timoshenko \(1922\)](#) where shear strains are computed when relaxing the conditions in Equations 3.29 and 3.30. The computation of Hughes-Liu beams is much more efficient and robust, while beams using Timoshenko formulations are preferably used for large deformation but are computationally more expensive.

### Boundary conditions

The borehole is constrained in any direction, as the borehole wall should only serve as a physical boundary for the cable to limit its motion and lead to equilibrium conditions.

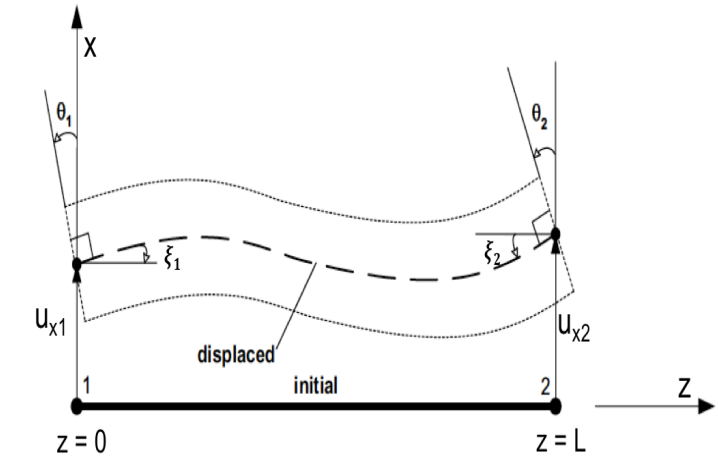


Figure 3.24: Bernoulli-Euler beam (adapted from [Astley \(1992\)](#)).

Gravitational acceleration  $a_z = 9.81 \text{ m/s}^2$  is applied to all nodes of the cable to simulate the movement of the cable when tension is released and only gravity forces are acting, similarly to what happens during the wireline deployment of DAS cables. The very end of the cable is constrained in any direction to simulate the bottom of the borehole. Furthermore, over time more cable is lowered down the borehole by displacing nodes of the upper part of the cable in vertical direction ( $z$ ).

An additional step in this simulation is to account for the contact problem, because nodes of the cable would simply penetrate the nodes of the borehole as the two bodies are initially modelled separately without defined law of interaction via elements. The contact discretisation can be categorised according to:

- Node-to-Surface,
- Surface-to-Surface,
- Node-to-Face,
- Edge-to-Edge.

The first two methods are used by implicit solvers (e.g. AnSYS) and the last two by explicit solvers (e.g. LS-dyna). During the simulation the distance between the two bodies is iteratively determined and if a defined minimum distance is reached, equations of a friction model (see Equation 3.32) are computed. While in the first two methods master and slave nodes need to be defined specifically, no distinction is made between master and slave surfaces in explicit solvers since contact is enforced everywhere. Even though different ideas have been proposed ([Shirakashi and Usui, 1974](#); [Iwata et al., 1984](#); [Eldridge et al., 1991](#); [Sekhon and Chenot, 1993](#); [Wu et al., 1996](#)), friction

is usually modeled based on Coulomb's law assuming that frictional forces  $F_f$  is directly proportional to the normal forces  $F_N$  via the friction coefficient  $\beta$ :

$$F_f = \beta F_N, \quad (3.32)$$

and hence slipping between the two bodies occurs when

$$F_f > \beta F_N, \quad (3.33)$$

and stick conditions are found as soon as

$$F_f \leq \beta F_N. \quad (3.34)$$

The implementation of the numerical model and corresponding numerical solutions will be shown in Chapter 4 where we analyse real data.

## 3.6 Conclusions

After describing the purpose of using numerical approximations to find solutions for PDEs, we briefly presented the theory of the FEM (Section 3.2) with application to the elastic wave equation. Here, the decomposition of the PDE into smaller subdomains is equivalent to discretising the model into smaller elements (Section 3.3), which is the main advantage of FEM since it allows arbitrary geometries and mesh refinement. After having discussed other numerical methods, we concluded that due to irregular and complex geometries evolve in our problems (e.g. streamer, borehole, casing and borehole fluid), FEM is the most suitable numerical method. Then, a typical workflow of FEA has been described, starting from a 1D model, and extending to 3D.

Following, a 3D seismic wave propagation model has been solved in Section 3.4, with the seismic wave expression in fluid-filled boreholes being of main interest. A novel meshing approach has been presented allowing us to reduce the computation time significantly. Here, we proposed a horizontal and azimuthal mesh refinement technique of a 3D model to allow seismic wave propagation from coarse (3 m) to very fine ( $1.4 \cdot 10^4$  m) sized elements. This approach was required because the computational resources were not sufficient for the application of the automatised meshing algorithm of ANSYS. The analytical solutions presented in Chapter 2 have then been compared with the solution of this model. The analytical solutions of vertical and horizontal motion generated by an impinging seismic plane wave in a fluid-filled borehole have been confirmed by the numerical model. Since we can assume that the numerical solution is correct, we can apply variations of this model to compare numerical data with conventional acquired seismic recordings, and data acquired by DAS in the following chapter.

Finally, a numerical model has been presented to predict the exact position of the cable during the survey. While the first model solves for the elastic

### *3 Numerical modelling and simulation*

and acoustic wave equations, this second model analyses resulting displacement for a beam under the action of bending moment, axial force and shear force (Pickhaver, 2006). While the numerical model solving for seismic wave equations described in Section 3.4 assumes the wireline cable to be straight vertical in the borehole, this model tracks the movement of the cable inside the borehole during the deployment technique. The results of this model are presented in the next chapter and compared to real data.

## Applications to real data

### Résumé du chapitre

L'application de modèles numériques précédemment développés à des données réelles est essentielle car l'objectif global du travail est de déterminer quand DAS enregistre des données avec un rapport signal sur bruit élevé. Dans la section 4.1, nous utilisons le modèle numérique développé dans la section 3.4 pour analyser le test de terrain présenté par Hartog et al. (2014) à Bottesford, Royaume-Uni. Nous comparons les données sismiques acquises par DAS et par une vertical seismic imager (VSI) avec les résultats numériques de notre modélisation. La solution numérique nous permet d'interpréter les événements visibles dans les enregistrements DAS de haute qualité lorsque les données de terrain sont acquises dans des conditions parfaites, c'est-à-dire lorsque 2% du câble supplémentaire a été introduit dans le puits. Nous étudions également les différents paramètres du modèle numérique pour comprendre les enregistrements DAS lorsque la qualité des données est plus faible, c'est-à-dire lorsque le câble est entièrement sous tension (ou avec une libération de tension intermédiaire) dans le puits. Ici, ce modèle numérique ne peut pas expliquer complètement le phénomène. Par conséquent, une autre analyse par éléments finis a été utilisée pour suivre le mouvement du câble lors du déploiement dans le puits. Ce modèle numérique a été décrit dans la section 3.5, et les premiers résultats sont présentés dans la section 4.1.2. Ce modèle nous permet également de trouver les conditions, en termes de force de contact, nécessaires pour s'assurer que des données sismiques de bonne qualité seront acquises par DAS. Dans la section 4.2, un autre essai sur le terrain sera présenté, où des données sismiques ont été acquises dans un autre puits à Livingston, Royaume-Uni. La configuration était similaire à la configuration de Bottesford, car l'unité d'enregistrement optique et le câble de détection étaient les mêmes et le trou de forage était vertical malgré de légères différences de dimension. Cet essai sur le terrain a été planifié pour confirmer les observations faites à Bottesford et confirmer que les conditions trouvées grâce aux modèles numériques nous permettent d'obtenir

des données de bonne qualité.

## 4.1 Introduction

The application of previously developed numerical models to real data is essential, since the overall objective of the PhD is to identify when DAS is recording data with a high SNR. A numerical solution sometimes enables further insights and could eventually give guidance to acquire seismic data using DAS.

In Section 4.2, we use the numerical model developed in Section 3.4 to analyse the field test presented by [Hartog et al. \(2014\)](#) in Bottesford, UK. We compare seismic data acquired by DAS and a versatile seismic imager (VSI) and the numerical results of our modelling. The numerical solution allows us to interpret the events visible in the high quality DAS recordings when the field data is acquired in perfect conditions, that is when 2% of additional cable has been lowered down the borehole. We also investigate different settings of the numerical model to understand DAS recordings when the data quality is lower, that is when the cable is fully under tension (or with intermediate tension release) in the borehole. Here, this numerical model cannot completely explain the phenomenon. Therefore, another finite element analysis (FEA) has been used to track the movement of the cable during wireline deployment. This numerical model has been described in Section 3.5, and first results are shown in Section 4.2.2. This model also allows us to find the conditions, in terms of the contact force, that are required in order to assure that data with good quality will be acquired by DAS. In Section 4.3 another field trial will be presented, where seismic data have been acquired in Livingston. The set-up was similar to the set-up in Bottesford because both the optical recording unit and the sensing cable were the same, and the borehole was straight vertical despite minor differences in dimension. This field test has been planned to confirm observations made in Bottesford and support our preliminary conclusions.

## 4.2 Real data application I - Bottesford

A field trial using DAS technology on wireline cable (Section 1.4.2) has been carried out by [Hartog et al. \(2014\)](#) in Bottesford, UK. It was the very first field trial using this acquisition setup and the test took place in 2013. Bottesford is a training test site in the north of England, near Nottingham (Figure 4.1). The borehole spans a length of 600 m, is straight vertical and has an inner diameter of 26 cm. The seismic source used to generate vibrations was a seismic airgun located in a portable airgun tank ([Clark and Mackie, 2013](#)) located a few meters away from the wellbore and is therefore considered to be zero-offset. In contrast to commonly used vibration trucks, the airgun

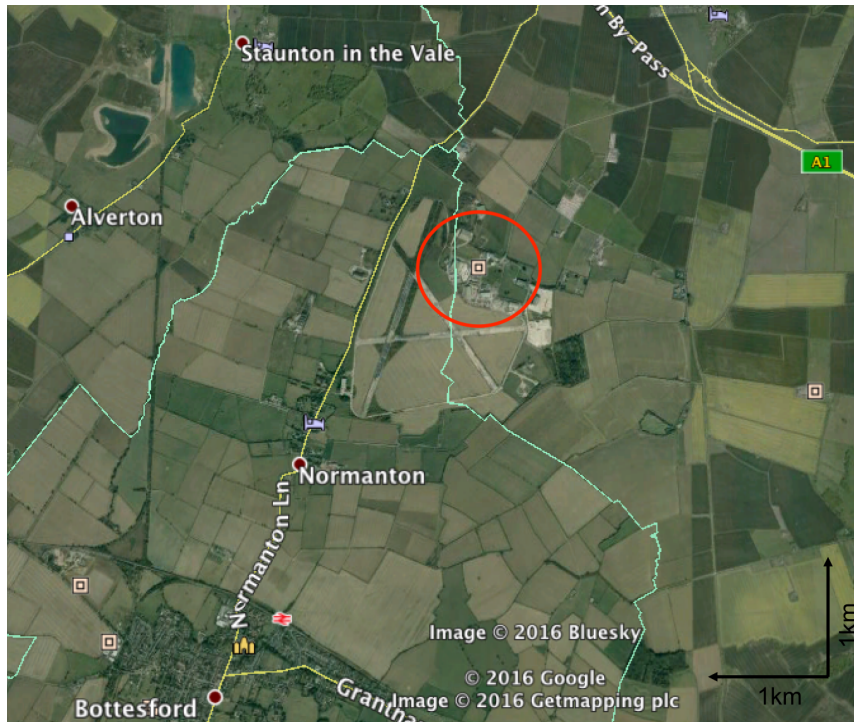


Figure 4.1: The Schlumberger training site near Bottesford indicated within the a red circle.

initiates a short but intense pulse into the subsurface (Sheriff and Geldart, 1995). The numerical model that has been used to compare DAS and VSI data was presented in Section 3.4, where the numerical model was shown in Figure 3.12. The borehole consists of the casing, the borehole fluid and the cable located in the center of the fluid as seen in Figure 3.13. All material properties and seismic velocities have been shown in Table 3.1 and 3.2, respectively.

#### 4.2.1 Analysis of recorded seismic waves using DAS, VSI and numerical data

The differences between the two measurement systems, DAS and VSI, have been reviewed in Section 1.5.1. The results of the VSI and DAS and the numerical solution are presented in Figure 4.2. The vertical axis represents depth in meters, while the horizontal axis is the recording time in milliseconds.

To record conventional seismic data, a VSI was lowered into borehole (Arroyo et al., 2003). The VSI carries three orthogonally oriented accelerometers in an acoustically isolated sensor package, which, once at the required depth, is physically clamped to the borehole to ensure good coupling. We only show the results of the vertically oriented accelerometer, to be able to compare the

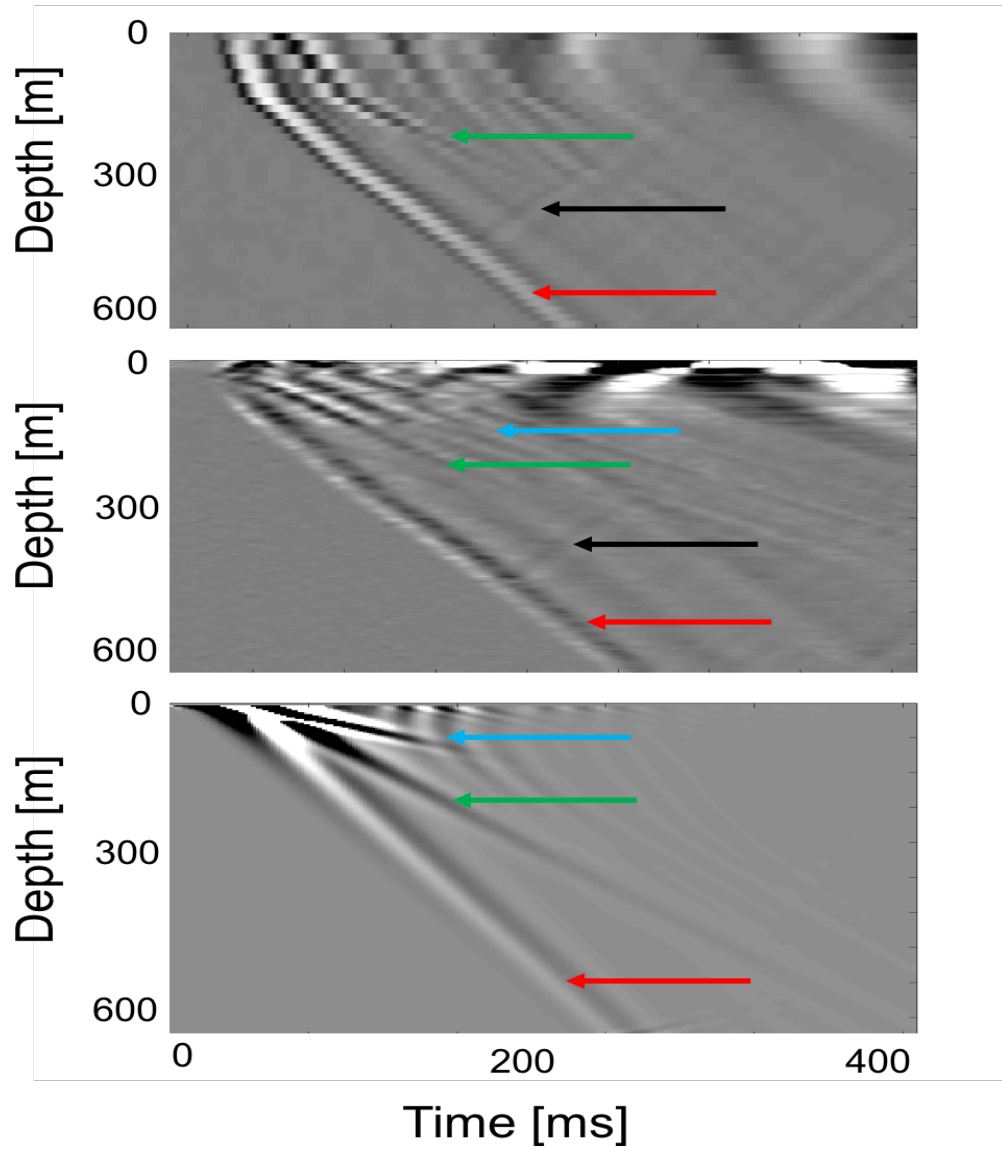


Figure 4.2: Comparison of VSI data (top panel), DAS data (middle panel) and numerical results (lower panel) of the field test in Bottesford. The arrows indicate different wave modes. Arrows in red are point to P-wave first arrivals, green ones to S-waves, black arrows to reflections and blue ones to tube waves.

output with the axial strain sensed by DAS. The tool is then re-positioned at predetermined spatial increments down the borehole in order to provide full well coverage. The VSI toolstring consisted of four levels (i.e. four acoustically isolated sensor packages each containing three orthogonally oriented accelerometers) separated by 15 m and so a single position of the short VSI array used in the field experiment covered a span of only 60 m. In order to provide full well coverage the toolstring had to be re-positioned 9 times. A linear stack for five seismic shots per position is shown in the upper panel of Figure 4.2. The P-wave arrival (red arrow) is detectable throughout the entire well, while also shear waves (green arrow) are visible. Furthermore, some reflections (black arrow) could be recorded.

DAS measurements are shown in the middle panel of Figure 4.2. The gauge length  $\Delta t$  in Equation 1.14 (Section 1.3) has been set to a value to obtain a spatial resolution of 10 m. To record this dataset with a high SNR, additional cable had to be lowered down the borehole as it will be described later in Figure 4.3. Maximum tension release of the cable was obtained after lowering 2% of extra cable down the borehole. Then, 12 seismic shots have been triggered and the results were summed. P-wave arrivals, reflections and shear waves as seen in the VSI plot are also visible in the DAS dataset. Furthermore, in contrast to VSI recordings, Rayleigh and tube waves (blue arrow) are visible in the upper part of the borehole. Note that the accelerometer of the VSI is clamped to the borehole wall. Galperin (1974) observed that the amplitude of tube waves decreases "as the force of clamping the probe to the borehole wall increased". Balch and Lee (1984) showed that the vertical motion of the surrounding solid generated by the tube wave is negligible compared to the boundary wave and Cheng and Toksöz (1984) derived that the ratio of radial displacement to axial displacement of highest at the borehole wall. In addition, Hardage (1983) found that axial displacement at the fluid-structure interface drops by a factor of 100 or more for tube waves with frequencies of 80 Hz or lower.

Numerical results are shown in the lower panel of Figure 4.2. The receiver spacing of the numerical data shown here is 1 m, even though the numerical model was obtained with sampling points every 0.01 m (Section 3.4.1). The numerical model described in Section 3.4 is used here to confirm and interpret real data observations. The numerical results present the same P- and S-wave arrivals as recorded by the VSI and DAS. Furthermore, also tube waves are visible which are recorded by DAS, but absent in VSI recordings. Seismic reflections are not seen in the numerical solution because we simulated a single homogeneous layer. Simulating heterogeneous media will be subject to further research.

Despite a few differences, VSI and DAS recordings are fairly similar. Most of the seismic events have also been observed in numerical data. Considering that DAS has a much cheaper installation cost, and full well coverage is

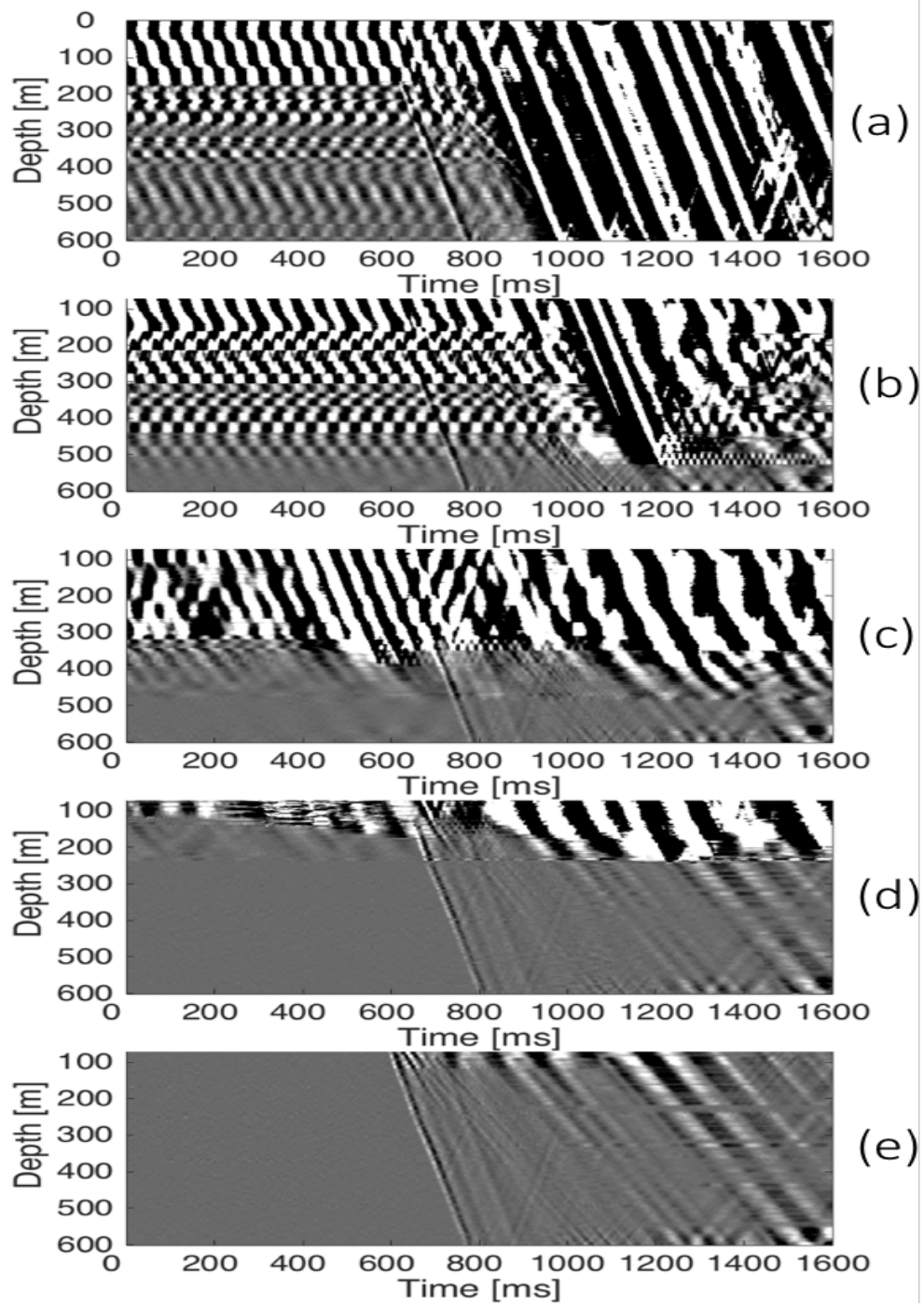


Figure 4.3: Recorded signal by the DAS system with increasing tension release (after [Hartog et al. \(2014\)](#)). From top to bottom: 0.0%, 0.5%, 1.0%, 1.5% and 2.0% of additional cable lowered down the borehole.

provided from the very first shot compared to a VSI survey, DAS seems to be the better solution. However, it was only possible to acquire such data when more cable was lowered into the borehole. Hartog et al. (2014) have found that for the given set-up, 2% of additional cable length needed to be lowered down the borehole in order to produce the results presented in Figure 4.2. Figure 4.3 shows DAS data when different lengths of wireline cable are lowered down the borehole. In Figure 4.3 (a) the wireline cable is held under tension in the borehole. In (b) 0.5%, equivalent to 3 m, of extra cable were lowered down the borehole. In (c) 1.0%, or 6 m, in (d) 1.5%, or 9 m, and in (e) 2.0%, or 12 m, of additional cable were lowered down the borehole. After each stage of cable slack, 12 seismic shots were triggered and the results in Figure 4.3 show the linear stack of each of those settings. In (a) the cable is located in the approximate center in the borehole and is free to move laterally in the fluid column. We can observe that DAS records high amplitude, and harmonic noise. This noise superimposes any signal of interest (i.e. P- and S-wave arrivals). As more cable is lowered down the borehole (b) – (d), we acquire data with an increase in signal-to-noise ratio (SNR) starting from the bottom of the well. In the last setting (e), where 12 m of additional cable has been lowered down the borehole, the first break is detectable throughout the entire well. In this scenario, the DAS cable is considered to be *perfectly coupled* and tracks the motion of the incident wavefield accurately. We would expect that lowering more cable down the borehole changed the position of the cable inside the borehole in some way, so that higher data quality is obtained. We attempt to simulate this scenario by changing the position of the cable in our numerical model (Figure 3.13). Therefore, the cable is moved closer to the casing. Three scenarios are presented in Figure 4.4. In the top part, a depth slice of the numerical model and the cable position are shown, while the bottom plots show the numerical solution. In the left panel, the cable is located in the center of the borehole 15 cm away from the casing. In the middle panel, the distance between the cable and casing is reduced to 11.8 cm, while results presented in the right panel show the configuration when the cable is only 3.8 cm away from the casing. The vertical component of particle velocity as it would be recorded by the cable is shown in the middle panels of Figure 4.4, while the corresponding horizontal component is presented in the lower panels. In all cases the difference is only marginal, in particular not as significant as observed in real data (Figure 4.3). We also changed the in-line position of the cable w.r.t. the source, changed the elastic properties of the casing to amplify fluid velocities (Schoenberg, 1987) and modified the mesh size. All these approaches did not change the recorded signal significantly.

However, in the numerical model there are a few differences w.r.t. the recorded real data that we did not account for: modes such as cultural noise can be initiated on the surface and sensed by the cable while the numerical simulations assume perfectly silent conditions. In addition, the cross-section of the modelled cable is assumed to be constant, while various coatings, and

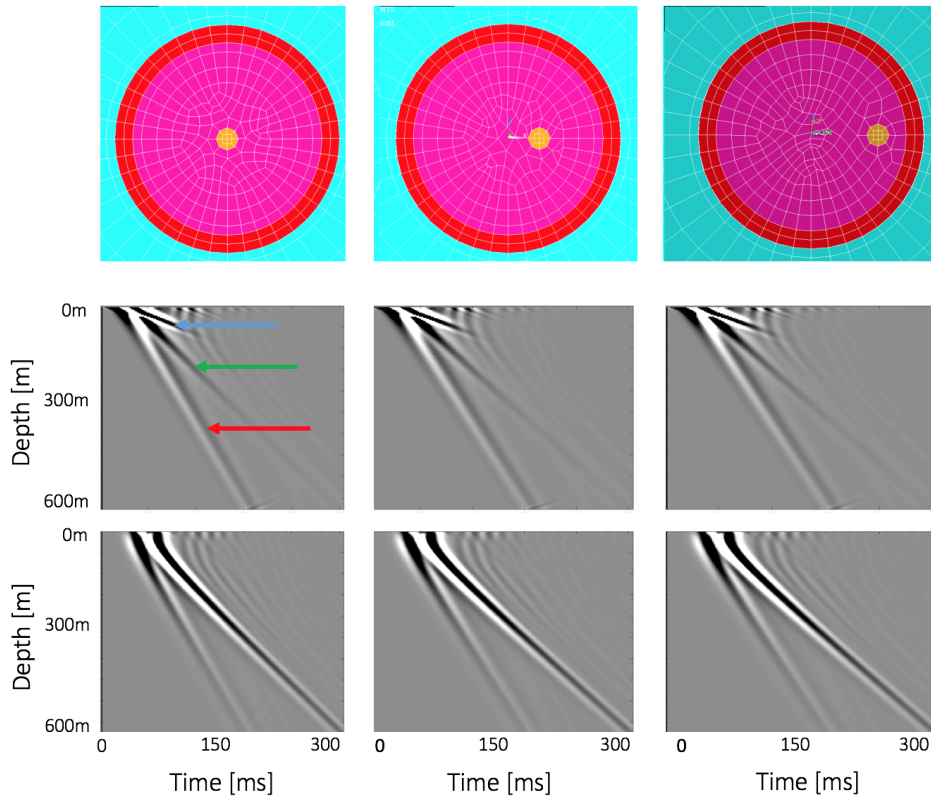


Figure 4.4: Numerical analysis when the position of the cable in the borehole is altered. Top: slices of the mesh used in the numerical modeling with the DAS cable represented in yellow, the fluid in pink, the casing in red and the formation in turquoise; middle: numerical solution of the vertical component of particle velocity as detected by the cable; bottom: numerical solution of the horizontal component of particle velocity as detected by the cable. The tube wave arrival is indicated with a blue arrow, S-wave with a green arrow and P-wave with a red arrow.

cable reinforcement layer of the original cable damp acoustic signals. And more importantly, the cable in the numerical simulation is always held in a straight position, fixed in the well and therefore the cable perfectly records the particle velocity of the borehole fluid, while the DAS cable is floating loosely in the fluid column. It appears, however, that conditions of perfect coupling are found when more cable (in this real data example 12 m) is lowered down the borehole. In order to better understand how the cable is moving during multiple stages of cable slack of the wireline cable, the model of next section will be used to model the precise movement of the cable within the borehole.

Object	Material Property	Value	Unit
Heptacable	$\rho$ Density	4451	kg/m <sup>3</sup>
	$E$ Young's Modulus	$1.83 \cdot 10^{11}$	kg/(m · s <sup>2</sup> )
	$\nu$ Poisson's ratio	0.33	dimensionless

Table 4.1: Material properties of the heptacable (Figure 3.23).

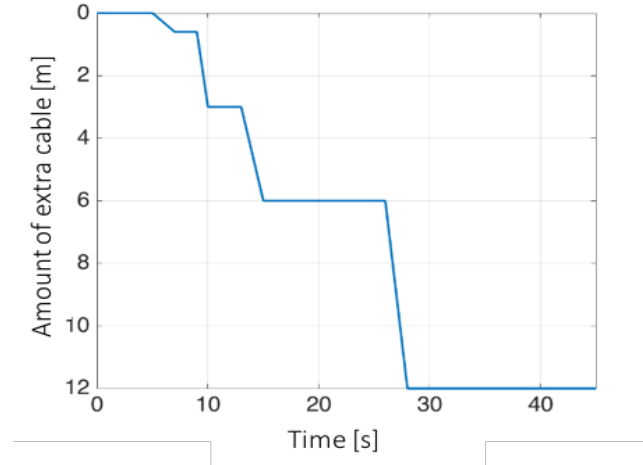


Figure 4.5: Amount of extra cable that has been lowered in the borehole. Equivalently to the real survey, we lower a total of 12 m of extra cable down the numerical model of the borehole in stages to analyse the new positions of the cable in the borehole. The time in seconds corresponds to the simulation time.

### 4.2.2 Cable coupling

In order to track the precise position of the cable during wireline deployment, the numerical model presented in Section 3.5 will be used. Here, instead of the extensive model solving for wave equations that has been used in the previous section, only the borehole wall has been modeled using rigid elements, and a beam formulations has been used to model the heptacable (Figure 3.22). The dimensions of the borehole are identical to the parameters of the field test, i.e. 600 m in depth with an inner diameter of 26 cm. The elastic properties of the cable correspond to the heptacable (Figure 3.23) and are listed in Table 4.1. The length of the cable is slightly more than 600 m, because we will lower more cable down the borehole over time. The amount of extra cable corresponds to the exact amount that has been used during the survey described through Figure 4.3. Approximately 615 m of cable are modelled to lower the additional amount of 12 m of cable down the well.

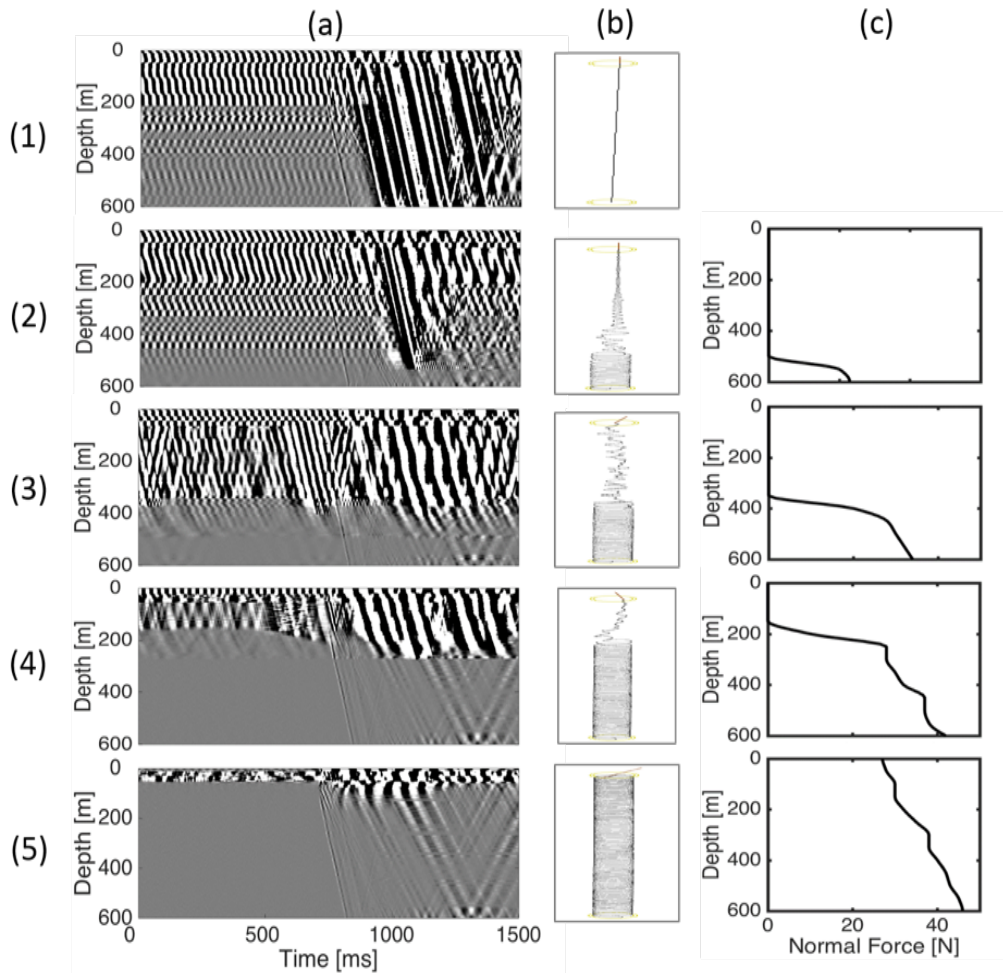


Figure 4.6: DAS data recorded with increasing tension release (a) and corresponding numerical results (b and c). From top to bottom: (1) cable under full tension; (2) cable with minimal tension release; (3) cable with 0.5%, (4) 1.0% and (5) 2.0% of extra cable being lowered down the borehole. Numerical results in (b) illustrate the motion of the cable during this procedure. Results in (c) represent the contact forces between the cable and borehole wall numerically evaluated for each stage of cable slack along the well depth.

### Numerical results of cable movement

The cable movement with increasing tension release is numerically evaluated in Figure 4.6 (b) while corresponding DAS data acquired by Hartog et al. (2014) are shown in Figure 4.6 (a). In our numerical model we lower more cable down the borehole over time as described in Figure 4.5. After each stage of cable slack, we take a snapshot of the cable position as seen in plots in row (1). Figure 4.6 (b,1) is a snapshot of the numerical model, that has been taken when the cable was under full tension. The borehole wall of the numerical model has been omitted, so that only the cable is visible. Figure 4.6 (b,2) shows a snapshot of the numerical simulation when 1 m of extra cable, equivalent to 0.1% total cable length, was lowered down the well. Similarly, (b,3) is a snapshot taken at 0.5% cable slack, (b,4) at 1.0% and (b,5) shows a snapshot that has been taken when 2.0% of additional cable has been lowered down the borehole. The numerical simulation shows that lowering more cable down the borehole evolves in a helix starting from the bottom of the well. After lowering 12 m of cable down the well, equivalent to 2.0% of cable length, the helical bending reached the top of the well. When the cable reaches the stable position with the helical shape, we assume that the cable is in immediate contact with the borehole wall. This study reveals that a direct cable-casing contact for DAS recordings is required to record high data quality, because a high SNR is recorded only when contact occurs. Then, DAS is recording only white noise prior to any seismic arrival, and the detection of first break is straightforward. When lowering the maximum amount of cable down the borehole (in this case 12 m), consequently the first break is detectable throughout the entire well length.

An additional parameter to validate the hypothesis that the cable and the casing are in contact is to determine contact forces between the two media. Furthermore, quantifying contact forces will allow us to determine the amount of force that is required such that the cable reaches equilibrium conditions and is considered perfectly coupled. The contact forces are directly computed in the numerical solution and in this scenario, they are normal (reaction) forces of the borehole wall, which are identical in magnitude but opposite in direction than normal forces exerted by the cable equivalent to Newton's third law of motion. For each stage of cable slack the contact force is evaluated along the entire cable length. The results are shown in Figure 4.6 (c). Here, zero contact forces are measured when the cable was under tension. First contact forces were recorded after 0.1% of cable slack from around 500 m to the end of the borehole (i.e. 600 m). This depth roughly corresponds to the depth to which the cable coiled up in form of a helix and the SNR of DAS recordings increased. When the first break is detectable throughout the entire well and the helical bending of the cable reached the wellhead, contact forces were detected along the entire well length. Furthermore, 20 N of normal force are necessary, so that the cable can overcome slipping conditions (Equation 3.34), and stick to the formation, thus being in equilibrium



Figure 4.7: The training site for the second test was located in Livingston near Edinburgh.

conditions and considered perfectly coupled.

Note that the amount of contact force depends on the dimension of the cable and the borehole, their elastic properties, and the friction coefficient. Note also that when more cable has been lowered down the borehole, higher contact forces are measured in the lower part of the borehole due to the additional weight of the cable, but this did not alter the recorded signal quality of the DAS system.

## 4.3 Real data application II - Livingston

### 4.3.1 Cable coupling

The field test in Bottesford in 2013 was the first trial where seismic data have been acquired using a DAS system, with multiple stages of tension release of the wireline cable. In 2016, we made an additional test, in a different well and in a different environment, with the aim to reproduce observations made in the first field test three years before and to validate numerical results. This second field trial has taken place at a Schlumberger training site in Livingston near Edinburgh (Figure 4.7). The length of the borehole was 240 m with an inner diameter of 33 cm from 0-100 m and a narrower section of 22 cm from 100-240 m depth (Figure 4.8). The seismic source was an airgun located in a water-filled tank approximately 100 m away from the well. The recording unit and the sensing cable were the same that have been used in Bottesford. Also processing of DAS data was similar, where a gauge length has been chosen such that a spatial resolution of 10 m was obtained.



Figure 4.8: The set-up of the field test in Livingston. The DAS cable is lowered down the borehole from a winch visible in the background of the image.

### Numerical results of cable movement

The numerical model of the borehole and the cable is shown in Figure 4.9. Equivalent to the results presented in the previous section of the field test in Bottesford, shown in Figure 4.6, the results of both DAS and numerical data of the field test in Livingston are shown in Figure 4.10. In contrast to the field test in Bottesford, where we used the numerical solution in Figure 4.6 (b) and (c) to confirm observations of real data in Figure 4.6 (a), we used the numerical solution in 4.10 (b) and (c) to predict the helical bending of the cable, such that we could plan the field test to acquire data shown in 4.10 (a). Hence, while for the Bottesford dataset, numerical simulations were used to explain real data, numerical solutions for the Livingston test are now used to design the field test. We decided to produce DAS data over four stages of cable slack. The most convenient way was to lower 0.1%, 0.5%, 1.0%, and finally 2.0% of additional cable down the borehole. Those numbers correspond to 0.48 m, 1.2 m, 2.4 m and 4.8 m of actual cable length. After each stage of cable slack, snapshots have been taken to analyse the position of the cable in Figure 4.10 (b). Similar to the field test in Bottesford, we observe that helical bending starts from the bottom of the borehole and that after 2.0% of addition cable being lowered down the borehole, the helix reached the wellhead. Furthermore, we also derived the contact forces of the numerical solutions along the well and obtained similar results to the previous field test. Note that the contact forces differ slightly because the dimension (length and diameter) of the borehole differ. However, around 20 N of contact force were again required for the cable to be coupled to the casing and remain in equilibrium conditions. The obtained numerical results were then used to acquire seismic data using DAS. After each stage of cable slack, 8 seismic shots have been triggered and DAS data has been stacked. The results of the linear stacks are shown in Figure 4.10 (a). Similar to the field test in Bottesford, the conclusion ties in with observations made previously. The DAS system records high data quality as soon as the cable is in immediate contact with the borehole wall. Coupling is poor when the cable is loosely floating in the fluid column and, consequently, records high amplitude and harmonic noise events. Full well coverage is obtained when a contact force of about 20 N or more are measured along the entire well length. At this point, the cable is considered to be well coupled. Note that the horizontal stripes in DAS data is a type of noise related to optical fading (Healey, 1984), that commonly occurs in DAS systems.

## 4.4 Conclusions

The comparison of numerical simulations with real data have enabled us to give answers to the research objectives of the PhD thesis. In the first part of this chapter, the seismic wave propagation model described in Section 3.4 allowed us to analyse seismic waves in fluid filled boreholes created by an

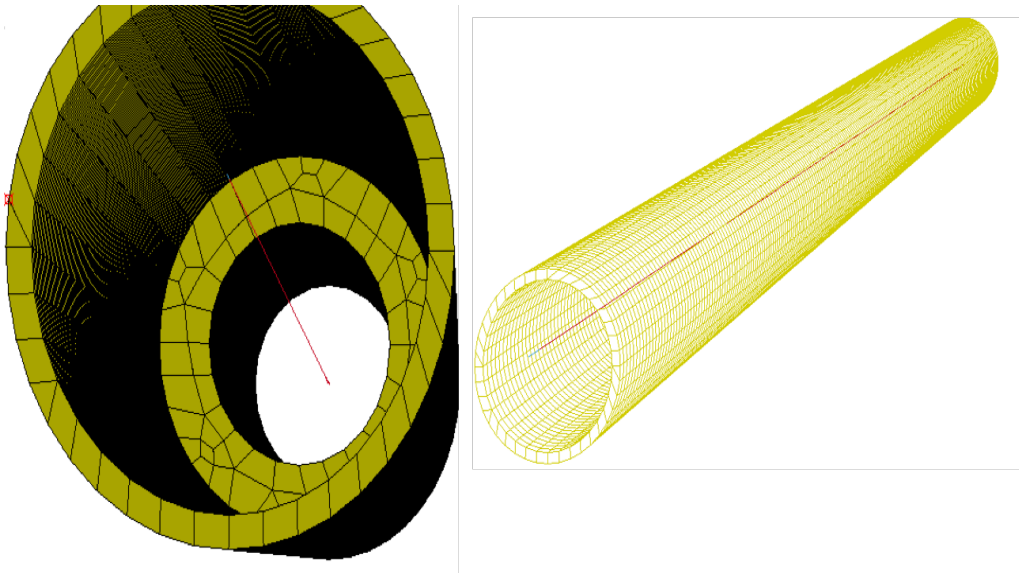


Figure 4.9: The numerical model that is used to analyse the movement and position of the cable during the DAS survey in Livingston. The borehole wall is in yellow, while the DAS cable is in red. A topview is shown on the left where the varying inner diameter of the borehole can be observed, and a side-view is given on the right.

impinging elastic wavefield. Numerical results were similar to conventional acquired seismic data using the VSI (Arroyo et al., 2003), as well as DAS data when maximum tension of the wireline cable has been released. In this scenario, the DAS cable was considered well coupled. However, when the DAS cable was fully under tension, or only a small amount of additional cable was lowered down the borehole, the DAS data quality was poor, and the employed numerical model could not explain observations made in real data. We would expect that lowering more cable down the borehole would alter the position of the cable in the borehole in some way, but altering the cable position in the numerical model did not change the recorded signal as significantly as it happens in real data. The numerical model did not account for cultural noise, assumed a constant cross-section of the cable, and most importantly, the cable in the numerical model was held in a straight vertical, and fixed position inside the well. Then, the cable is sensing the particle velocity of the borehole fluid perfectly. Under real scenarios, however, the cable is floating loosely in the fluid column.

Therefore, another numerical model, described in Section 3.5, was used to track the precise movement and position of the cable and to better analyse its coupling with the borehole wall. Instead of solving for wave equations, the intention of this numerical model was to monitor the displacement and bending moments of the cable when lowering more cable down the borehole.

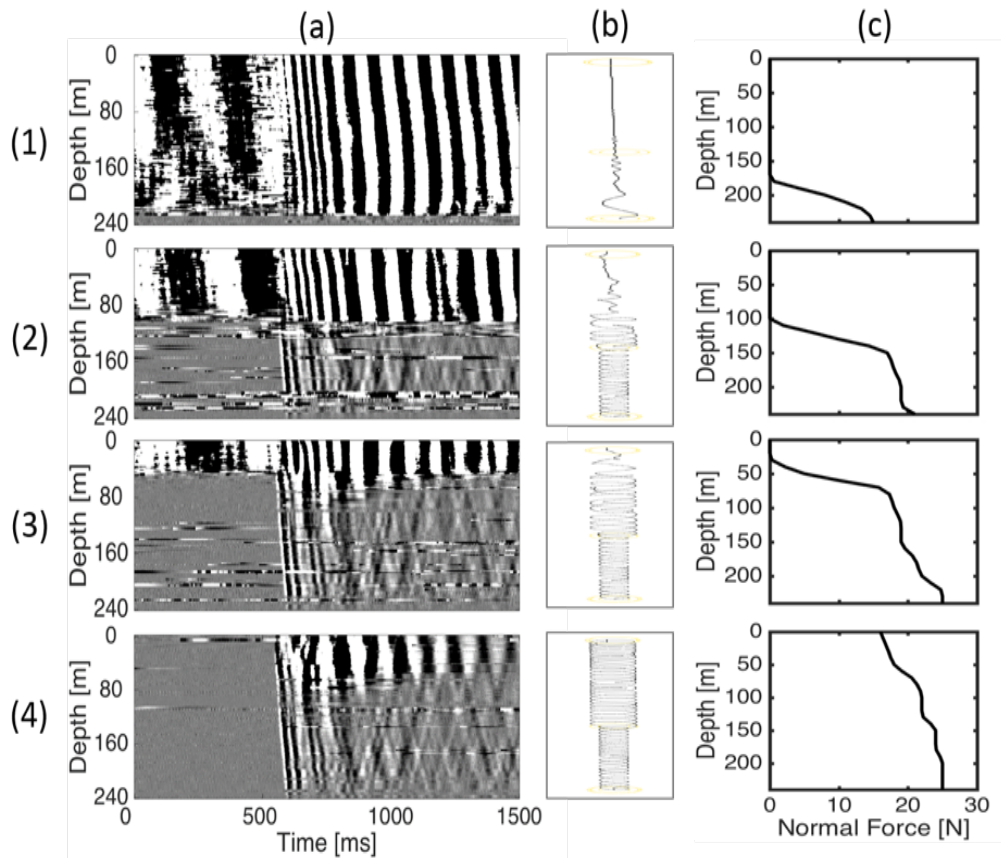


Figure 4.10: The same analysis as shown in Figure 4.6 for a second field trial conducted in March 2016 in Livingston, UK. From top to bottom: (1) corresponds to minimal tension release, (2) 0.5% (3) 1.0% and (4) 2.0% of cable slack. In (a) seismic data acquired by the DAS system are shown. Numerical results are presented in (b) and (c), where in (b) the position of the cable is shown after each stage of cable slack and in (c) the corresponding contact force is plotted along the entire borehole length.

The results of this simulation allowed us to conclude that a direct cable-casing contact of the DAS cable is required to record high data quality. The depth to which the cable coiled up in a helical shape and found a stable position, corresponded to the depth to which the DAS system could record data with a high SNR. This hypothesis has been supported by measuring the contact forces along the entire well. Furthermore, the quantification of contact forces allowed us to conclude that the cable stops slipping and sticks to the borehole wall as soon as contact forces of approximately 20 N or higher were found. Therefore, the contact force also allows us to confirm whether coupling conditions are satisfied (note that this number depends on the dimension of the cable and borehole, their elastic properties and the friction coefficient: those quantities were similar in both field tests). This numerical model was used to tie in DAS data acquisitions made in 2013. Another field trial has been carried out to confirm those observations in 2016. Even though the dimension of the well and the environment were different, the observations were similar. High quality data could be acquired as soon as the cable was in contact with the borehole wall and found equilibrium conditions.

We can therefore conclude that DAS is considered poorly coupled if the DAS cable is not in immediate contact with the borehole during VSP surveys on wireline cable. The cable is considered well coupled when the cable is in contact with the borehole wall and in equilibrium conditions. These conditions are reached when approximately 20 N of contact force are created, and thus the cable stopped slipping and sticks to the borehole wall (Equation 3.34).



## Optimising coupling using DAS

### Résumé du chapitre

Au chapitre 4, nous avons observé qu'un contact direct du câble avec la paroi du puits est nécessaire pour enregistrer les données sismiques avec un rapport signal sur bruit raisonnable en utilisant DAS. En sachant que les paramètres qui pourraient impliquer le couplage sont: la force de contact, les propriétés élastiques et les dimensions du câble et le milieu auquel le câble est couplé, nous analysons, dans ce chapitre, comment optimiser le couplage du câble avec la paroi du puits. Dans la section 5.1, nous analysons le couplage entre le câble et la paroi du puits en termes de forces de contact, tandis que dans la section 5.2, nous analysons le couplage en termes de propriétés élastiques. Les deux analyses sont basées sur le même modèle numérique, qui est présenté dans la première partie de la section 5.1 et qui consiste en modifications du modèle décrit dans la section 3.4. On montrera que l'augmentation de la force de contact et l'étalonnage des propriétés élastiques du câble modifient la sensibilité du câble pour détecter les ondes sismiques. De plus, nous avons observé dans des données réelles que le système DAS enregistre une grande amplitude et un bruit harmonique avant la première arrivée lorsque le câble n'est pas bien couplé. Ces enregistrements sont également visibles sans que des sources sismiques ne soient déclenchées auparavant. Par conséquent, dans la section 5.3, nous proposons un algorithme de détection de ces signaux caractéristiques afin d'assurer un câble DAS bien couplé avant le début de l'acquisition.

### 5.1 Introduction

In Chapter 4 we observed that a direct contact of the cable with the borehole wall is required to record seismic data with a reasonable SNR using DAS. From Equation 2.55 we know that the parameters that might influence coupling are: the contact force, the elastic properties and the dimensions of the

cable and the medium to which the cable is coupled to. In this chapter we analyse how to optimise the coupling of the cable with the borehole wall.

In Section 5.2 we analyse the coupling between the cable and the borehole wall in terms of contact forces, while in Section 5.3 we analyse the coupling in terms of cable elastic properties. Both analyses are based on the same numerical model, which is presented in the first part of Section 5.2 and which consists of modifications of the model described in Section 3.4. It will be shown that increasing the contact force and making a calibration of cable elastic properties alters the sensitivity of the cable to detect seismic waves.

Moreover, we observed in real data that the DAS system records high amplitude, and harmonic noise before the first arrival when the cable is not well coupled. These recordings are also visible without any seismic source being triggered beforehand. Therefore, in Section 5.4, we propose a feature detection algorithm in order to ensure a well coupled DAS cable before the start of the survey.

## 5.2 Contact forces

In Section 4.2 and 4.3 we have seen that the amount of contact force determines the ability of the DAS cable to maintain equilibrium conditions and to record a high SNR. The heptacable, that has been used for the field data survey and therefore also for the numerical modelling, required a contact force of approximately 20 N to be well coupled to the borehole wall. This number can change depending on the elastic properties and the dimensions of the cable and of the borehole. In this section we are using numerical simulations to analyse the coupling of the heptacable with the borehole wall in terms of the contact force between the two media. The technological method proposed by Munn et al. (2017), and discussed in Section 1, uses a borehole liner that can be used to press the cable against the borehole wall. Since their instrument is capable to control the force that is exerted on the cable, their method would allow to make similar tests under real-case scenarios.

### 5.2.1 Numerical analysis

The numerical model used to analyse the influence of the contact force is shown in Figure 5.1. The hollow cylinder shown in the upper panel represents the borehole and some outer formation. In the lower panel, another cylindrical body is modelled inside the borehole, representing the cable. Since deformations of the cable are of interest, the cable is modelled using elastic elements to compute for multidirectional strains instead of using beam formulations as in the previous chapter and discretised with elements as small as 1 mm. A lateral force (indicated in white in Figure 5.1) is applied to all

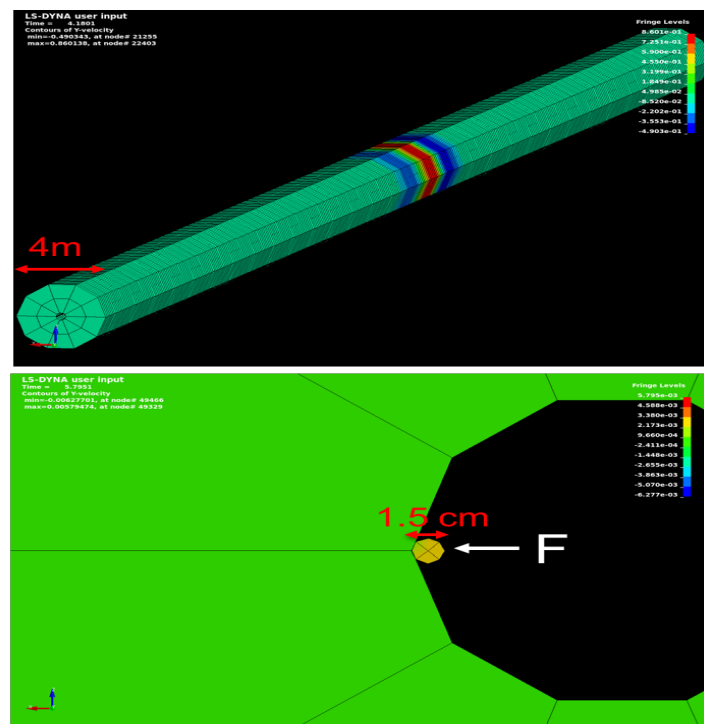


Figure 5.1: The numerical model used to analyse the sensitivity of the cable to seismic waves. The upper panel shows the borehole wall including some outer formation. The lower panel is a zoom of the hollow part of the borehole, where the cable is shown in yellow.

cable nodes to press the cable against the borehole wall, similar to the borehole liner presented in [Munn et al. \(2017\)](#). An application of 20 N of constant lateral force corresponds to the case when the cable is well coupled to the borehole wall and in equilibrium condition as derived in Section 4.2 and 4.3, when we used numerical methods to track the cable movement during the field tests in Bottesford and Livingston, respectively. We will use the numerical model shown in Figure 5.1 to analyse the influence of increasing contact force from 5 N to 120 N, while we only present the main results. The static friction coefficient  $\beta_s$ , presented in Section 3.5 in Chapter 3, is set to an intermediate value of 0.6, while kinetic friction  $\beta_k$  is 0.5. During the numerical experiment, it has been observed that a sudden temporal increase in the lateral force causes a lot of distortion and damage to the cable, therefore the applied lateral force is gradually increasing. As soon as the cable is in equilibrium conditions, a directional point source,  $v_y(t) = s(t)$ , in form of a Ricker wavelet of 40 Hz central frequency (Equation 3.26) is applied to the group of nodes located at the top of the borehole. The horizontal components of particle velocity of the borehole have been constrained to create plane-wave propagation in vertical direction because in zero-offset surveys (i) the vertical component of particle velocity is the most dominant ([Schoenberg, 1986](#)) (ii) and we are primarily interested in vertical displacement since DAS is sensitive to axial strain. Furthermore, (iii) 3D wave propagation would lead to a significant amount of artificial reflections or (iv) would require an extensive use of PML, thus driving computation cost unnecessarily.

The seismic signals registered by the borehole wall and by the cable at a depth of 150 m are shown in Figure 5.2. The seismic signal detected by the borehole wall is shown in blue, and the signal detected by the cable is in red. The results are numerical experiments when we increased the lateral force that is used to press the cable against the borehole wall. In Figure 5.2 (a) this lateral force was 10 N, in (b) 15 N, in (c) 20 N, in (d) 40 N and in (e) 80 N. The signal as detected by the cable and as detected by the borehole wall is neither matching in amplitude nor in phase, when the lateral force is only 10 N in Figure 5.2 (a). The same observation applies to the case when the lateral force is 15 N shown in (b), where the recorded signal by the cable is lower in amplitude and is shifted in phase. With a lateral force of 20 N, the two waves are more in-phase in (c), although the difference in amplitudes is still large. Doubling the lateral force to 40 N in (d) does not seem to improve the match significantly, and similar observations were made in (e), when the lateral force was 80 N. In general, increasing the contact force did not minimise the differences in recorded signal significantly, and even in the unrealistic case of 120 N of lateral force (not shown here), the seismic signal as recorded by the cable is still barely matches the signal as recorded at the borehole wall. Therefore, the alternative solution to minimise the difference in acquired signal is to analyse the two other variables defined in the mechanics of surface contact (Equation 2.55): geometry and elastic properties.

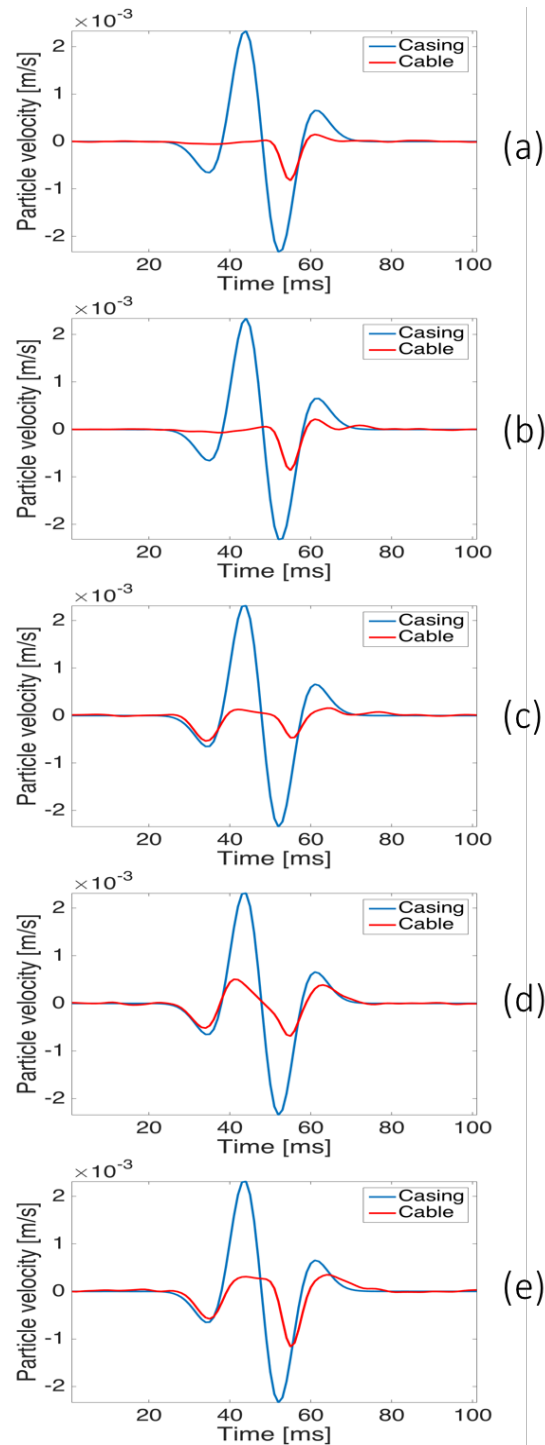


Figure 5.2: Seismic signals with increasing contact force. Blue is the particle velocity as detected by the borehole wall (reference) and red is the particle velocity as detected by the cable at the same position in depth. Shown are signals with increasing contact force, where the lateral force in (a) is 10 N, in (b) 15 N, in (c) 20 N, in (d) 40 N and in (e) 80 N.

## 5.3 Elastic properties

The borehole geometry cannot be arbitrarily changed once it has been drilled. However, cable dimensions and elastic properties can be modified by producing cables with different thickness, Young's modulus, density and/or Poisson's ratio. Changing the elastic properties of a cable, does, in general, change the resistance of the cable to deform elastically. A high Young's modulus leads to stiff cables, while a high density increases the overall weight. Modifying those parameters can potentially minimise the difference between the seismic signal as detected at the borehole wall and as detected by the cable.

### 5.3.1 Numerical analysis

Object	Material Property	Value	Unit
Rubber	$\rho$ Density	1100	kg/m <sup>3</sup>
	$\nu$ Poisson's ratio	0.45	dimensionless
	$E$ Young's Modulus	$1.5 \cdot 10^6$	kg/(m · s <sup>2</sup> )
PVC	$\rho$ Density	1220	kg/m <sup>3</sup>
	$\nu$ Poisson's ratio	0.40	dimensionless
	$E$ Young's Modulus	$1.63 \cdot 10^9$	kg/(m · s <sup>2</sup> )
Heptacable	$\rho$ Density	4451	kg/m <sup>3</sup>
	$\nu$ Poisson's ratio	0.25	dimensionless
	$E$ Young's Modulus	$1.83 \cdot 10^{11}$	kg/(m · s <sup>2</sup> )

Table 5.1: Material elastic properties of numerical cable configurations used to analysis the cable sensitivity during a borehole seismic survey.

The code for the model in Section 5.2 has been written in Ansys Parametric Design Language (APDL) in a automatised and repetitive way (and to enable a smooth knowledge transfer after this work). The same model can be used to analyse the cable coupling related with its elastic properties, thus making the analysis straightforward because only a few parameters need to be changed. In a first attempt, three possible cable configurations have been analysed that is (1) the heavy and stiff heptacable, (2) a cable composed of PVC material and (3) of light and flexible rubber material. The corresponding elastic properties of these three cables are listed in Table 5.1. To allow a valid comparison, the lateral force is 20 N for all cable models and also the friction coefficients have not been changed and kept to  $\beta_s = 0.6$ , and  $\beta_k = 0.5$ . While increasing the contact force did not influence the recorded signal significantly, the results shown in Figure 5.3 highlight the importance of the cable elastic properties when acquiring seismic data. The response of the heptacable is plotted in the upper panel, while the response of the cable composed of PVC material is shown in the middle, and the response of the cable with elastic properties

similar to rubber is plotted in the lower panel of Figure 5.3. While the signal detected by the heptacable is barely matching with the signal detected at the borehole wall, the difference in acquired signal is minimised using the lighter and more flexible cable composed of PVC material. A nearly perfect match is obtained when using the cable composed of rubber material, being very light and very flexible.

In order to obtain a more quantitative study, we will present results for varying values of Young's modulus and density, while Poisson's ratio has been kept to a constant value of 0.3 since the range of possible ratios is limited and we do not expect a large influence compared to the other two properties. The analysis of these results provides a general trend for cable configurations that are more suitable for DAS acquisitions. Moreover, results can be used to give guidance to the in-house manufacturing center, and therefore can provide a valuable asset when producing the next generation DAS cable. Since amplitude as well as phase variations between the signals recorded by the cable and by the casing have been observed in the first tests, the results of this second test are expressed in terms of root-mean-square error ( $RMS_{error}$ ), peak-to-peak error ( $peak2peak_{error}$ ) and normalised cross-correlation coefficients ( $\hat{\Theta}_{xy}(t)$ ) at zero lag defined in Equations 5.1, 5.2 and 5.3, respectively:

$$RMS_{error} = \sqrt{\frac{1}{n} \sum_{i=1}^n (x_i - y_i)^2}, \quad (5.1)$$

$$peak2peak_{error} = \max(x) - \max(y) \quad (5.2)$$

and

$$\hat{\Theta}_{xy}(t) = \frac{\Theta_{xy}(t)}{\sqrt{\Theta_{xx}(0)\Theta_{yy}(0)}}, \quad (5.3)$$

where  $n$  are the number of time samples,  $x_i$  is the amplitude of the signal sample  $i$  as detected by the cable and  $y_i$  the equivalent recordings at the borehole wall.  $\Theta_{xy}$  is the cross-correlation given as

$$\Theta_{xy}(t) = \int_{-\infty}^{\infty} x(\ell - t)y(\ell)d\ell, \quad (5.4)$$

where  $\ell$  is the timelag and  $\Theta_{xx}$  and  $\Theta_{yy}$  are the autocorrelations of  $x$  and  $y$ , respectively. The autocorrelation is the cross-correlations of a signal with itself and in this case required to normalise the result.  $\Theta_{xx}$  and  $\Theta_{yy}$  are therefore defined as

$$\Theta_{xx}(t) = \int_{-\infty}^{\infty} x(\ell - t)x(\ell)d\ell, \quad (5.5)$$

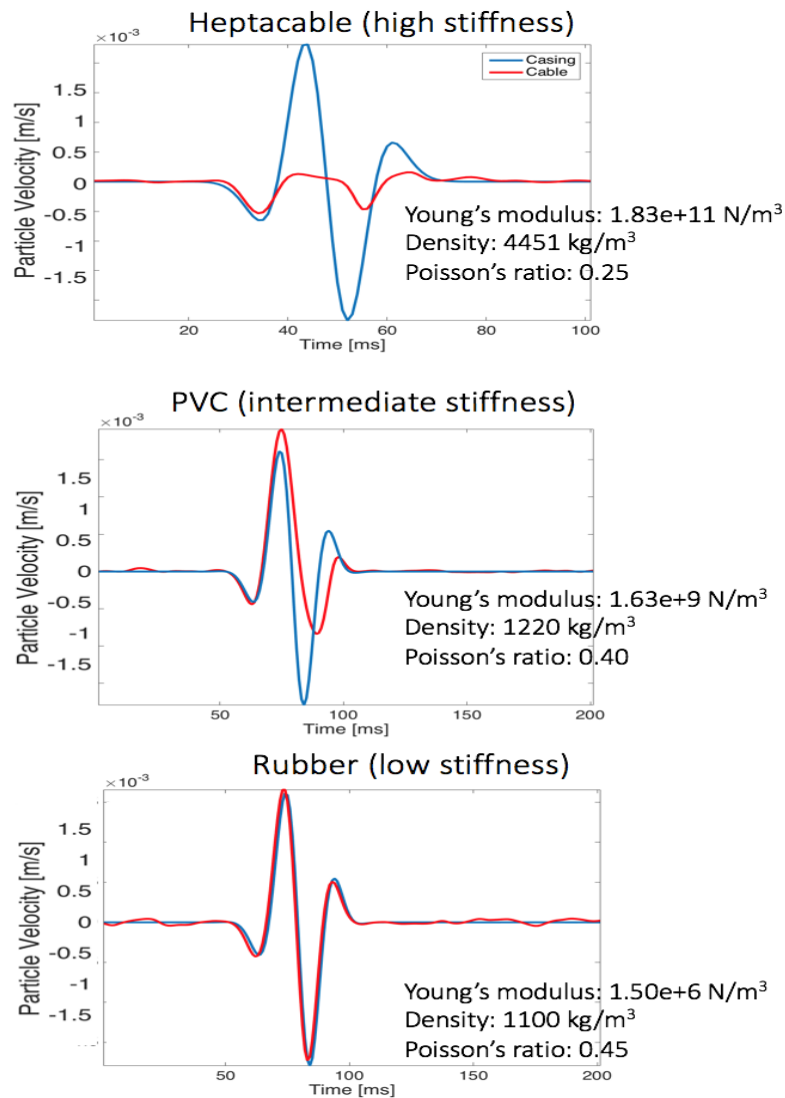


Figure 5.3: Three theoretical cable configurations that are used to detect seismic signals when coupled to the borehole wall. Blue is the particle velocity recorded at the borehole wall (reference) and red is the particle velocity recorded by the cable. The top panel shows the recordings of the heptacable (high stiffness), the middle panel recordings of a cable composed of PVC material (intermediate stiffness) and the bottom panel shows a cable made of rubber (very low stiffness).

and

$$\Theta_{yy}(t) = \int_{-\infty}^{\infty} y(\ell - t)y(\ell)d\ell. \quad (5.6)$$

At zero lag, a value of  $\widehat{\Theta}_{xy}(0)=1$  indicates that the two time series have the exact same shape, while they are completely uncorrelated when  $\widehat{\Theta}_{xy}(0)=0$ . The results of this parametric study are shown in Figure 5.4. The vertical axis shows values of different Young's modulus, while the horizontal axis shows values of different densities. The values of Young's modulus range in  $10^6 - 10^{11} \text{ N/m}^2$ , and the values of density range in  $1000 - 6000 \text{ kg/m}^3$ . The left plot shows the actual error values for 36 different cable configurations, and the right plot represents the same matrices after cubic interpolation (note that an analysis which verify the application of the interpolation by producing a much finer sampling is currently ongoing). Blue indicates a good match in signal recorded at the borehole wall and by the cable while red indicates a poor match. Cable configurations with low density and low stiffness as well as intermediate stiffness and high density tend to follow the vertical movement of the borehole wall accurately. The signal match with cable configurations of very high stiffness is in general poor, but also the sensitivity to seismic waves of cables having a high density and a low stiffness is very low. The heptacable, having a high stiffness and high density falls within the area of low sensitivity. However, a nearly perfect match is detected by decreasing the Young's modulus by only two orders of magnitude ( $10^9 \text{ N/m}^2$ ) while keeping the density identical ( $5000 \text{ kg/m}^3$ ). To ease visualisation the waveforms of realistic cable configurations are plotted in Figure 5.5. Comparing results of the heptacable (Figure 5.3) and some results when calibrating cable elastic properties (Figure 5.5) highlights the differences between the data that are currently acquired in real field surveys, based on the numerical solutions, and that can potentially be acquired. The influence of Poisson's ratio and friction is analysed to complete the study on elastic properties. A Poisson's ratio of 0.05, 0.25 and 0.45 has been tested and results are shown in Figure 5.6. With 20 N lateral force and given cable elastic properties, a variation in Poisson's ratio, which is the ratio of transversal strain over axial strain or in other words a measure of transversal expansion when under axial compression, did not alter the detected signal. Moreover, the friction coefficient is analysed for very sticky conditions ( $\beta_s = 0.9$ ), using an intermediate friction ( $\beta_s = 0.5$ ) and for very slippery conditions ( $\beta_s = 0.05$ ) as seen in Figure 5.7. The recordings of the cable when using high and intermediate friction coefficients are in match with the borehole wall. Recordings using a low friction coefficient results in a poorer match, but the detected signal still better ties in with recordings at the borehole wall than most other cable configurations using higher friction coefficients. However, it has been observed that the influence of the friction coefficient varies depending on density, contact force and stiffness. In general, more research will be required to fully understand the impact of each individual variable.

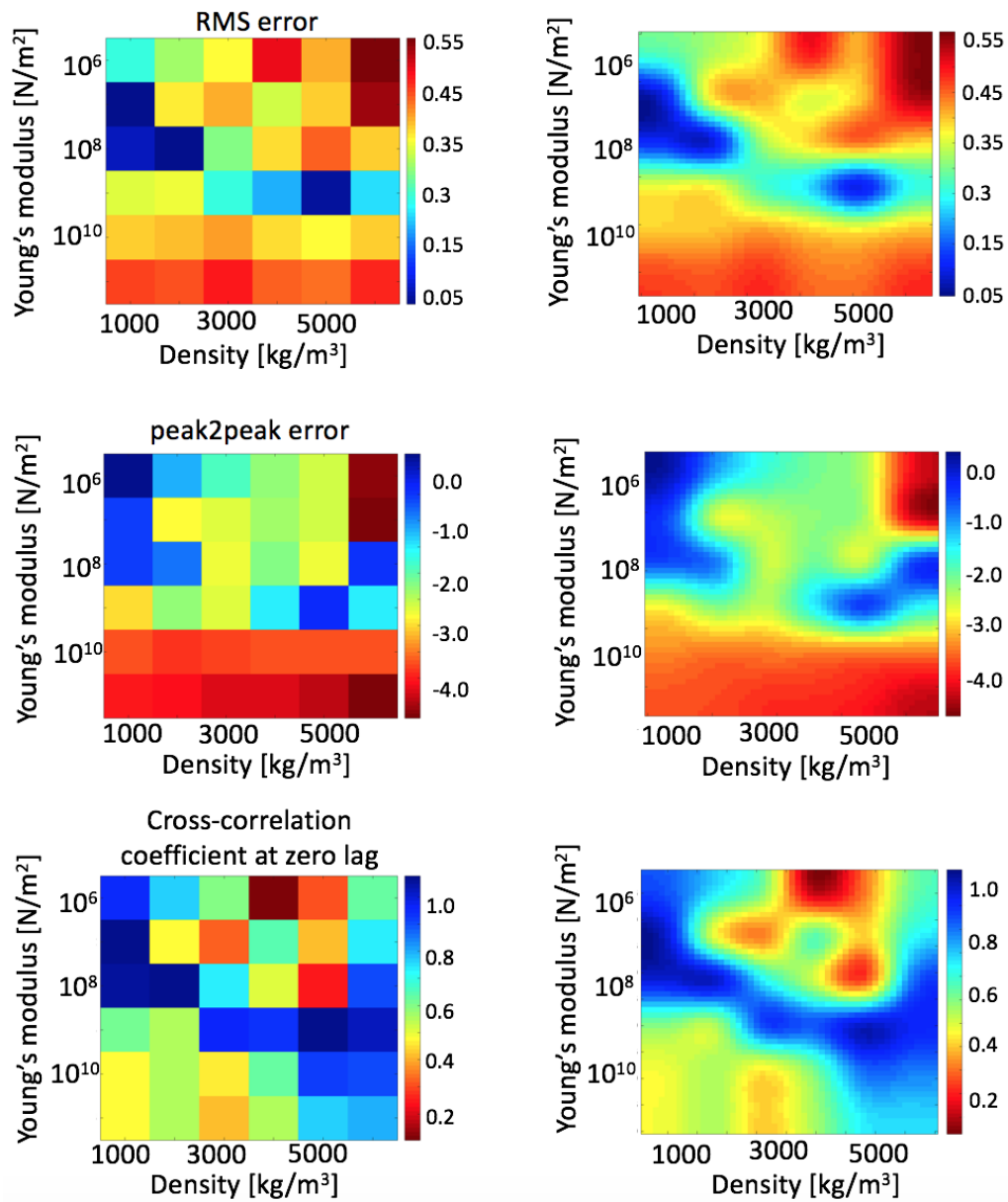


Figure 5.4: The root-mean-square error (top) and the peak-to-peak error (center) and the normalised cross-correlation coefficients at zero lag (bottom) for different cable configuration. The left plot shows the actual error values for 36 different cable configurations, and the right plot represents the same matrices after cubic interpolation.

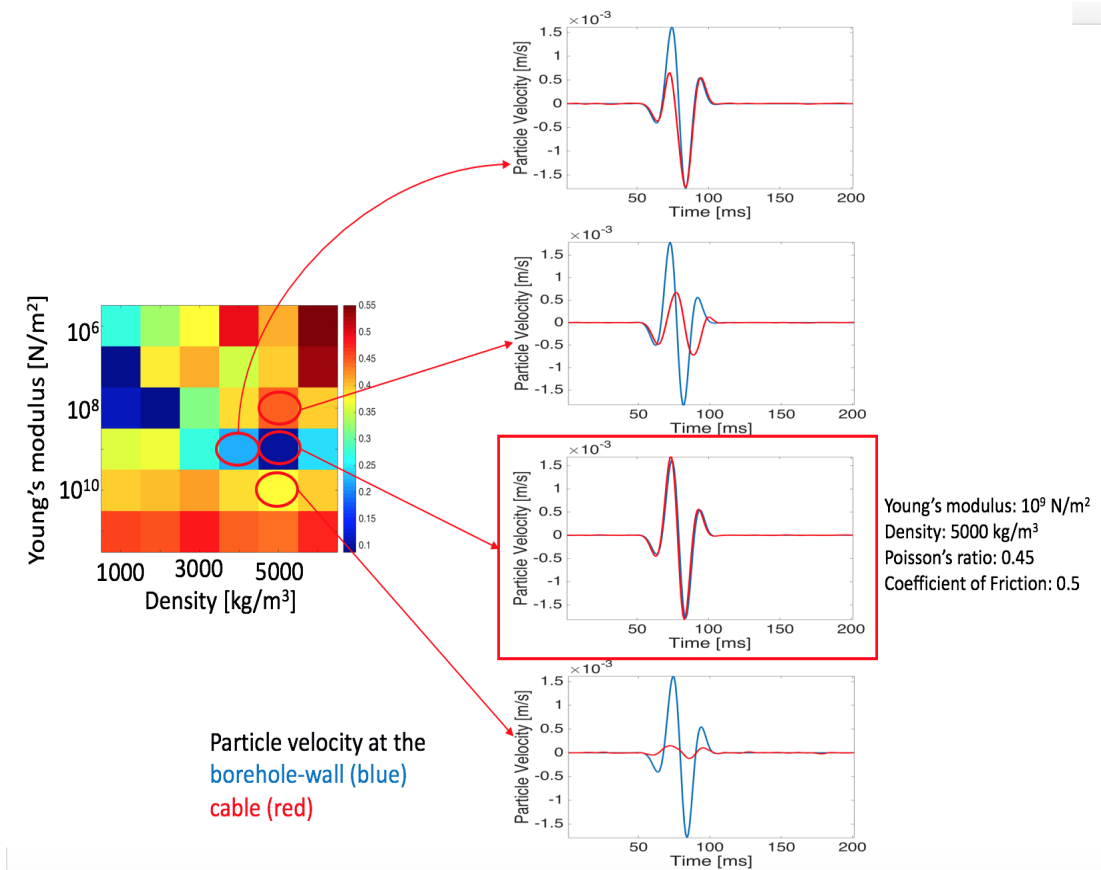


Figure 5.5: Waveforms of realistic cable configurations with different elastic properties. The best match is a cable with a Young's modulus of  $10^9 \text{ N/m}^2$  and a density of  $5000 \text{ kg/m}^3$  and a Poisson's ratio of 0.45, while the static friction coefficient is 0.5.

## 5 Optimising coupling using DAS

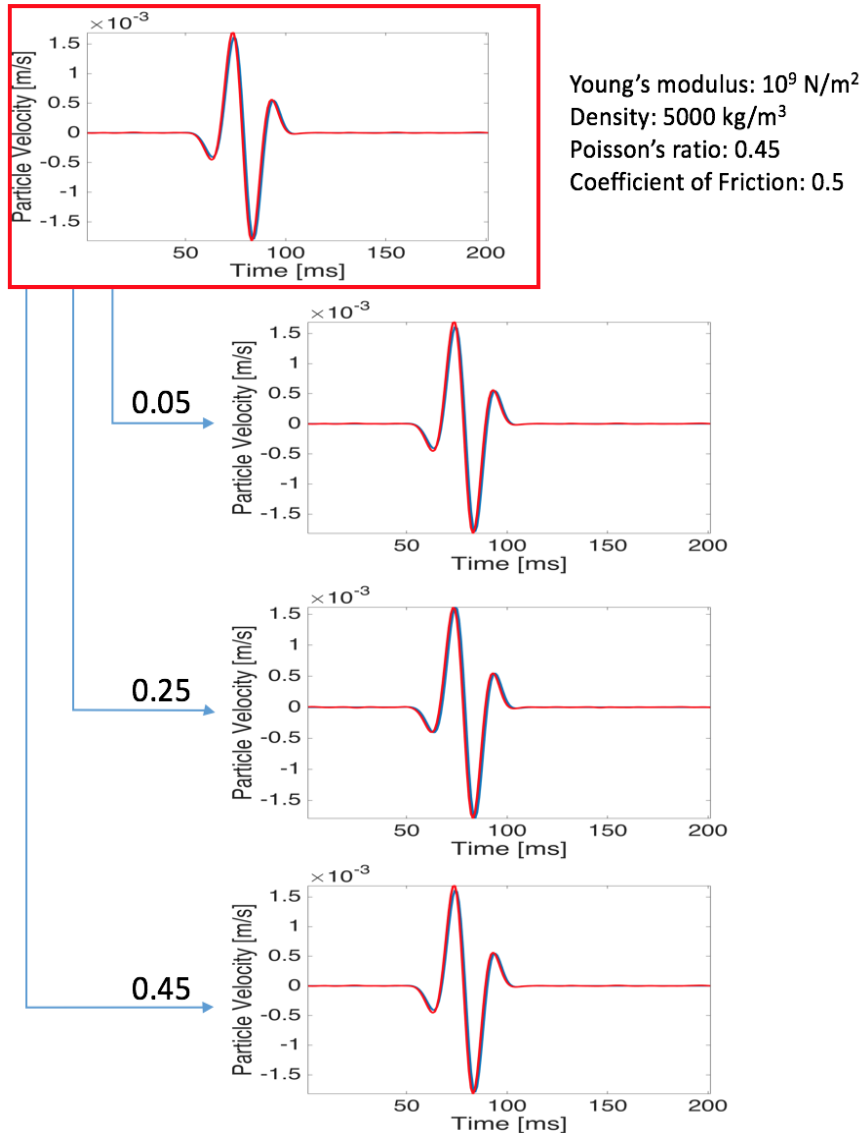


Figure 5.6: Analysis of varying Poisson's ratio using the cable configuration in Figure 5.5 with a Young's modulus of  $10^9$  N/m<sup>2</sup> and a density of 5000 kg/m<sup>3</sup>. Shown are results with a Poisson's ratio of 0.05, 0.25 and 0.45, while the static friction coefficient is 0.5.

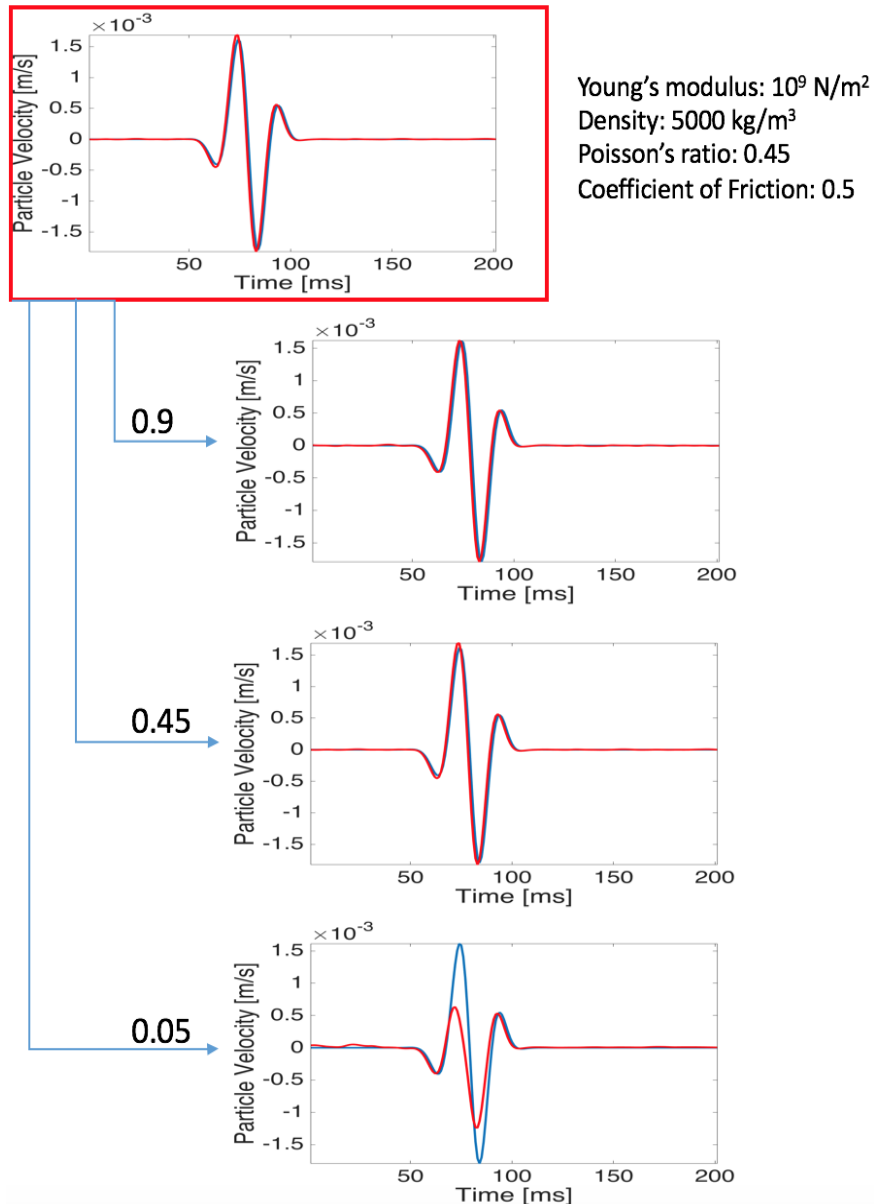


Figure 5.7: Analysis of varying static coefficient of friction using the cable configuration in Figure 5.5 with a Young's modulus of  $10^9$  N/m<sup>2</sup> and a density of 5000 kg/m<sup>3</sup>. Shown are results with a friction coefficient of 0.9, 0.45 and 0.05, while Poisson's ratio is 0.45.

## 5 Optimising coupling using DAS

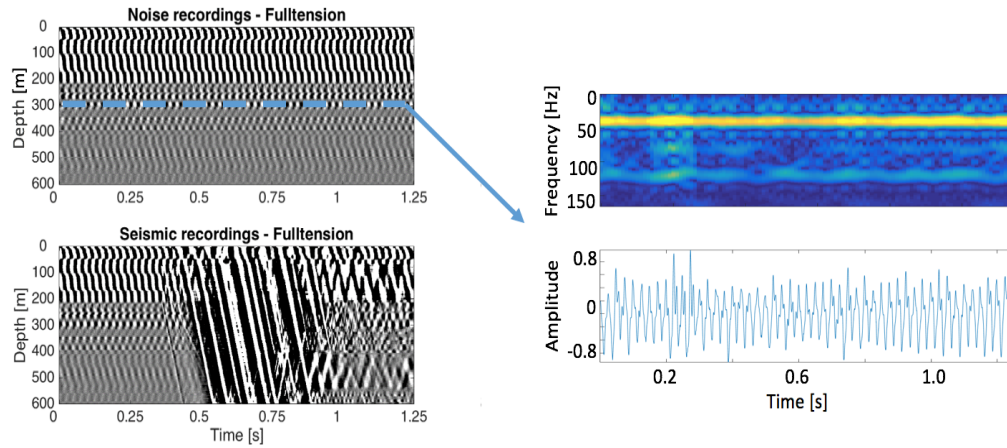


Figure 5.8: Noise analysis of DAS data acquired in Bottesford when the cable is under full tension. Left: noise recordings (upper panel) and seismic recordings (lower panel); right: time-domain signal (lower panel) and corresponding time-frequency analysis (upper panel).

### 5.4 Exploiting cable noise for DAS coupling

In the previous sections, numerical methods have been used to analyse the signal when varying the contact forces and the cable elastic properties with the aim to optimise DAS acquisitions. In addition to those findings, we observed that also real data can be used to optimise DAS acquisitions. In particular by analysing the data recorded before the first seismic arrival in VSP surveys using DAS on wireline cable.

#### 5.4.1 Noise recordings

Figure 4.6 has already been discussed to determine when DAS records high data quality, but only little attention so far has been drawn to what DAS records before the first seismic arrival. It appears that DAS records characteristic and consistent signals before the first arrival of the seismic wave when it is considered not well coupled. The DAS system is recording high amplitude, and harmonic signals, that are considered noise. These recordings correspond to the movement of the cable when it is floating loosely in the borehole fluid. Once the cable is in contact with the borehole wall and found equilibrium conditions, this noise disappears from the data. While we have only seen DAS recordings of active seismic data so far, there exist passive seismic data of DAS recordings, initially for simple training purposes on how to use the interrogation system.

The first dataset that is presented corresponds to the Bottesford test, discussed in Section 4.2, and shown in Figures 5.8 – 5.12. On the left side of Figure 5.8, noise recordings (upper panel) and seismic recordings (lower panel)

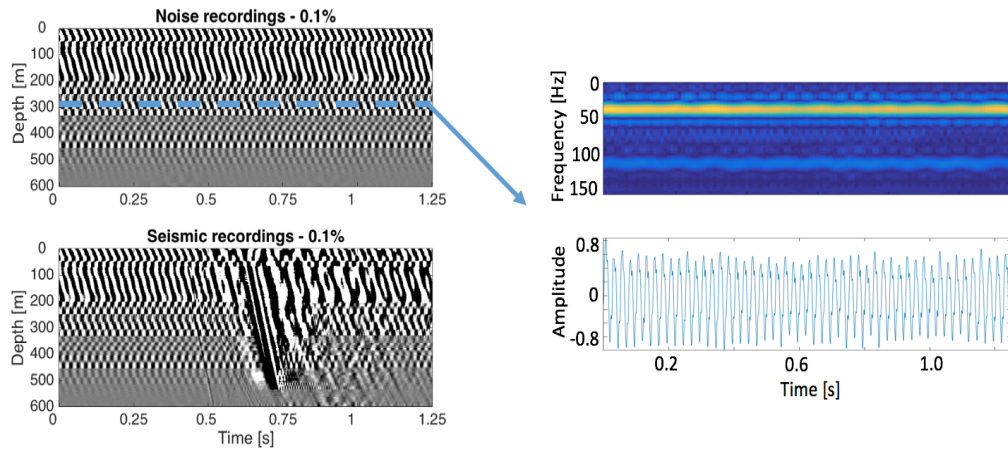


Figure 5.9: Noise analysis of DAS data acquired in Bottesford when 0.1% of excess cable were lowered down the borehole. Left: noise recordings (upper panel) and seismic recordings (lower panel); right: time-domain signal (lower panel) and corresponding time-frequency analysis (upper panel).

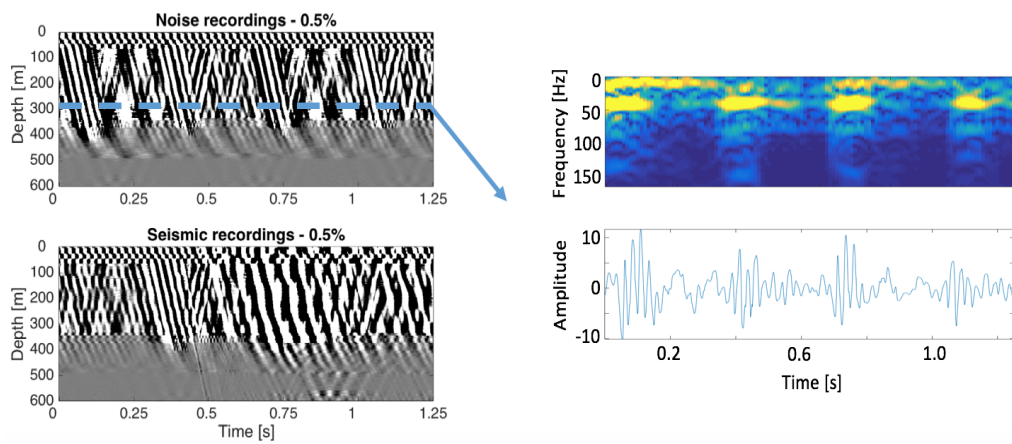


Figure 5.10: Noise analysis of DAS data acquired in Bottesford when 0.5% of excess cable were lowered down the borehole. Left: noise recordings (upper panel) and seismic recordings (lower panel); right: time-domain signal (lower panel) and corresponding time-frequency analysis (upper panel).

## 5 Optimising coupling using DAS

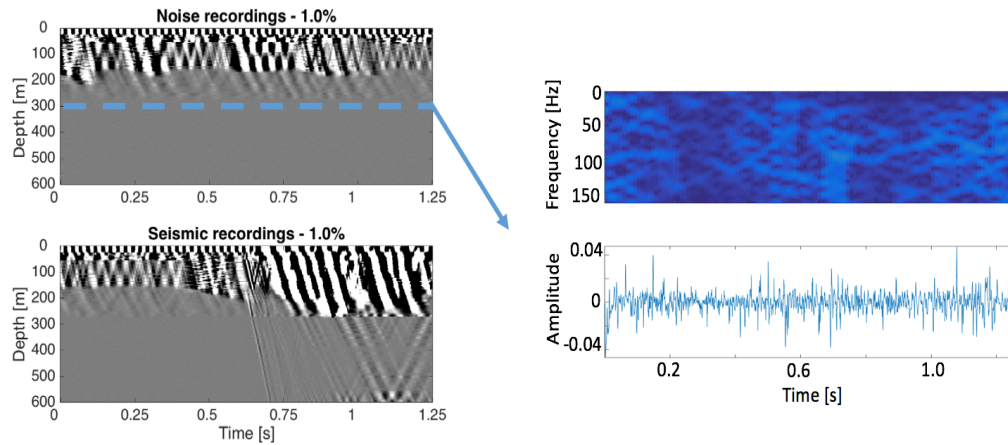


Figure 5.11: Noise analysis of DAS data acquired in Bottesford when 1.0% of excess cable were lowered down the borehole. Left: noise recordings (upper panel) and seismic recordings (lower panel); right: time-domain signal (lower panel) and corresponding time-frequency analysis (upper panel).

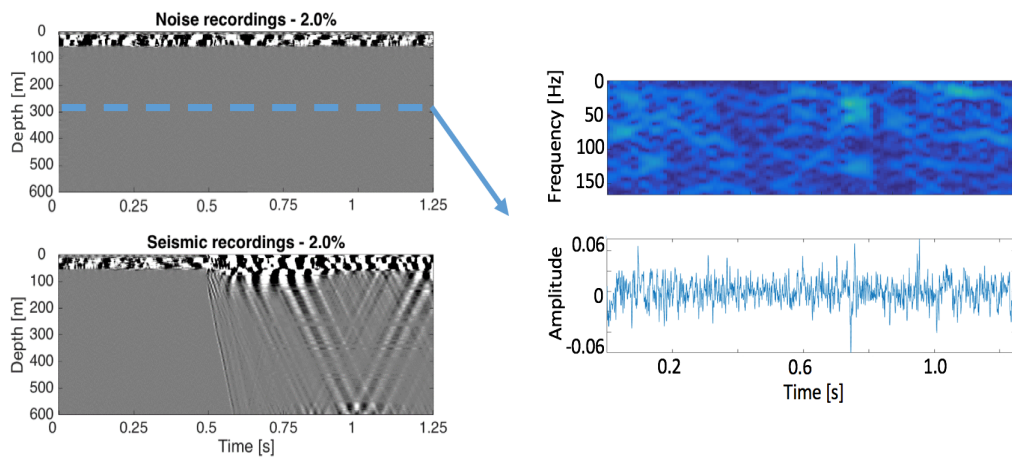


Figure 5.12: Noise analysis of DAS data acquired in Bottesford when 2.0% of excess cable were lowered down the borehole. Left: noise recordings (upper panel) and seismic recordings (lower panel); right: time-domain signal (lower panel) and corresponding time-frequency analysis (upper panel).

of the DAS system are shown, when the wireline cable was held under tension. We can observe that noise recordings (upper panel) are very similar to recordings before the first seismic arrival, i.e. until 0.5 s (lower panel). Furthermore, this noise appears to be of a characteristic nature as it seems to be sinusoidal with a constant frequency. To further analyse this type of noise, a single trace plot at 300 m depth is used to investigate its frequency content over time using the Short-Time Fourier Transform (STFT). Results of this time-varying frequency analysis are shown on the right side of Figure 5.8 (top panel), while the time-domain representation of the trace is plotted in the lower panel. We can observe that most of the energy is distributed in the low frequency range, in particular around 40 Hz. Similar observations were made for the scenario when 0.1% of additional cable were lowered down the borehole (Figure 5.9). Noise (upper panel) and seismic recordings (lower panel) are shown on the left, while the time-domain signal at 300 m depth and its time-varying frequency analysis are presented on the right. Again, the main energy is at 40 Hz and we can conclude that this noise detected by the DAS cable is harmonic with a fundamental frequency around 40 Hz. The same analysis was carried out for the remaining scenarios. Noise and seismic recordings and the frequency analysis when 1.0%, 1.5% and 2.0% of additional cable were lowered down the borehole are shown in Figures 5.10, 5.11 and 5.12, respectively. While in Figure 5.10 the tube wave is the dominant feature around a depth of 300 m and where the cable is not well coupled, Figure 5.11 allows to better interpret what DAS records when the cable is considered well coupled to the borehole wall. In this case, the harmonic noise disappears in both noise (upper panel) and seismic recordings (lower panel). Furthermore, the first seismic arrival in seismic recordings is easily detectable up to the depth to which the cable is well coupled (Section 4.2.2). Additionally, the time-frequency analysis on the right shows that the frequency spectra is dense and continuous, i.e. the energy is spread across the frequency spectrum, which is an indicator that DAS records solely white noise (Hayes, 1996). Similar results were found when maximum tension of the wireline cable was released in Figure 5.12. Here, the cable was considered well coupled throughout the entire well and DAS detected only white noise prior to the first seismic arrival. We also note that the amplitude of the white noise is 1 – 2 orders of magnitude lower than the amplitude of recorded harmonic noise, when the cable is poorly coupled.

Very similar observations were made for the field test data in Livingston, where the same analyses are presented in Figures 5.13 – 5.15. In Figure 5.13 the DAS cable is held under tension. Noise and seismic recordings are presented on the left, while a single trace around 40 m depth and its time-varying frequency analysis are shown on the right. The noise is harmonic, as also observed in the Bottesford dataset, but the fundamental frequency differs. In contrast to 40 Hz, most energy in this dataset is detected around 4 Hz. The same analysis, when 0.5% of additional cable was lowered down

## 5 Optimising coupling using DAS

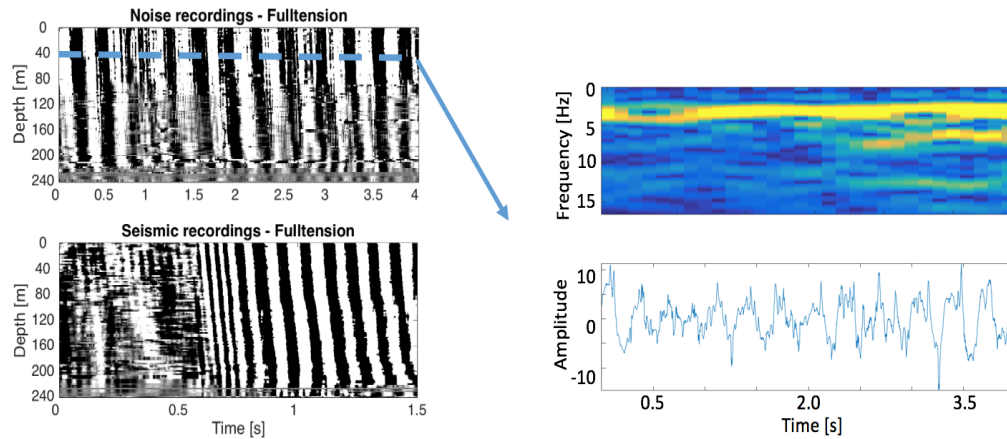


Figure 5.13: Noise analysis of DAS data acquired in Livingston when the cable was held under tension the borehole. Left: noise recordings (upper panel) and seismic recordings (lower panel); right: time-domain signal (lower panel) and corresponding time-frequency analysis (upper panel).

the borehole, is shown in Figure 5.14. The results are similar to the results, when the cable was held under tension in Figure 5.13, in that the fundamental frequency of the harmonic noise is at 4 Hz. Figure 5.15 shows data when 1.0% of additional cable was lowered down the borehole, and in Figure 5.16 it was 2.0%. Here, the cable is considered well coupled throughout the entire borehole. Similar to the results of the analysed dataset of the Bottesford test, DAS records only white noise.

The absolute value of the recorded amplitudes in the time-domain might be different in the Livingston dataset compared to the Bottesford dataset, and also the frequency content is different (4 Hz compared to 40 Hz), however, the basic characteristics of noise in that the noise is of high amplitude and harmonic was observed in both datasets.

### 5.4.2 Feature detection

Based on the observations made in the previous section, we present a coupling detection algorithm in this section. This algorithm intends to detect coupling conditions automatically and will be applied to the two datasets.

In the previous section, we have analysed noise and seismic recordings of the field tests in Bottesford and Livingston. It has been observed that the noise is of characteristic nature when the DAS cable is considered poorly coupled and is floating in the borehole fluid. Based on the results presented in Figures 5.8 – 5.16, we chose two features to determine whether coupling conditions are satisfied or not, that are the high amplitude of the time-domain signal and its distinctive representation in the frequency spectrum while

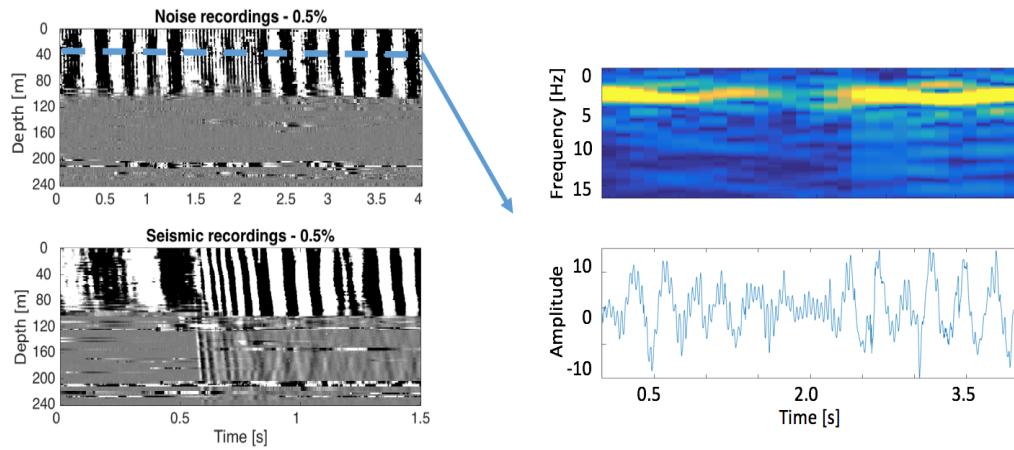


Figure 5.14: Noise analysis of DAS data acquired in Livingston when 0.5% of extra cable was lowered down the borehole. Left: noise recordings (upper panel) and seismic recordings (lower panel); right: time-domain signal (lower panel) and corresponding time-frequency analysis (upper panel).

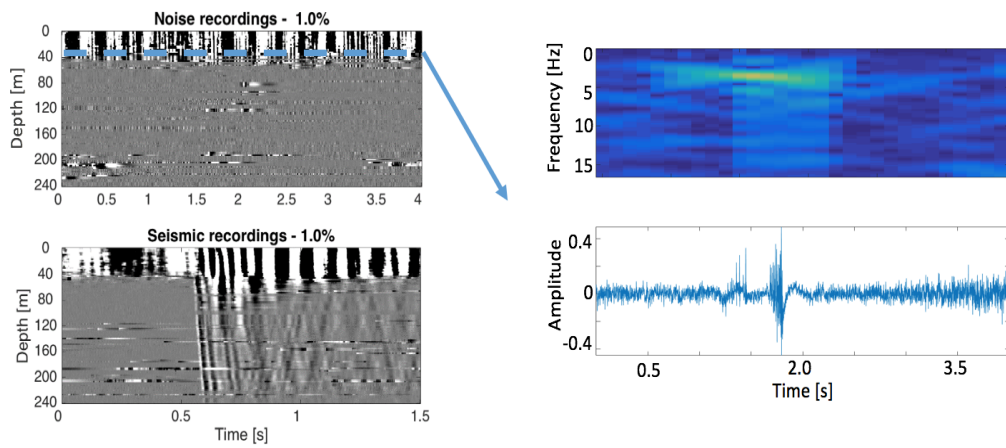


Figure 5.15: Noise analysis of DAS data acquired in Livingston when 1.0% of extra cable was lowered down the borehole. Left: noise recordings (upper panel) and seismic recordings (lower panel); right: time-domain signal (lower panel) and corresponding time-frequency analysis (upper panel).

## 5 Optimising coupling using DAS

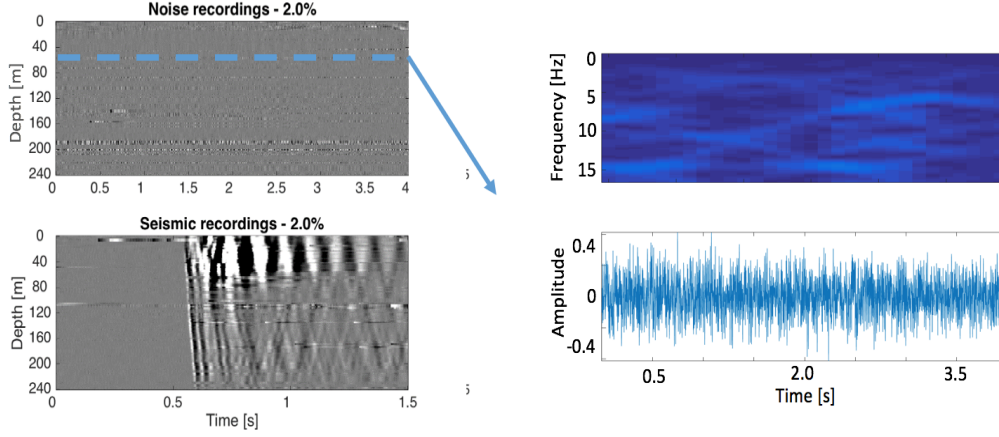


Figure 5.16: Noise analysis of DAS data acquired in Livingston when 2.0% of extra cable was lowered down the borehole. Left: noise recordings (upper panel) and seismic recordings (lower panel); right: time-domain signal (lower panel) and corresponding time-frequency analysis (upper panel).

being harmonic. This allows us to develop a feature detection algorithm. The initial requirements for this method is to establish thresholds for both the amplitude of the time-domain signal  $w(t)$  and the magnitude of the frequency components  $|W(f)|$ . The algorithm then scans through all traces in depth, producing two vectors  $\Lambda(z)$  and  $\Psi(z)$  holding information about whether the thresholds are crossed (= 1) or not (= 0):

$$\Lambda(z) = \begin{cases} 1, & \text{if } [w(t)]_z > w_{max} \text{ for any } t \\ 0, & \text{otherwise} \end{cases} \quad (5.7)$$

and

$$\Psi(z) = \begin{cases} 1, & \text{if } [|W(f)]_z > W_{max} \text{ for any } f \\ 0, & \text{otherwise.} \end{cases} \quad (5.8)$$

$w_{max}$  and  $W_{max}$  are the thresholds and the subscript  $z$  is an index over the spatial directions. In order to add robustness to the algorithm both vectors are combined in a boolean statement that requires both conditions of good coupling (= 0) to be satisfied:  $\varsigma(z) = \Lambda(z) \vee \Psi(z)$ , where  $\vee$  is the truth-functional operator OR. This let us obtain a vector  $\varsigma(z)$  allowing us to determine whether the DAS cable is considered poorly coupled (= 1) or well coupled (= 0) as a function of depth. The algorithm has been applied to the data acquired in Livingston in Figure 5.17. Figure 5.17 (a) presents the seismic recordings and (b) the results of the detection algorithm. The thresholds for both the amplitude and magnitude have been determined empirically, where we used 1/2 the magnitude of the fundamental frequency and the mean value of the amplitude of a single trace acquired when the coupling was poor. Here,

0 corresponds to good coupling, and 1 to poor coupling. The results show that the algorithm works well and good coupling is indicated to the depth, to which DAS considered to be well coupled to the borehole wall and detects only white noise prior to the first seismic arrival. We applied the algorithm with the same thresholds to the data acquired in Bottesford and the results are shown in Figure 5.18. Again, seismic recordings are plotted in (a) and the results of the algorithm are shown in (b) and we note that good coupling is indicated, where we consider the cable to be well coupled that is when it is in a stable position in contact with the borehole wall. However, we can already identify some limitations in terms of robustness of the algorithm in Figure 5.18 (3). Here, we can see that around 200 m – 300 m the algorithm indicates good coupling, even though first seismic arrivals are barely visible. This will be further discussed in Chapter 6.

Since the utilization of a seismic source is a significant cost of an entire seismic survey, knowing if DAS is capable to record a reasonable SNR prior to starting acquisitions is of great advantage. Especially since the major advantage of DAS compared to conventional seismic acquisitions is its cost effectiveness. The application of the detection algorithm is relatively straightforward provided that the thresholds are known. Moreover, the noise is consistent over time, hence the test can be applied at any time once the cable has been deployed. In addition, due to its time efficiency, the test can be applied between surveys or even individual shots to ensure good coupling conditions since the cable might alter its position or slip when the borehole is vibrating.

## 5.5 Conclusions

We have developed a numerical model allowing us to analyse the influence of contact forces between a cable and the borehole wall in terms of sensitivity to seismic waves (Section 5.2). Here, the cable is moved towards the borehole wall when applying a constant lateral force to the nodes of the cable. Then, a plane wave is propagating along the borehole wall. The sensitivity of the cable commonly used by Schlumberger in field operations has been analysed when varying the contact force between the cable and the borehole wall from 5 N - 120 N, while only a few results have been presented. Based on the numerical solutions, we have concluded that with the given elastic properties of the heptacable, an increase in contact force does not alter the recorded signal significantly. Even increasing the contact force to unrealistic amounts of 120 N did not seem to minimise the error in recorded signal.

Instead of varying contact forces, the cable elastic properties have been altered, while keeping the contact force to a constant 20 N in Section 5.3. This analysis showed that when changing the Young's modulus and the density

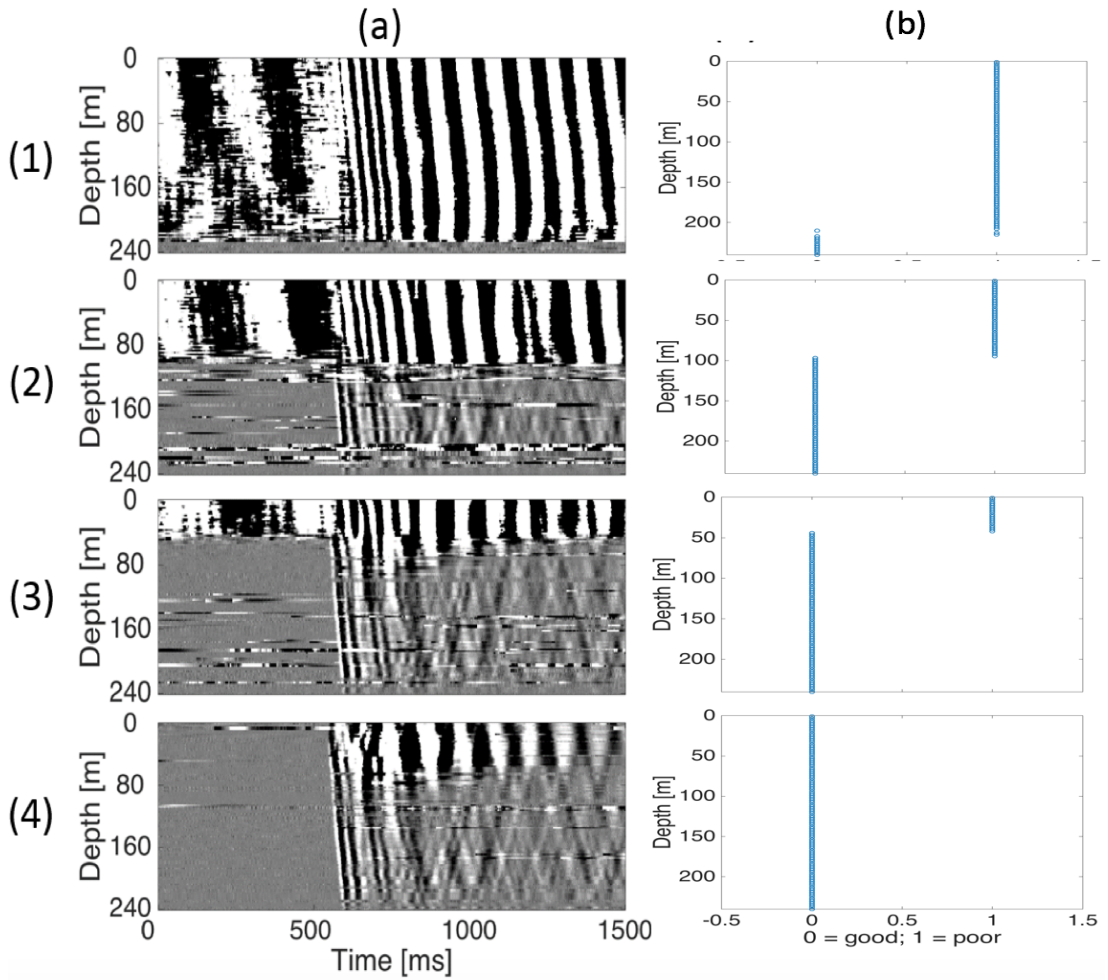


Figure 5.17: The coupling detection algorithm applied to the DAS acquired data in Livingston. Left: DAS recordings; right: results of the coupling detection algorithm, where 0 is good coupling and 1 is poor coupling.

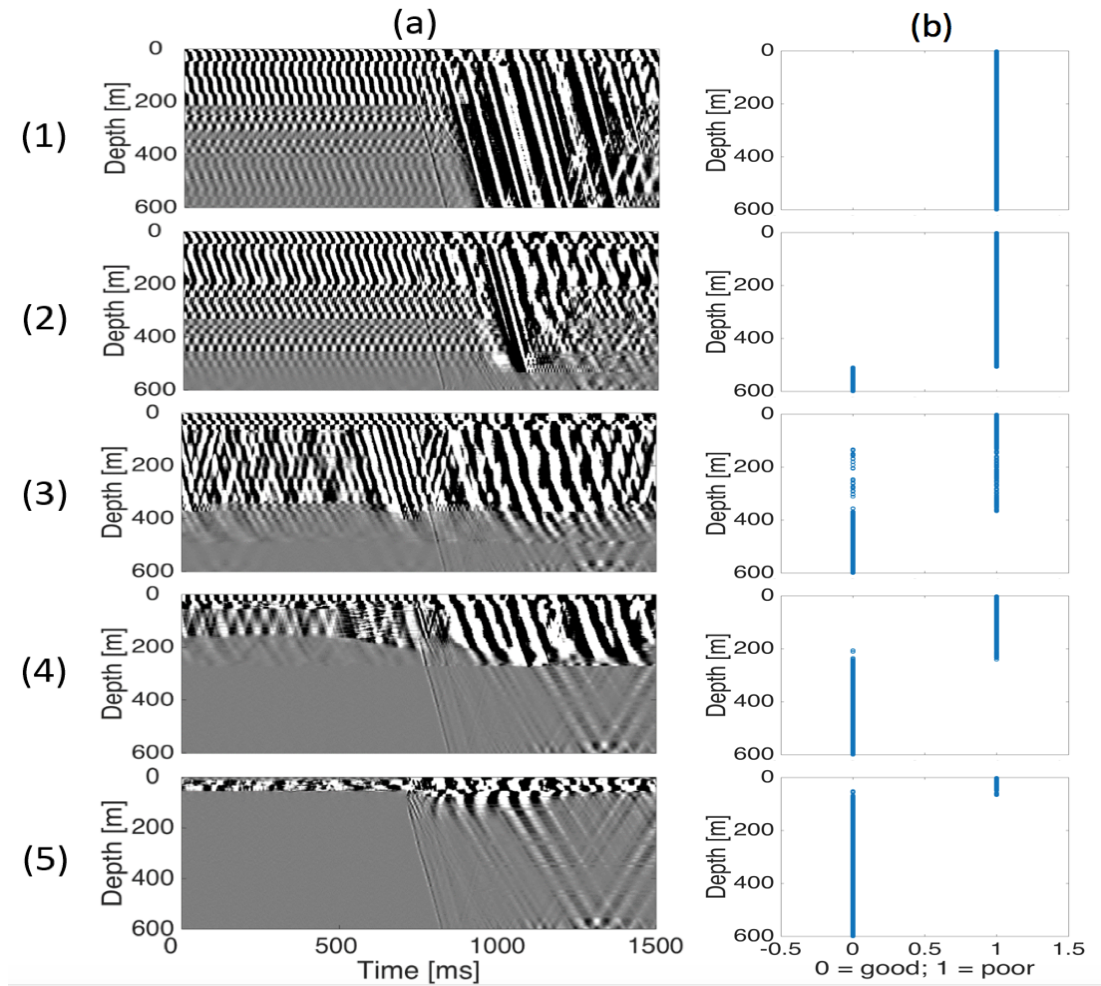


Figure 5.18: The coupling detection algorithm applied to the DAS acquired data in Bottesford. Left: DAS recordings; right: results of the coupling detection algorithm, where 0 is good coupling and 1 is poor coupling.

## 5 Optimising coupling using DAS

of the cable, also the seismic signal recorded by the cable changes significantly. Some cable configurations combined a high tensile strength with a high sensitivity to seismic waves arriving at the borehole wall (Figure 5.5). Here, a cable with a diameter of 1.5 cm, a Young's modulus of  $10^9$  N/m<sup>2</sup> and a density of 5000 kg/m<sup>3</sup> produced perfect coupling conditions because the error between the seismic signal recorded at the borehole wall and by the cable was minimised to negligible residuals. Those cable configurations provide potential to become a new generation DAS cable.

In the last part a more practical example without numerical modelling was presented. The characteristics of noise recorded by the DAS system before the seismic arrival have been used to create a feature detection algorithm to automatise DAS acquisitions. If poorly coupled, DAS is continuously recording high amplitude, harmonic noise that is superimposing any signal of interest. This noise converts to white noise when the cable is well coupled to the borehole wall. Given these simple features, an automatised detection algorithm can be applied before the survey in order to avoid repeating seismic source shots.

## Conclusions and perspectives

The main part of the budget of the upstream oil and gas business is dedicated to the production of the reservoir. The smaller part is given to exploration and an even smaller part to monitor the reservoir. In order to keep the cost the seismic data required for the operation, DAS is considered to be a cost-effective alternative to conventional seismic acquisition for VSP surveys. The main advantages of DAS are the **high spatial resolution**, the ability to provide **full well coverage**, the **cheap installation cost** and the general **robustness of the system**. As for any new technology the commercial use of DAS systems is sometimes inhibited due to a few disadvantages, that are the **low SNR**, the fact that DAS is a **single-component sensor** and the **poor coupling**. The poor coupling often occurs when the sensing cable is simply lowered down the borehole and not physically clamped to the casing or cemented behind the casing. This deployment technique is also called wireline deployment. A field trial in 2013 ([Hartog et al., 2014](#)) was the start to analyse the problem of coupling during wireline deployment, to understand real data recordings and how these relate to conventional seismic acquisition.

In this thesis, we analysed seismic wave expressions in fluid-filled boreholes using numerical methods and compared those with real data recordings. We concluded that the numerical model, presented in Section 3.4, confirms DAS recordings as long as DAS is perfectly coupled. We analysed coupling conditions using another numerical model, presented in Section 3.5, and concluded that a direct cable-casing contact is required for DAS to be considered well coupled and to acquire high data quality. Furthermore, we proposed solutions to optimise DAS acquisitions in terms of a required contact force, a calibration of cable elastic properties and an event detection algorithm.

## 6.1 Conclusions

### 6.1.1 The coupling of DAS in borehole VSP

[Hartog et al. \(2014\)](#) have shown that when the DAS cable is used to record seismic data on wireline cable, any signal of interest was overlaid with high amplitude and sinusoidal noise as long as the cable was held under tension (or with minimal tension release) in the borehole. High quality data was acquired after 2% of additional cable being lowered down the borehole.

In this thesis, we compared numerical simulations with real data using a 3D seismic wave propagation model described in Section 3.4. This model allowed us to analyse seismic waves in fluid filled boreholes induced by an impinging elastic wavefield. Numerical results were similar to DAS data when tension of the wireline cable was released to the maximum possible extent. In this scenario, the DAS cable was considered well coupled. However, when the DAS cable was fully under tension, or only a small amount of additional cable was lowered down the borehole, the quality of acquired data using DAS was poor. This particular numerical model could not explain observations made in real data. Assuming that lowering more cable down the borehole would alter the position of the cable in the borehole in some way, we altered the cable position in the numerical model but could not observe changes in the recorded signal. Here, the numerical solution was not perturbed by environmental noise, considered the cable of a constant cross-section, and most importantly, the cable in the numerical model was positioned in a straight, and fixed position in the borehole. Then, the cable is sensing the particle velocity of the borehole fluid perfectly. In real VSP surveys, however, the cable is floating loosely in the fluid column.

We addressed this problem with another numerical model, described in Section 3.5. This model was used to track the precise position and movement of the cable and to better analyse its coupling with the borehole wall. The results of this simulation allowed us to conclude that DAS is well coupled if the cable is in contact with the borehole wall and in equilibrium conditions. Here, the depth to which the cable coiled up in a helical shape, corresponded to the depth to which the DAS system recorded high data quality. This conclusion has been confirmed by deriving the contact force along the entire well in the numerical solution. Additionally, the quantification of the contact force allowed us to conclude that the cable stops slipping and sticks to the borehole wall as soon as contact forces of approximately 20 N or higher were established. Hence, the amount of contact force allows us to determine whether good coupling conditions are satisfied. Another field trial has been carried out to confirm those observations in 2016. Even though the dimension of the well and the environment were different, the observations were similar. High quality data could be acquired as soon as the cable was in contact with the borehole wall and found equilibrium conditions. Note that the amount of contact force, however, can vary and depends on the dimension

of the borehole and the cable as well as on their elastic properties and the friction coefficient. Those quantities were in both field tests similar but can differ for other set-ups.

We can therefore conclude that DAS is considered poorly coupled if the DAS cable is not in immediate contact with the borehole during VSP surveys on wireline cable. The cable is considered well coupled when the cable is in contact with the borehole wall and in equilibrium conditions, that are found when approximately 20 N of contact force are established. Then the cable stops slipping and sticks to the borehole wall.

### 6.1.2 Analysis to improve the coupling using DAS

In Chapter 5 we developed a numerical model allowing us to analyse the influence of the contact force (Section 5.2) and cable elastic properties (Section 5.3) in terms of sensitivity to seismic waves. Here, the cable is moved towards the borehole wall, when applying a constant lateral force to the nodes of the cable. Then, a plane wave is propagating along the borehole wall. The sensitivity of the cable commonly used by Schlumberger in field operations has been analysed when varying the contact force between the cable and the borehole wall from 5 N - 120 N. Based on the numerical solutions, we concluded that with the given elastic properties of the heptacable, an increase in contact force does not alter the recorded signal significantly. Even increasing the contact force to unrealistic amounts of 120 N did not seem to minimise the error in recorded signal. Instead of varying the contact force, the cable elastic properties have been altered, while keeping the contact force to a constant 20 N in Section 5.3. This analysis showed that when changing the Young's modulus and the density of the cable, also the recorded seismic signal by the cable changes dramatically. Some cable configurations combined a high tensile strength with a high sensitivity to seismic waves arriving at the borehole wall (Figure 5.5). Here, the error between the seismic signal recorded at the borehole wall and by the cable has been minimised to negligible residuals and those cable configurations provide potential to become the new DAS cable.

Furthermore, the characteristic nature of noise before the seismic arrival have been used to create a feature detection algorithm. The intention of this algorithm is to automatise DAS acquisitions and ensure good coupling conditions. If the DAS cable is poorly coupled, high amplitude, harmonic noise is recorded that is superimposing any signal of interest. This noise disappears as soon as the cable is well coupled to the borehole wall and consequently, the DAS system only detects white noise prior to the first seismic arrival. Using characteristic noise features of a high amplitude in the time-domain and a harmonic frequency spectrum, an automatised detection algorithm can be applied before the survey in order to avoid repeating seismic source shots.

## 6.2 Perspectives

During this work theoretical and practical knowledge about the DAS technology has been acquired. While we tried to analyse the recorded signal using numerical methods, we have not analysed the system in terms of more practical approaches. In the following we will discuss both fields for future perspectives and investigate potential for improvement.

### 6.2.1 Numerical modelling improvements

#### Modelling poor coupling conditions

The seismic wave propagation model presented in Section 3.4 assumes the cable to be in a straight and fixed position in the fluid-filled borehole. Due to limitations of computational resources, we were not able to allow the cable to move freely in the fluid column or to allow a direct (frictional) contact between the cable and the casing, because this would evolve in a high mesh distortion of the modelled borehole fluid. First, this high mesh distortion would produce finer and finer elements, reducing the time step of the computation according to the CFL condition (Equation 3.19). Moreover, the fluid-structure interaction problem would become an elastic-elastic interaction, when the cable eventually established contact with the casing, thus preventing to obtain a numerical solution because the numerical software that we were using cannot handle this type of problem in a single numerical model. Therefore, we have used another numerical model to track the precise position of the cable. Nevertheless, over the past few years optimisations of the conventional discretisation step of the finite element method have been proposed. Liu (2005) described the mesh-free approach and Wall and Ramm (1998), Tezduyar (2004) or Baines et al. (2005) proposed meshes to be more adaptive, or *moving* meshes. Here, the mesh is updated iteratively, allowing high mesh distortion without affecting the computation time and allowing to analyse more difficult fluid-structure interaction problems. This would allow us to simulate the scenario when DAS is considered poorly coupled with the numerical model of seismic wave propagation described in Section 3.4. Furthermore, the implementation of mentioned methods would enable modelling of problems such as frictional contact, when two elastic bodies (i.e. the borehole wall and the cable) are initially separated by an acoustic interface (i.e. the borehole fluid). Hence, we would be able to produce numerical results for each scenario when more cable was lowered down the borehole (see Figure 4.6 for the results obtained in Bottesford and Figure 4.10 for the results obtained in Livingston).

#### Efficient modelling using wavefield grid injection

While implementing frictional contact and a moving cable in the borehole fluid in the seismic wave propagation model will certainly increase the com-

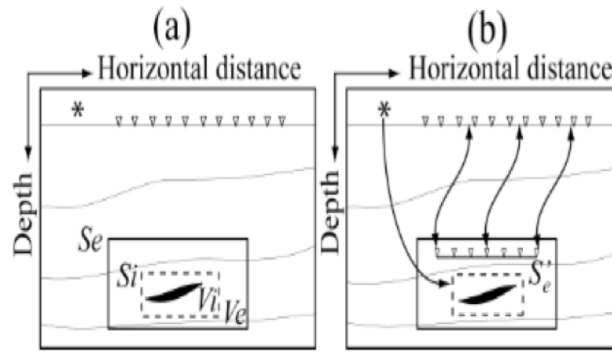


Figure 6.1: Schematic diagram showing the basic concept of the grid injection method (adapted from [Robertsson and Chapman \(2000\)](#)). Initial model with source and receivers placed at the surface (a), and new source and receivers position close to the region of interest(b).

computational cost to some extent, we analysed methods to reduce the computation time of the numerical solution and tested the wavefield grid injection method ([Robertsson and Chapman, 2000](#)). A schematic diagram showing the basic concept of the grid injection method is shown in Figure 6.1. In the initial model source and receivers are placed at the surface in (a). This simulation is computationally expensive because the entire domain must be discretised even though the main interest is in a small part of the model, that is the volume  $V_i$ . For problems, such as time-lapse seismic, the solution for the same model needs to be computed several times. In order to save computational cost, the entire numerical model is solved only once in the grid injection method. Then, the wavefield recorded at the boundary  $S_i$  of  $V_i$  is injected as a source term in a second model shown in Figure 6.1 (b), where the concept of new source and receivers positions close to the region of interest is shown. This model is the initial volume  $V_i$  with boundaries  $S_i$ , where wavefield is injected, and an additional volume volume  $V_e$  with boundaries  $S_e$ , where perfectly-matched-layer are used to absorb wave energy. The same idea can be applied to our problem, where we could simulate far-offset surveys without the need of the entire model simulating the long offset of the source as shown in the sketch in Figure 6.2. Here, we reduced the model size by a factor of 2 in length. In fact, we can always keep a relatively small model, and inject wavefields on the boundary of the model that correspond to arbitrary offset scenarios. A first numerical result is shown in Figure 6.3 where the dimensions of the numerical model were equivalent to the dimensions presented in the sketch in Figure 6.2. The seismic source is a vertical point source with the shape of a Ricker wavelet of 45 Hz of central frequency. The upper panel on the left of Figure 6.3 shows the solution of the radial component of particle velocity detected by a line of 25 receivers in-line with the seismic source ( $x=0$ ) with offset  $y=400 - 450$  m at depth  $z=10$  m with

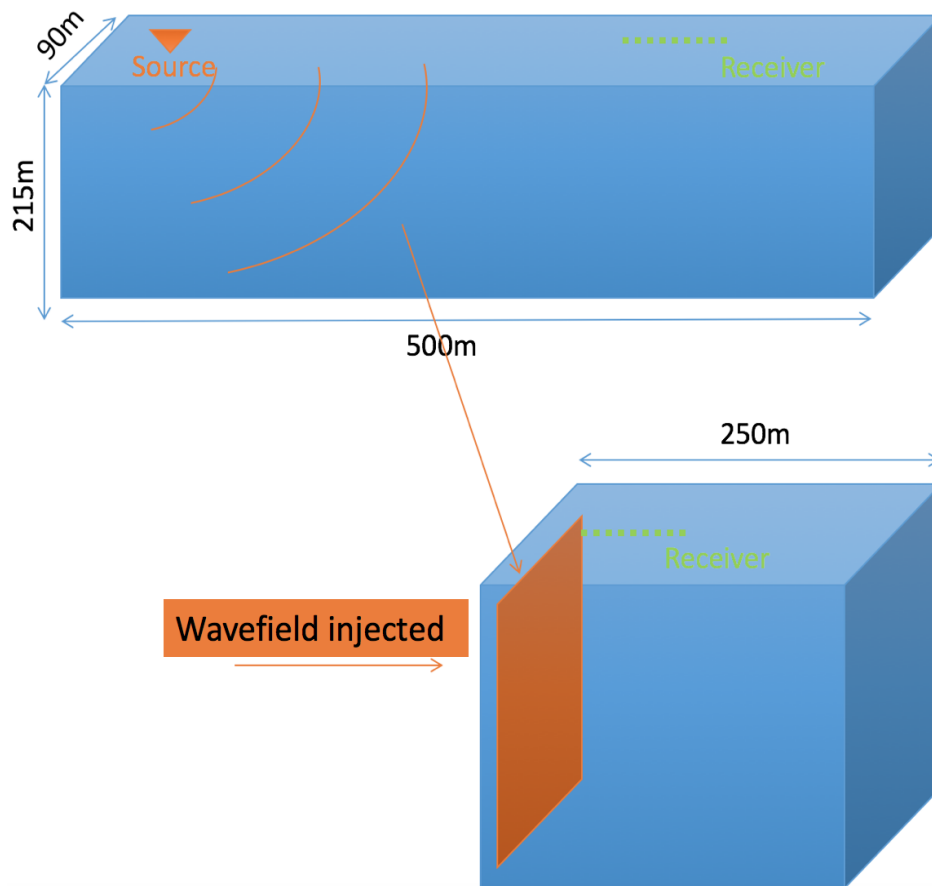


Figure 6.2: Sketch of the numerical model that has been used to test the grid injection method.

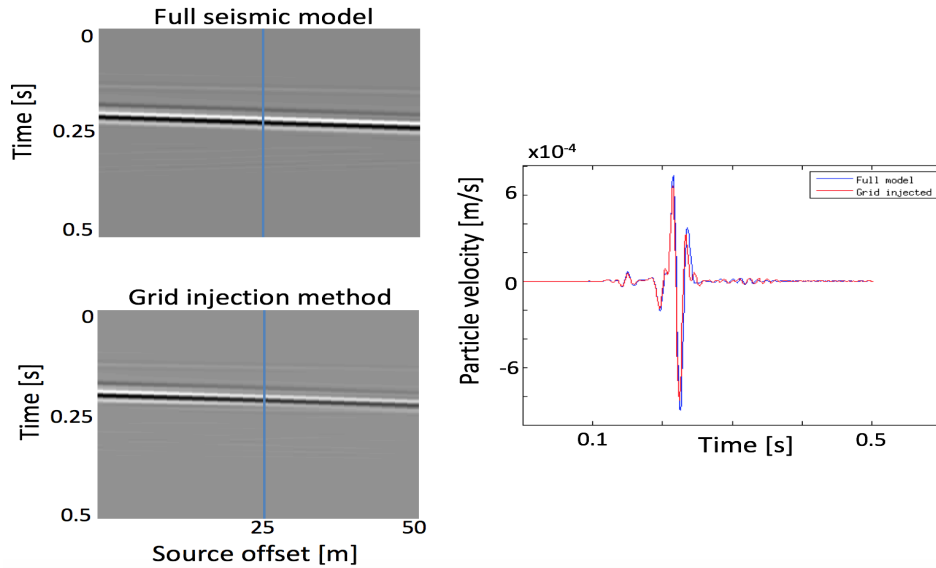


Figure 6.3: Numerical results of the grid injection method test. The upper panel on the left shows numerical results of the full seismic wave propagation model and the results of the grid injection method are shown in the lower panel. A comparison of a single trace of receiver  $x=0$  m,  $y=25$  m and  $z=10$  m is shown on the right.

respect to the source location. The lower panel presents the solution of the grid injection method with receiver locations at  $x=0$ ,  $y=0 - 50$  m and  $z=10$  m with respect to the source. The single trace plot shown on the right are recordings of a receiver at offset  $y=25$  m. The numerical results show that we successfully implemented the grid injection method for our purpose, since there are no obvious differences in the gray scale plot and the residuals in the single trace plot shown on the right of Figure 6.3 are negligible. This first test allowed us to reduce the number of elements by a factor of 2, and we think we can further increase the efficiency of the grid injection method.

## 6.2.2 Practical improvements

### Adding robustness to the coupling detection algorithm

The coupling detection algorithm in Section 5.4 allowed us to determine the coupling conditions. In the case of poor coupling, high amplitude and harmonic noise is superimposing any signal of interest i.e. P- and S-waves. However, the detection algorithm is not very robust because we only use a few distinctive features to detect the coupling conditions, that are a threshold for the amplitude of the time-domain representation and a threshold for the magnitude of the frequency spectrum of the signal. Both thresholds were empirically determined. However, in Figure 5.18 (3) the algorithm indicates good coupling conditions around 150m – 300 m even though the seismic

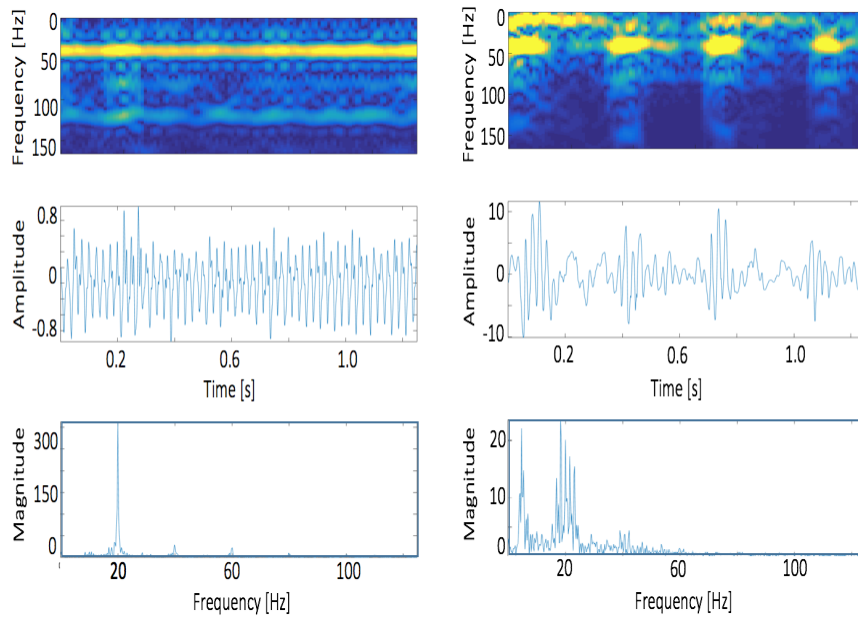


Figure 6.4: Noise analysis of DAS data at a depth of 300 m acquired in Bottesford when 0.1% (left) and 0.5% (right) of extra cable was lowered down the borehole. For both signals, the time-frequency analysis is shown in the upper panel, the time-domain signal is in the middle panel and its frequency spectrum is presented in lower panel.

recordings do not allow clear first seismic arrivals detection. This is due to the fact that the noise is in this case not exclusively of harmonic and high amplitude nature, but it is also a different noise originating from tube waves. Tube waves are considered to be of low frequency and relatively dispersive (Biot, 1952). Figure 6.4 compares the results presented in Figure 5.9, where 0.1% of cable was lowered down the borehole and the coupling detection algorithm confirmed poor coupling conditions and Figure 5.10, where 0.5% of cable was lowered down the borehole and the coupling detection algorithm indicated good coupling conditions even though this was not true. In addition to the time-domain signal and the time-varying frequency analysis, Figure 6.4 also shows the frequency spectrum in the lower panel of both signals. We note that the magnitude is lower in the right panel because the energy is spread across more frequencies. Then, the detection algorithm indicated good coupling because the threshold was not crossed. Of course, we can simply lower the threshold, but there are other ways to improve the algorithm in terms of robustness so that it can be reliably used in most scenarios (Nixon and Aguado, 2002). For example, in our algorithm we require the spectrum to be harmonic where the energy at the fundamental frequency is clearly peaking and the spectrum contains only frequencies that are multiples of the fundamental frequency. Requiring the spectral distribution function to be constant across all frequencies, would prevented the the wrong information about the coupling conditions and only allowed the signal to be white noise (Hayes, 1996), as shown in Figure 6.5. In general, signal detection theory has a long history in electrical engineering and many applications have been proposed (Schonhoff and Giordano, 2007). Implementing some of these methods would allow us to add more robustness to the algorithm and provide more reliable results.

### Multi-component DAS to record the entire wavefield

One of the disadvantages of DAS is the limitation of the system to be sensitive to axial strain only. This implies that DAS is a single-component measurement system and, consequently, allows only limited wavefield recordings. In VSP surveys with large source offsets, for instance, compressional waves arrive perpendicular to the fibre cable, and thus DAS is not able to detect the event. Den Boer et al. (2013) and Crickmore and Hill (2014) proposed to alter the cable design to make the cable sensitive to broadside signals, while Martin et al. (2013) altered the pattern of the cable during land acquisition. However, all these methods have not been implemented on a commercial basis and it appears that research and development in this area still offers great potential to improve the technology.

### Performance test using different cable designs

Farhadiroushan et al. (2015) proposed to alter the properties of the cable to improve the sensitivity to acoustic waves. In Section 5.3 we showed, using

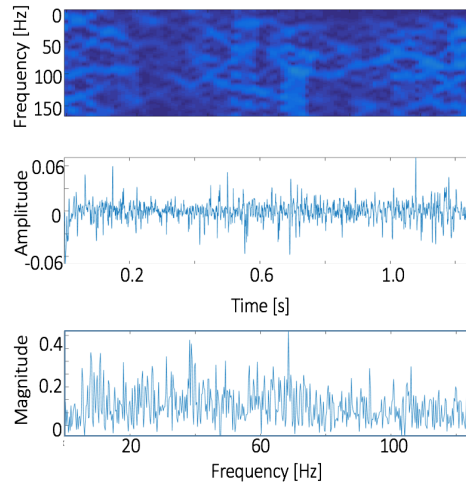


Figure 6.5: Noise analysis of DAS data acquired in Bottesford, when 2.0% of additional cable were lowered down the borehole. In addition to the results of the STFT and the time-domain representation of the signal, the frequency spectrum is presented in lower panel.

numerical methods, that changing the elastic properties of the cable does influence the recorded signal significantly. Since we proposed definite numbers, a manufactured cable with optimised properties will certainly increase the overall performance of the DAS system. Ideally, manufacturing cables with varying elastic properties could be used to confirm numerical results, and consequently allow us to find the optimal solution for a DAS cable in VSP surveys.

### **A fibre with densely spaced reflectors to increase the SNR**

In addition to changing the cladding, coating and cable reinforcement layers, as suggested in the previous section, another way to increase the sensitivity of the system to seismic waves is to modify the silica glass of the fibre cable. In Section 1.1, we have seen that the light pulse is backscattered at heterogeneities within the fibre, that are intrinsic, and thus randomly caused during the manufacturing process. Instead of this random distribution, [Englich and Hartog \(2016\)](#) proposed manufacturing a fibre with densely spaced, non-naturally occurring discrete reflectors. The general idea is illustrated in Figure 6.6 (modified from Figure 1.3), where the three reflectors are indicated with relatively large circles. This method would potentially allow us to increase the reflection coefficient at known locations, and therefore to increase the overall SNR of the measurement.

### **A higher spatial resolution with DAS**

Besides the SNR, also the spatial resolution of DAS can be optimised. In general, DAS systems require the user to make trade-offs between the SNR

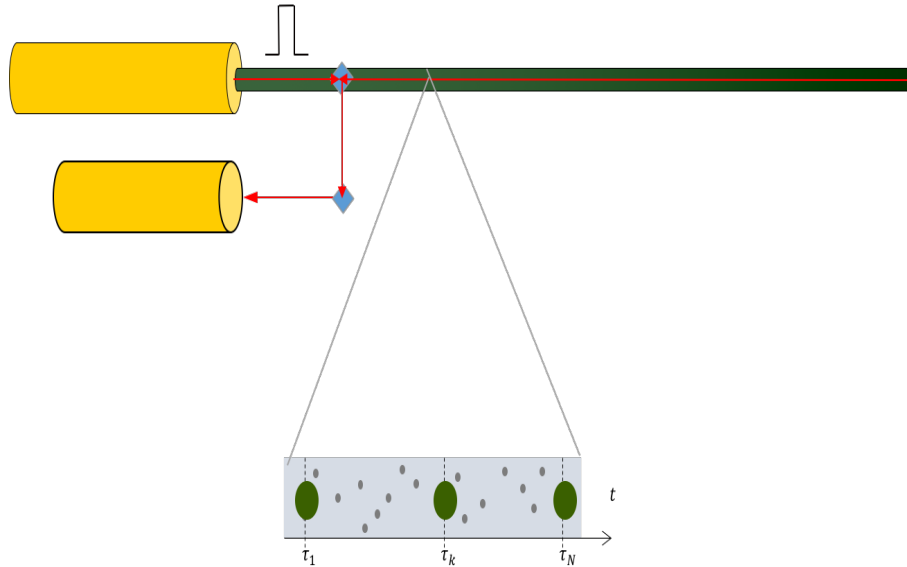


Figure 6.6: A schematic sketch adapted from Figure 1.3 to illustrate the concept of a fibre with densely spaced, non-naturally occurring reflectors.

and the spatial resolution of acquired data. In Section 1.3, we have seen that a gauge length is usually chosen, such that a spatial resolution of 10 m is obtained. Recall that the gauge length is the differentiation between two samples, that is required to maintain a monotonic signal because the length on the injected light pulse is usually a few meters, and thus larger than the sampling. For borehole seismic applications, a gauge length chosen to be 1/2 the wavelength of the seismic wave is sufficient to detect the features of interest (Dean et al., 2015). However, for applications such as microseismic detection where interest is in higher frequencies, a large gauge length can cause problems (Molteni et al., 2016). To obtain a shorter gauge length, a shorter pulse duration is required and to maintain a reasonable SNR for the shorter pulse duration, the peak power of the laser needs to be increased. However, the level of peak power cannot be increased to arbitrary levels owing to optical non-linear effects (Hartog, 2017).



## List of Figures

1.1	Submarine fibre optical cable used for data transition, similar to the wireline cable that is used for VSP with a diameter of 1 cm. . . . .	3
1.2	Sketch of a VSP survey using an array of conventional point sensors (left) and DAS technology (right). . . . .	4
1.3	Rayleigh backscattering and OTDR. . . . .	9
1.4	Schematic arrangement and specimen signals DAS system with coherent optical detection (adapted from Hartog et al. (2013)). . . . .	10
1.5	Displaced position of an individual backscatter with travel-time $\tau_k$ shown in Figure 1.3. . . . .	12
1.6	Processing of optical data. . . . .	13
1.7	Survey design for Chambon dataset, with a walkaround geometry measurements to test the response of the fiber at different angles of incidence. . . . .	15
1.8	Comparison of in-line component of geophones (black) and the bare fiber measurement (red) (adapted from (Papp, 2013)).	16
1.9	Comparison of cross-line component of geophones (black) and the bare fiber measurement (red) (adapted from (Papp, 2013)). . . . .	16
1.10	Comparison of vertical component of geophones (black) and the bare fiber measurement (red) (adapted from (Papp, 2013)).	17
1.11	Comparison of in-line component of geophones transformed into strain (blue) and the bare fiber measurement (black). . .	18
1.12	Survey design of the dataset acquired in Cambridge. . . . .	19
1.13	Comparison of hDVS data (left), inline-component of geophone (center) and inline-geophone data after transform to reproduce hDVS data (right). . . . .	20

List of Figures

1.14	Different fibre samples side by side: (1) 9/125 $\mu\text{m}$ Low Smoke, Zero Halogen (LSZH) kevlar jacketed cable; (2) SMF-28e bare fibre inside a 1 mm diameter metal tube; (3) 900 $\mu\text{m}$ buffered fibre; (4) SMF-28e bare fibre (adapted from Papp (2013)). . . . .	21
1.15	Comparison of in-line component of geophones (black) and the fiber with metal tubing measurement (red) (adapted from (Papp, 2013)). . . . .	22
1.16	Comparison of in-line component of geophones (black) and the 900 $\mu\text{m}$ buffered fiber measurement (red) (adapted from (Papp, 2013)). . . . .	22
1.17	Deployment techniques using DAS for VSP surveys. 1. on the left the cable is cemented behind the casing, 2. in the center the cable is attached with rigid clamps to the tubing, and 3. on the right the cable is loosely lowered down the borehole, also called wireline deployment. . . . .	23
1.18	Fibre recordings when cemented behind the casing. Linear stack of 10 shots in 1000 m long vertical well. . . . .	24
1.19	Fibre recordings when clamped to the tubing. Linear stack of 20 sweeps in 4300 m long vertical well (adapted from Barberan et al. (2012)). . . . .	24
1.20	Fibre recordings when deployed on wireline cable, where the signal is expected to be around 850 ms and indicated with a red circle. Linear stack of 8 shots in a 240 m long vertical well. . . . .	25
1.21	hDVS data using different cable length; a) cable under tension b) small tension release c) intermediate tension release d) maximum tension release (adapted from Hartog et al. (2014)). . . . .	27
2.1	The moment of a force $\mathbf{F}$ about an axis $o$ (adapted from Kelly (2013)). . . . .	34
2.2	An elastic plane wave with wavenumber vector $\mathbf{k}$ incident on a circularly cylindrical fluid-filled borehole at an angle $\delta$ . The borehole axis and $\mathbf{k}$ define the $x,z$ -plane and the azimuthal angle $\theta$ is measured from the $x$ -axis as shown. $\alpha_f$ and $\rho_f$ are the sound speed and density, respectively, of the fluid. $\alpha$ , $\beta$ , and $\rho$ are the compressional wave velocity, shear-wave velocity, and density, respectively, of the elastic medium (Schoenberg, 1986). . . . .	41
2.3	Contrast response $C$ varying with the length (in m) of the spike $h$ . The density of the geophone is $\rho_{geophone} = 7800 \text{ kg/m}^3$ , and the densities of the ground are $\rho_{soil} 2000 \text{ kg/m}^3$ (solid line), $3000 \text{ kg/m}^3$ (long dashed line) and $4000 \text{ kg/m}^3$ (short dashed line) (adapted from Vos et al. (1995)). . . . .	45
2.4	One-dimensional mapping of contact loaded normally (adapted from Popov and Hess (2015)). . . . .	47

2.5	Setting of a simple model with a pressure load ( $F_N$ ) pressing the cylinder onto a flat surface. $R = 2R_1$ denotes the diameter of the cylinder, while $E_1, E_2$ are the Young's modulus of the cylinder and the half-space, $\nu_1, \nu_2$ their Poisson's ratios and $\rho_1, \rho_2$ their densities, receptively. . . . .	49
2.6	Snapshot of the simulation when the contact between the two bodies occurred. On the bottom part of the flat elastic half-space, nodes have been constrained to prevent any vertical displacement. The load (vertical force $F_N$ in Equation 2.55) pressing the cylinder onto the flat surface has been applied on all nodes of the cylinder. . . . .	50
2.7	Radius of contact area with increasing contact force. The solid line denotes the analytical solution (Equation 2.55), while the dots are results of the numerical approximation. The cylinder has a Young's modulus of $2.7 \cdot 10^{11}$ Pa. . . . .	50
2.8	Radius of contact area with increasing contact force as seen in Figure 2.7. The Young's modulus of the cylinder has been modified to $4.5 \cdot 10^{11}$ Pa. . . . .	51
2.9	Radius of contact area with increasing contact force and varying elastic properties. While stiff and heavy materials (high $E$ , high $\rho$ ) only form a small contact area, more flexible and lighter materials (low $E$ , low $\rho$ ) form a bigger contact area. . . . .	51
3.1	A set of basis functions $\gamma_i$ used to approximate $p$ . . . . .	56
3.2	Scheme of the general procedure followed by weighted residual methods, such as the Galerkin approach. . . . .	59
3.3	FEM summarised in 4 steps. . . . .	63
3.4	Workflow of a typical FEA job. . . . .	64
3.5	Example of different finite elements (adapted from Dean (2016)). . . . .	65
3.6	2D Numerical model with dimensions 400 m x 400 m. The seismic source is located in the center, and a receiver is placed at distance offset $x=50$ m and $y=25$ m. . . . .	67
3.7	Numerical (blue) and analytical (red) solution of the vertical (left panel) and horizontal (right panel) components of particle velocity for different grid sizes. 5 m of grid size is presented in 1a and 1b, 3 m in 2a,b, 2 m in 3a,b and in 4a,b a grid size of 1 m is shown. . . . .	68
3.8	Plane P-wave propagation in a beam structure with PML applied at one end. . . . .	70
3.9	Particle velocity at a receiver at $y=350$ m in Figure 3.8. Upper panel: $v_y$ without PML; lower panel: $v_y$ with PML included . . . . .	71
3.10	Numerical model for 3D elastic wave propagation. The directional point source is located in the center of the free surface. PML have been implemented on the edges. . . . .	71

*List of Figures*

3.11	Cross-section of the numerical model, where upper part of the numerical model is elastic medium, and the lower part is acoustic medium. The upper panel shows wave propagation at $t = 0.1256$ s and the lower panel at $t = 0.1544$ s. The directional point source is buried in the elastic medium. . . .	72
3.12	Numerical model with dimensions 240 m x 120 m x 600 m. The red part illustrates the region of linear isotropic element i.e. where seismic wave propagation is computed, while the blue elements are perfectly matched layer to simulate an infinite domain. . . . .	74
3.13	Zoom region of the borehole. The part of the formation is visible in turquoise, in red is the casing, in pink the fluid column and in yellow the streamer. The grid size is approximately 0.001 m. . . . .	75
3.14	Automatised meshing creating tetrahedral-shaped brick elements. The sudden decrease in grid size from 3 m to 0.01 m causes strong artificial reflections due to the apparent stiffness of the elements. . . . .	76
3.15	A numerical model to test mapped meshing with the objective to develop a horizontally (black circle) and azimuthally (blue circle) optimised meshing algorithm to avoid artificial reflections commonly found when a sudden change in element size occurs. . . . .	77
3.16	Mapped meshing with continuous refinement of elements. An azimuthally and horizontally optimised mesh grid prevents strong artificial reflections, but is more difficult to implement as a repetitive meshing needs to be coded beforehand. . . . .	78
3.17	2D seismic wave propagation in the numerical model with uniform meshing. The seismic source is located at $x=24$ m. . . . .	79
3.18	2D seismic wave propagation in the mesh refined numerical model. The seismic source is located at $x=24$ m and the mesh refined area is around $x=0$ m. . . . .	80
3.19	Comparison of the vertical component of particle velocity between the model with uniform mesh and the model with the mesh refined area. The upper panel shows the particle velocity at $y=46$ m and $x=23$ m and the lower panel shows the particle velocity at $y=46$ m and $x=-23$ m. . . . .	80
3.20	Horizontal motion. The gray scale plot in the upper left corner shows the radial particle velocity of the streamer in the borehole fluid. The radial particle velocity at the borehole wall is presented in the upper right corner. A single trace plot of both results at 300 m depth is shown in the bottom plot highlighting the similarity of the two measurements. . . . .	83

3.21	Vertical motion. The gray scale image in the upper left corner presents the vertical particle velocity of the streamer in the borehole fluid. The vertical particle velocity at the borehole wall is shown in the upper right corner. A single trace plot of both results at 300 m depth is shown in the bottom plot. . . . .	84
3.22	The numerical model that is used to analyse the movement and position of the cable during the DAS VSP survey on wire-line cable. The borehole wall is in green, while the DAS cable is in red. A topview is shown on the left, and a side-view is given on the right. . . . .	86
3.23	Model of the heptacable. The three fibre cables are indicated in red, while other materials are for electrical or cable reinforcement purposes. . . . .	87
3.24	Bernoulli-Euler beam (adapted from Astley (1992)). . . . .	88
4.1	The Schlumberger training site near Bottesford indicated within the a red circle. . . . .	93
4.2	Comparison of VSI data (top panel), DAS data (middle panel) and numerical results (lower panel) of the field test in Bottesford. The arrows indicate different wave modes. Arrows in red are point to P-wave first arrivals, green ones to S-waves, black arrows to reflections and blue ones to tube waves. . . . .	94
4.3	Recorded signal by the DAS system with increasing tension release (after Hartog et al. (2014)). From top to bottom: 0.0%, 0.5%, 1.0%, 1.5% and 2.0% of additional cable lowered down the borehole. . . . .	96
4.4	Numerical analysis when the position of the cable in the borehole is altered. Top: slices of the mesh used in the numerical modeling with the DAS cable represented in yellow, the fluid in pink, the casing in red and the formation in turquoise; middle: numerical solution of the vertical component of particle velocity as detected by the cable; bottom: numerical solution of the horizontal component of particle velocity as detected by the cable. The tube wave arrival is indicated with a blue arrow, S-wave with a green arrow and P-wave with a red arrow. . . . .	98
4.5	Amount of extra cable that has been lowered in the borehole. Equivalently to the real survey, we lower a total of 12 m of extra cable down the numerical model of the borehole in stages to analyse the new positions of the cable in the borehole. The time in seconds corresponds to the simulation time. . . . .	99

*List of Figures*

4.6	DAS data recorded with increasing tension release (a) and corresponding numerical results (b and c). From top to bottom: (1) cable under full tension; (2) cable with minimal tension release; (3) cable with 0.5%, (4) 1.0% and (5) 2.0% of extra cable being lowered down the borehole. Numerical results in (b) illustrate the motion of the cable during this procedure. Results in (c) represent the contact forces between the cable and borehole wall numerically evaluated for each stage of cable slack along the well depth. . . . .	100
4.7	The training site for the second test was located in Livingston near Edinburgh. . . . .	102
4.8	The set-up of the field test in Livingston. The DAS cable is lowered down the borehole from a winch visible in the background of the image. . . . .	103
4.9	The numerical model that is used to analyse the movement and position of the cable during the DAS survey in Livingston. The borehole wall is in yellow, while the DAS cable is in red. A topview is shown on the left where the varying inner diameter of the borehole can be observed, and a side-view is given on the right. . . . .	105
4.10	The same analysis as shown in Figure 4.6 for a second field trial conducted in March 2016 in Livingston, UK. From top to bottom: (1) corresponds to minimal tension release, (2) 0.5% (3) 1.0% and (4) 2.0% of cable slack. In (a) seismic data acquired by the DAS system are shown. Numerical results are presented in (b) and (c), where in (b) the position of the cable is shown after each stage of cable slack and in (c) the corresponding contact force is plotted along the entire borehole length. . . . .	106
5.1	The numerical model used to analyse the sensitivity of the cable to seismic waves. The upper panel shows the borehole wall including some outer formation. The lower panel is a zoom of the hollow part of the borehole, where the cable is shown in yellow. . . . .	111
5.2	Seismic signals with increasing contact force. Blue is the particle velocity as detected by the borehole wall (reference) and red is the particle velocity as detected by the cable at the same position in depth. Shown are signals with increasing contact force, where the lateral force in (a) is 10 N, in (b) 15 N, in (c) 20 N, in (d) 40 N and in (e) 80 N. . . . .	113

5.3	Three theoretical cable configurations that are used to detect seismic signals when coupled to the borehole wall. Blue is the particle velocity recorded at the borehole wall (reference) and red is the particle velocity recorded by the cable. The top panel shows the recordings of the heptacable (high stiffness), the middle panel recordings of a cable composed of PVC material (intermediate stiffness) and the bottom panel shows a cable made of rubber (very low stiffness). . . . .	116
5.4	The root-mean-square error (top) and the peak-to-peak error (center) and the normalised cross-correlation coefficients at zero lag (bottom) for different cable configuration. The left plot shows the actual error values for 36 different cable configurations, and the right plot represents the same matrices after cubic interpolation. . . . .	118
5.5	Waveforms of realistic cable configurations with different elastic properties. The best match is a cable with a Young's modulus of $10^9$ N/m <sup>2</sup> and a density of 5000 kg/m <sup>3</sup> and a Poisson's ratio of 0.45, while the static friction coefficient is 0.5. . . . .	119
5.6	Analysis of varying Poisson's ratio using the cable configuration in Figure 5.5 with a Young's modulus of $10^9$ N/m <sup>2</sup> and a density of 5000 kg/m <sup>3</sup> . Shown are results with a Poisson's ratio of 0.05, 0.25 and 0.45, while the static friction coefficient is 0.5. . . . .	120
5.7	Analysis of varying static coefficient of friction using the cable configuration in Figure 5.5 with a Young's modulus of $10^9$ N/m <sup>2</sup> and a density of 5000 kg/m <sup>3</sup> . Shown are results with a friction coefficient of 0.9, 0.45 and 0.05, while Poisson's ratio is 0.45. . . . .	121
5.8	Noise analysis of DAS data acquired in Bottesford when the cable is under full tension. Left: noise recordings (upper panel) and seismic recordings (lower panel); right: time-domain signal (lower panel) and corresponding time-frequency analysis (upper panel). . . . .	122
5.9	Noise analysis of DAS data acquired in Bottesford when 0.1% of excess cable were lowered down the borehole. Left: noise recordings (upper panel) and seismic recordings (lower panel); right: time-domain signal (lower panel) and corresponding time-frequency analysis (upper panel). . . . .	123
5.10	Noise analysis of DAS data acquired in Bottesford when 0.5% of excess cable were lowered down the borehole. Left: noise recordings (upper panel) and seismic recordings (lower panel); right: time-domain signal (lower panel) and corresponding time-frequency analysis (upper panel). . . . .	123

*List of Figures*

5.11	Noise analysis of DAS data acquired in Bottesford when 1.0% of excess cable were lowered down the borehole. Left: noise recordings (upper panel) and seismic recordings (lower panel); right: time-domain signal (lower panel) and corresponding time-frequency analysis (upper panel). . . . .	124
5.12	Noise analysis of DAS data acquired in Bottesford when 2.0% of excess cable were lowered down the borehole. Left: noise recordings (upper panel) and seismic recordings (lower panel); right: time-domain signal (lower panel) and corresponding time-frequency analysis (upper panel). . . . .	124
5.13	Noise analysis of DAS data acquired in Livingston when the cable was held under tension the borehole. Left: noise recordings (upper panel) and seismic recordings (lower panel); right: time-domain signal (lower panel) and corresponding time-frequency analysis (upper panel). . . . .	126
5.14	Noise analysis of DAS data acquired in Livingston when 0.5% of extra cable was lowered down the borehole. Left: noise recordings (upper panel) and seismic recordings (lower panel); right: time-domain signal (lower panel) and corresponding time-frequency analysis (upper panel). . . . .	127
5.15	Noise analysis of DAS data acquired in Livingston when 1.0% of extra cable was lowered down the borehole. Left: noise recordings (upper panel) and seismic recordings (lower panel); right: time-domain signal (lower panel) and corresponding time-frequency analysis (upper panel). . . . .	127
5.16	Noise analysis of DAS data acquired in Livingston when 2.0% of extra cable was lowered down the borehole. Left: noise recordings (upper panel) and seismic recordings (lower panel); right: time-domain signal (lower panel) and corresponding time-frequency analysis (upper panel). . . . .	128
5.17	The coupling detection algorithm applied to the DAS acquired data in Livingston. Left: DAS recordings; right: results of the coupling detection algorithm, where 0 is good coupling and 1 is poor coupling. . . . .	130
5.18	The coupling detection algorithm applied to the DAS acquired data in Bottesford. Left: DAS recordings; right: results of the coupling detection algorithm, where 0 is good coupling and 1 is poor coupling. . . . .	131
6.1	Schematic diagram showing the basic concept of the grid injection method (adapted from Robertsson and Chapman (2000)). Initial model with source and receivers placed at the surface (a), and new source and receivers position close to the region of interest(b). . . . .	137

6.2	Sketch of the numerical model that has been used to test the grid injection method. . . . .	138
6.3	Numerical results of the grid injection method test. The upper panel on the left shows numerical results of the full seismic wave propagation model and the results of the grid injection method are shown in the lower panel. A comparison of a single trace of receiver $x=0$ m, $y=25$ m and $z=10$ m is shown on the right. . . . .	139
6.4	Noise analysis of DAS data at a depth of 300 m acquired in Bottesford when 0.1% (left) and 0.5% (right) of extra cable was lowered down the borehole. For both signals, the time-frequency analysis is shown in the upper panel, the time-domain signal is in the middle panel and its frequency spectrum is presented in lower panel. . . . .	140
6.5	Noise analysis of DAS data acquired in Bottesford, when 2.0% of additional cable were lowered down the borehole. In addition to the results of the STFT and the time-domain representation of the signal, the frequency spectrum is presented in lower panel. . . . .	142
6.6	A schematic sketch adapted from Figure 1.3 to illustrate the concept of a fibre with densely spaced, non-naturally occurring reflectors. . . . .	143



## Bibliography

- B. Ainslie, K. Beales, C. Day, and J. Rush. Interplay of design parameters and fabrication conditions on the performance of monomode fibers made by MCVD. *17(6):854–857*, 1981. (Cit. on pp. [8](#).)
- K. Aki and P. G. Richards. *Quantitative Seismology*. W.H. Freeman & Co, 1980. (Cit. on pp. [2](#), [32](#), and [73](#).)
- W. Aki. *Scattering and Attenuation of Seismic Waves, Part II*. Springer, 1989. (Cit. on pp. [66](#).)
- D. Arney and J. Flaherty. An adaptive mesh moving and local refinement method for time dependent partial differential equations. *ACM Transactions on Mathematical Software*, *16(1):48–71*, 1990. (Cit. on pp. [62](#).)
- J. Arroyo, P. Breton, S. Dingwall, R. Guerra, R. Hope, B. Hornby, M. Williams, R. Jimenez, T. Lastenner, J. Tullet, S. Leany, T. Lim, H. Menkiti, J-C. Puech, S. Tcherkashnev, T. Burt, and M. Verliac. Superior seismic data from the borehole. *Oilfield Review*, *15(1):2–23*, 2003. (Cit. on pp. [6](#), [93](#), and [105](#).)
- R. J. Astley. *Finite Elements in Solids and Structures: An Introduction*. Chapman & Hall, 1992. (Cit. on pp. [86](#), [88](#), and [149](#).)
- I. Babuska and B. Guo. The h, p and h-p version of the finite element method: basis theory and applications. *Advances in Engineering Software*, *15(3-4):159–174*, 1992. (Cit. on pp. [62](#).)
- I. Babuška, B. Szabó, and I. Katz. The p-version of the finite element method. *SIAM Journal of Numerical Analysis*, *18(3):515–545*, 1981. (Cit. on pp. [62](#).)
- M. Baines, M. Hubbard, and P. Jimack. A moving mesh finite-element algorithm for the adaptive solution of time-dependent partial differential equations with moving boundaries. *Applied Numerical Mathematics*, *54(3-4):450–469*, 2005. (Cit. on pp. [136](#).)

## Bibliography

- A. Balch and M. Lee. *Vertical Seismic Profiling: Technique, Applications and Case Histories*. D. Reidel Publishing Company, 1984. (Cit. on pp. 2 and 95.)
- C. Barberan, C. Allanic, D. Avila, J. Hy-Billiot, A. Hartog, B. Frignet, and G. Lees. Multi-offset seismic acquisition using optical fiber behind tubing. *74th EAGE Conference Exhibition, Copenhagen, Denmark*, 2012. (Cit. on pp. 5, 23, 24, 42, and 146.)
- U. Basu and A. K. Chopra. Perfectly matched layers for time-harmonic elastodynamics of unbounded domains: theory and finite-element implementation. *Computer Methods in Applied Mechanics and Engineering*, 19(11-12): 1337–1375, 2003. (Cit. on pp. 81.)
- U. Basu and A.K. Chopra. Perfectly matched layers for transient elastodynamics of unbounded domains. *International Journal for Numerical Methods in Engineering*, 61(1):156–157, 2004. (Cit. on pp. 81.)
- K-J. Bathe. *Finite Element Procedures*. Prentice Hall, 1996. (Cit. on pp. 55, 57, and 60.)
- M. Batzle and Z. Wang. Seismic properties of pore fluids. *Geophysics*, 57(11): 1396–1408, 1992. (Cit. on pp. 6.)
- O.A. Bauchau and J.I. Craig. Solid mechanics and its applications. In *Euler-Bernoulli beam theory*, volume 163, chapter Structural Analysis, pages 173–221. Springer, 2009. (Cit. on pp. 86.)
- K. Beales, C. Day, W. Duncan, A. Dunn, P. Dunn, G. News, and J. Wright. Low loss graded index fiber by double crucible technique. *5th European Conference on Optical Fibre Communications, Amsterdam, Netherlands*, 1979. (Cit. on pp. 8.)
- J-P. Berenger. A perfectly matched layer for the absorption of electromagnetic waves. *Journal of Computational Physics*, 114(2):185–200, 1994. (Cit. on pp. 69 and 81.)
- P. Bettinelli and B. Frignet. Optical fiber seismic acquisition for well-to-seismic tie at the Ketzin pilot site (CO<sub>2</sub>storage). *85th SEG Annual Meeting, New Orleans, USA*, 2015. (Cit. on pp. 5.)
- M. A. Biot. Propagation of elastic waves in cylindrical borehole containing a fluid. *Journal of Applied Physics*, 23(9):997–1005, 1952. (Cit. on pp. 43 and 141.)
- J. Blackledge. *Digital Signal Processing: Mathematical and Computational Methods, Software Development and Applications*. Elsevier, 2006. (Cit. on pp. 14.)

- J. Blanco, G.S. Knudsen, and F. X. Bostick. Timelapse VSP field test for gas reservoir monitoring using permanent fiber optic seismic system. *76th SEG Annual Meeting, New Orleans, USA*, 2006. (Cit. on pp. 3.)
- N. Bleistein, J. Cohen, and W. Stockwell. *Mathematics of Multidimensional Seismic Imaging, Migration, and Inversion*. Springer, 2001. (Cit. on pp. 12.)
- J. Bunch and J. Hopcroft. Triangular factorization and inversion by fast matrix multiplication. *Mathematics of Computation*, 28(125):231–236, 1974. (Cit. on pp. 61.)
- C. Chapman. *Fundamental of seismic waves propagation*. Cambridge University Press, 2004. (Cit. on pp. 2, 32, and 73.)
- C.H. Cheng and M.N. Toksöz. Elastic wave propagation in a fluid-filled borehole and synthetic acoustic logs. *Geophysics*, 46(7):1042–1053, 1981. (Cit. on pp. 43.)
- C.H. Cheng and M.N. Toksöz. Generation, propagation and analysis of tube waves in a borehole. In *Vertical Seismic Profiling. Part B: Advanced Concepts*. Geophysical Press, 1984. (Cit. on pp. 23, 43, and 95.)
- S. Chopra, L. Lines, D. Schmitt, and M. Batzle. 1. Heavy-oil reservoirs: Their characterization and production. In *Heavy Oils*, pages 1–69. Society of Exploration Geophysicists, 2012. (Cit. on pp. 6.)
- M. Clark and D. Mackie. Portable airgun tank - a new approach to land BHS using airguns. *Second EAGE Workshop on Borehole Geophysics, Malta*, 2013. (Cit. on pp. 25 and 92.)
- A. Constantinou, A. Farahani, T. Cuny, and A.H. Hartog. Improving DAS acquisition by real-time monitoring of wireline cable coupling. *86th SEG Annual Meeting, Dallas, USA*, 2016. (Cit. on pp. 5.)
- B. Cox, B. Wills, D. Kiyashchenko, J. Mestayer, S.B. Lopez, R. Lupton, G. Solano, N. Henderson, D. Hill, and J. Roy. Distributed acoustic sensing for geophysical measurement, monitoring, and verification. *CSEG Recorder*, 37(2):7–13, 2012. (Cit. on pp. 5.)
- J. Cressler and H. Mantooth. *Extreme Environment Electronics*. CRC Press, 2012. (Cit. on pp. 3.)
- R. Crickmore and D. Hill. Fibre optic cable for acoustic/seismic sensing. WO 2014064460, 2014. (Cit. on pp. 4, 7, and 141.)
- T. Daley, B. Freifeld, J. Ajo-Franklin, S. Dou, R. Pevzner, and Shulakova V. Field testing of fiber-optic distributed acoustic sensing (DAS) for subsurface seismic monitoring. *Leading Edge*, 32(6):699–706, 2013. (Cit. on pp. 5.)

## Bibliography

- A.T. de Hoop. A modification of Cagniard's method for solving seismic pulse problems. *Applied Scientific Research*, B8:349–356, 1960. (Cit. on pp. 67.)
- J. Dean. *Introduction to the Finite Element Method (FEM)*. University of Cambridge, 2016. (Cit. on pp. 65 and 147.)
- T. Dean, T. Cuny, and A.H. Hartog. Determination of the optimum gauge length for borehole seismic surveys acquired using distributed vibration sensing. *77th EAGE Conference and Exhibition, Madrid, Spain*, 2015. (Cit. on pp. 4, 7, and 143.)
- T. Dean, T. Cuny, A. Constantinou, P. Dickenson, C. Smith, and E. Hamouche. Depth calibration of fibre-optic distributed vibration sensing measurements. *78th EAGE Conference and Exhibition, Vienna, Austria*, 2016. (Cit. on pp. 5.)
- J. Den Boer, A. Mateeva, J.G. Pearce, J. Mestayer, W. Birch, and J. Lopez. Detecting broadside acoustic signals with a fiber optical distributed acoustic sensing (DAS). WO 2013090544, 2013. (Cit. on pp. 4, 7, and 141.)
- J. Diaz and A. Ezziani. Analytical solution for waves propagation in heterogeneous acoustic/porous media. part I: The 2D case. *Communications in Computational Physics*, 7(1):171–194, 2010. (Cit. on pp. 67 and 69.)
- G. Drijkoningen. The usefulness of geophone ground coupling experiments to seismic data. *Geophysics*, 65(6):1780–1787, 2000. (Cit. on pp. 44.)
- K.F. Eldridge, O.W. Dillon, and W.Y. Lu. Thermo-viscoplastic finite element modelling of machining under various cutting conditions. *Journal of Manufacturing Science and Engineering*, 181(4):162–169, 1991. (Cit. on pp. 88.)
- F. Englich and A.H. Hartog. Fiber optic array having densely spaced, weak reflectors. US 20170010385, 2016. (Cit. on pp. 142.)
- M. Farhadiroushan, D. Finfer, D. Strusevich, S. Shatalin, and T. Parker. Non-isotropic acoustic cable. WO 2015036735, 2015. (Cit. on pp. 5, 7, and 141.)
- E.I. Galperin. *Vertical Seismic Profiling*. Society of Exploration Geophysicists, 1974. (Cit. on pp. 2 and 95.)
- E.I. Galperin. *Vertical Seismic Profiling and its Exploration Potential*. D. Reidel Publishing Company, 1985. (Cit. on pp. 25.)
- J.E. Gentle. *Numerical Linear Algebra for Applications in Statistics*. Springer, 1998. (Cit. on pp. 61.)
- G. Green. An essay on the application of mathematical analysis to the theories of electricity and magnetism. *Harvard University*, 1828. (Cit. on pp. 58.)

- B.A. Hardage. An examination of tube wave noise in vertical seismic profiling. *Geophysics*, 46(6):892–903, 1981. (Cit. on pp. 25.)
- B.A. Hardage. *Vertical Seismic Profiling. Part A: Principles*. Geophysical Press, 1983. (Cit. on pp. 2, 23, 39, 44, and 95.)
- A. Hartog, O.I. Kotov, and L. Liokumovich. The optics of distributed vibration sensing. *Second EAGE Workshop on Permanent Reservoir Monitoring - Current and Future Trends, Stavanger, Norway*, 2013. (Cit. on pp. 4, 9, 10, and 145.)
- A. Hartog, B. Frignet, D. Mackie, and M. Clark. Vertical seismic optical profiling on wireline logging cable. *Geophysical Prospecting*, 62(4):693–701, 2014. (Cit. on pp. 5, 26, 27, 55, 85, 92, 96, 97, 101, 133, 134, 146, and 149.)
- A.H. Hartog. *An Introduction to Distributed Optical Fibre Sensors*. CRC Press, 2017. (Cit. on pp. 4, 8, 9, 10, 13, 14, and 143.)
- A.H. Hartog and K. Kader. Distributed fibre optic sensor system with improved linearity. WO 2012030814, 2012. (Cit. on pp. 7 and 9.)
- A.H. Hartog, L. Liokumovich, A. Ushakov, O. Kotov, T. Dean, T. Cuny, and A. Constantinou. The use of multi-frequency acquisition to significantly improve the quality of fibre-optic distributed vibration sensing. *78th EAGE Conference and Exhibition, Vienna, Austria*, 2016. (Cit. on pp. 4 and 7.)
- M. Hayes. *Statistical Digital Signal Processing and Modeling*. John Wiley & Sons, 1996. (Cit. on pp. 125 and 141.)
- P. Healey. Fading in heterodyne OTDR. *Electronic Letters*, 20(1):30–32, 1984. (Cit. on pp. 10 and 104.)
- H. Hertz. Ueber die Beruehrung fester elastischer Koerper. *Journal für reine und angewandte Mathematik*, 92(156-171), 1881. (Cit. on pp. 46 and 47.)
- G. Holzapfel. *Nonlinear Solid Mechanics*. John Wiley & Sons, 2001. (Cit. on pp. 32, 36, and 73.)
- K. Hornman. Field trial of seismic recording using distributed acoustic sensing with broadside sensitive fibre-optic cables. *Geophysical Prospecting*, 65(1):35–46, 2017. (Cit. on pp. 4 and 7.)
- K. Hornman, B. Kuvshinov, P. Zwartjes, and A. Franzen. Field trial of a broadside-sensitive distributed acoustic sensing cable for surface seismic. *75th EAGE Conference and Exhibition, London, UK*, 2013. (Cit. on pp. 4.)
- J. Houbolt. A recurrence matrix solution for the dynamic response of elastic aircraft. *Journal of the Aeronautical Sciences*, 17(9):540–550, 1950. (Cit. on pp. 60.)

## Bibliography

- T.J.R. Hughes and W.K. Liu. Nonlinear finite element analysis of shells: Part 1, three-dimensional shells. *Computer Methods in Applied Mechanics and Engineering*, (26):331–362, 1981. (Cit. on pp. 87.)
- K. Iwata, K. Osakada, and Y. Terasaka. Process modelling of orthogonal cutting by the rigid plastic finite element method. *Journal of Engineering Materials and Technology*, 106(2):132–138, 1984. (Cit. on pp. 88.)
- L. Jeunhomme. Single-mode fiber design for long haul transmission. *IEEE Journal of Quantum Electronics*, 18(4):727–732, 1982. (Cit. on pp. 8.)
- K.L. Johnson. *Contact Mechanics*. Cambridge University Press, 1985. (Cit. on pp. 32, 46, and 47.)
- P. Kelly. *Solid Mechanics Part I: An Introduction to Solid Mechanics*. University of Auckland, 2013. (Cit. on pp. 34 and 146.)
- M. Kittur and R. Huston. Mesh refinement in finite element analysis by minimization of the stiffness matrix trace. Technical report, University of Cincinnati, Cincinnati, USA, 1989. (Cit. on pp. 65 and 76.)
- K. Klem-Musatov, H. Hoerber, T. Moser, and M. Pelissier. *Seismic Diffraction*. Society of Exploration Geophysicists, 2016. (Cit. on pp. 32.)
- D. Komatitsch and J. Tromp. A perfectly matched layer absorbing boundary condition for the second-order seismic wave equation. *Geophysical Journal*, 154(1):146–153, 2003. (Cit. on pp. 69 and 81.)
- C. Krohn. Geophone ground coupling. *Geophysics*, 49(6):722–731, 1984. (Cit. on pp. 44.)
- B. Kuvshinov. Interaction of helically wound fibre-optic cables with plane seismic waves. *Geophysical Prospecting*, 64(3):671–688, 2016. (Cit. on pp. 4, 7, and 17.)
- H. Lamb. On the propagation of tremors over the surface of an elastic solid. *Philosophical Transactions of the Royal Society of London*, 204:1–42, 1904. (Cit. on pp. 66, 69, and 81.)
- M. Larson and F. Bengzon. *The Finite Element Method: Theory, Implementation, and Applications*. Springer, 2013. (Cit. on pp. 56.)
- R. Lee and A. Cangellaris. A study of discretization error in the finite element approximation of wave solutions. *IEEE Transactions on Antennas and Propagation*, 40(5):541–549, 1992. (Cit. on pp. 66.)
- A.R. Levander. Fourth-order finite-difference P-SV seismograms. *Geophysics*, 53(11):1425–1436, 1988. (Cit. on pp. 81.)

- G.R. Liu. *Meshfree Methods Moving Beyond the Finite Element Method*. CRC Press, 2005. (Cit. on pp. 85 and 136.)
- D. Lumley. Timelapse seismic reservoir monitoring. *Geophysics*, 66(1):50–53, 2001. (Cit. on pp. 2.)
- K. Madsen, T. Parker, and G. Gaston. A VSP field trial using distributed acoustic sensing in a producing well in the North sea. *74th EAGE Conference Exhibition, Copenhagen, Denmark*, 2012. (Cit. on pp. 4.)
- L. Malvern. *Introduction to the Mechanics of a Continuous Medium*. Pearson, 1977. (Cit. on pp. 36.)
- J. Martin, D. Donno, B. Papp, and A.H. Hartog. Fiber optic distributed vibration sensing with directional sensitivity. WO 2014201313, 2013. (Cit. on pp. 4 and 141.)
- A. Mateeva, J. Mestayer, B. Cox, D. Kiyashenko, P Wills, and S. Grandi. Distributed acoustic sensing (DAS) for reservoir monitoring with VSP. *Second EAGE Workshop on Borehole Geophysics, Malta*, 2013. (Cit. on pp. 5.)
- A. Mateeva, J. Lopez, H. Potters, J. Mestayer, B. Cox, D. Kiyashchenko, P. Wills, S. Grandi, K. Hornman, B. Kuvshinov, W. Berlang, Z. Yang, and R. Detomo. Distributed acoustic sensing for reservoir monitoring with vertical seismic profiling. *Geophysical Prospecting*, 62(4):679–692, 2014. (Cit. on pp. 5.)
- S.M. Maughan. *Distributed fibre sensing using microwave heterodyne detection of spontaneous brillouin backscatter*. PhD thesis, University of Southampton, Southampton, UK, 2001. (Cit. on pp. 8.)
- J. Mauro, R. Loucks, and P. Gupta. Fictive temperature and the glassy state. *Journal of the American Chemical Society*, 92(1):75–78, 2009. (Cit. on pp. 8.)
- J. Mestayer, G. S. Karam, B. Cox, P. Wills, A. Mateeva, and J. Lopez. Distributed acoustic sensing for geophysical monitoring. *74th EAGE Conference Exhibition, Copenhagen, Denmark*, 2012. (Cit. on pp. 4.)
- S. Moaveni. *Finite Element Analysis Theory and Application with ANSYS*. Prentice Hall, 3 edition, 2007. (Cit. on pp. 75 and 76.)
- D. Molteni, M.J. Williams, and C. Wilson. Comparison of microseismic events concurrently acquired with geophones and hDVS. *78th EAGE Conference and Exhibition, Vienna, Austria*, 2016. (Cit. on pp. 19 and 143.)
- K. Morton and D. Mayers. *Numerical Solution of Partial Differential Equations: An Introduction*. Cambridge University Press, 2005. (Cit. on pp. 62.)

## Bibliography

- J. Munn, T. Coleman, B. Parker, M. Mondanos, and A. Chalari. Novel cable coupling technique for improved shallow distributed acoustic sensor VSPs. *Journal of Applied Geophysics*, 138:72–79, 2017. (Cit. on pp. 5, 7, 110, and 112.)
- N. Newmark. A method of computation for structural dynamics. *ASCE Journal of Engineering Mechanics Division*, 85(3):67–94, 1959. (Cit. on pp. 60.)
- M Nixon and A. Aguado. *Feature Extraction and Image Processing*. Elsevier, 2002. (Cit. on pp. 141.)
- B. Papp. Rock-fiber coupling in distributed vibration sensing. Master’s thesis, Institut du Physique du Globe de Paris (IPGP), 2013. (Cit. on pp. 16, 17, 20, 21, 22, 145, and 146.)
- B. Papp, D. Donno, J. Martin, and A.H. Hartog. A study of the geophysical response of distributed fibre optic acoustic sensors through laboratory-scale experiments. *Geophysical Prospecting*, (0.1111/1365-2478.12471), 2017. (Cit. on pp. 4, 7, 15, 17, 18, and 19.)
- J.A. Pickhaver. Numerical modelling of building response to tunnelling. Master’s thesis, University of Oxford, Oxford, UK, 2006. (Cit. on pp. 86 and 90.)
- F. Poletto, D. Finfer, P. Corubolo, and B. Farina. Dual wavefields from distributed acoustic sensing measurements. *Geophysics*, 81(6):585–597, 2016. (Cit. on pp. 7 and 17.)
- V. Popov and M. Hess. *Method of Dimensionality Reduction in Contact Mechanics and Friction*. Springer, 2015. (Cit. on pp. 46, 47, and 146.)
- J. Reddy. *An Introduction to the Finite Element Method*. McGraw Hill Education, 3 edition, 2005. (Cit. on pp. 56.)
- R. Reinsch, J. Henniges, J. Götz, P. Jousset, D. Bruhn, and S. Lüth. Distributed acoustic sensing technology for seismic exploration in magmatic geothermal areas. *Proceedings World Geothermal Congress, Melbourne, Australia*, 2015. (Cit. on pp. 5.)
- J.A.O. Robertsson and C.H. Chapman. An efficient method for calculating finite-difference of seismograms after model alterations. *Geophysics*, 65(3):907–918, 2000. (Cit. on pp. 137 and 152.)
- S. Schilke, D. Donno, A. Hartog, A. Faharani, Y. Pico, and H. Chauris. Numerical evaluation of sensor coupling of distributed acoustic sensing systems in vertical seismic profiling. *86th SEG Annual Meeting, Dallas, USA*, 2016. (Cit. on pp. 5.)

- M. Schoenberg. Fluid and solid motion in the neighborhood of a fluid-filled borehole due to the passage of a low-frequency elastic plane wave. *Geophysics*, 51(6):1191–1205, 1986. (Cit. on pp. 23, 39, 40, 41, 42, 43, 73, 82, 112, and 146.)
- M. Schoenberg. Attenuation of acoustic modes due to viscous drag at the borehole wall. *Geophysics*, 52(1):1566–1569, 1987. (Cit. on pp. 25, 43, and 97.)
- T. Schonhoff and A. Giordano. *Detection and Estimation Theory*. Pearson, 2007. (Cit. on pp. 141.)
- J. Schroeder, R. Morh, P. Macedo, and C. Montrose. Rayleigh and Brillouin scattering in K2OP-SiO2 glasses, volume = 56, year = 1973. *Journal of the American Chemical Society*, (10):510–514. (Cit. on pp. 8.)
- G.S. Sekhon and J.L. Chenot. Numerical simulation of continuous chip formation during non-steady orthogonal cutting. *Engineering Computations*, 10(1):31–48, 1993. (Cit. on pp. 88.)
- J. Senior and Y. Jamro. *Optical Fiber Communications: Principles and Practice*. Prentice Hall, 2009. (Cit. on pp. 8.)
- R. E. Sheriff and L. P. Geldart. *Exploration Seismology*. Cambridge University Press, 1995. (Cit. on pp. 2, 6, and 93.)
- T. Shirakashi and E. Usui. Simulation analysis of orthogonal metal cutting mechanism. *Proceedings of the International Conference on Production Engineering, Tokyo, Japan*, 1974. (Cit. on pp. 88.)
- P. Šolín, K. Segeth, and I. Doležel. *Higher-order finite element methods*. Chapman & Hall/CRC Press, 2003. (Cit. on pp. 62.)
- T.H. Tan. Reciprocity theorem applied to the geophone-ground coupling problem. *Geophysics*, 52(12):1715–1717, 1987. (Cit. on pp. 44.)
- T. Tezduyar. *Finite Element Methods for Fluid Dynamics with Moving Boundaries and Interfaces*, chapter 17. Encyclopedia of Computational Mechanics, Volume 3: Fluids. John Wiley & Sons, 2004. (Cit. on pp. 85 and 136.)
- S. P. Timoshenko. On the correction factor for shear of the differential equation for transverse vibrations of bars of uniform cross-section. *Philosophical Magazine*, 41(245):744–746, 1921. (Cit. on pp. 87.)
- S. P. Timoshenko. On the transverse vibrations of bars of uniform cross-section. *Philosophical Magazine*, 43(253):125–131, 1922. (Cit. on pp. 87.)
- S. P. Timoshenko. *Strength of Materials - Part 1*. D. Van Nostrand Co Inc, 1957. (Cit. on pp. 87.)

## Bibliography

- M. Verliac, V. Lesnikov, and C. Euriat. The Rousse-1 DAS VSP experiment - observations and comparisons from various optical acquisition systems. *85th SEG Annual Meeting, New Orleans, USA*, 2015. (Cit. on pp. 4.)
- J. Virieux. SH-wave propagation in heterogeneous media: velocity-stress finite-difference method. *Geophysics*, 49(11):1933–1942, 1984. (Cit. on pp. 36.)
- J. Virieux. P-SV wave propagation in heterogeneous media: Velocity-stress finite-difference method. *Geophysics*, 51(4):889–901, 1986. (Cit. on pp. 36.)
- J. Virieux, H. Calandra, and Plessix R-E. A review of the spectral, pseudo-spectral, finite-difference and finite-element modelling techniques for geophysical imaging. *Geophysical Prospecting*, 59(5):794–813, 2011. (Cit. on pp. 58, 59, and 62.)
- J. Vos, G. Drijkoningen, and J. Fokkema. A theoretical and experimental approach to the geophone-ground coupling problem based on acoustic reciprocity. *65th SEG Annual Meeting, Houston, USA*, 1995. (Cit. on pp. 44, 45, and 146.)
- W. Wall and E. Ramm. Fluid-structure interaction based upon a stabilized (ALE) finite element method. *Computational Mechanics, New Trends and Applications, Barcelona, Spain*, 1998. (Cit. on pp. 85 and 136.)
- E. Wilson, I. Farhoomand, and K-J. Bathe. Nonlinear dynamic analysis of complex structures. *International Journal of Earthquake Engineering and Structural Dynamics*, 1(3):241–252, 1973. (Cit. on pp. 60.)
- W. Wood. *Practical Time-stepping Schemes*. Clarendon Press, 1990. (Cit. on pp. 60.)
- P. Wriggers. *Nonlinear finite element methods*. Springer, 2008. (Cit. on pp. 61.)
- J.S. Wu, O. W. Dillon, and W.Y. Lu. Thermo-viscoplastic modeling of machining process using a mixed finite element method. *Journal of Manufacturing Science and Engineering*, 118(4):428–470, 1996. (Cit. on pp. 88.)
- Ö. Yilmaz. *Seismic Data Analysis: Processing, Inversion and Interpretation of Seismic Data*. Society of Exploration Geophysicists, 2001. (Cit. on pp. 2.)
- Y. Zhu and A. Cangellaris. *Multigrid Finite Element Methods for Electromagnetic Field Modeling*. John Wiley & Sons, 2006. (Cit. on pp. 66.)
- O. Zienkiewicz. *The Finite Element Method in Engineering Science*. McGraw Hill, 2 edition, 1971. (Cit. on pp. 55 and 57.)
- M. Zoback. *Reservoir Geomechanics*. Cambridge University Press, 2009. (Cit. on pp. 2.)



## Résumé

Les capteurs distribués à fibre optique (aussi nommés DAS) sont une nouvelle technologie d'acquisition sismique qui utilise des câbles traditionnels à fibre optique pour fournir une mesure de la déformation le long du câble. Ce système d'acquisition est largement utilisé dans les profils sismiques verticaux (PSV). Le couplage est un facteur clé qui a une grande influence sur la qualité des données. Alors que, pour les acquisitions PSV, les géophones sont attachés à la paroi du puits, le câble de fibre optique est soit cimenté derrière le tubage, soit attaché avec des pinces rigides au tubage ou simplement descendu dans le puits. Cette dernière stratégie de déploiement donne généralement le plus petit rapport signal sur bruit, mais est considérée comme la plus rentable en particulier pour les installations dans des puits existants. Cette thèse porte sur la problématique du couplage du DAS quand le câble est simplement descendu dans le puits. Nous développons des modèles numériques pour analyser les données réelles. L'interprétation de ces résultats nous permet de conclure qu'un contact immédiat du câble avec la paroi du puits avec une force de contact calculée est nécessaire pour fournir des bonnes conditions de couplage. Sur la base de ces résultats, nous proposons des solutions pour optimiser davantage les acquisitions avec le système DAS. Nous modifions numériquement la force de contact et les propriétés élastiques du câble DAS et démontrons comment ces modifications peuvent améliorer mais aussi détériorer la qualité des données. Enfin, nous proposons un algorithme de détection du couplage qui permet d'assurer l'acquisition de données réelles avec un rapport signal / bruit élevé.

## Mots Clés

capteurs distribués à fibre optique • acquisition • profil sismique vertical • géophysique de puits •

## Abstract

Distributed Acoustic Sensing (DAS) is a new technology of seismic acquisition that relies on traditional fibre-optic cables to provide inline strain measurement. This acquisition system is largely used in vertical seismic profiling (VSP) surveys. Coupling is a key factor influencing data quality. While geophones and accelerometers are clamped to the borehole wall during VSP surveys, the fibre cable is either clamped and then cemented behind the casing, or attached with rigid clamps to the tubing, or loosely lowered into the borehole. The latter deployment strategy, also called wireline deployment, usually acquires the lowest level of signal but is regarded as the most cost-effective in particular for existing well installations. This PhD thesis addresses the problematic of coupling of DAS using wireline deployment. We develop numerical models that are used to analyse real data. The interpretation of these results allows us concluding that an immediate contact of the cable with the borehole wall with a computed contact force is required to provide good coupling conditions. Based on those findings, we propose solutions to further optimise DAS acquisitions. We numerically modify the contact force and the elastic properties of the DAS cable and show how these modifications can improve but also deteriorate data quality. Finally, we propose a coupling detection algorithm that is applied to real datasets and allows ensuring the acquisition of data with a high signal-to-noise ratio.

## Keywords

distributed acoustic sensing • acquisition • vertical seismic profiling • borehole geophysics •